THE ROLE OF OXYGEN IN HOT METAL DESULPHURIZATION WITH CALCIUM CARBIDE POWDER INJECTION

BY

YONGFU ZHAO, M.ENG.

A Thesis

Submitted to the School of Graduate Studies

in Partial Fulfilment of the Requirements

for the Degree

Doctor of Philosophy

McMaster University

THE ROLE OF OXYGEN IN HOT METAL DESULPHURIZATION WITH CALCIUM CARBIDE POWDER INJECTION

DOCTOR OF PHILOSOPHY (1992) McMASTER UNIVERSITY

(Materials Science and Engineering) Hamilton, Ontario

TITLE: The Role of Oxygen in Hot Metal Desulphurization with Calcium Carbide Powder Injection

AUTHOR: Yongfu Zhao

B.Eng. Tsinghua University, Beijing, China

M.Eng. Tsinghua University, Beijing, China

SUPERVISOR: Professor G.A. Irons

NUMBER OF PAGES: xxxvii, 338

ABSTRACT

It has been appreciated for some time that low oxygen activity is required for effective steel desulphurization, and recently this has been recognized for hot metal desulphurization. In the present experiments, calcium carbide was injected into 70 kg melts of iron during which desulphurization and deoxidation were studied by continuously measuring oxygen activity and frequently sampling for sulphur content. In some experiments, carbon dioxide was used either as a carrier gas or as generated from calcium carbide/ limestone mixtures. The experiments confirmed that the oxygen activity in hot metal was controlled by the silicon-silica equilibrium, except when aluminum was added. It was found that the rate of desulphurization was associated with the oxygen activity. The desulphurization rate increased as oxygen activity decreased in order from carbon dioxide-containing injections into iron-carbon-silicon melts, to calcium carbide/nitrogen injections into iron-carbon-silicon melts, to finally calcium carbide/nitrogen injected into iron-carbon-aluminum melts. The dependence of the incubation period with the melt oxygen activity was recognized. The incubation times coincide with periods of deoxidation before desulphurization proceeds.

In order to interpret the experimental results, a kinetic model was developed that takes simultaneous desulphurization and deoxidation into account. This model demonstrates clearly that the rate of desulphurization is controlled by the melt oxygen activity and the powder feed rate. Thus, low oxygen is required for effective hot metal desulphurization. In a log h_O-log h_S diagram, the refining trajectories determined from the kinetic model were found to be consistent with those obtained from the experiments. From the model calculations, it was found that the commercial calcium carbide which normally contains 30 per cent of lime can be employed for the melts pre-deoxidized with silicon or aluminum, without causing significant delay of desulphurization.

Another aspect of this work is the particle-liquid contact. The contact was measured by monitoring the melt temperature during injection, and applying calorimetric principles to analyze the results. It was found that a significant fraction of particles does not come in contact with the melt during their rise through it. The particle-liquid contact fraction is approximately 30-50 per cent. The same conclusion was obtained by analyzing the experimental rate constants of desulphurization on the basis of mass transfer theory.

ACKNOWLEDGEMENTS

I wish to express my sincere gratitude to my supervisor, Professor G. A. Irons, for the guidance, support, and encouragement he has given me. I gratefully acknowledge the influence he, as an educator, has had on me.

I wish to thank the members of my supervisory committee, Professor D. A. R. Kay and Professor R. H. Pelton, whose advice and recommendation proved to be beneficial. I also wish to thank Professor W-K. Lu for his encouragement and help during my study in McMaster University.

I wish to express my appreciation to the Natural Science and Engineering Research Council of Canada and Canadian International Development Agency for support of this work. The donations of iron by QIT-Fer et Titane Inc., calcium carbide by Cyanamid Canada Inc., and oxygen probes by Electro-Nite is sincerely appreciated. Special thanks are due to Messrs. O. Kelly and D. Lu for their help during experimentation.

Most importantly, I wish to express wholehearted thanks to my wife, Manli Sun, for her constant support and understanding through out the years of my education.

TABLE OF CONTENTS

LIST OF SYMBOLS

Numbers in parentheses refer to equations.

A	m^2	Area	
A_1		Constant	(5.75)
A_2		Constant	(5.75)
A_{lw}	m^2	Area of Liquid-Crucible Wall Interface	(5.14)
A_{sw}	m^2	Area of Silica-Crucible Wall Interface	(5.14)
A_{sl}	m^2	Interface Area between Liquid and Silica	(5.14)
a		Constant	(5.67)
a		Activity	(5.111)
B		Constant	(5.9)
b	s^{-1}	Constant	(5.42)
C		Constant	(5.102)
C_1		Coefficient	(5.79)
C_2		Coefficient	(5.80)
C_D		Bubble Drag Coefficient	(5.102)
C_O	%	Oxygen Content	
$C_{O,l}^*$	%	Equilibrium Oxygen Content with CaC_2	(5.62)

$C_{O.2}^{*}$	%	Equilibrium Oxygen Content with CaO	(5.62)
C_P^l	J/kg/K	Heat Capacity of Liquid Iron	
C_P^p	J/kg/K	Heat Capacity of Powder	
C_S	%	Sulphur Content	
$C_{S.1}^{*}$	%	Equilibrium Sulphur Content with CaC_2	(5.61)
$C_{S.2}^{*}$	%	Equilibrium Sulphur Content with CaO	(5.61)
C_x	%	Concentration of Species X	(5.60)
C_x^{eq}	%	Equilibrium Concentration of Species X	(5.60)
C_μ		Dissipation Constant	(5.102)
D	m/s	Diffusivity	
D	m	Diameter of Crucible	(5.103)
D_O	m/s	Oxygen diffusivity	
D_S	m/s	Sulphur Diffusivity	
d	m	Bubble Diameter	(5.4)
E	volt	Electromotive force	(2.19)
e_i^j		Interaction Coefficient of i on j	(2.1)
F		Faraday's Constant	(2.19)
f		Particle-Liquid Contact Fraction	(5.48)
f_1		Fraction of CaC_2 in Powder	(5.90)
f_2		Fraction of CaO in Powder	(5.90)
f_i		Activity Coefficient of Species i	(2.2)
Gr		Grashof Number	
ΔG	J	Free Energy Change	

g	m/s^2	The Gravitational Acceleration Constant	
H_0	W/K	Heat Transfer Constant	(5.20)
H_1	W/K	Heat Transfer Constant during Gas Injection	(5.28)
h	$W/m^2/K$	Heat Transfer Coefficient	(4.1)
h_i		The Henrian Activity of Species i	(2.2)
h_m	$W/m^2/K$	Heat Transfer Coefficient (from Melt to Wall)	(5.23)
h_O		Oxygen Activity	
ΔH	J/kg-mole	The Change of Enthalpy	
J_s	m/s	Sulphur Flux	(2.11)
K'	$s^{-1/2}$	Constant	(5.102)
K_1	$m^{1/3}$	Constant	(5.102)
K_1		Equilibrium Constant	(2.21)
K_1	s^{-1}	Mass Transfer Rate Constant to CaC_2 Particles	(5.90)
K_2	s^{-1}	Mass Transfer Rate Constant to CaO Particles	(5.90)
K_2		Equilibrium Constant	(2.21)
K_{eq}		Equilibrium Constant	(5.64)
K_m	s^{-1}	Mass Transfer Rate Constant	(5.90)
K_{OV}	s^{-1}	Overall Mass Transfer Rate Constant	(2.12)
K_S	s^{-1}	Desulphurization Rate Constant	(4.5)
K_T	s^{-1}	Bath Cooling Rate Constant Measured	(4.4)
$K_{T,0}$	s^{-1}	Bath Cooling Rate Constant (in Analysis)	(5.21)
$K_{T,1}$	s^{-1}	Bath Cooling Rate Constant of Gas Injection	(5.29)
$K_{T,2}$	s^{-1}	Bath Cooling Rate Constant of Powder Injection	(5.34)

K_x	s^{-1}	Mass Transfer Rate Constant of Species X	(5.60)
k'	s^{-1}	Constant	(5.41)
k_1	W/m/K	Thermal Conductivity of Crucible Wall	(5.23)
k_2	W/m/K	Thermal Conductivity of Lining Martials	(5.23)
k_l	W/m/K	Thermal Conductivity of Liquid Iron	(5.27)
k_m	$mole/m^2/s$	Mass Transfer Coefficient	(5.3)
k_O	m/s	Mass Transfer Coefficient of Oxygen	(5.114)
k_p	s^{-1}	Mass Transfer Rate Constant (for Permanent Reaction)	(5.104)
k_S	m/s	Mass Transfer Coefficient of Sulphur	(5.113)
k_t	s^{-1}	Mass Transfer Rate Constant (for Transitory Reaction)	(5.104)
L	m	Dimension	(5.27)
L	m	Bath Depth	(5.103)
L_p	m	Particle Travelling Distance	(5.100)
M_l	kg	Mass of Liquid Iron	
N		Numbers of Particle in Liquid	(5.99)
n_i	mole/s	Transfer Rate of Species i	(2.10)
Nu		Nusselt Number	
P	atm	Supersaturation of Homogeneous Nucleation	(5.9)
P'	atm	Supersaturation of Heterogeneous Nucleation	(5.9)
P_a	atm	Atmospheric Pressure	(5.11)
P_S	atm	Static Pressure	(5.11)

P_{CO}	atm	Pressure of CO	(5.11)
$P_{e'}$	atm	Specific Oxygen Partial Pressure	(2.19)
P'_{O_2}	atm	Oxygen Partial Pressure of Liquid Metal	(2.19)
P''_{O_2}	atm	Oxygen Partial Pressure of Reference Electrode	(2.19)
Pr		Prandtl Number	
Q	SLPM	Gas Flow Rate	
q	J/s	Thermal Effect of CaC_2 Desulphurization	(5.45)
q'	K/s	Thermal Effect of Reaction on Bath Cooling	(5.41)
R		The Gas Constant	
R	m	Radius of Vessel	(5.101)
R		Correlation Coefficient	
R	$m^2 \cdot K/W$	Thermal Resistance	(5.23)
r_{min}	m	Minimum radius of Cavity	(5.11)
r_{max}	m	Maximum radius of Cavity	(5.12)
Re		Renolds Number	
Sc		Schmidt Number	
Sh		Sherwood Number	
T	K	Temperature	
T_0	K	Initial Temperature of the Melt	
T_l	K	Temperature of Liquid Iron	
T_p	K	Temperature of Solid Particle	
T_R	K	Room Temperature	
t	s	Time	

t_c	s	Contact Time	(5.4)
t_i		Ionic Transport Number	(2.26)
U_p	m/s	Plume Velocity	(5.101)
u_b	m/s	Rising Velocity of Bubbles	(5.5)
V	m^3	Volume	
V_l	m^3	Volume of Liquid Iron	
V_t	m/s	Particle-Liquid Relative Velocity	(5.97)
v_t	m^2/s	Turbulent Kinematic Viscosity	(5.103)
W_p	g/min	Powder Flow Rate	
x		Coefficient	(2.18)
y		Coefficient	(2.18)

GREEK LETTERS

α	s^{-1}	Constant	(5.36)
α		Gas Fraction in Plume	(5.103)
α_1	s^{-1}	Constant	(5.31)
β	K^{-1}	Volume Expansion Efficiency	(5.36)
β		Fraction of Lance Submergence	(5.101)
β_1	s^{-1}	Constant	(5.31)
γ	s^{-1}	Constant	(5.36)
γ_{lw}	kg/s^2	Interfacial Tension between Liquid and Wall	(5.13)
γ_{sw}	kg/s^2	Interfacial Tension between Silica and Wall	(5.13)

γ_{sl}	kg/s^2	Interfacial Tension between Liquid and Silica	(5.13)
δ_1	m	Thickness of Crucible Wall	(5.23)
δ_2	m	Thickness of Lining Materials	(5.23)
λ		Characteristic Root	(5.71)
μ	kg/m/s	Viscosity of Liquid Iron	
ρ_g	kg/m^3	Density of Gas	
ρ_l	kg/m^3	Density of Liquid Iron	
ρ_s	kg/m^3	Density of Solid Particles	
σ	kg/s^2	Surface Tension	
τ	s	Particle Resident Time	(5.100)
τ_i	s	Incubation Time	(4.7)
ϕ		Solid-Liquid Contact Angle	(5.13)

SUBSCRIPTS

b	Bubble
g	Gas
l	Liquid
p	Particle
O	Oxygen
S	Sulphur
s	Solid
0	Diameter or Starting

SUPERSCRIPTS

i	Interface
eq	Equilibrium

LIST OF FIGURES

LIST OF TABLES

CHAPTER 1
INTRODUCTION

During the past two decades, there has been great emphasis on producing low sulphur hot metal. To accomplish this, a large number of commercial desulphurization processes have been developed, such as liquid-basic slag practice, and injection processes for lime, calcium carbide powder and various magnesium based reagents. One of the major advantages of pneumatic powder injection is that it can provide much greater reagent-melt contact area than top slag, and thus increase reaction rates. So far, considerable efforts have been made that improve our understanding of thermodynamics and kinetics of injection metallurgy. However, there are still many gaps in our knowledge, especially, in the aspects of transport phenomena: mass transfer, heat transfer and fluid dynamics during powder injection.

One important issue associated with lime and calcium carbide injection is the role of oxygen activity in hot metal desulphurization. From a thermodynamic point of view, it has been recognized for some time that low oxygen activities are required to obtain low sulphur levels, but its effect on the kinetics has not been satisfactorily clarified. Desulphurization of hot metal by

submerged calcium carbide injection was recently studied in detail by Chiang et al. [1]. They found that low oxygen activity was correlated with low sulphur content. However, no further analysis from a kinetic point of view was presented.

The primary aim of this study is to clarify the role that oxygen plays in the kinetics of hot metal desulphurization. In the present experiments in which calcium carbide was injected into 70 kg melts, desulphurization and deoxidation were studied by continuously measuring oxygen activity and frequently sampling for sulphur content. The oxygen activities were varied by changing the silicon contents (0.1-2.0 percent), and aluminum contents (0.001-0.2 percent). In some experiments, carbon dioxide was used (either as a carrier gas or as generated from calcium carbide/limestone mixtures) to simulate the effect of limestone decomposition, which is used to enhance stirring in practice.

Obviously, accurate knowledge of reaction area is important for model calculations. During powder injection, some particles may be suspended in bubbles, others positioned on the bubble interfaces or dispersed in the liquid. It is very difficult to measure the fraction of the particles which come into contact with liquid directly. Farias and Irons injected sand into liquid lead and observed that the bath cooling rate was only 30 percent of that which would be expected if all the particles were in the melt [2]. Stimulated by their finding, the bath cooling rate of liquid iron was measured very carefully during powder injection to determine the fraction of calcium carbide particles in contact with the melt.

In order to interpret the experimental results, a kinetic model was developed that takes simultaneous desulphurization and deoxidation into account. This model demonstrates clearly the role of oxygen in hot metal desulphurization. It points the way for steelmakers to determine proper injection conditions and melt compositions to reduce desulphurization cost, and for suppliers to develop better combinations of desulphurization reagents which are more effective and less expensive.

CHAPTER 2
LITERATURE REVIEW

Sulphur is one of the most harmful elements affecting steel quality. The hot metal sulphur content has a direct effect on steel sulphur content. External desulphurization has become the first step towards low sulphur steel specifications mainly due to the following reasons [3-6]:

- Although thermodynamic conditions favour sulphur removal from hot metal within the blast furnace, low sulphur operation requires high quality and low sulphur raw materials, high basicity slag, high slag volume and high operating temperature. As a result, it raises the silicon content of hot metal and causes a significant loss in blast furnace productivity. External desulphurization removes this restriction on the blast furnace, thereby higher productivity and flexibility of operation can be achieved.

- Although high basicity slag can be generated within the BOF (Basic Oxygen Furnace), the oxidizing conditions that prevail in the BOF process adversely affect the transfer of sulphur from metal to slag. The sulphur transferred to the slag during steelmaking is about one-half or one-third

that present in the hot metal. To increase the production capacity and reduce the operating cost, a recent trend has been to separate desulphurization from the BOF process and to limit its function to heating and decarburization.

- External hot metal desulphurization has two significant advantages. Firstly, carbon and silicon in hot metal increase the activity of sulphur and decrease the activity of oxygen, thus, the removal of sulphur from hot metal is easier than from steel. Secondly, by far, submerged gas-powder injection has become the most common technique used for hot metal external desulphurization. It can provide much greater reagent-melt contact area than top slag, and create intensive stirring in the melt. Thereby, rapid and effective desulphurization can be achieved during hot metal external treatment.

Many investigations have been conducted in hot metal desulphurization. For extensive reviews, one may refer to references [7-11]. This chapter is concerned with the following aspects:

- desulphurization and deoxidation equilibria in hot metal
- the rate phenomena of hot metal desulphurization during calcium carbide injection and
- the determination of oxygen activity in hot metal

2.1 DESULPHURIZATION AND DEOXIDATION EQUILIBRIA IN HOT METAL DURING CALCIUM CARBIDE INJECTION

A knowledge of the thermodynamics of desulphurization and deoxidation is necessary for a clear understanding of the refining processes. In this section, all data are taken from research paper compilations [12-27]. The thermodynamic data for this thesis will be selected on the basis of comparison of the data available. For this thesis, the following standard states are adopted: one atmosphere for gases, one per cent solution in liquid iron for solutes with the reference state as infinite dilution.

Selected free energies of solution in liquid iron are listed in Table 2.1. It can be seen that there is not much difference in the data recommended by references [12-14]. The data selected for this thesis are taken from reference [12], considering that it has been widely used by researchers in the steel industry.

The standard free energy changes of deoxidation by some alloying elements in liquid iron are listed in Table 2.2. For the silicon and carbon deoxidation reactions, it can be seen that the thermodynamic data recommended by references [15] and [13] are very close. The free energy-temperature dependence of aluminum deoxidation in liquid iron is shown in Figure 2.1. Discrepancies among the data of references [13-18] are approximately within ±5 per cent of the average value. The data selected for this thesis are taken from reference [15], considering that it has been widely used by steelmakers.

TABLE 2.1

FREE ENERGY OF SOLUTIONS OF SELECTED ELEMENTS [a]

Reaction	ΔG^{O} (J)	Reference
$\frac{1}{2}O_2$=O(1 wt%)	-117200-2.89T -117100-3.39T	Sigworth & Elliott [12] JSPS [13]
$\frac{1}{2}S_2$=S(1 wt%)	-135100+23.43T -125100+18.5T	Sigworth & Elliott [12] JSPS [13]
Si(l)=Si(1 wt%)	-131500-17.24T	Sigworth & Elliott [12] JSPS [13]
Al(l)=Al(1 wt%)	-63180-27.91T -71100-19.4T -62800-27.93T	Sigworth & Elliott [12] JSPS [13] Fruehan [14]

a The data selected for this thesis are taken from reference [12].

TABLE 2.2

FREE ENERGY OF SOME DEOXIDATION REACTIONS IN LIQUID IRON

ΔG^{O} (J)	Reference
$\underline{C}$(1 wt%)+$\underline{O}$(1 wt%)=CO(g)	
-22400-39.69T [a] -22200-38.34T	Elliott et al. [15] [b] JSPS [13]
$\underline{Si}$(1 wt%)+2$\underline{O}$(1 wt%)=SiO_2(s)	
-594600+230.3T [a] -576400+218.2T	Elliott et al. [15] [b] JSPS [13]
2$\underline{Al}$(1 wt%)+3$\underline{O}$(1 wt%)=Al_2O_3(s)	
-1243000+377.9T [a] -1225000+393.8T -1207000+373.1T -1215000+381.6T -1206000+390.7T	Elliott et al. [15] [b] JSPS [13] Turkdogan [16] [b] Ghosh & Kay [17] [b] Schenck et al. [18]

a The data selected for this thesis are taken from reference [15].

b ΔG^{O} is calculated from ΔG^{O} of solutions (See Table 2.1) and ΔG^{O} given by the references for oxide formation from elements in their standard states.

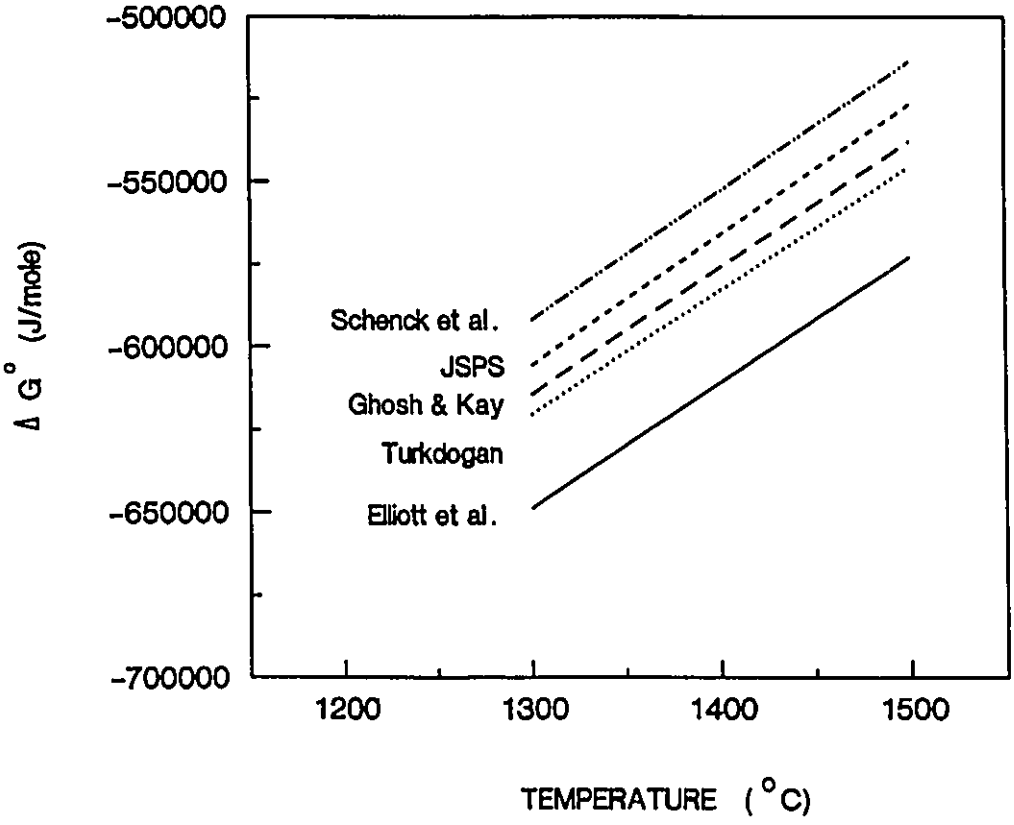

Figure 2.1 The free energy-temperature dependence of aluminum deoxidation in liquid iron (Refer to Table 2.2)

The standard free energy of CaO formation is a very important thermodynamic property in metallurgical processes. The value available in JANAF is generally accepted [19]. However, a question about the validity of this value has been recently raised by Kay and Subramanian [20]. They derived a quite different value from Edmunds and Taylor's data [21] (See the annotation of Table 2.3). The data from selected references are given in Table 2.3, and temperature dependence of the standard free energy is illustrated in Figure 2.2.

The value of the free energy of CaO formation which is derived from the experimental data of Edmunds and Taylor [21] is quite different for those generally accepted ([15,19]). Using those data, one may calculate the free energy for the reaction of calcium carbide with oxygen dissolved in carbon saturated liquid iron. The free energy data from selected references are given in Table 2.4.

For hot metal desulphurization with calcium carbide, the equilibrium of oxygen-sulphur-lime-calcium sulphide has a particular importance, because the commercial calcium carbide always contains a proportion of lime, which takes part in the reaction. Also, some calcium carbide reacts with oxygen and forms oxide, which may continue to react with sulphur. The selected thermodynamic data are given in Table 2.5.

The values for the activity coefficient and interaction parameters of elements in iron alloy have been compiled by several authors [12,13,15]. In the case of using weight percent, the activity coefficient f_i is defined by

TABLE 2.3

FREE ENERGY OF CaO FORMATION

ΔG^{O} (J) $Ca(l)+½O_2(g)=CaO(s)$	Reference
-628000+118T	Wakasugi & Sano [22]
-564000+108T	Edmunds & Taylor [21] [a]
-642000+111T	JANAF [19]
-640000+108T	Elliott et al. [15]
-631000+95.7T	Rai & Gregory [23]
-645000+111T	Sata et. al [24]

a Originally, based on Edmunds and Taylor's data [21], Kay and Subramanian calculated the standard free energy of CaO formation from calcium vapour only [20]. In the same way, Wakasugi and Sano did their calculation and presented this equation for liquid calcium [22].

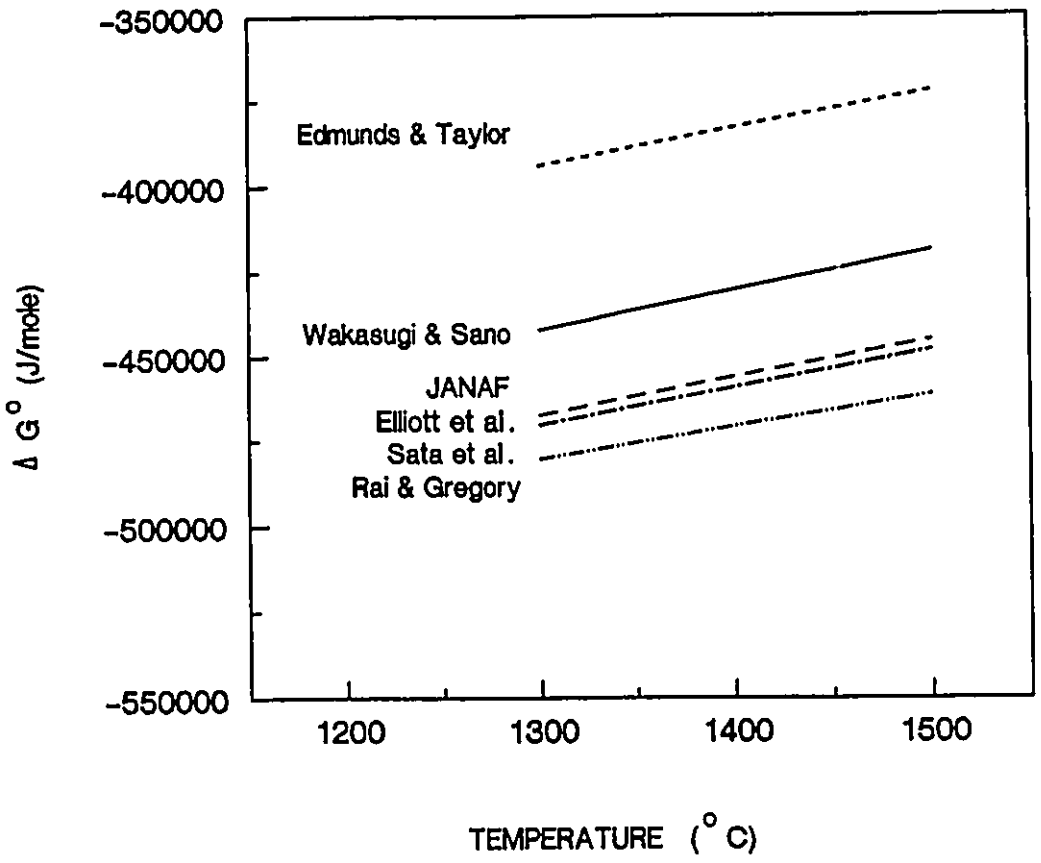

Figure 2.2 The free energy-temperature dependence of CaO formation in liquid iron (Refer to Table 2.3). The difference between the results of Elliott et al. and Sata et al. is less than one per cent. Thus, these two lines coincide with each other in this diagram.

TABLE 2.4

FREE ENERGY OF CaC_2 DEOXIDATION

ΔG^O (J) for Reaction $CaC_2(s)+\underline{O}(1\ wt\%)=CaO(s)+2C(s)$	Reference
-462500+129.7T [a]	Elliott et al. [15] [b]
-462800+132.0T	Kubaschewski [25] [b]
-386600+131.4T	Edmunds & Taylor [21] [b,c]
-465000+139.2T	Riboud and Olette [26]

a This one is selected for this thesis, considering that at 1350°C, the differences in the results given by references [15], [25] and [26] are less than 5 per cent. The value calculated from reference [21] is about 30 per cent greater than those calculated from other references, therefore, it is excluded from consideration.

b ΔG^O is calculated from ΔG^O of solutions (See Table 2.1) and ΔG^O given by the references for the reaction:

$$Ca(l)+\frac{1}{2}O_2(g)-CaO(s)$$

c See the annotation of Table 2.3.

TABLE 2.5

FREE ENERGY OF CaO-CaS EQUILIBRIUM [a]

ΔG (J) for Reaction CaO(s)+S(1 wt%)=CaS(s)+O(1 wt%)	Reference
104800-21.05T [b]	Elliott et al. [15]
106300-25.75T	Kubaschewski [25]
109400-26.57T	Kumar & Kay [27]
113800-34.08T	Riboud & Olette [26]

a ΔG^O is calculated from ΔG^O of solutions (See Table 2.1) and ΔG^O of the following reaction (Refer to the references listed in this table):

$$CaO(s)+\frac{1}{2}S_2(g)=CaS(s)+\frac{1}{2}O_2(g)$$

b This one is selected for this thesis, considering that at 1350°C, the differences in the results given by references [15], [25] and [27] are less than 10 per cent. The value calculated from reference [26] is about 20 per cent greater than those calculated from other references, therefore, it is excluded from consideration.

$$f_i = \frac{h_i(\%)}{[\%i]} \tag{2.1}$$

$$\log f_i = \sum_{j=2}^{n} e_i^j \cdot [\%j] \tag{2.2}$$

where, [%i] is the weight percent of i, h_i is the Henrian activity with reference to hypothetical one per cent solution. Selected first order interaction coefficients required in the present work are listed in Table 2.6.

From the known free energy changes of deoxidation and desulphurization in liquid iron, Kay and Kumar have developed a h_O-h_S phase stability diagram (as shown in Figure 2.3 for 1500°C [28]). It shows that CaC_2 is an effective deoxidizer and desulphurizer of hot metal; lime also has a great desulphurization power, but does not control oxygen potential by itself. One can see that a greater driving force of desulphurization by CaO can be expected by adding reactive elements, like silicon, aluminum and magnesium into the melt, or using lime-calcium carbide mixture to lower the oxygen activity of the melt.

TABLE 2.6

FIRST ORDER INTERACTION COEFFICIENTS IN LIQUID IRON ALLOY

i	j	Sigworth & Elliott [12]		JSPS [13]		Used in This Work
		Temperature Dependence	1600°C	Temperature Dependence	1600°C	1350°C [a]
C	Al	n.a [b]	0.043	n.a	0.043	0.043
O	Al	-20600/T+7.15	-3.9	n.a	-1.17	-3.9
S	Al	n.a	0.035	n.a	0.041	0.035
Si	Al	n.a	0.058	n.a	0.058	0.058
C	C	158/T+0.0581	0.14	n.a	0.243	0.16
O	C	n.a	-0.45	n.a	-0.421	-0.45
S	C	n.a	0.11	n.a	0.111	0.11
Si	C	380/T-0.023	0.18	380/T-.023	0.18	0.22
C	Si	162/T-0.008	0.08	162/T-0.008	0.08	0.09
O	Si	n.a	-0.131	n.a	-0.066	-0.13
S	Si	n.a	0.063	n.a	0.075	0.063
Si	Si	34.5/T+0.089	0.11	n.a	0.103	0.11

a The data compiled by Sigworth and Elliott [12] are very close to the data recently recommended by JSPS [13]. In this thesis, the interaction coefficients are selected from reference [12], considering that the standard free energy data are selected from references [12] and [15]. The interaction coefficients for 1350°C are calculated from the temperature dependence when they are available; otherwise, the data of 1600°C are adopted.

b n.a = not available

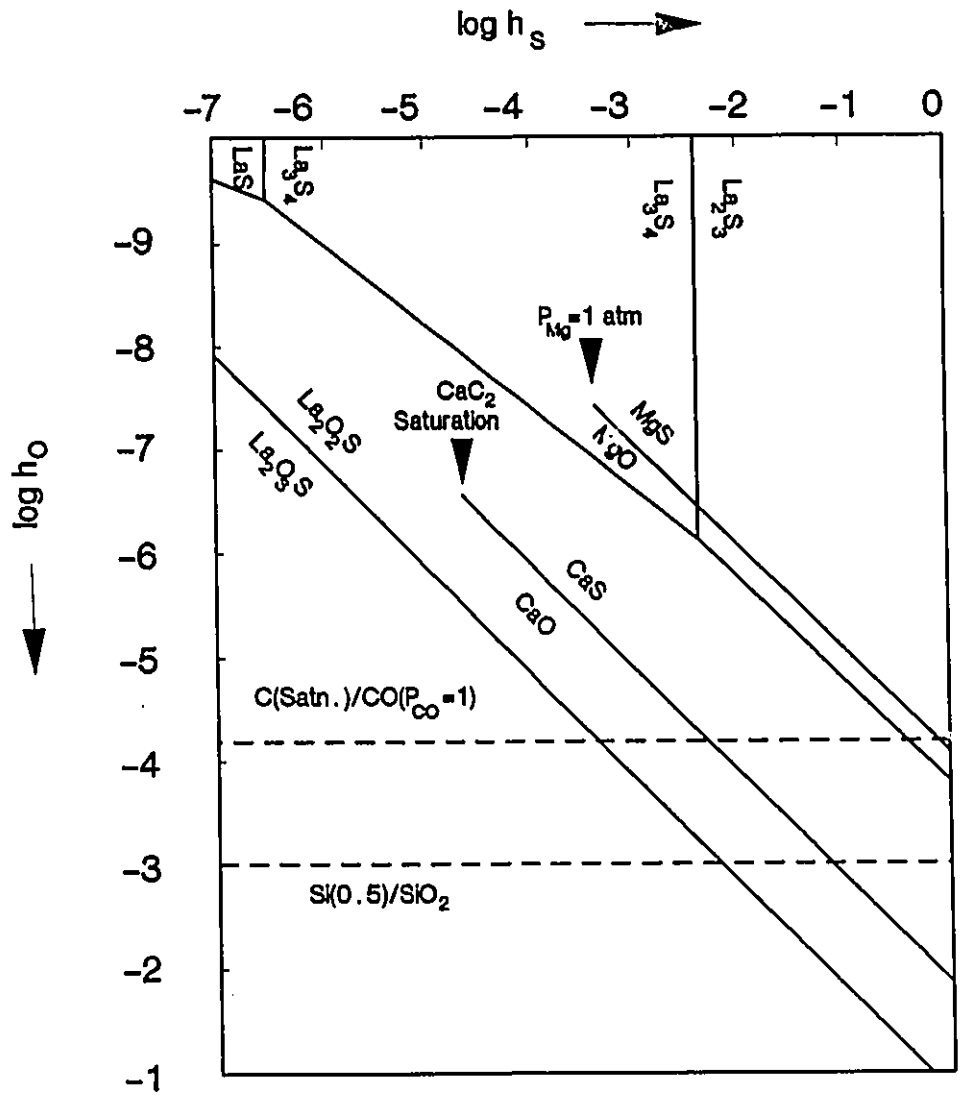

Figure 2.3 M-S-O phase stability diagram for carbon saturated liquid iron at 1500°C (M = Ca, Mg, and La), taken from [28].

2.2 THE DESULPHURIZATION RATE PHENOMENA DURING CALCIUM CARBIDE POWDER INJECTION IN HOT METAL

The kinetics of the desulphurization reaction has been a subject of metallurgical interest for several decades. Various aspects of rate phenomena have been studied to improve desulphurization processes. This section is concerned with the following aspects:

- sulphur transfer between slag and metal
- the reaction mechanism of CaO and CaC_2 desulphurization
- the rate phenomena during submerged powder injection
- the desulphurization reaction paths

2.2.1 Sulphur Transfer between Slag and Metal

The first quantitative studies of the rate of transfer of sulphur from carbon saturated iron to $CaO-Al_2O_3-SiO_2$ slags, which were conducted by Chang and Goldman [29], Goldman, Derge and Philbrook [30], showed that the reaction follows first order kinetics, in that the rate of transfer is proportional to the concentration of sulphur in the metal. A straight line can be obtained for the early stages of the reaction if the logarithm of the sulphur content of the metal is plotted against time. These findings were confirmed by other classic studies [31-32]. Goldman et al. also found that C, Si, Mn, and Al increase the rate of desulphurization [30], which was independently observed by Turkdogan et al.

[33]. These authors explained the observed influence of the solute elements Al, Mn and Si as being due to their removal of oxygen dissolved in the metal phase and presented the overall sulphur reaction as

$$[S]+(O)=[O]+(S) \tag{2.3}$$

The nature of the sulphur transfer reaction can be explained by using the electrochemical theory [34,35]. Ramachandran et al. measured simultaneously the rates of transfer of all reacting elements during desulphurization and the evolution of CO gas between carbon saturated-iron and $CaO-Al_2O_3-SiO_2$ slags [34]. This study showed conclusively that the transfer of sulphur from metal to slag is accompanied by exchange of electrons between the reacting species:

$$\underline{S}+2e^- = (S^{2-}) \tag{2.4}$$

$$\underline{Fe} = (Fe^{2+})+2e^- \tag{2.5}$$

$$\underline{Si} = (Si^{4+})+4e^- \tag{2.6}$$

$$\underline{Mn} = (Mn^{2+})+2e^- \tag{2.7}$$

$$\underline{Al}-(Al^{3+})+3e^- \tag{2.8}$$

$$\underline{C}+(O^{2-})-CO+2e^- \tag{2.9}$$

The transfer of sulphur should satisfy the stoichiometric requirements

$$2n_S-2n_{Fe}+2n_{Mn}+3n_{Al}+4n_{Si}+2n_C \tag{2.10}$$

where, the sign of n is the transfer rate in mole/s. Based on the principles of electrochemical theory and irreversible thermodynamics, Lu et al. developed a kinetic model, which suggests that the rate of interfacial chemical reactions are determined by the electrical potential differences across the interface [36]. Their model has not been employed in quantitative predictions of the rate controlling steps, because it is very difficult to determine the concentration of free oxygen ions in slags and the phenomenological coefficients in their linear equations. Even so, their work has led to a better understanding of the electrochemical nature of the sulphur transfer kinetics.

In order to describe desulphurization kinetics quantitatively, another approach has been developed and widely used by many researchers [37-50]. This approach assumes that chemical equilibria are reached at the slag-metal interface, and the desulphurization rate is determined by the mass transfer in metal and slag phases.

According to the mass transfer theory, the sulphur flux, J_S, is proportional to the overall driving force:

$$J_S = k_S(C_S - C_S^{eq}) \tag{2.11}$$

where, k_S is the conventional mass transfer coefficient (m/s), C_S is the sulphur content and C_S^{eq} is the equilibrium sulphur content (mol/m^3). According to Equation (2.11), the desulphurization rate can be reasonably described by

$$\frac{dC_s}{dt} = -K_{ov}\left(C_S - C_S^{eq}\right) \tag{2.12}$$

K_{ov}, the overall mass transfer rate constant (1/s) is given by

$$K_{ov} = \frac{k_S A}{V} \tag{2.13}$$

where, A is the contact area between slag and metal (m^2), V is the volume of the melt (m^3).

Based on the assumption of mass transport control, Robertson et al. developed a more general multicomponent kinetic model [40]. They considered that the sulphur transfer during desulphurization is accompanied by the transfer of some other components. They reported that the results calculated with their

model were in good agreement with the experimental data presented by Kim [41] and King and Ramachandran [30].

Equation (2.12) has been used in many studies [1,42-46]. At the initial desulphurization stage or with basic slag, C_S^{eq} is much smaller than C_S, it is reasonable to ignore the second term in Equation (2.12), resulting in

$$\frac{dC_S}{dt} = -K_{ov}C_S \qquad (2.14)$$

This equation has been widely applied to analyze the desulphurization rate in steelmaking [47-50].

2.2.2 Desulphurization Mechanism of Liquid Iron by Solid CaO and CaC_2

(1) CaC_2 Desulphurization

For the case of calcium carbide desulphurization, Oeters [51] suggested that because calcium carbide and calcium sulphide form a solid solution, the reaction could be expressed as

$$2CaC_2 + \underline{S} = Ca_2(C_2,S) + 2\underline{C} \qquad (2.15)$$

where, $Ca_2(C_2,S)$ represents the solid solution of calcium carbide and sulphide. Desulphurization proceeds by counter-current diffusion of S^{2-} and C_2^{2-}, developing opposing gradients of sulphur and carbon [51]. Talballa et al. investigated the desulphurization of liquid iron with solid CaC_2 and CaO by placing a small melt of the carbon-sulphur-iron alloy in a small crucible made of the desulphurizer, CaC_2 or CaO [52]. The mechanism of CaO desulphurization will be discussed later. According to their results, calcium carbide first decomposes to form graphite and calcium vapour. The calcium vapour then reacts with the sulphur in the iron to form a layer of calcium sulphide over the graphite layer. The layers of graphite and calcium sulphide progressively thicken, so that the calcium vapour must diffuse through them [52]. Based on Talballa's experimental data, Chiang et al. explained the phenomena occurring at the surface of injected CaC_2 particles. Chiang et al. indicated that during powder injection, sulphur is less likely than calcium to be the dominant transport species in the porous product layer. They calculated the thermodynamic equilibrium partial pressures of sulphur and calcium vapour which is produced by thermal decomposition of calcium carbide, and then compared the diffusion rates of sulphur and calcium vapour through the product layer. They found that the rate of calcium diffusion through the product layer is 50 times greater than the rate of sulphur diffusion through the particle-liquid boundary layer. Therefore, Chiang et al. concluded that the desulphurization rate is determined by the rate at which sulphur diffuses through the liquid boundary layer to the particles, rather than the product layer [1].

(2) CaO Desulphurization

The mechanism of CaO desulphurization has been studied more extensively. The overall reaction is

$$CaO(s)+\underline{S}=CaS(s)+\underline{O} \qquad (2.16)$$

If the oxygen activity in hot metal is controlled by silicon, the oxygen released by lime desulphurization may react with silicon:

$$4CaO(s)+2\underline{S}+2\underline{Si}=2Cas(s)+2CaO\cdot SiO_2(s) \qquad (2.17)$$

The formation of a layer of lime-silicate on the lime surface seriously hinders the diffusion of sulphur into lime grains.

The presence of aluminum in carbon-saturated liquid iron was shown to improve desulphurization attained with lime desulphurizers [53-56]. The reaction may be expressed as

$$xCaO(s)+2y\underline{O}+3y\underline{Al}=(CaO)_x\cdot(Al_2O_3)_y \qquad (2.18)$$

where, x and y can be determined by the $CaO-Al_2O_3$ phase diagram. Niedringhaus explained that at 1450°C, a temperature above the lime-alumina eutectic, at least a portion of the calcium aluminate exists as a liquid. The formation of this fluid phase on the lime particles facilitates the penetration of sulphur into each lime particle. At 1350°C, below the eutectic, any calcium aluminate phase formed during desulphurization remains a solid. Before significant solid layer formation has occurred, aluminum may improve the desulphurization reaction through deoxidation of the melt. However, after the reaction has progressed, significant solid product layer formation occurs on each lime particle, and aluminum appears to have no beneficial effect on desulphurization [56].

On the other hand, Oeters suggested that during lime powder injection, the desulphurization rate was controlled by the transport of sulphur through the liquid boundary layer [57]. As mentioned above, Talballa et al. placed iron-carbon-sulphur alloys into CaO crucibles. They observed that a rapid desulphurization occurred first which lasted about 3 minutes, then, a slow desulphurization proceeded. The solid CaS product layer was found after 2 minutes of desulphurization and apparently formed on the CaO side of the interface. They further indicated that fine powder permits rapid desulphurization without the development of the heavy film of reaction products [52]. Based on an analysis of some experimental data, recently, Deo and Grieveson confirmed that the rate controlling step of desulphurization in molten iron is mass transport in the metal phase [58].

2.2.3 Rate Phenomena during Submerged Powder Injection

The reaction mechanisms of submerged powder injection are more complicated. There are two possible reaction modes [46]:

(1) Transitory reaction which is the reaction between the liquid and powder particles dispersed in and rising through the plume.

(2) Permanent reaction which is the reaction between slag and metal.

Several numerical models have been developed to simulate the powder injection process [1,45,46]. They were based on the assumption that both permanent and transitory reactions were controlled by mass transfer of sulphur. El-Kaddah and Szekely developed a numerical model on the basis of fluid flow and particle motion and distribution [45]. Ohguchi and Robertson developed a relatively simple model which allowed them to calculate the contributions of permanent and transitory reactions separately [46]. Recently, Chiang et al. investigated the transport phenomena and chemical reactions occurring in the plume during calcium carbide injection [1]. As shown in Figure 2.4, the gas and particles penetrate into the liquid and form a plume. The particles may be positioned on the bubble interface or dispersed in the liquid. Only the particles in contact with the liquid react as they rise. Chiang et al. proposed two possible controlling steps for desulphurization in the plume:

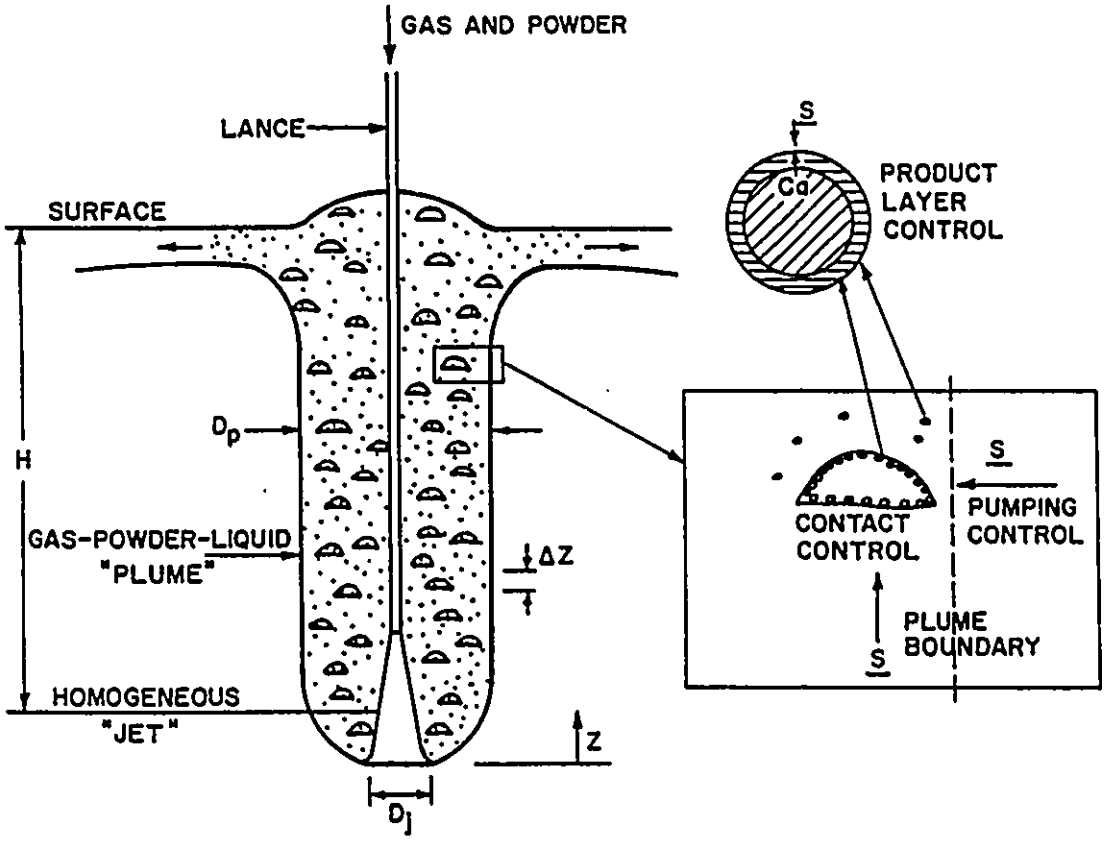

Figure 2.4 Schematic representation of the physical and chemical phenomena in the rising plume. The carrier gas and injected particles rise and react through the plume. The inset indicates that particles may be on the bubble interfaces or in the liquid. At individual particles, calcium vapour diffuses through the product layer [1].

(1) The rate at which sulphur-rich liquid is pumping into the plume by entrainment. This is pumping control.

(2) The rate at which sulphur diffuses through the boundary layer to particles. This rate depends on whether the particles are located in liquid or in the bubbles. This is contact control.

Chiang et al. developed a three-phase plume model which included mass transfer, heat transfer, momentum transfer and chemical reactions [1]. Their work demonstrated that the particle-liquid contact governed the rate of mass transfer. The first quantitative study of the particle-liquid contact was made by Farias and Irons [2]. They injected sand into liquid lead and observed that the bath cooling rate was only 30 per cent of that which would be expected if all the particles were in the melt. The particle-liquid contact is an important aspect of powder injection. More discussion will be given in Section 5.2.2.

2.2.4 Desulphurization Reaction Paths

When liquid iron undergoes desulphurization and deoxidation reactions, by combining the knowledge of thermodynamics and kinetics, various reaction paths can be shown in a two-dimensional diagram. Kay et al. used a [%O]-[%S] diagram showing the possible sequence of reactions which take place when rare earths are added to liquid steel containing different oxygen [58]. Based on an assumption of thermodynamic equilibrium between the reaction products and

the melt, they discussed several cases of precipitation and separation of oxide/oxysulphide, then, predicted possible reaction paths for sequential and coupled deoxidation-desulphurization reactions. Ototani et al. investigated the rate phenomena of lime desulphurization in liquid iron with aluminum addition, and plotted their experimental data on a log [%S]-log [%O] diagram [47]. This diagram clearly showed that deoxidation and desulphurization proceeded simultaneously. However, no further explanation was made.

2.3 OXYGEN DETERMINATION IN HOT METAL

After Kiukkola and Wagner successfully used zirconia as the solid electrolyte in the study of high temperature reactions [59], a great deal of research work has been done on the development of galvanic oxygen sensors for determination of oxygen activity in liquid metals. For extensive reviews, one may refer to references [60-67]. This section will focus on the particular points related to the measurement of oxygen activity in hot metal.

Early attempts to measure the oxygen activity in hot metal, as opposed to steel, using commercial single-use probes were not very successful. The experimental data of those measurements were scattered in a wide range [68].

The unsatisfactory performance of oxygen probes in hot metal is believed to be associated with its low oxygen activity, high carbon and silicon or

aluminum contents [69,70]. Low oxygen activity may bring about the following problems: considerable electronic conduction, polarization at one or both electrodes, and chemical reaction with other elements, or dissolution in hot metal. The following text will discuss the possible errors induced by these factors and compare the problems encountered in hot metal with those in liquid steel.

2.3.1 Ionic and Electronic Conduction

Magnesia-stabilized zirconia tubes are commonly used in commercial oxygen probes for the determination of oxygen activity of liquid metal. The oxygen reference electrode is a mixture of chromium and chromic oxide (Cr_2O_3). The cell is represented as

$$Mo(s)|Cr-Cr_2O_3(s)|ZrO_2(MgO)|[O]_{Fe}|Mo(s)$$

When the cell is immersed in liquid iron, the emf signal generated is related to the dissolved oxygen in melt. The relationship between oxygen partial pressures and emf is expressed as

$$E=\frac{RT}{F}\ln\frac{P''^{1/4}_{O_2}+P^{1/4}_{e'}}{P'^{1/4}_{O_2}+P^{1/4}_{e'}} \qquad (2.19)$$

where, R is the gas constant, F is the Faraday constant. T is the temperature in degrees Kelvin, E is the open-circuit cell voltage, P'_{O_2} and P''_{O_2} are the oxygen partial pressures at each electrode, and the parameter P_e is the partial pressure of oxygen at which the ionic and electronic conductivities are equal [71].

The oxygen partial pressures of the melt and the reference electrode are determined from the following thermodynamic data [12]

$$O_2(g) = 2\underline{O}(1wt\%)$$
$$\Delta G^o = -RT\ln K_1 = -234300 - 5.77T \quad (J) \tag{2.20}$$

$$K_1 = \frac{h_o^2}{P'_{O_2}} \tag{2.21}$$

and

$$\frac{4}{3}Cr(s) + O_2(g) = \frac{2}{3}Cr_2O_3(s)$$
$$\Delta G^o = -RT\ln K_2 = -754650 + 171.7T \quad (J) \tag{2.22}$$

$$K_2 = \frac{1}{P''_{O_2}} \tag{2.23}$$

Substituting K_1 and K_2 into Equation (2.19), when $P''_{O_2} > P'_{O_2}$, gives

$$h_o = \left\{ \frac{\left(\frac{K_1}{K_2}\right)^{1/4}}{\exp\left(\frac{EF}{RT}\right)} + \frac{(K_1 P_{e'})^{1/4}\left[1-\exp\left(\frac{EF}{RT}\right)\right]}{\exp\left(\frac{EF}{RT}\right)} \right\}^2 \qquad (2.24)$$

when $P''_{O_2} < P'_{O_2}$,

$$h_o = \left\{ \left(\frac{K_1}{K_2}\right)^{1/4} \exp\left(\frac{EF}{RT}\right) + (K_1 P_{e'})^{1/4}\left[\exp\left(\frac{EF}{RT}\right)-1\right] \right\}^2 \qquad (2.25)$$

It has been found that the values of the parameter $P_{e'}$ depend on the impurity contents, the phase composition, the microstructure and the temperature. The temperature dependence of $P_{e'}$ and the chemical composition of several $ZrO_2(MgO)$ electrolytes, which are currently available [72-75], are given in Table 2.7.

The influence of ionic and electronic conduction is described by the ionic transport number, t_i. This number is a function of the parameter $P_{e'}$ and the oxygen partial pressure of liquid metal Po_2 [76].

$$t_i = \frac{1}{1+\left(\frac{P_{e'}}{P_{O_2}}\right)^{1/4}} \qquad (2.26)$$

As shown in Figure 2.5, the ionic transport number is related to the parameters P_e, as well as oxygen activity. For example, if the oxygen activity is 0.5×10^{-4}, the ionic transport number, t_i, varies in the range of 0.75 to 0.95. The equations of P_e used in the calculation are given in Table 2.7. The electronic conduction becomes less significant at higher oxygen activities.

Figure 2.6 is a comparison between the values of t_i at ironmaking and steelmaking temperatures, based on the value of P_e given by Janke and Richter [67] (See No.3 in Table 2.7). According to Turkdogan and Fruehan [64], zirconia can be used at 1600°C down to oxygen partial pressures of about 3×10^{-13} atm, which corresponds to oxygen activity of about 10^{-3} in unalloyed iron, and does not exhibit significant electronic conductivity. This value of oxygen activity corresponds to an ionic transfer number about 0.8 (See the broken line in Figure 2.6). At 1350°C, an ionic transport number of 0.8 corresponds an oxygen activity less than 0.1×10^{-4} (See the solid line in Figure 2.6). Thus, when zirconia oxygen cells are used in hot metal, although the oxygen activities in hot metal are much lower than in liquid steel, the degree of electronic conduction is in the same range as in liquid steel.

According to Equations (2.24) and (2.25), the oxygen activities can be calculated from emf readings. The emf-h_O conversions are shown in Figure 2.7. Different P_e values (as tabulated in Table 2.7) have been used in the calculations. The solid line represents the case of ionic conduction only. At emf of -150 mv, the maximum difference between the calculated oxygen activities is 0.081×10^{-4}.

The relative error is about 40 per cent. At emf of -50 mv, the maximum difference between the calculated oxygen activities is 0.075×10^{-4}. The relative error is about 8.8 per cent. As can be seen in Chapter 4, most of the experiments were performed at 1350°C, and the typical oxygen activity of the melts was about 10^{-4}, corresponding to an emf reading of -50 mv approximately. Thus, under the present experimental conditions, the relative error caused by uncertainty of P_{e^-} will be less than 10 per cent based on the value of P_{e^-} given in Table 2.7.

TABLE 2.7

CHEMICAL COMPOSITION OF ZrO_2(MgO) SOLID ELECTROLYTE

Analysis % (by mass)						log P_{e^-}	No.	Ref
MgO	CaO	SiO_2	Al_2O_3	Fe_2O_3	TiO_2			
3.1	0.3	0.6	1.3	0.1	0.1	-67956/T+22.77	1	[73]
1.6	5.5	0.15	1.0	0.4	n.a[a]	-68400/T+21.59	2	[67]
2.4	0.2	0.3	0.15	0.05	n.a	-74370/T+24.42 [b]	3	
5.4	0.4	0.2	0.4	0.05	0.11	-65000/T+20.33	4	[74]
3.1	0.4	0.2	0.4	0.05	0.14	-64500/T+20.40	5	

a n.a = not available.

b The chemical composition of the solid electrolyte used in our experiments (See Table 3.2) is close to this type of zirconia oxide, thus, this equation is selected for the calculations of this work.

fig24

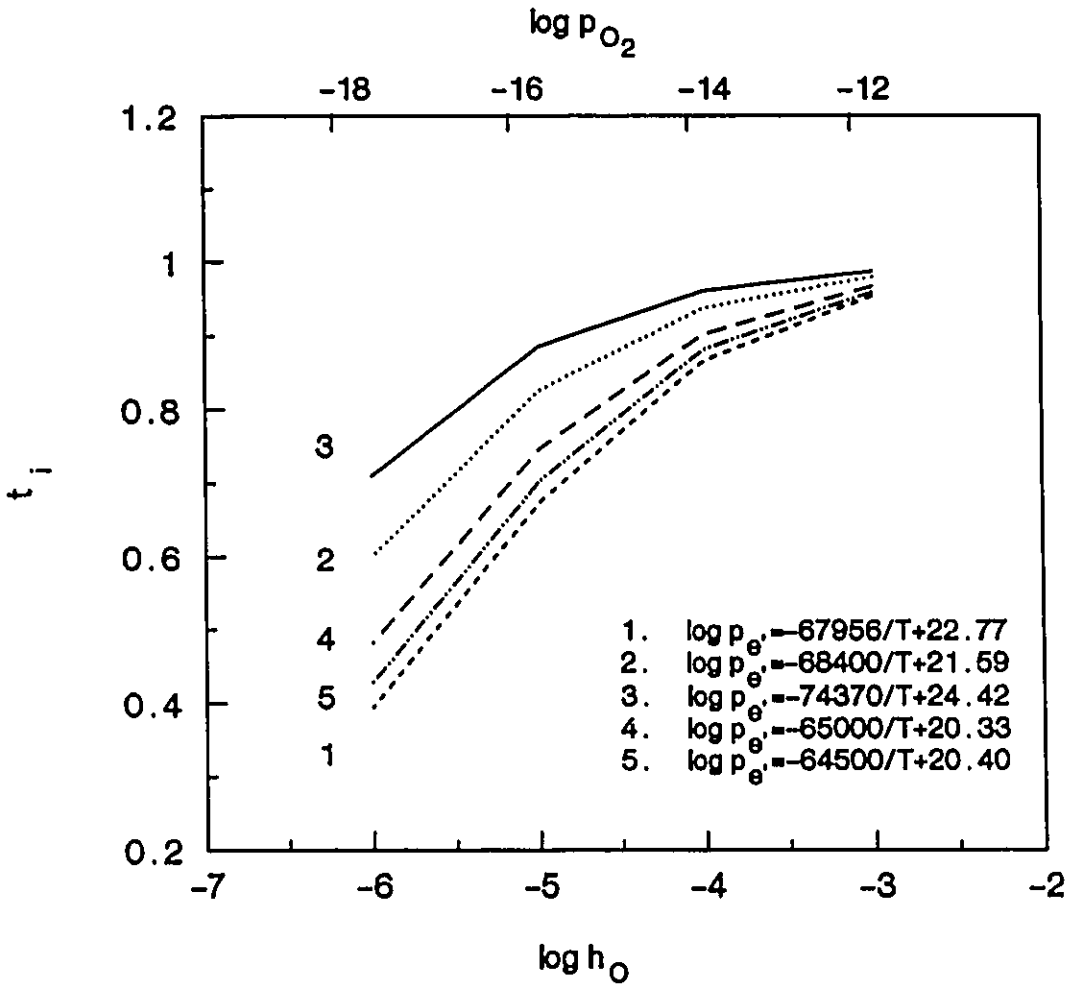

Figure 2.5 The ionic transport number t_i is a function of parameter $P_{e'}$, plotted in a typical range of oxygen activity of hot metal at 1350°C for electrolytes in Table 2.7.

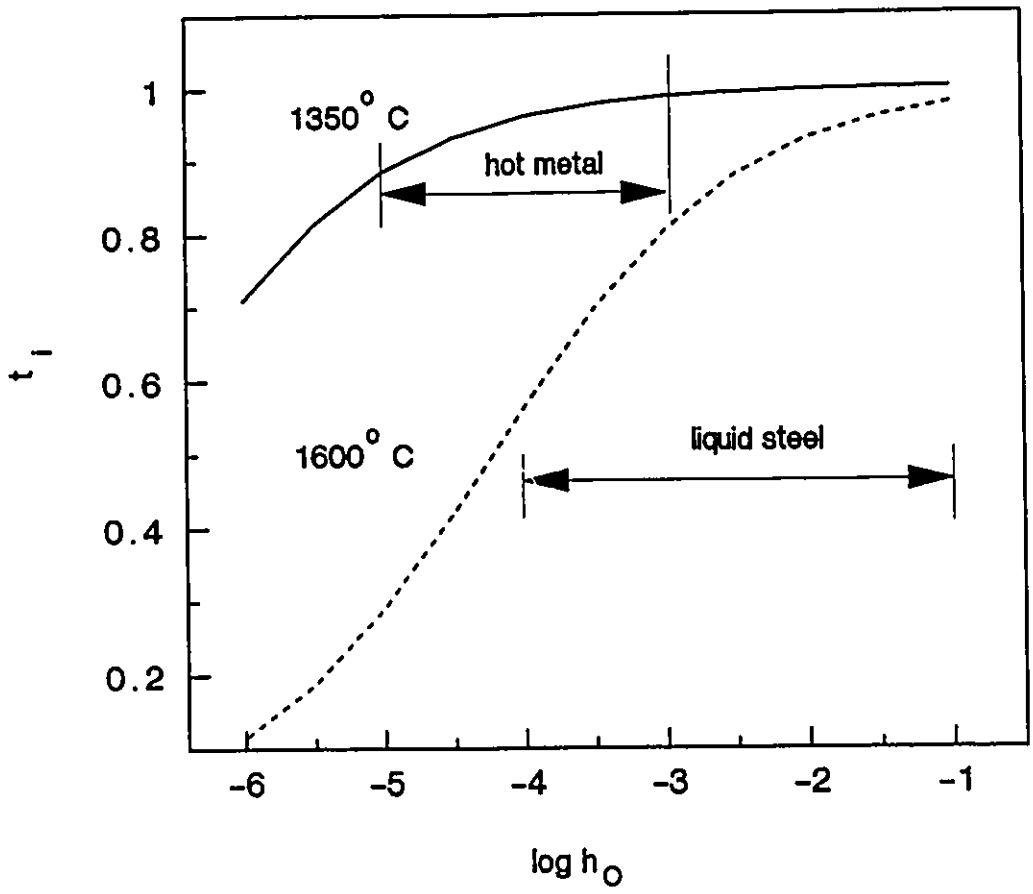

Figure 2.6 The ionic transport number t_i changes with temperature. The range of oxygen activity of hot metal and liquid steel has been labelled. The parameter $P_{e'}$ is calculated from

$$\log p_{e'} = -\frac{74370}{T} + 24.42$$

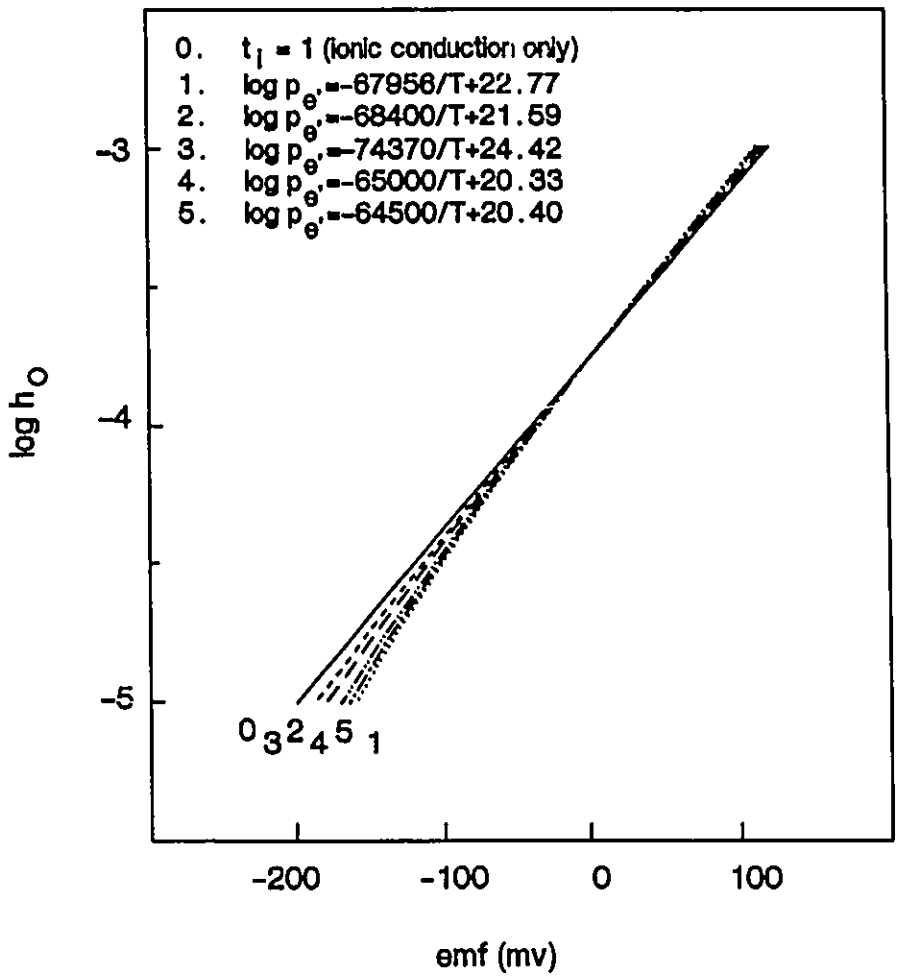

Figure 2.7 The relationship of emf and oxygen activity is plotted in a typical range of oxygen activity in hot metal at 1350°C, using different values of the parameter $P_{e'}$.

2.3.2 Polarization of ZrO_2 Oxygen Cell

Equation (2.19) can be used only if the chemical equilibrium is reached at the electrolyte-electrode interfaces. If the equilibrium is disturbed, polarization may occur. This problem has to be taken into account during continuous measurement.

The term polarization refers to the overvoltage at the interfaces between the solid electrolyte and electrodes. Polarization is related to oxygen transport phenomena due to electronic conduction or oxygen diffusion through the solid electrolyte [66,67,77,78].

Figure 2.8 is a schematic polarization diagram showing the oxygen potential gradients in the solid electrolyte and the melt-electrolyte boundary layer. The gradient at the interface between the metal and the oxide of the reference materials and the gradient at the interface between the solid electrolyte and the electrode are not given in this diagram [66]. For a given gradient, the oxygen transport ability depends on the impurity content and cell microstructure [75,79,80]. Small amounts of aluminum oxide and silicon oxide, which are usually present in commercial ZrO_2 cells, are segregated at the grain boundaries, as a result, the oxygen diffusivity increases significantly [81,82]. Ferrous oxides have an even worse effect on the cell performance since their valency state changes with the local oxygen pressure [83]. Some fundamental aspects of diffusion polarization in ZrO_2 electrolyte cells were discussed in reference [84].

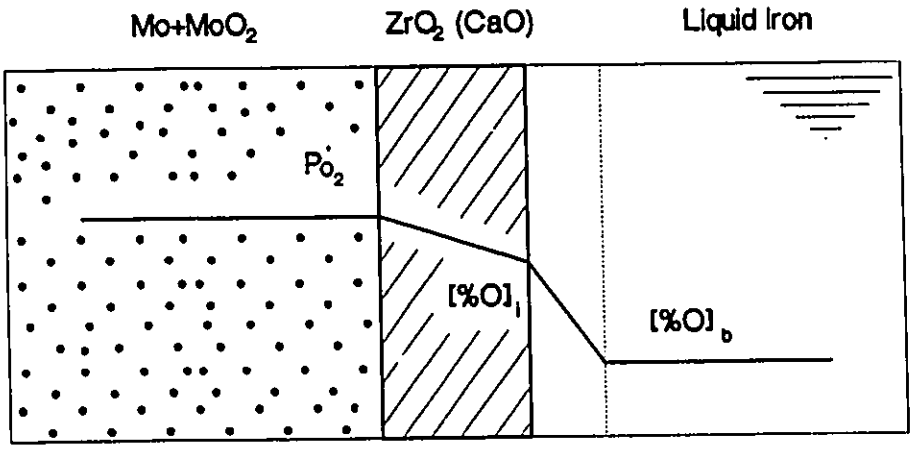

Figure 2.8 Oxygen potential gradient across the solid electrolyte, taken from [66]

No work has been reported on the investigations of polarization at the electrode-electrolyte interface and the reference metal-oxide interface. Recently, a correction for polarization at the liquid iron and electrolyte interface has been attempted with limited success [84]. Some literature reported that intensive stirring of the melt could minimize that error [67,85].

Niedringhaus et al. observed that the cells supplied by Electro Nite (The same type of cells were used in the present study) could work up to 20 minutes and longer, but, in general, after two or three minutes, the sensors exhibited polarization indicated by a decrease in emf, but could be depolarized by passing a reverse current [70].

2.3.3 Chemical Reduction of ZrO_2 Solid Electrolyte

At low oxygen activity, decomposition of zirconia may bring about a change of local oxygen content, cause oxygen polarization at the melt-electrolyte interface and result in some measurement errors.

Reference [65] compared the chemical stabilities of ZrO_2 with several other oxides. Romero et al. suggested that dissolution of ZrO_2 should be considered only when oxygen activity is around or below 10^{-4} at 1600°C. They further indicated that formation of ZrC due to reaction

$$ZrO_2(s)+3\underline{C}-ZrC(s)+2CO(g) \qquad (2.27)$$

can be excluded at the temperature up to 1600°C, but has to be taken into account at higher temperature [69].

As shown in Figure 2.9, an oxygen activity of 10^{-4} at 1350°C corresponds to a zirconium activity of about 10^{-5} (The free energy data are tabulated in Table 2.8). In the present work, the zirconium content in the melt is about 0.001 per cent. Assuming the activity coefficient of one and all zirconium dissolved, zirconia can be considered essentially stable in the melt.

In their laboratory experiments, Janke and Richter observed that at medium oxygen activities (h_O>0.002, 0.0013 %Al, at 1600°C), the cell surface remained stable and smooth in contact with liquid iron; at extremely low oxygen activities (h_O=0.00055, 0.16 %Al, at 1600°C) the cell surface became rough, indicating the onset of ZrO_2 chemical reduction. They pointed out that inaccurate and uncontrolled emf signals were measured when zirconia tubes were completely coated with alumina [67].

TABLE 2.8

FREE ENERGY OF OXIDATION REACTIONS IN LIQUID IRON

Reaction	ΔG^O (J)	Reference
$\underline{Si}$(1 wt%)+2$\underline{O}$(1 wt%)=SiO_2(s)	-576400+218.2T	JSPS [13]
2$\underline{Al}$(1 wt%)+3$\underline{O}$(1 wt%)=Al_2O_3(s)	-1225000+393.8T	JSPS [13]
$\underline{Zr}$(1 wt%)+2$\underline{O}$(1 %)=ZrO_2(s)	-1090000+417T	JSPS [13]
$\underline{Mg}$(1 wt%)+$\underline{O}$(1 wt%)=MgO(s)	-496100+140.4T	Sigworth & Elliott [12] [a]
$\underline{Ca}$(1 wt%)+$\underline{O}$(1 wt%)=CaO(s)	-629570+144.7T	Sigworth & Elliott [12][15] [a]

a ΔG^O is calculated from ΔG^O of solution (Refer to [12] and [15]) and ΔG^O of oxide formation from elements in their standard states (Refer to [12]).

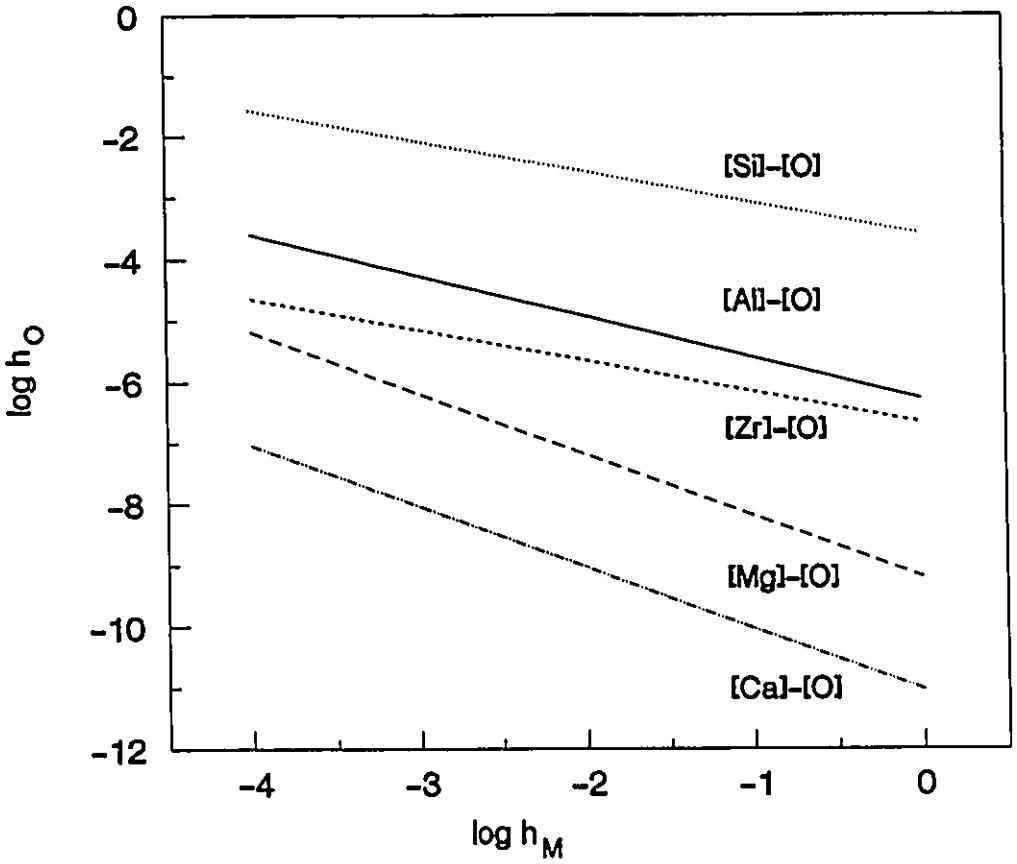

Figure 2.9 The oxide stability in contact with liquid iron at 1350°C for reaction:

$$x[M]\ (1\ wt\%)+y[O]\ (1\ wt\%)-M_xO_y(s)$$

2.4 SUMMARY

The thermodynamic data associated with desulphurization and deoxidation in hot metal by lime and calcium carbide were compared. The data which will be used in the calculations of this work were selected.

The rate of desulphurization during calcium carbide powder injection is generally controlled by the mass transfer of sulphur across the liquid-solid boundary layer. The rate can be approximated as a first order with respect to the desulphurization driving force.

When using zirconia oxygen probes in hot metal, at extremely low oxygen activity, one has to consider the problems zirconia electrolyte may have, such as electronic conduction, polarization and chemical reactions. For the present experiments, at temperature about 1350°C and oxygen activity about 10^{-4}, zirconia is essentially stable in the melts. The error caused by the uncertainty of P_{e^-} is less than 10 per cent. More work is required for a better understanding of polarization.

CHAPTER 3
APPARATUS AND PROCEDURE

The general configuration of the experimental apparatus used in the present work is shown in Figure 3.1. The desulphurization experiments were carried out in a laboratory induction furnace. The liquid metal was contained in a MgO crucible. The desulphurizer was injected from a powder dispenser. Nitrogen, or in some instances, carbon dioxide was used as a carrier gas. The exhaust gas was connected to a high temperature bag filter. All experimental conditions were monitored by a data-logging minicomputer.

3.1 FURNACE SYSTEM

About 70 kg of iron was melted and held in MgO crucibles (230 mm inside diameter, 365 mm high) contained in a 75 kW water cooled induction melting furnace. The crucible composition was 90.7% magnesia, 5.7% silica, 1.8% alumina and 1.2% calcium oxide supplied by Dresser Canada Inc. [86].

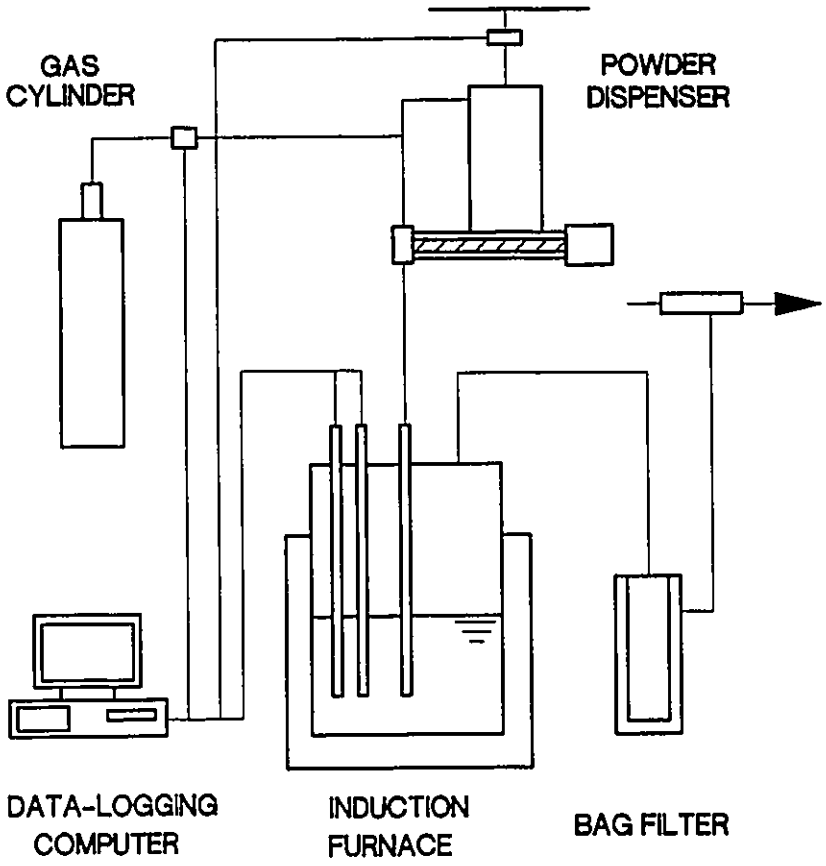

Figure 3.1 Schematic diagram of experimental apparatus

During the injections, the furnace was covered by the lid illustrated in Figure 3.2. The radiation and conduction heat losses from the melt to the atmosphere were minimized by using an insulating alumina board under the lid and filling the lid with alumina fibre. The lid was fitted with ports for the injection lance, a thermocouple, an oxygen probe, a sampling port and an exhaust. The exhaust was connected by a flexible steel tube to a high temperature bag filter and consecutively to a venturi vacuum extractor (both shown in Figure 3.3). The lance was located at the centre of the furnace and submerged into melt 100 mm. All lances were machined from graphite (3 mm inside diameter, 25 mm outside diameter).

3.2 POWDER DISPENSER

A schematic diagram of the powder dispenser system is shown in Figure 3.4. The powder was injected from a custom designed pressurized screw feeder, using nitrogen as a carrier gas (except for the carbon dioxide trials). The powder rate depended on the rotation rate of the screw motor. The carrier gas flow rate was accurately controlled by a needle valve. The pressure balance between the chamber and the nozzle was considered carefully in the design of this system. Therefore, the powder flow rate fluctuations were largely avoided. As the motor stopped, the powder flow also stopped immediately. The powder dispenser system was equipped with a load cell, a gas flow rate transducer and a pressure transducer. More details will be discussed in the next section.

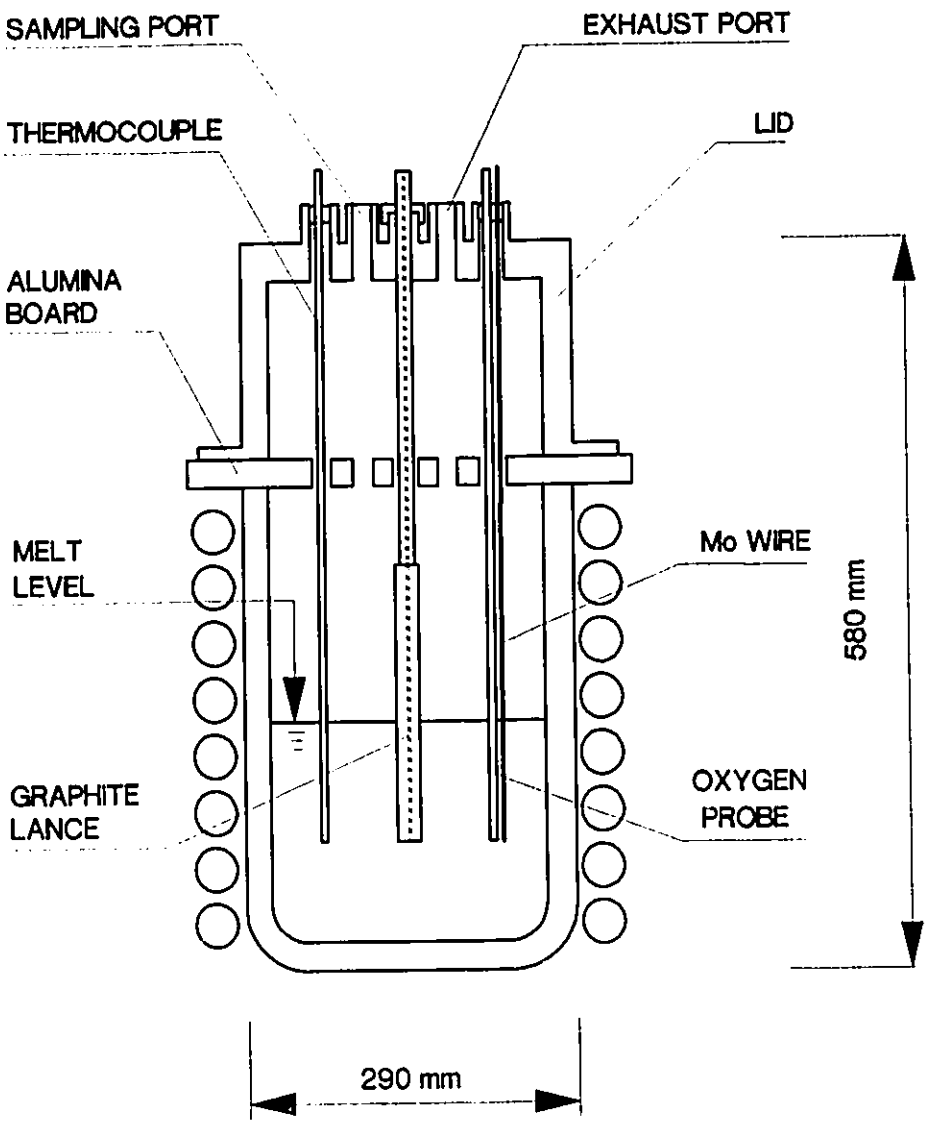

Figure 3.2 Schematic diagram of the crucible and lid assembly, to scale

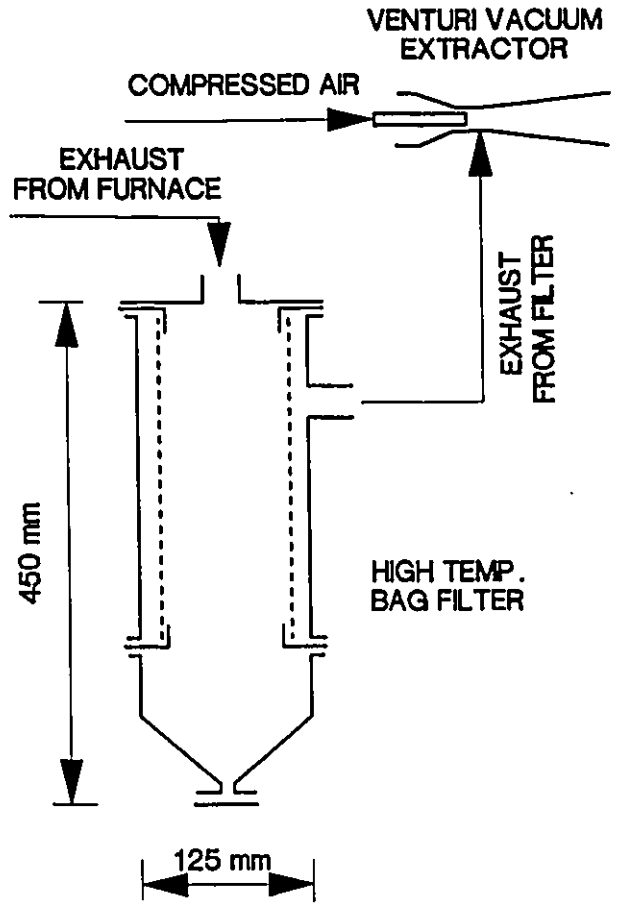

Figure 3.3 Schematic diagram of the exhaust bag filter and venturi vacuum extractor

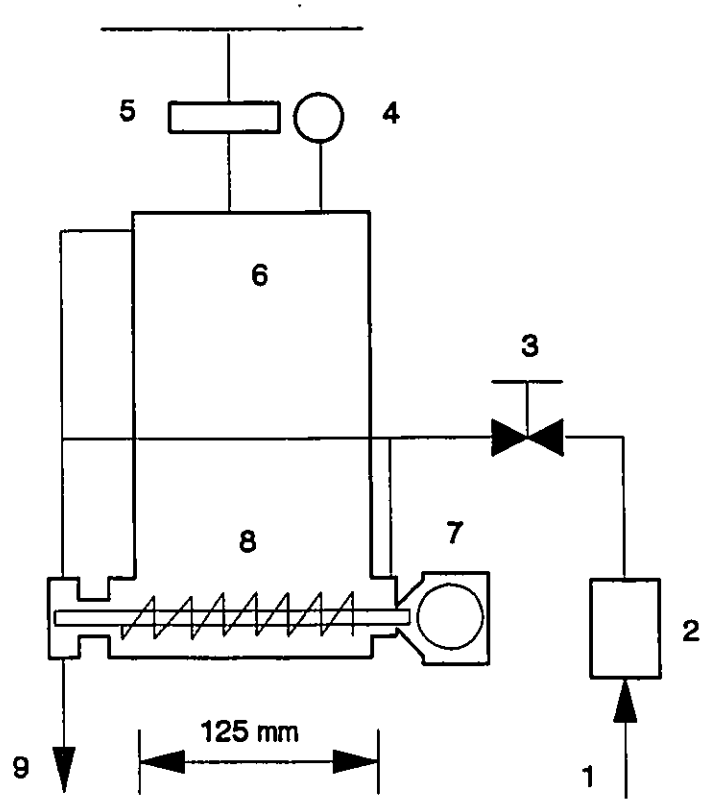

1. CARRIER GAS
2. MASS FLOW METER
3. NEEDLE VALVE
4. PRESSURE GAUGE
5. LOAD CELL
6. POWDER CONTAINER
7. SCREW FEEDER MOTOR
8. SCREW FEEDER
9. GAS-SOLID MIXTURE TO LANCE

Figure 3.4 Schematic diagram of the pressurized screw feeder system

3.3 MEASUREMENT DEVICES

The measurement devices are summarized in Table 3.1. Their arrangement is shown in Figure 3.5.

The melt temperature was measured with a Pt/Pt-13%Rh thermocouple sheathed in a fused satin quartz tube (5 mm inside diameter and 7 mm outside diameter, Heraeus-Amersil Inc.). One end of the tube was sealed by heating in a oxygen-natural gas flame. The thermocouple was dipped into the melt about 100 mm. The potential of the thermocouple, after amplification by a signal amplifier with a gain of 100 (OMNI-AMP TM III, Omega Eng. Inc.), was recorded by a minicomputer.

The MgO-stabilized ZrO_2 cells with a Cr/Cr_2O_3 reference electrode (supplied by Electro-Nite) were used for continuous oxygen measurement. The chemical composition and dimension of the cell are listed in Table 3.2. The electrical contact with the melt was made with molybdenum wire sheathed in a quartz tube with dimensions 4 mm O.D × 500 mm long. The contact with the Cr/Cr_2O_3 reference materials was also made with molybdenum wire, hence, no thermal emf correction was needed. The cell was fitted into a quartz tube (same grade and size as used for the thermocouple) and sealed with dry, pure alumina fibre and powder. A schematic diagram of the continuous oxygen activity measurement system is shown in Figure 3.6. The probes were able to work continuously for 6 to 15 minutes.

TABLE 3.1

SUMMARY OF MEASUREMENT DEVICES

Objective	Device Type & Model No.	Uncertainty	Suppliers
Temperature	Thermocouple Pt/Pt-13%Rh	1.5°C	Johnson Matthey Ltd.
Gas Flow Rate	Flowmeter 810L/1209	2%	Dresser Industries Inc.
Gas Pressure	Pressure Transducer AB	1%	Data Instruments Inc.
Powder Weight	Load Cell 3167	1%	Durham Instruments Inc.
Oxygen Activity	ZrO_2 Cell & Probe Celox/2 CLL	n.d [a]	Electro-Nite Co.

a n.d = not determined. The estimated value is about 10 per cent (See Section 2.3.1). More discussion will be given in the next chapter.

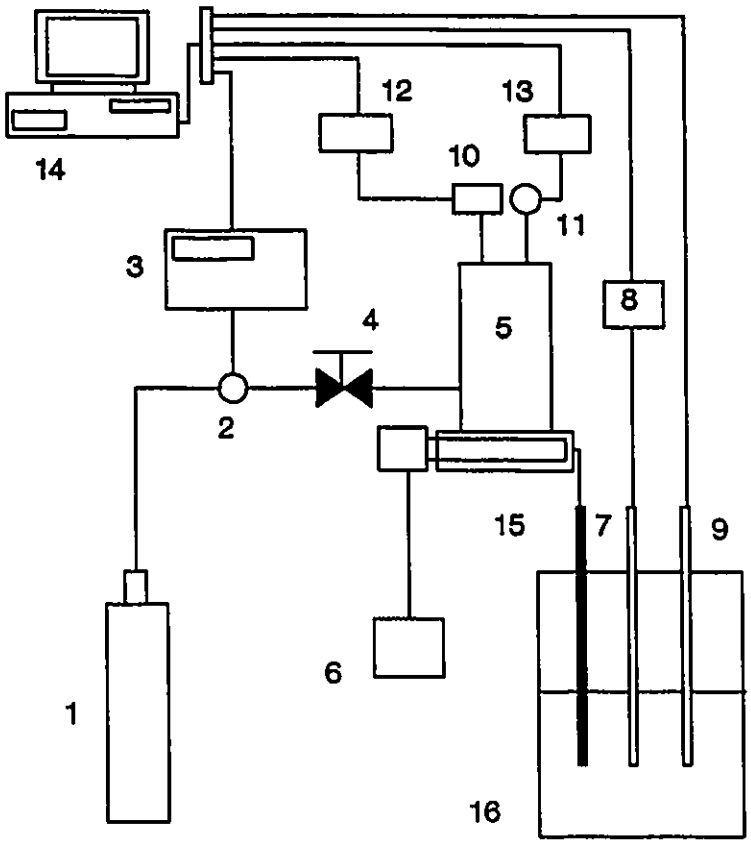

1. GAS CYLINDER
2. MASS FLOW RATE TRANSDUCER
3. MASS FLOW METER
4. NEEDLE VALVE
5. POWDER DISPENCER
6. MOTOR CONTROLLER
7. THERMOCOUPLE
8. SIGNAL AMPLIFIER
9. OXYGEN PROBE
10. LOAD CELL
11. PRESSURE TRANSDUCER
12. LOAD CELL CONVERTER
13. PRESSURE CONVERTER
14. COMPUTER
15. LANCE
16. CRUCIBLE

Figure 3.5 Schematic diagram of the measurement system

TABLE 3.2

CHEMICAL ANALYSIS AND DIMENSION OF ZrO_2 CELL

(SUPPLIED BY Electro-Nite Co.)

Composition (%)	MgO	SiO_2	CaO	Al_2O_3	Fe_2O_3	TiO_2
	2.0	0.3	0.24	0.14	0.15	0.08
Cell Dimensions (mm)	Length		Inside Dia.		Outside Dia.	
	27.1		2.72		4.92	

The weight of the powder dispenser was measured with a load cell during powder injection. The pressure in the dispenser chamber was measured with a pressure transducer. The mass flow rate of the carrier gas was measured with a mass flow meter. The load cell, the pressure transducer, the mass flow meter, the oxygen probe and the thermocouple were all connected to the interface of a data-logging minicomputer (DEC LSI II/2). The resolution of the A/D converter is 12 bits.

Disposable, single-use oxygen probes were also used (Electro-Nite, Celox/2 CLL) in some instances. The cell emf (mv) measured with the single-use probes was converted to oxygen activity (ppm) according to the following equation:

$$\log h_O = 1.36 + 0.0059[E + 0.54(T - 1550) + 0.00021E(T - 1550)] \quad (3.1)$$

which was taken from the work of CRM and Hoogovens conducted in steel at steelmaking temperature [87].

3.4 MATERIALS

Iron and calcium carbide were two principal materials used in the experiments of the present work. The iron ingot was donated by QIT-Fer et Titane Inc. The nominal chemical composition is listed in Table 3.3. After the iron was melted, ferrosilicon, iron sulphide, and in some instances, aluminum were added to achieve the desired starting melt composition. The calcium carbide powder was a commercially available desulphurizing reagent (kindly supplied by Cyanamid Canada Inc.). Its nominal composition is 72% CaC_2, 26% CaO and 2% $CaCO_3$. The powder was screened before injection to avoid lance blockage by large particles. In some trials, limestone was added to the calcium carbide powder to investigate its effect on desulphurization. The chemical composition and particle size of the powder is given in Table 3.4, which was provided by Cyanamid Canada Inc. The size distribution of screened powder is shown in Figure 3.7.

3.5 PROCEDURE

Figure 3.8 is the flow chart of the experimental procedure. The operating conditions are given in Table 3.5.

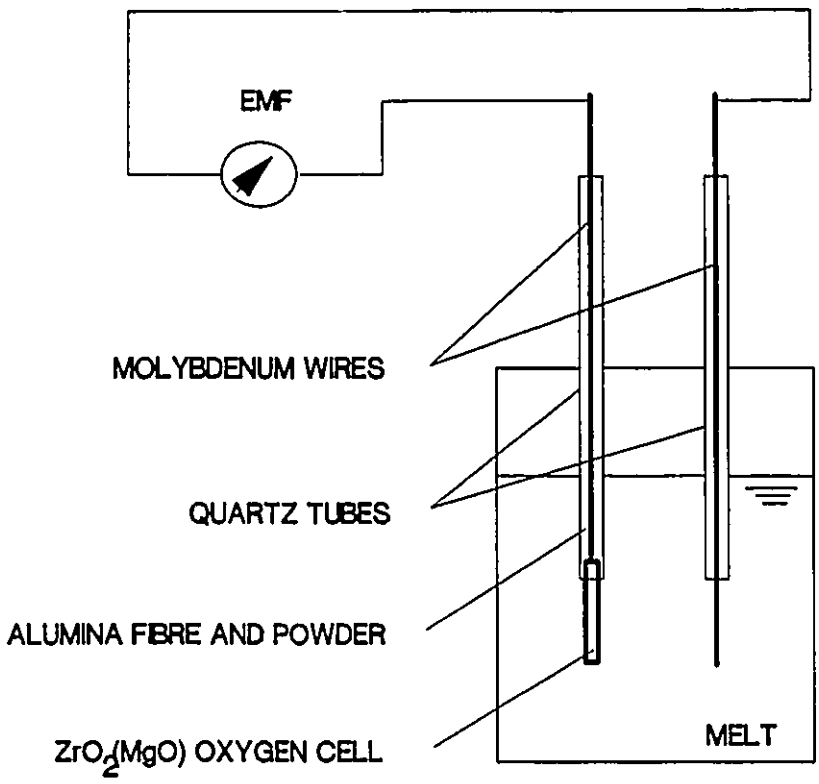

Figure 3.6 Schematic diagram of continuous oxygen activity measurement system

TABLE 3.3

THE NOMINAL CHEMICAL COMPOSITION OF IRON INGOT

Chemical Composition of Iron Ingot (%)	C	Si	Mn	Al
	4.2	0.12	0.02	<0.0001

TABLE 3.4

THE CHEMICAL COMPOSITION AND PARTICLE SIZE OF CALCIUM CARBIDE POWDER [88]

Chemical Composition	CaC_2	CaO	$CaCO_3$
Before limestone addition	72	26	2
after limestone addition	43	36	21
Particle Diameter of the Powder Mixture (μm)	48 (Volume Mean)		
	12 (Area Mean)		

After the iron was melted, the bath temperature was adjusted to 1350°C. Iron sulphide and ferrosilicon, or in some instances, aluminum was added to the melt to achieve the desired starting chemical composition. One or two spoon ingot samples were taken. The temperature and oxygen activity were measured with disposable, single-use probes. The lid was then placed on the top of the crucible. The thermocouple was dipped into the melt. The temperature was displayed by a digital thermometer. The melt temperature was stabilized at 1350±5°C for five minutes. Electric power was then shut off. The melt was stirred for approximately three minutes with nitrogen, during which two or three pin samples were taken, temperature and oxygen activity were measured. After gas injection, the electric power was returned to raise the temperature back to 1350°C and to maintain it for three minutes.

The electric power was shut off again. The continuous oxygen probe was dipped into the melt. The dispenser was then started and the gas-solid mixture was injected into the melt. Pin samples for sulphur content were taken as frequently as possible. After three to four minutes of powder injection, the dispenser was turned off, and carrier gas bubbling and sampling were continued for three to five minutes. The melt was then prepared for another injection.

During gas and powder injection, the output of the load cell, the mass flow meter, the pressure transducer, the oxygen probe, and the bath thermocouple were all read and stored by the data-logging minicomputer three times each second.

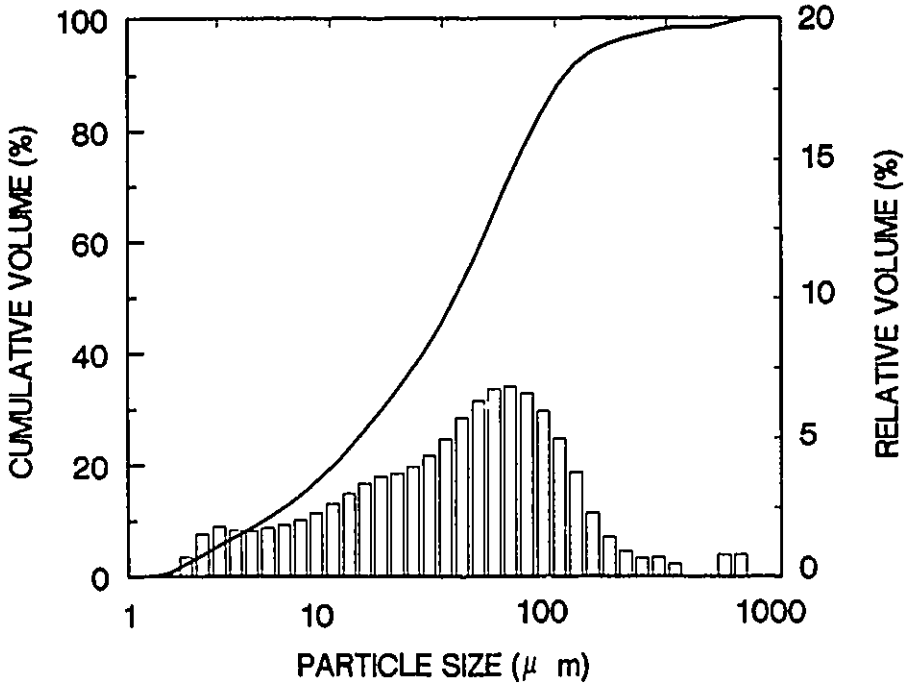

Figure 3.7 The particle size distribution of CaC_2 powder [88]

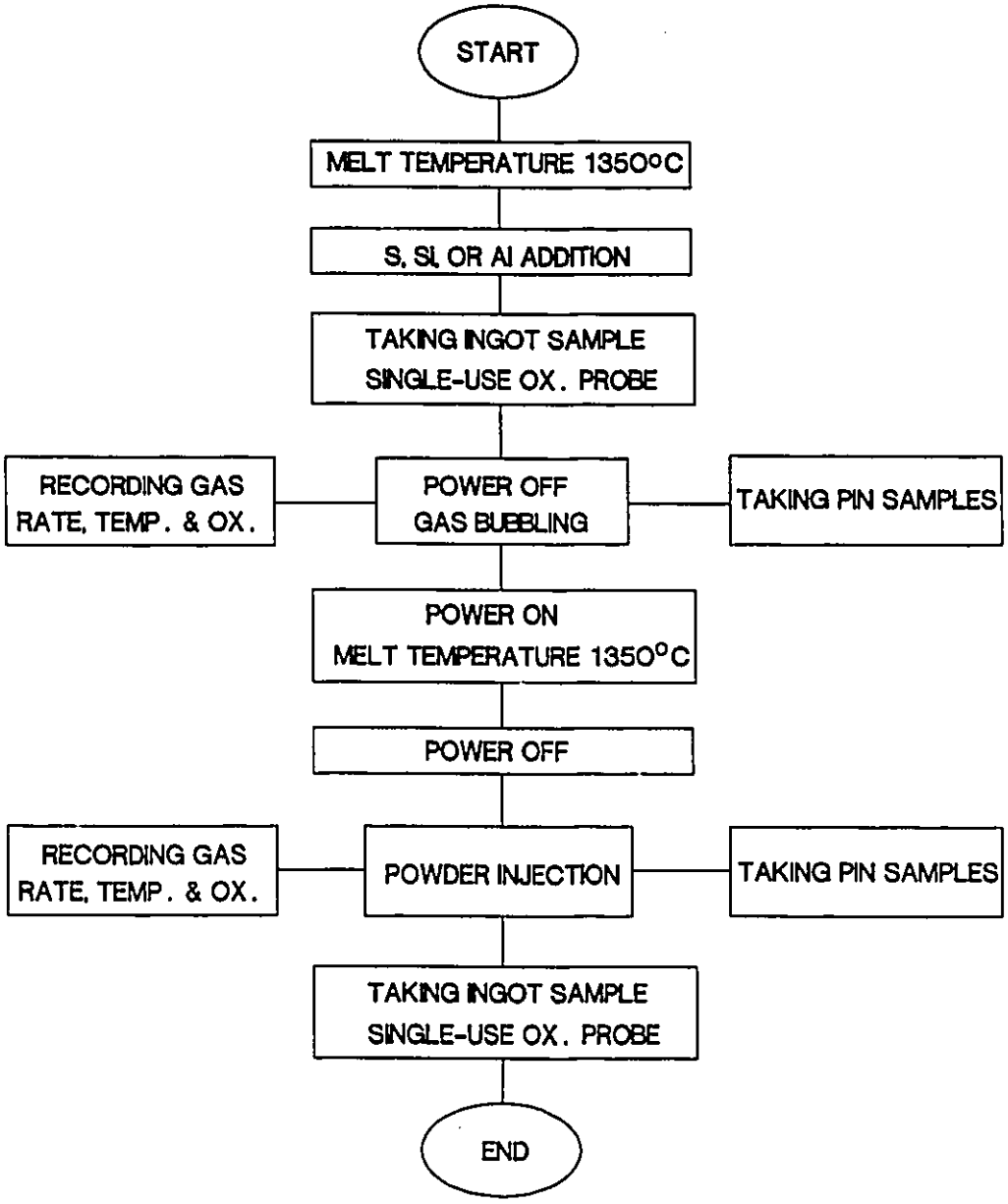

Figure 3.8 Flowchart of experimental procedure during a heat

TABLE 3.5

THE RANGE OF EXPERIMENTAL CONDITIONS

Carrier Gas		N_2 or CO_2	
Injection Reagent		CaC_2 72-43%	
		CaO 26-36%	
		$CaCO_3$ 2-21%	
Hot Metal Temperature		°C	1300-1350
Powder Rate		kg/s	0.001-0.01
Loading (Solid/Gas Ratio)		kg/Nm^3	15-100
Gas Flow Rate		SLPM	3-15
Computer Reading Time		s	360
Hot Metal Composition	Aluminum	%	<0.2
	Silicon		0.1-2
	Sulphur		<0.06
	Carbon		3.8-4.5

3.6 CHEMICAL ANALYSIS

As shown in Table 3.6, the samples were analyzed by combustion-iodate titration (Leco, Model 5-18) for sulphur, direct combustion for carbon (Leco, Model 577-100), and optical emission spectrometry (Jarrell-Ash ICAP Solid Sampling System 9000) for total silicon and aluminum. The possible errors will be discussed with regard to the experimental data in Section 4.4.

TABLE 3.6

THE DEVICE AND TECHNIQUE FOR CHEMICAL ANALYSIS

Substances	Technique	Device	Estimated Uncertainty
Analysis for Pin Samples			
Sulphur	Combustion-Iodate Titration	Leco, Model 5-18	± 0.002 %S
Carbon	Direct Combustion	Leco, Model 577-100	± 0.1 %C
Analysis for Ingot Samples			
Silicon	Optical Emission Spectrometry	Jarrell-Ash ICAP Solid Sampling System	± 0.02 %Si
Aluminum			± 0.002 %Al
Manganese			± 0.05 %Mn

CHAPTER 4
EXPERIMENTAL RESULTS

Over eighty injection tests were performed. The tests were in three parts: gas injections, calcium carbide powder injections and limestone-calcium carbide powder mixture injections. As described earlier, each test produced four groups of the experimental data:

- the voltage signals which were recorded by a minicomputer and generated by the load cell, the mass flowmeter, the pressure transducer, the continuous oxygen probe and the melt thermocouple.
- the sulphur contents of the pin samples which were taken during the injection and then analyzed by using combustion-iodate titration technique.
- the chemical composition of the ingot samples which were taken before and after the injection and then analyzed by using optical emission spectrometry technique.
- the oxygen activities which were measured by the disposable, single-use oxygen probes before and after the injection.

A summary of the experimental conditions of gas injections is given in Table 4.1. A summary of the experimental conditions of powder injections is given in Table 4.2. The results of sulphur analysis of all pin samples are listed in Appendix I. The experimental results of this work will be presented in the following sequences:

1. Gas Injection

   - the effect of the silicon-silica equilibrium on the oxygen activity in hot metal.
   - the effect of the gas flow rate on the bath cooling rate.

2. Calcium Carbide Powder Injection

   - the effect of the oxygen activity and the powder feed rate on the desulphurization rate.
   - the effect of the oxygen activity on the desulphurization path.
   - the effect of the gas flow and powder feed rate on the bath cooling rate.

3. The Effect of Carbon Dioxide on the Rate of Desulphurization

   - limestone-calcium carbide-nitrogen injection.
   - calcium carbide-carbon dioxide injection.

TABLE 4.1

SUMMARY OF GAS INJECTION EXPERIMENTS

Run No.	Inj. Time		Gas Flow Rate		Melt Temp.		Oxygen Activity		Si	C	Al
	Start	End			Start	End	Start	End			
	s		SLPM		°C		×10⁻⁴		%		
3-002	50	260	N_2	12.5	1352	1302	n.d [a]	n.d	n.d	n.d	n.d
3-004	30	260		0.0	1380	1348	n.d	n.d	n.d	n.d	n.d
6-001	200	333		10.0	1353	1318	n.d	n.d	0.10	4.0	/ [b]
6-003	150	333		10.3	1355	1292	1.06	n.d	0.51	3.4	/
6-005	95	333		8.2	1335	1275	n.d	n.d	1.03	4.0	/
7-001	110	333		10.2	1356	1292	1.35	0.89	0.13	3.8	/
7-003	50	333		9.9	1340	1285	n.d	0.20	0.11	3.9	0.200
7-005	75	333		10.5	1365	1305	0.08	0.24	0.12	3.8	0.175
8-001	0	265		10.0	1340	1285	1.52	0.74	0.11	3.9	/
8-003	0	333		10.0	1355	1300	0.80	n.d	0.98	4.3	/
8-005	0	333		10.0	1358	1306	0.54	n.d	1.82	3.8	/
9-001	30	333		10.2	1373	1308	1.45	0.63	0.90	4.6	/
9-003	30	333		10.3	1373	1306	1.20	0.62	0.83	4.6	/
9-005	20	270		10.2	1393	1327	1.64	n.d	0.72	4.4	/
10-003	25	240		10.4	1350	1295	0.66	0.24	1.50	4.3	/
10-005	10	210		10.2	1344	1293	0.53	0.28	1.46	4.3	/
10-007	80	220		5.1	1345	1296	0.16	0.20	1.45	4.0	0.014
11-004	25	225		10.2	1358	/	0.48	n.d	1.89	4.7	0.001
11-007	20	200		10.2	1355	1299	0.53	n.d	1.87	4.4	/
12-001	20	333	CO_2	5.2	1346	1285	1.75	n.d	0.12	4.2	/
12-003	0	333		5.0	1358	1310	1.50	n.d	0.12	4.2	/
12-005	0	333	N_2	5.3	1341	1293	0.23	n.d	0.11	4.1	0.010
13-003	60	330		5.2	1345	1290	0.75	n.d	0.91	4.5	/
13-011	15	333	CO_2	15.5	1348	1292	0.72	n.d	0.85	4.2	/

a n.d = not determined

b The content is less than 0.001.

TABLE 4.2 SUMMARY OF EXPERIMENTAL CONDITIONS OF POWDER INJECTIONS

a n.d = not determined b The content is less than 0.001

Run No.	Inj. Time		Powder			Carrier Gas			Melt Temp.		Ox. Activity		Si	C	Al	S	
	Start	End	Type	Quant.	Rate	Type	Press.	Rate	Start	End	Start	End				Start	End
	s			g	g/min		kg/cm²	SLPM	°C		×10⁻⁴		%				
3-003	40	265		1180	480		0.77	11.2	1350	1298	n.d[a]	n.d	n.d	n.d	n.d	n.d	n.d
3-005	80	200		800	417		0.56	10.2	1375	1340	n.d	n.d	n.d	n.d	n.d	n.d	n.d
5-002	250	380		300	140		0.63	8.8	1420	1345	n.d	n.d	n.d	n.d	n.d	n.d	n.d
6-002	70	300		800	209		0.32	4.5	1338	1285	n.d	n.d	0.10	4.0	/[b]	0.019	0.002
6-004	40	300		540	125		0.28	4.5	1340	1290	n.d	n.d	0.52	3.4	/	0.014	0.003
6-006	30	180		520	208		0.32	4.8	1345	1295	n.d	n.d	1.04	4.0	/	0.026	0.010
7-002	65	310		1200	294		0.35	4.1	1350	1295	1.58	0.52	0.12	3.6	/	0.036	n.d
7-004	80	295		1070	299		0.32	4.4	1350	1290	0.09	0.08	0.12	3.9	0.199	0.017	0.003
7-006	40	280	CaC_2	500	125	N_2	0.28	4.9	1350	1290	0.12	0.26	0.12	3.7	0.127	0.002	0.002
8-002	30	210		495	165		n.d	5.0	1365	1313	n.d	n.d	0.10	4.2	/	0.019	0.011
8-004	45	205		420	155		n.d	5.0	1365	1290	0.98	0.29	0.93	3.9	0.009	0.019	0.006
8-006	15	210		460	142		n.d	5.0	1372	1327	0.61	0.05	1.79	4.7	0.003	0.011	0.006
8-007	-30	180		300	86		n.d	18.5	1340	1195	0.22	0.05	1.75	4.5	0.002	0.013	0.003
9-002	30	200		480	169		0.28	5.2	1350	1303	1.11	0.49	0.91	4.8	/	0.028	0.010
9-004	30	230		600	180		0.30	5.0	1345	1296	0.79	0.51	0.80	4.8	/	0.018	n.d
9-006	50	230		630	210		0.30	5.0	1372	1324	1.38	0.38	0.68	4.6	/	0.022	0.005
9-007	40	240		570	171		0.30	5.2	1368	1317	n.d	0.23	0.66	4.0	0.016	0.017	0.005
9-008	23	200		260	88		0.21	5.2	1365	1326	0.15	0.12	0.68	4.7	0.009	0.016	0.007

TABLE 4.2 (CONTINUED)

Run No.	Inj. Time		Powder			Carrier Gas			Melt Temp.		Ox. Activity		Si	C	Al	S	
	Start	End	Type	Quant.	Rate	Type	Press.	Rate	Start	End	Start	End				Start	End
	s			g	g/min		kg/cm²	SLPM	°C		×10⁻⁴		%				
10-001	55	270	CaC_2	480	134	N_2	0.28	5.0	1350	1310	0.75	0.35	0.93	4.0	/	0.043	0.012
10-002	40	250		890	254		0.37	5.0	1355	1296	0.52	0.32	1.48	4.2	/	0.025	0.006
10-004	90	210		510	255		0.53	9.5	1342	1293	0.57	0.35	1.47	4.3	/	0.031	0.010
10-006	55	215		1560	585		0.70	8.5	1348	1286	0.65	0.29	1.45	4.2	/	0.036	0.004
10-008	34	225		580	182		0.32	6.1	1348	1306	0.20	0.15	1.45	4.1	0.008	0.042	0.009
11-001	20	208		1030	329		0.37	5.5	1356	1300	1.40	n.d	0.11	4.0	/	0.041	0.015
11-002	50	248		920	280		0.32	5.0	1353	1298	0.87	0.40	0.97	4.4	/	0.022	0.004
11-003	35	265		860	224		0.32	5.2	1348	1293	0.36	0.18	1.89	4.8	0.001	0.016	0.003
11-005	30	150		0	0		n.d	10.0	1355	1300	n.d	n.d	1.89	4.7	/	0.029	0.024
11-008	30	185		1650	639		0.77	9.0	1360	1294	n.d	n.d	1.87	4.4	/	0.037	0.003
12-002	25	90		80	74	CO_2	0.49	9.0	1348	1290	1.35	n.d	0.12	4.2	/	0.047	0.045
12-004	30	130		180	108		0.21	5.2	1350	1310	1.88	n.d	0.11	4.2	/	0.030	0.027
12-006	30	60		80	160		0.21	5.1	1348	1306	n.d	n.d	0.11	4.5	/	0.043	0.041
13-002	45	243	$CaC_2/CaCO_3$	320	97	N_2	0.25	5.0	1350	1300	0.75	0.51	0.93	4.8	/	0.039	0.032
13-004	15	225		670	191		0.32	5.1	1345	1293	n.d	0.46	0.91	4.7	/	0.052	0.040
13-006	55	200		590	245		0.28	5.0	1343	1293	0.27	0.26	0.89	4.3	0.003	0.062	0.035
13-008	55	237	CaC_2	500	165	CO_2	0.63	8.5	1396	1352	1.28	1.12	0.88	4.2	/	0.065	0.050
13-010	60	223		100	37		0.42	9.6	1393	1348	1.32	1.05	0.85	4.2	/	0.085	0.078
13-012	117	270		510	200		0.81	12.5	1350	1315	1.00	0.56	0.83	4.1	/	0.101	0.050

4. The Experimental Error Analysis

- errors in sampling and chemical analysis
- errors in determination of the first order rate constant of desulphurization
- errors in measurement of the bath temperature and determination of the bath cooling rate constant
- errors in determination of the melt oxygen activity

4.1 GAS INJECTION

The gas injections were designed to investigate the factors which control the oxygen activity in hot metal and the effect of gas bubbling on the melt cooling rate. Another reason for doing gas injection before every powder injection was to prevent the melt from being oxidized by air and to homogenize the melt after the addition of ferrous sulphide and ferro-silicon or aluminum.

4.1.1 The Effect of the Silicon-Silica Equilibrium on the Melt Oxygen Activities

The typical curves of the melt temperature and the oxygen activity measured by the continuous probe during a gas injection are shown in Figures 4.1 a and b, where, h_O is the Henrian activity of oxygen referred to one percent

solutions in liquid iron as the standard state. In Figure 4.1 a, the melt temperature decreased continuously throughout the injection due to conductive heat losses through the crucible wall and lining materials. The broken lines plotted in Figure 4.1 b are the equilibrium silicon and carbon deoxidation curves with the silica activity of one and the carbon monoxide pressure of one atmosphere (The reason will be discussed in Chapter 5). The thermodynamic data on iron-carbon-silicon melts and the conversion from oxygen probe emf to oxygen activity have been given in Chapter 2. The results in Figure 4.1 b show that the oxygen activity tended to follow the silicon-silica equilibrium. This equilibrium is calculated at the instantaneous bath temperature. It dropped through out the injection as the temperature fell.

As shown in Figure 4.2, the oxygen activities measured before gas injection tended to fall between those of the carbon-carbon monoxide and silicon-silica equilibria. The experimental data are tabulated in Table 4.3. The oxygen activities measured after one or two minutes of nitrogen injection tended to approach the silicon-silica equilibrium, as shown in Figure 4.3. The experimental data are tabulated in Table 4.4.

The single-use disposable oxygen probe readings and the ingot samples were taken before injection. A summary of the oxygen activities, the melt temperatures (both were recorded by the single-use disposable probes) and the chemical compositions is given in Table 4.5. The results are also shown in Figures 4.4-4.6, corresponding to 1330, 1350 and 1375°C respectively (with the

data tabulated in Table 4.5). The changes of oxygen activity with temperature and silicon content has the characteristics of the silicon-silica equilibrium. However, the single-use probes returned higher oxygen activities. As an example, Figure 4.7 presents a comparison of the oxygen activities measured by the continuous and single-use probes at the temperature 1350°C. The higher oxygen activities produced by the single-use probes were probably due to the large extrapolation of the CRM-Hoogoven calibration correlation developed for steel.

The oxygen activity measured by the continuous probes show clearly:

- At a given temperature, the variation of oxygen activity with silicon content is consistent with Si-SiO_2 equilibrium.
- At a given silicon content, the dependency of oxygen activity on temperature follows Si-SiO_2 equilibrium.

Thus, it is sufficient to prove that the oxygen activity of the melt is controlled by the silicon content. For this reason, ferrosilicon was added into the melts to adjust the starting oxygen activities in the present experiments.

4.1.2 The Effect of the Gas Flow Rate on the Bath Cooling Rate

As described in Section 3.5, the power of the induction furnace was shut off before injection started. Thus, the melt temperature dropped continuously due to the heat losses from the melt to the surroundings.

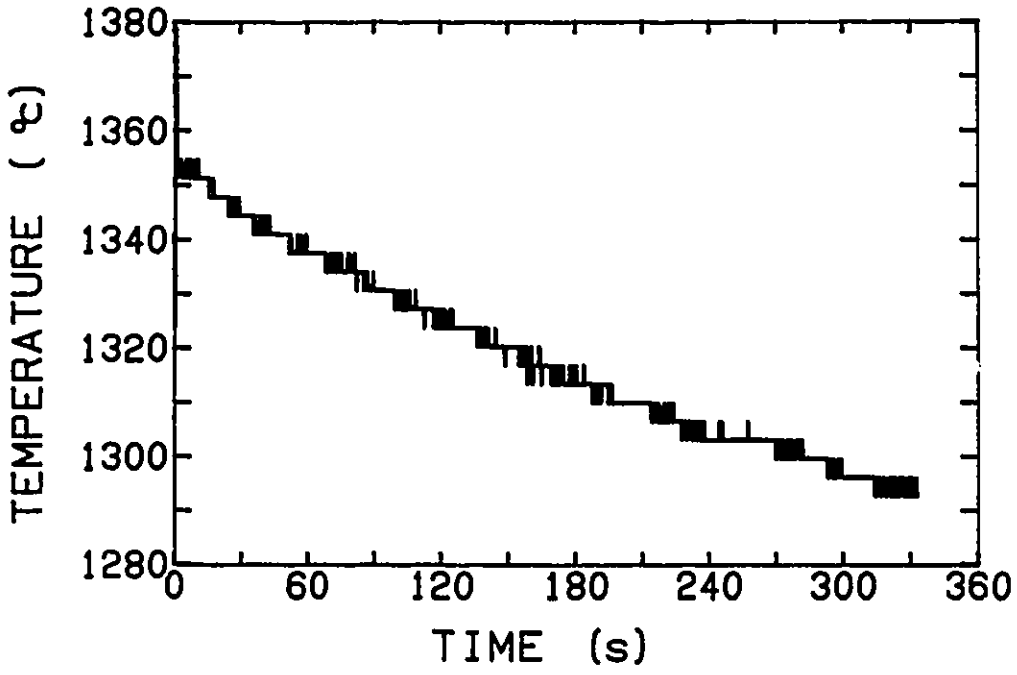

CHPT417.DRW DT1063

Figure 4.1 a The temperature of the iron during nitrogen injection. The melt composition was 1.5% silicon, 4.2% carbon and <0.001% aluminum. The nitrogen gas flow rate was 10.4 SLPM.

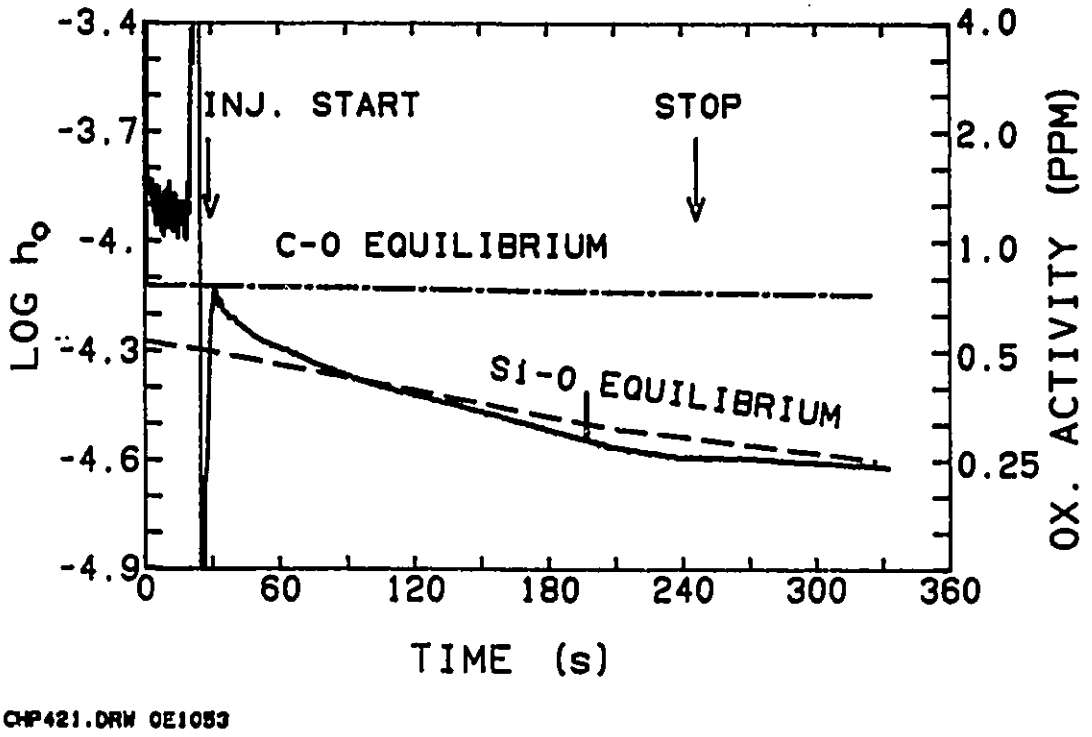

Figure 4.1 b The oxygen activity during the injection compared with the carbon-carbon monoxide and silicon-silica equilibria. It was calculated at the instantaneous temperature shown in Figure 4.1 a.

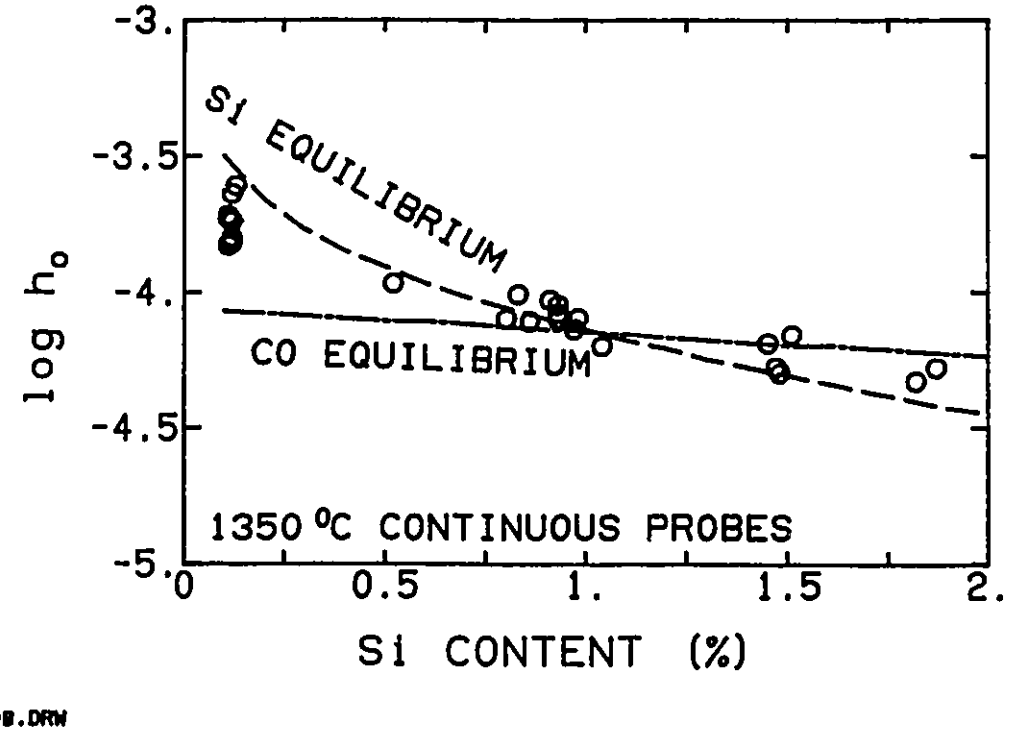

CHP40B.DRW

Figure 4.2 The variation of the oxygen activity from the continuous oxygen probes as a function of silicon content at 1350°C before nitrogen bubbling. The activities corresponding to the equilibria of silicon-silica and carbon-carbon monoxide are also shown.

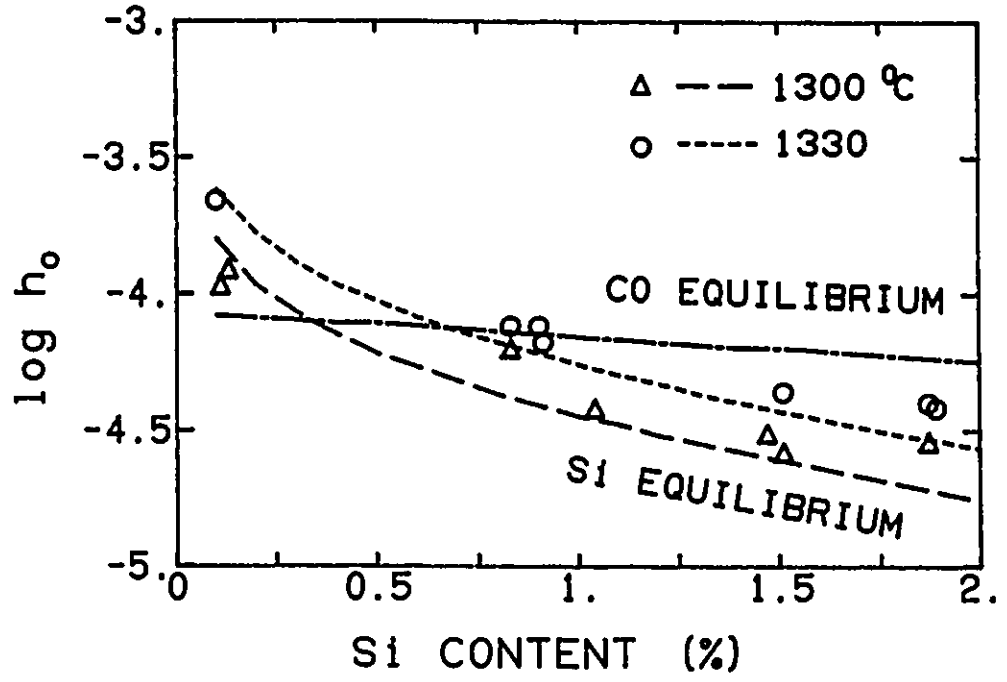

CHP407.DRW

Figure 4.3 The variation of the oxygen activity from the continuous oxygen probes as a function of silicon content at 1300 and 1330°C after one or two minutes of nitrogen bubbling. The activities corresponding to the equilibria of silicon-silica and carbon-carbon monoxide are also shown.

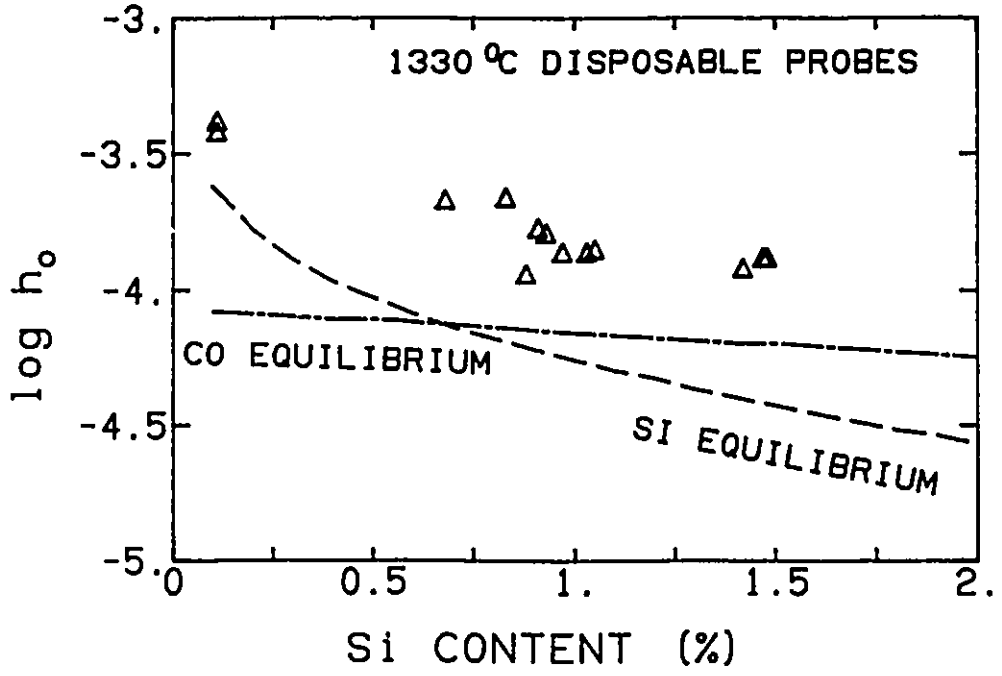

CHP404.DRW

Figure 4.4 The variation of the oxygen activity from the single-use disposable oxygen probes as a function of silicon content at 1330°C before nitrogen bubbling. The activities corresponding to the equilibria of silicon-silica and carbon-carbon monoxide are also shown.

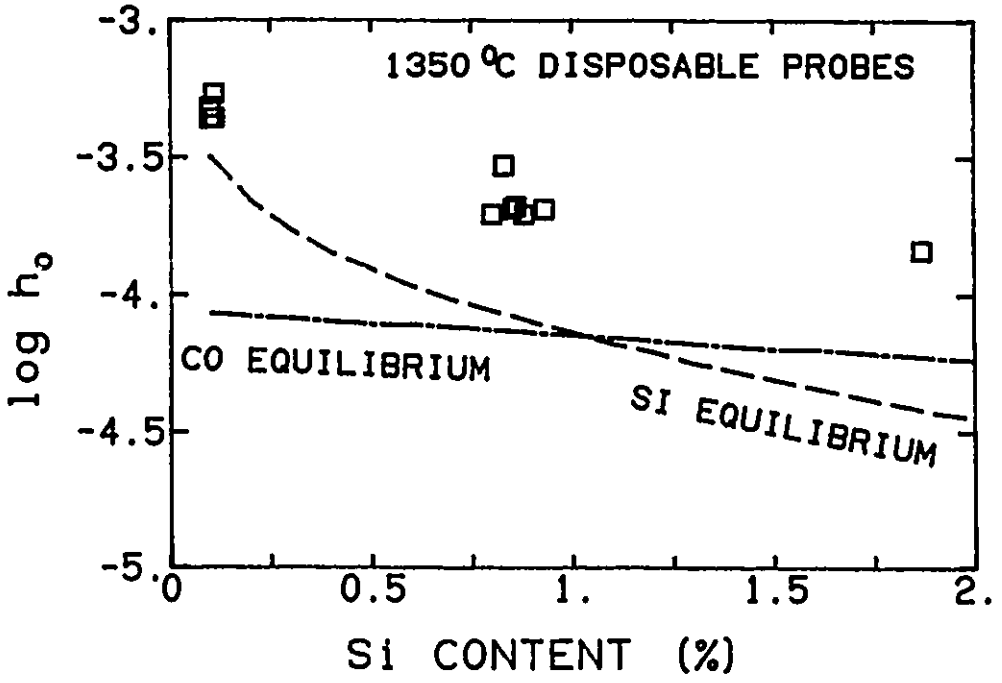

CHP405.DRW

Figure 4.5 The variation of the oxygen activity from the single-use disposable oxygen probes as a function of silicon content at 1350°C before nitrogen bubbling. The activities corresponding to the equilibria of silicon-silica and carbon-carbon monoxide are also shown.

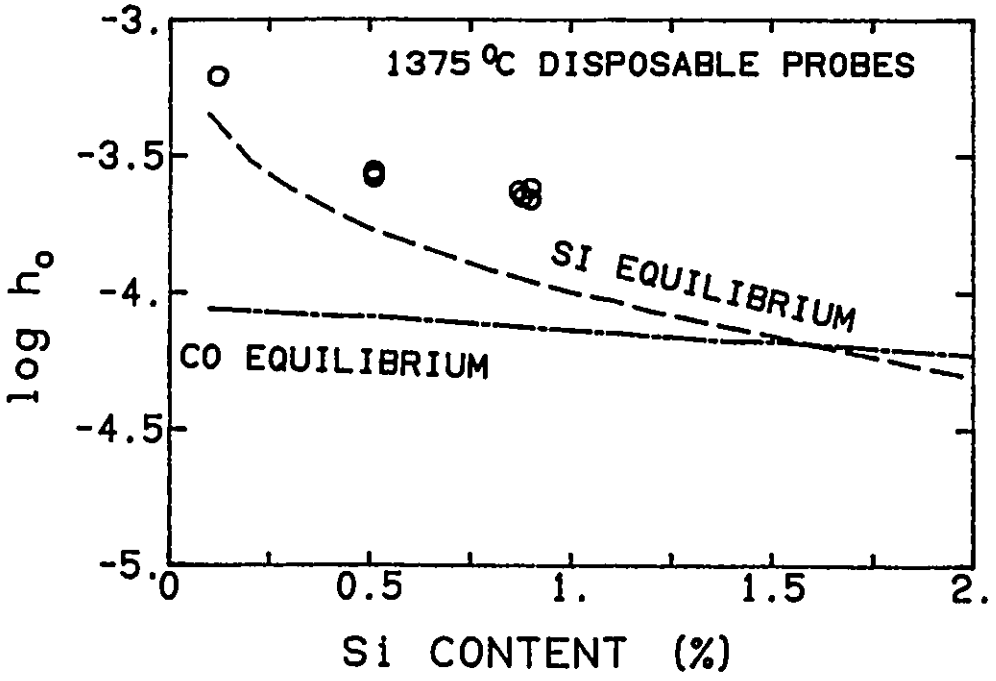

Figure 4.6 The variation of the oxygen activity from the single-use disposable oxygen probes as a function of silicon content at 1375°C before nitrogen bubbling. The activities corresponding to the equilibria of silicon-silica and carbon-carbon monoxide are also shown.

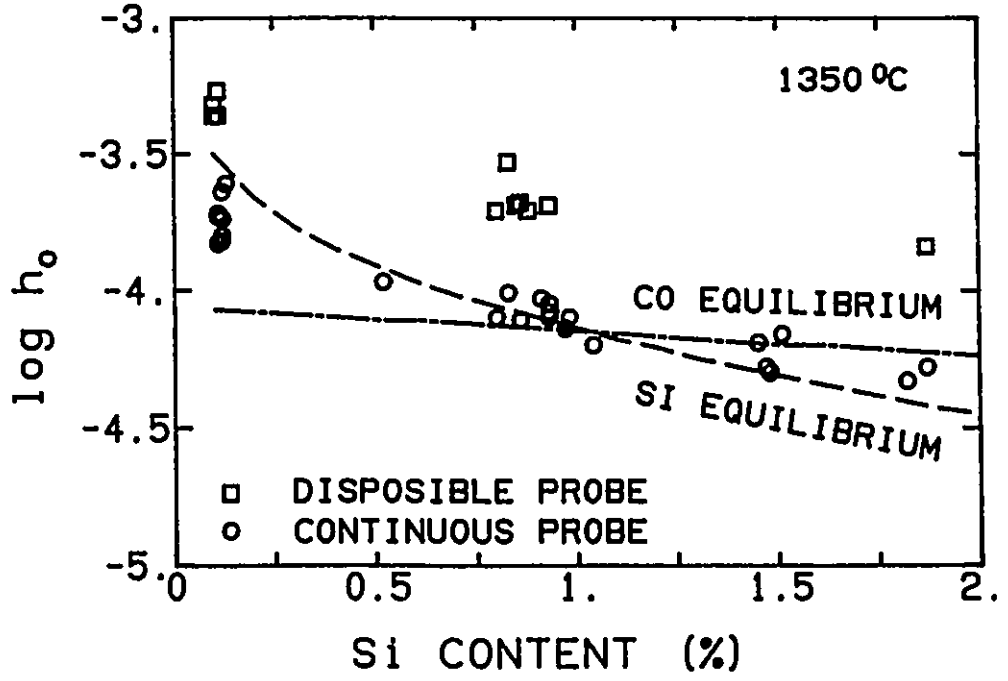

Figure 4.7 The comparison of the oxygen activities measured by the continuous and single-use oxygen probes at 1350°C.

TABLE 4.3

SUMMARY OF EXPERIMENTAL RESULTS BEFORE GAS INJECTIONS (WITH CONTINUOUS OXYGEN PROBES)

Run No.	Si	C	Al	Temp.	h_o	log h_o
	%			°C	$\times 10^{-4}$	/
6-003	0.52	4.2		1348	1.07	-3.97
6-006	1.04	4.2		1342	0.63	-4.20
7-001	0.13	3.7		1350	2.45	-3.61
7-002	0.12	3.6		1347	2.29	-3.64
8-001	0.11	3.9		1330	1.48	-3.83
8-003	0.98	4.3		1353	0.79	-4.10
8-004	0.93	3.9		1346	0.83	-4.08
8-005	1.82	3.8		1353	0.47	-4.33
9-002	0.91	4.7		1343	0.93	-4.03
9-004	0.80	4.7		1342	0.79	-4.10
10-001	0.93	4.0		1351	0.79	-4.10
10-002	1.48	4.2	<0.001	1341	0.50	-4.30
10-003	1.51	4.3		1346	0.69	-4.16
10-005	1.47	4.3		1337	0.52	-4.28
10-006	1.45	4.1		1345	0.65	-4.19
11-001	0.11	4.0		1352	1.91	-3.72
11-002	0.97	4.4		1342	0.72	-4.14
11-007	1.87	4.4		1345	0.52	-4.28
12-001	0.12	4.2		1344	1.82	-3.74
12-002	0.12	4.2		1342	1.51	-3.82
12-003	0.12	4.2		1351	1.58	-3.80
12-004	0.11	4.2		1346	1.86	-3.73
13-001	0.86	4.3		1350	0.78	-4.11
13-002	0.93	4.8		1338	0.89	-4.05
13-012	0.83	4.1		1350	0.98	-4.01

TABLE 4.4

SUMMARY OF EXPERIMENTAL RESULTS AFTER GAS INJECTION (WITH CONTINUOUS OXYGEN PROBES)

Run No.	Si	C	Al	Temp.	h_o	log h_o
	%			°C	$\times 10^{-4}$	
6-001	0.10	4.0		1330	2.19	-3.66
9-001	0.90	4.7		1334	0.76	-4.12
9-003	0.83	4.6		1330	0.76	-4.12
10-003	1.51	4.3	<0.001	1335	0.44	-4.36
11-004	1.89	4.7		1335	0.38	-4.42
11-007	1.87	4.4		1326	0.40	-4.40
13-003	0.91	4.5		1320	0.66	-4.18
6-005	1.04	4.0		1300	0.37	-4.43
7-001	0.13	3.7		1300	1.20	-3.92
8-001	0.11	3.9		1298	1.05	-3.98
9-003	0.83	4.6	<0.001	1308	0.62	-4.21
10-003	1.51	4.3		1300	0.26	-4.59
10-005	1.47	4.3		1300	0.30	-4.52
11-007	1.87	4.4		1300	0.28	-4.55

TABLE 4.5

SUMMARY OF EXPERIMENTAL RESULTS

(WITH SINGLE-USE OXYGEN PROBES)

Run No.	Si	C	Al	T	emf	h_o
	%			°C	mv	$\times 10^{-4}$
4-1	0.62	3.3		1382	-42	3.85
4-2	0.62	3.3		1366	-70	2.37
4-3	0.64	3.2		1396	-50	3.83
4-4	0.64	3.2	<0.001	1427	-52	4.65
4-5	0.63	3.3		1397	-50	3.86
4-6	0.63	3.3		1349	-62	2.33
4-7	0.63	3.3		1429	-53	4.68
4-8	0.63	3.3		1381	-54	3.25
5-1	0.60	3.2		1423	-50	4.66
5-2	0.60	3.2		1374	-46	3.45
5-3	0.55	3.5	<0.001	1352	-54	2.64
5-4	0.56	3.5		1348	-40	3.08
5-5	0.57	3.1		1366	-190	0.49
5-6	0.59	3.1		1360	-188	0.48
6-1	0.11	3.9		1352	0	5.34
6-2	0.10	4.0		1352	-8	4.81
6-3	0.51	3.5	<0.001	1377	-68	2.63
6-4	0.51	3.4		1377	-65	2.74
6-5	1.03	4.5		1327	-92	1.35
6-6	1.04	3.5		1327	-90	1.38
7-1	0.10	3.6	<0.001	1316	22	5.45
7-2	0.12	3.9	0.199	1316	/	/
7-3	0.12	3.8	0.175	1359	/	/
8-1	0.12	3.8		1377	-3	6.17
8-2	0.11	3.9	<0.001	1332	-10	4.07
8-3	0.10	4.2		1350	-14	4.40
8-4	0.93	3.9		1393	-85	2.37
8-5	1.79	4.7	0.002	1343	-111	1.18
8-6	1.74	4.5	0.002	1404	-110	1.85

TABLE 4.5 (CONTINUED)

Run No.	Si	C	Al	T	emf	h_c
	%			°C	mv	$\times 10^{-4}$
9-1	0.90	4.7		1379	-84	2.18
9-2	0.91	4.7		1335	-80	1.67
9-3	0.83	4.6	<0.001	1332	-59	2.15
9-4	0.80	4.8		1349	-75	1.97
9-5	0.72	4.4		1377	-60	2.11
9-6	0.68	4.6		1331	-98	1.22
10-1	0.88	4.0		1397	-78	2.67
10-2	0.93	4.0		1322	-78	1.57
10-3	1.42	4.0		1324	-102	1.16
10-4	1.48	4.2	<0.001	1327	-95	1.30
10-5	1.51	4.3		1307	-104	1.01
10-6	1.47	4.3		1321	-92	1.30
10-7	1.47	4.3		1328	-96	1.30
10-8	1.44	4.2		1316	-34	2.64
10-9	1.45	4.0	0.014	1327	-152	0.62
10-10	1.45	4.1	0.008	1317	-136	0.71
11-1	0.13	4.0		1363	-36	3.62
11-2	0.11	4.0	<0.001	1324	-12	3.73
11-3	0.97	4.4		1321	-89	1.35
11-4	1.83	4.7	0.007	1338	-100	1.31
11-5	1.89	4.7	0.001	1357	-110	1.32
11-6	1.89	4.7	0.001	1377	-104	1.64
11-7	1.88	4.7		1360	-100	1.54
11-8	1.87	4.4	<0.001	1367	-100	1.61
11-9	1.87	4.4		1346	-97	1.45
12-1	0.12	4.2		1363	-6	5.36
12-2	0.11	4.1	<0.001	1367	-48	3.20
12-3	0.11	4.4		1352	-16	4.34
13-1	0.87	4.7		1354	-78	1.97
13-2	0.93	4.8		1354	-76	2.02
13-3	0.91	4.5		1363	-76	2.15
13-4	0.92	4.6		1374	-74	2.38
13-5	0.91	4.7		1366	-28	4.10
13-6	0.89	4.3	<0.001	1318	-100	1.14
13-7	0.88	4.3		1333	-110	1.12
13-8	0.88	4.2		1374	-78	2.26
13-9	0.87	4.1		1371	-73	2.37
13-10	0.85	4.1		1350	-73	2.04
13-11	0.85	4.2		1347	-70	2.08
13-12	0.83	4.1		1352	-46	2.93

Figures 4.8 a and b show an example of the gas flow rate and the bath cooling during a gas injection. In this case, the nitrogen gas injection started with the flow rate of 2 SLPM, then, jumped to 10 SLPM at 20 seconds. after three minutes, fell to 2 SLPM again until the injection ended. As can be seen in Figure 4.8 b, the bath cooling was relatively slow before 30 seconds and after 210 seconds, indicating that the heat losses from the melt were directly related to the gas flow rate. The response of the thermocouple to the gas flow rate change was delayed by about ten seconds. This may be explained by the thermal resistance of the thermocouple shell.

A general heat balance of the melt is

$$\rho_l V_l C_p^l \frac{dT_l}{dt} = -hA(T_l - T_R) \qquad (4.1)$$

where, T_l is the bath temperature, T_R is the temperature of the cooling water and the atmosphere (°C), t is the time (s), ρ_l is the density of liquid iron, C_p^l is the specific heat of the liquid iron (J/kg/K), V_l is the volume of the melt (m^3). A is the heat exchange area (m^2), and h is the overall heat transfer coefficient ($W/m^2/K$), which represents the effect of heat conduction, convection and radiation. For simplicity, an overall heat transfer rate constant K_T (1/s) was used to analyze the experimental data and was defined as

$$K_T = \frac{hA}{\rho_l V_l C_p^l} \tag{4.2}$$

Then, Equation 4.1 becomes

$$\frac{dT_l}{dt} = -K_T(T_l - T_R) \tag{4.3}$$

The heat transfer rate constants have been calculated by fitting the experimental data of the temperature-time response to Equation 4.3. The results are shown in Figure 4.9. One can see that the constant, K_T, is directly related to gas flow rate. The experimental data are given in Table 4.6. By using linear regression, it was found that

$$K_T = [(10.74 \pm 0.38) + (0.376 \pm 0.034)Q] \times 10^{-5} \quad (R^2 = 0.94) \tag{4.4}$$

where, Q is the gas flow rate (SLPM); R is the correlation coefficient.

4.2 CALCIUM CARBIDE POWDER INJECTION

Compared with injection of gas, the experiments of powder injection were more complicated to control and monitor. Typical experimental results are given

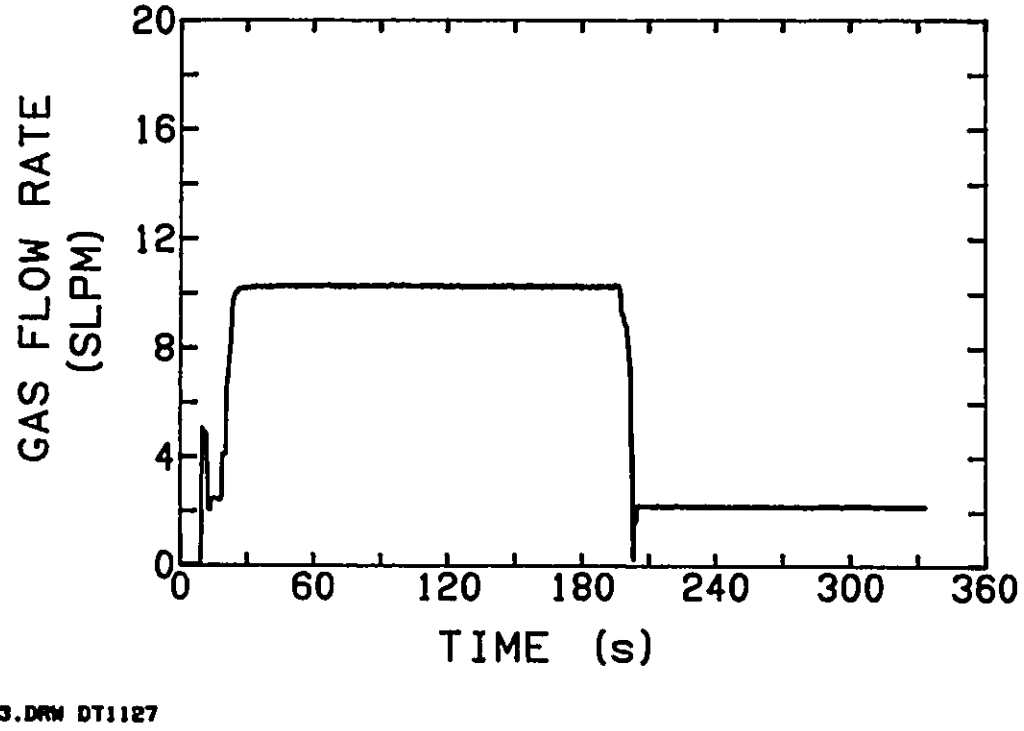

Figure 4.8 a The nitrogen flow rate during a typical gas injection.

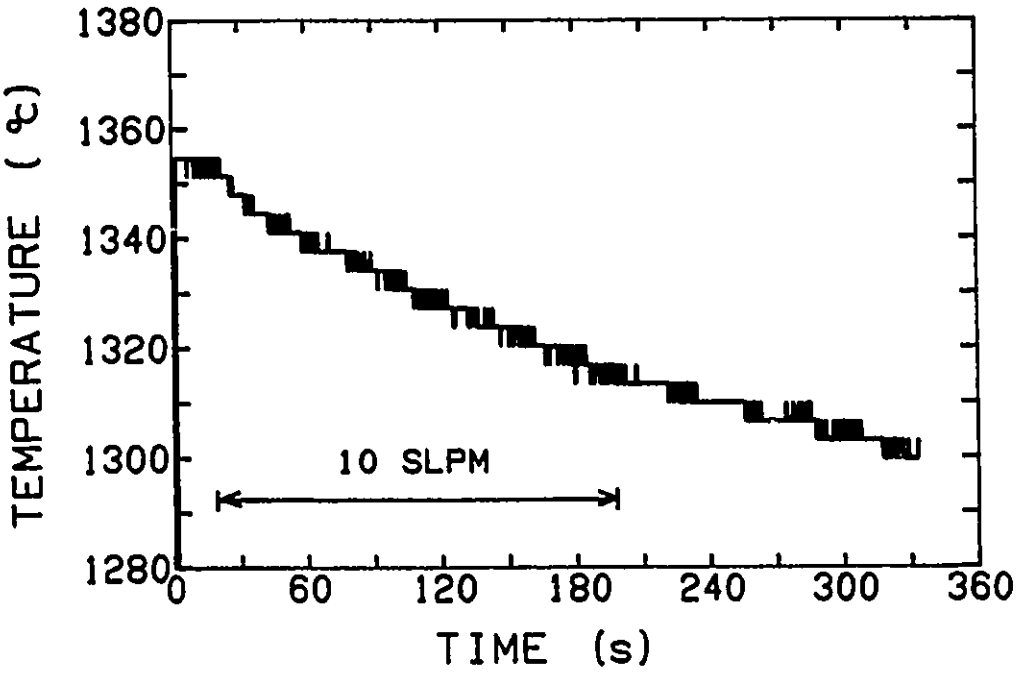

CHPT422.DRW DT1167

Figure 4.8 b The bath temperature change during the same gas injection as in Figure 4.8 a. Fast bath cooling is related to a high gas flow rate (10 SLPM).

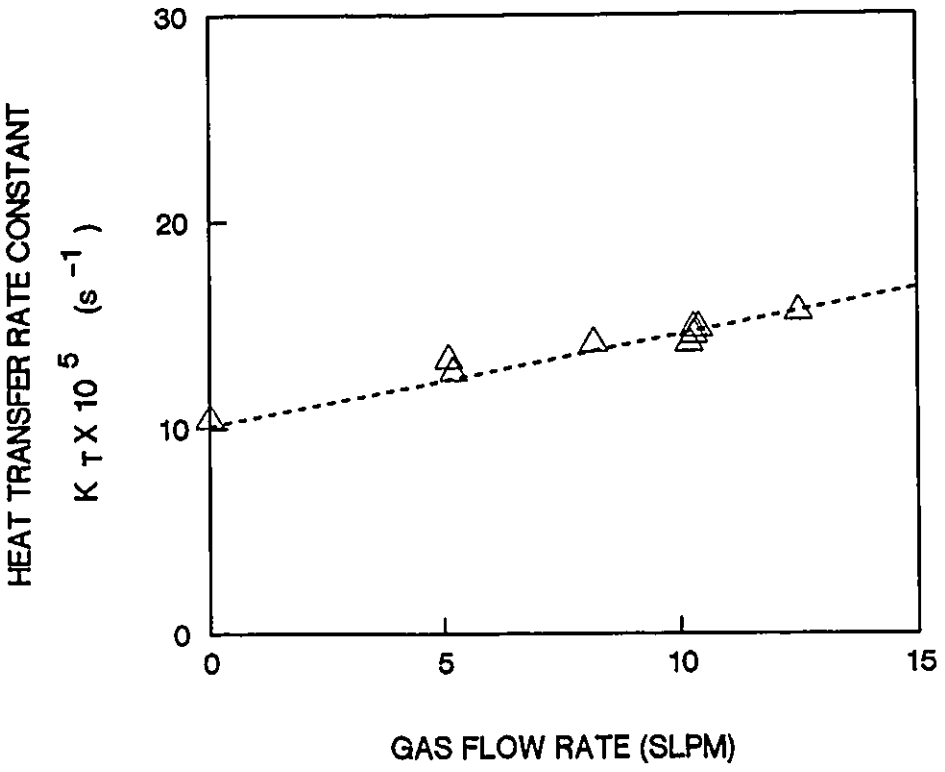

Figure 4.9 The dependence of the heat transfer rate constant on the gas flow rate during nitrogen gas bubbling. The dashed line is given by linear regression.

TABLE 4.6

HEAT TRANSFER RATE CONSTANT OF GAS INJECTIONS

Run No.	Gas Flow Rate	Temperature	Constant $K_T \times 10^5$	Weight of Melt
	SLPM	°C	1/s	kg
3-002	12.5	1345	15.6	73
3-004	0.0	1380	10.4	73
6-003	10.3	1327	14.8	68
6-005	8.2	1310	14.1	68
9-001	10.2	1358	14.1	69
9-003	10.3	1358	14.5	69
10-003	10.4	1340	14.8	70
10-007	5.1	1333	13.3	70
11-007	10.2	1341	14.1	72
13-003	5.2	1332	12.7	69

in Figures 4.10 a, b, c and d. Figure 4.10 a shows that the gas flow rate was 8.5±1 SLPM throughout the powder injection period. During the injection, the weight in the dispenser declined linearly (Figure 4.10 b). The solid feed rate was determined from the slope of the line by linear regression. There was a substantial temperature drop during injection, for example, 60°C in Figure 4.10 c because the induction power was turned off before the injection. The output of the oxygen probe, converted to oxygen activity, is shown in Figure 4.10 d. (These activities are calculated at the instantaneous melt temperature as given in Figure 4.10 c). The gaps in the curve occurred at approximately 200 seconds because the molybdenum electrode in the bath dissolved, and had to be pushed down into the melt again.

The progress of the sulphur content and the oxygen activity throughout a typical injection into an iron-carbon-silicon melt are shown in Figures 4.11 a and b, respectively. As shown by two horizontal sections in Figure 4.11 a, the desulphurization was rather slow at the beginning of the powder injection as well as after the injection stopped. The initial period of the desulphurization delay was referred to as an incubation time. The incubation phenomena will be discussed in Section 4.2.1. The inclined dashed line represents a fast desulphurization after the incubation. In Figure 4.11 b, the oxygen activity was well below that expected from the equilibrium with either carbon-carbon monoxide or silicon-silica, which are represented by two dashed lines (The latter one declined with the falling temperature). Figure 4.11 gives a clear evidence that deoxidation took place during desulphurization with calcium carbide.

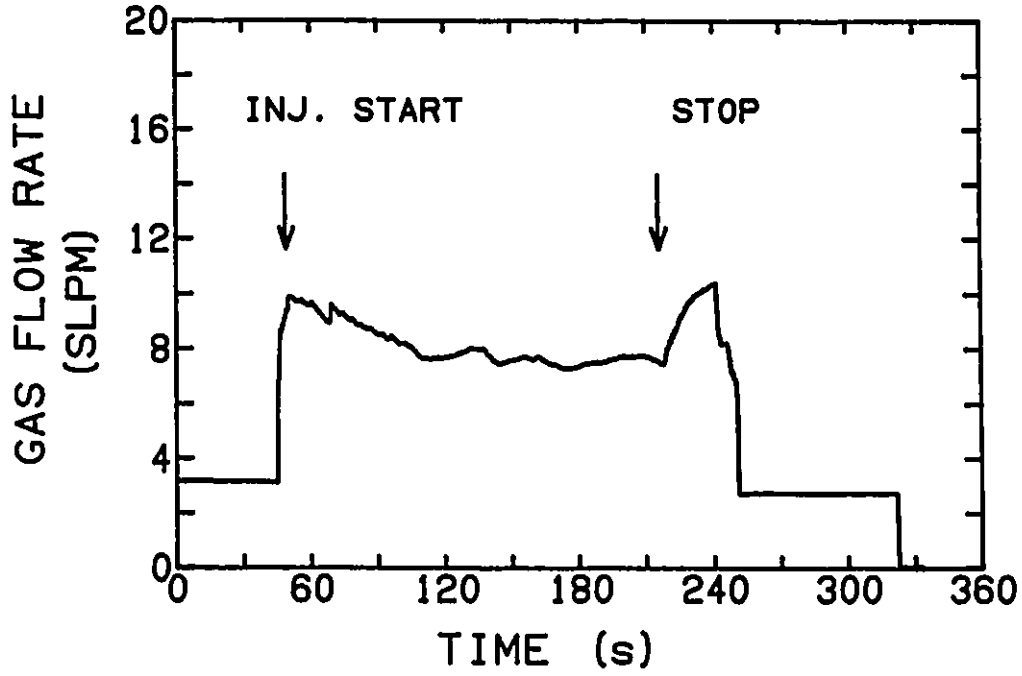

CHPT410.DRW DT1026

Figure 4.10 a The nitrogen flow rate during a typical calcium carbide injection.

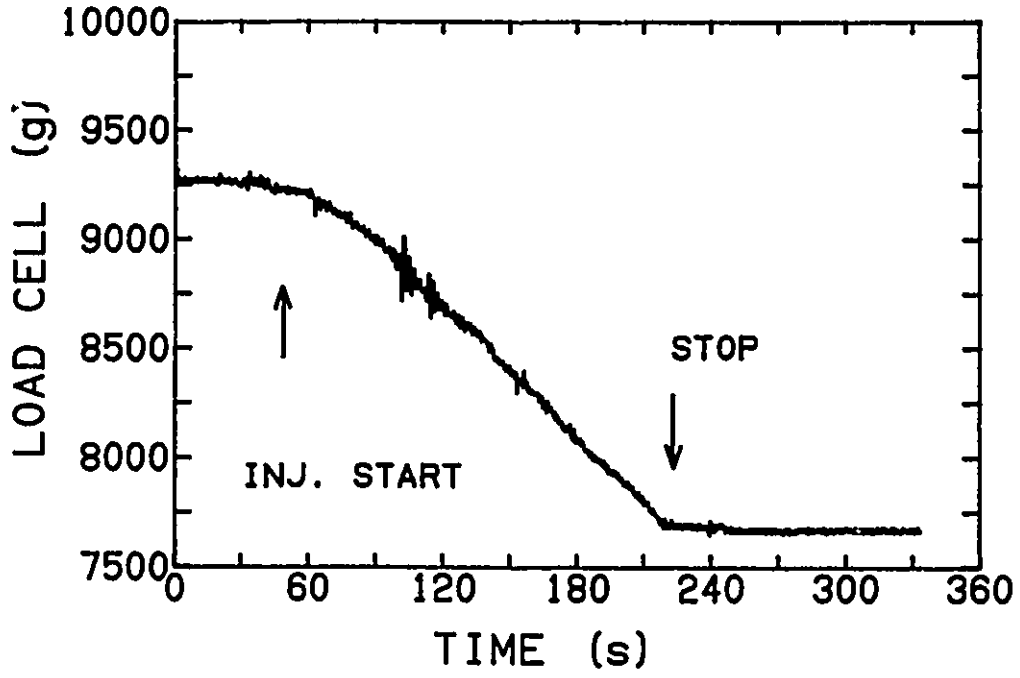

CHPT411.DRW DT1036

Figure 4.10 b The weight of calcium carbide powder and the dispenser during the same injection as in Figure 4.10 a.

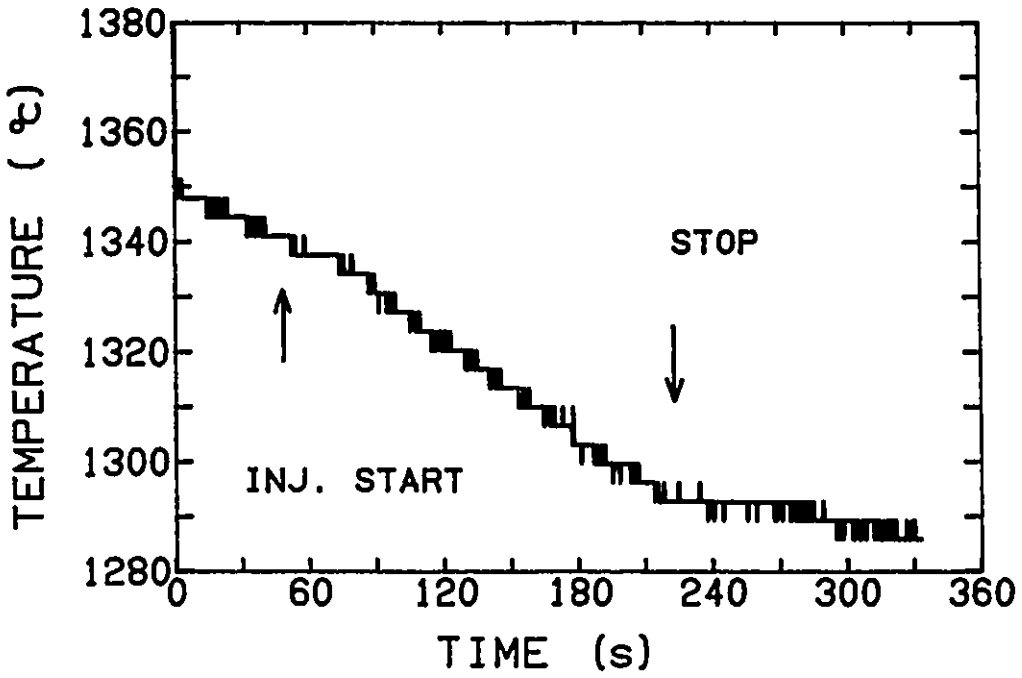

CHPT413.DRW DT1066

Figure 4.10 c The temperature of the iron during the injection.

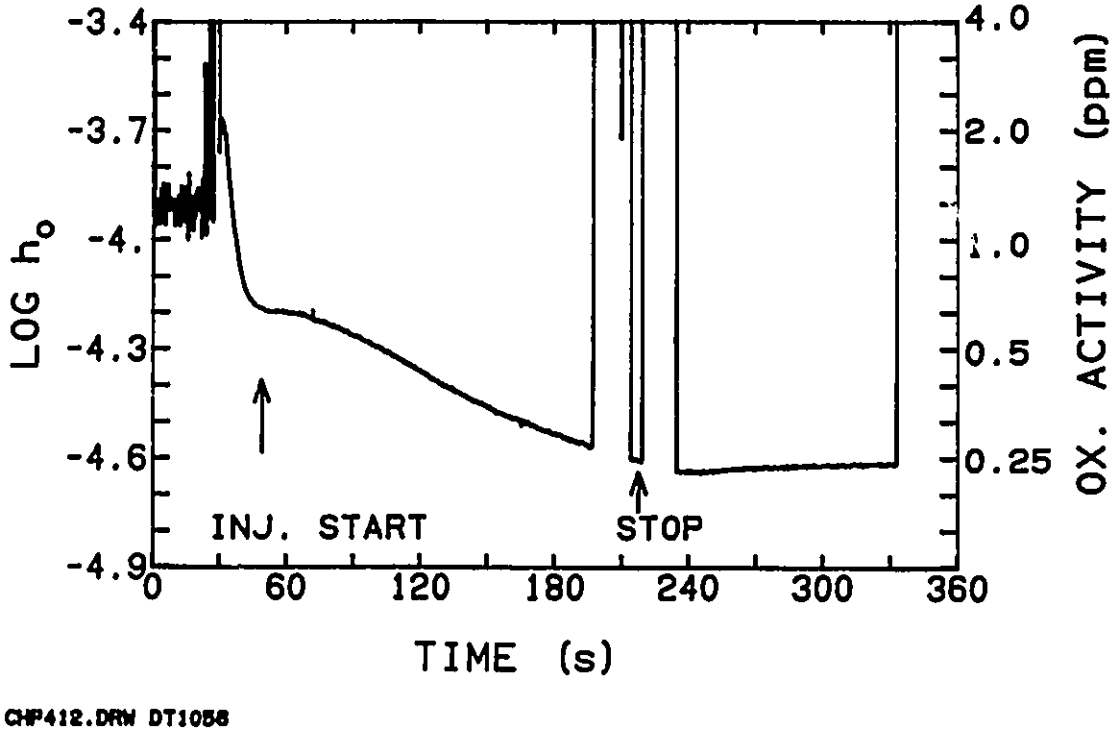

Figure 4.10 d The oxygen activity during the injection calculated at the instantaneous temperature shown in Figure 4.10 c. The discontinuities at approximately 200 seconds correspond to the dissolution and subsequent re-entry of the molybdenum lead wire.

More experiments were carried out to examine the role of oxygen activity on desulphurization. In these experiments, the oxygen activity was varied in a wide range by changing the silicon contents (0.1-2.0%), and aluminum contents (0.001-0.2%). Figures 4.12 a and b show another example. It can be seen that the melt which was initially deoxidized with aluminum exhibited lower oxygen activity, shorter incubation period and faster desulphurization. The information drawn from the statistic analysis of the experimental data will be shown in the following section.

4.2.1 The Effect of the Oxygen Activity and the Powder Feed Rate on the Desulphurization Rate

This section consists of three parts:

- the desulphurization rate after incubation
- the determination of the incubation period
- the desulphurization rate after powder injection

As reviewed in Chapter 2, it has often been found that the overall rate of desulphurization can be expressed as:

$$\frac{d\%S}{dt} = -K_S\%S \qquad (4.5)$$

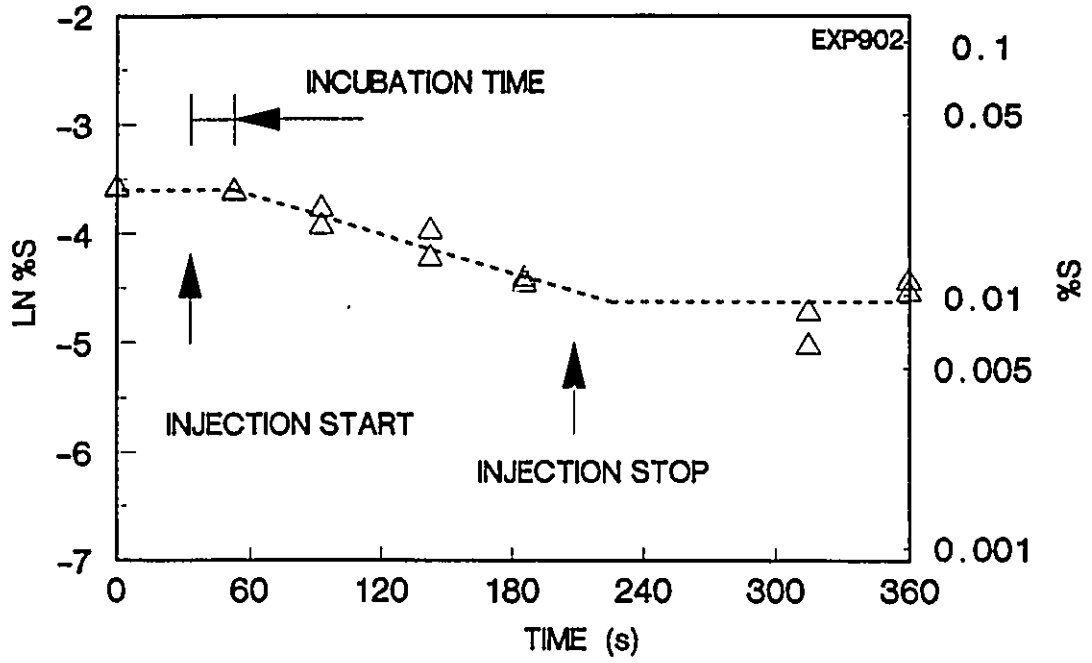

Figure 4.11 a The change of sulphur content with time during an injection of calcium carbide at 0.17 kg/min and nitrogen gas flow rate 5.2 SLPM into iron-4.2% carbon-0.91% silicon melt with an initial temperature 1350°C. The lines were used to determine the first order constants.

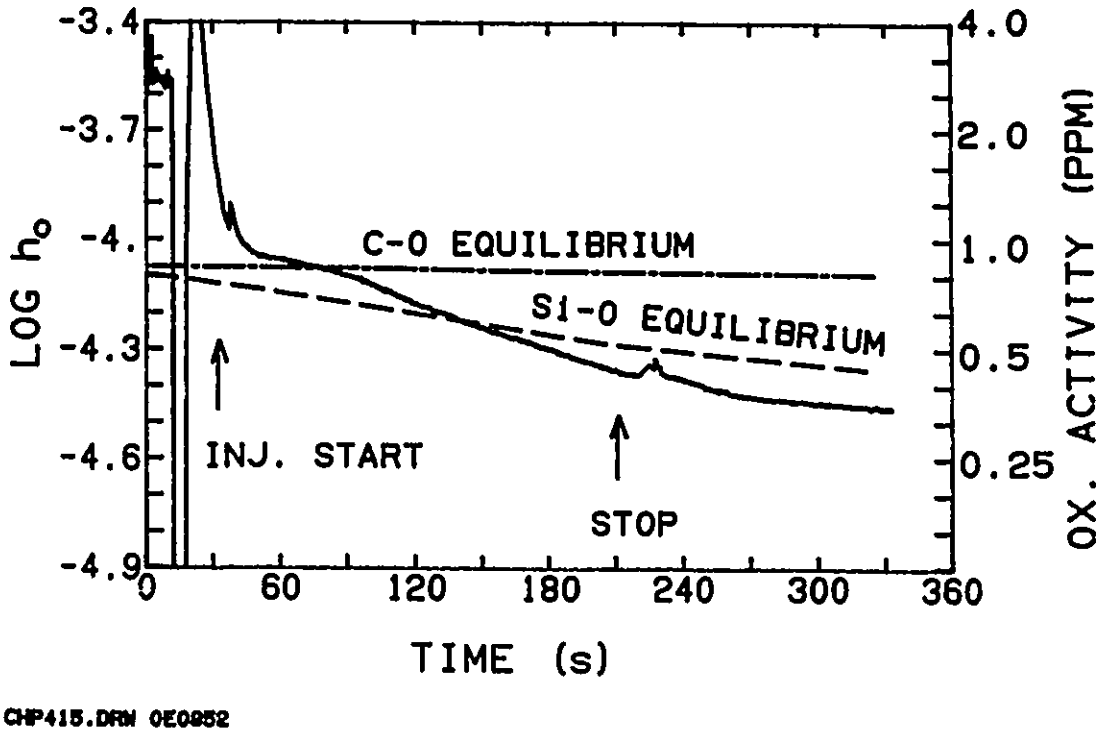

Figure 4.11 b The oxygen activity during the same injection as in Figure 4.11 a. The carbon-carbon monoxide and silicon-silica equilibria are also shown.

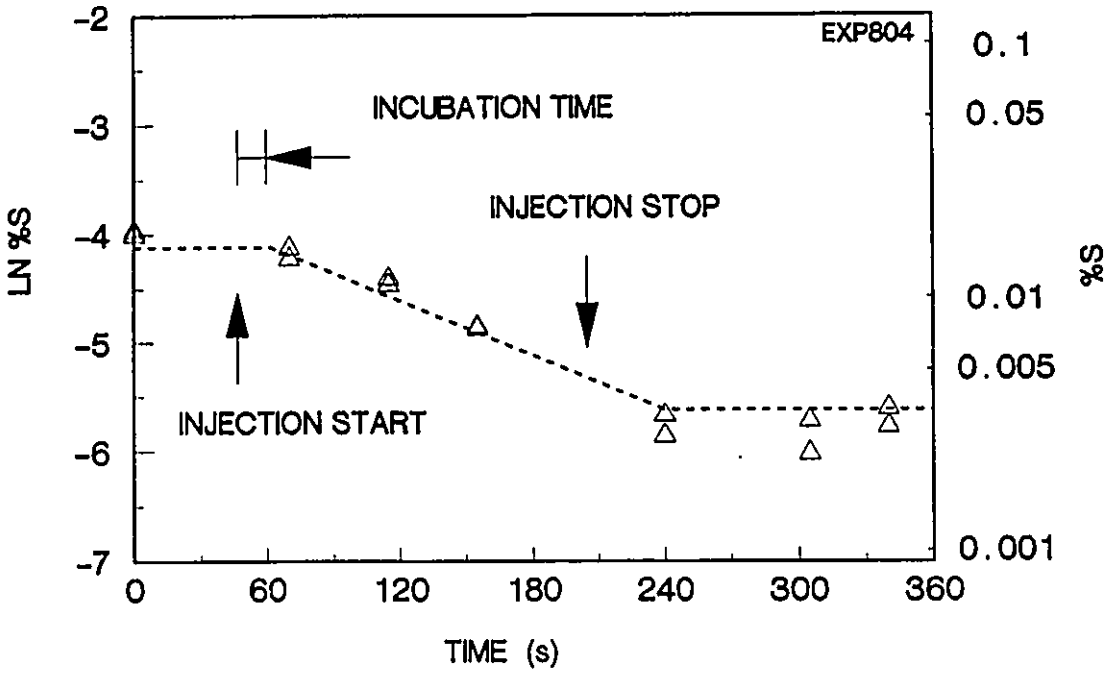

Figure 4.12 a The change of sulphur content with time during an injection of calcium carbide at 0.15 kg/min and nitrogen gas flow rate 5 SLPM into iron-4.2% carbon-0.93% silicon-0.009% aluminum melt with an initial temperature 1350°C. The lines were used to determine the first order rate constant and the incubation time.

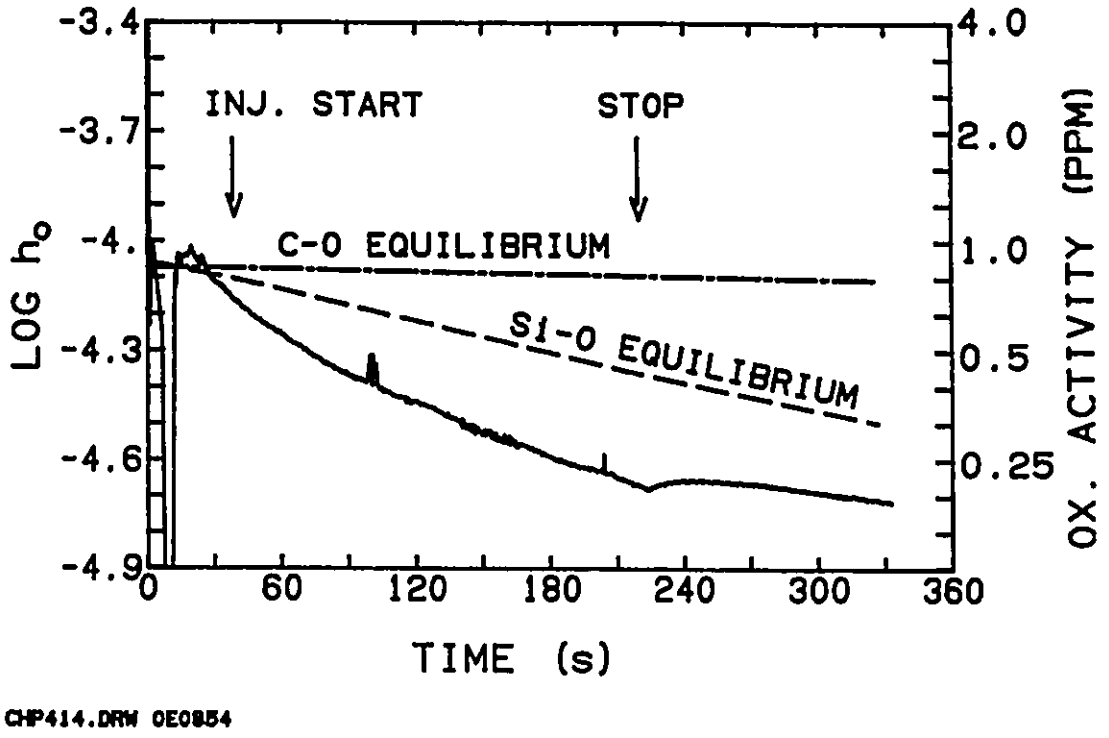

Figure 4.12 b The oxygen activity during the same injection as in Figure 4.12 a. The carbon-carbon monoxide and silicon-silica equilibria are also shown.

where, K_S is the first order rate constant of desulphurization (1/s). Rearrangement and integration demonstrates that the logarithm of sulphur content drops linearly with time:

$$\ln\left(\frac{\%S}{\%S^o}\right) = -K_S t \qquad (4.6)$$

where, %S is the instantaneous sulphur content and %S° is the initial sulphur content. According to Equation (4.6), the logarithm of sulphur content is a linear function of time.

As seen in Figures 4.11 a and 4.12 a, the logarithm of sulphur content declined linearly with time after the incubation period. The slope of the inclined lines represents the first order rate constant, K_S. More examples are given in Figures 4.13-4.20. These examples confirm that the kinetics of desulphurization can be described as first-order with respect to the sulphur content in the iron for injection after incubation.

The first order rate constants, K_S, were determined from linear regressions of the logarithm of sulphur contents on time. The results are summarized in Table 4.7. The average correlation coefficient is 0.94. The relative error is only 9 per cent (See Section 4.4.2 for more details). Thus, it is reasonable to consider the kinetics of desulphurization as first-order with respect to the sulphur content in the iron for injection after incubation.

The rate constant is plotted against the rate of powder injection in Figure 4.21. One can see that the rate constant of desulphurization depends on silicon and aluminum content, as well as powder rate. The rate constant increases with increasing silicon content from 0.1 to 1%. But, further increasing silicon content from 1 to 2% does not make significant difference. Moreover, a small amount of aluminum addition (0.003-0.2%) contributes towards the highest desulphurization rate. It has been known that oxygen activity decreases as silicon and aluminum content increases. However, it has not been previously appreciated that the rate of calcium carbide desulphurization increases with decreasing oxygen activity. The results on limestone and carbon dioxide are also shown in Figure 4.21 and will be discussed in Section 4.3.

The incubation time was calculated from the variation of sulphur content with time. The calculation procedures are

(1) determination of the equation of the inclined line (which corresponds a period of fast desulphurization) by linear regression, as discussed above

(2) determination of the intersection point of the inclined line and the initial horizontal line (which corresponds a period of slow desulphurization)

The difference between the injection starting point and the intersection point was considered as the incubation period. In Figures 4.11-4.20, the incubation period has been marked by a two-arrowhead line. Further results on

the incubation time are summarized in Table 4.9. The multiple regression of the experimental data on the solid flow rate, the silicon and aluminum contents of the iron yields:

$$\tau_i = (45.3\pm5.2) - (0.0143\pm0.0168)W_p - (18.6\pm4.2)[\%Si] - (47.5\pm62.1)[\%Al] \quad (R^2 = 0.64) \tag{4.7}$$

where, τ_i is the incubation time (s), W_p is the powder flow rate (g/min). Note that the coefficient of silicon content has a very small uncertainty. The experimental results are also shown in Figure 4.22. The incubation time was found to be strongly related to the silicon content of the iron. As indicated in Section 4.1.1, the oxygen activity in the melt was controlled by its silicon content. Aluminum addition significantly lowered the oxygen activity. As shown in Figure 4.22, the melts containing 0.003-0.16% Al exhibit shorter incubation periods. The incubation time did not change with silicon content. This may be explained by that the oxygen activity of the melts was no longer controlled by silicon.

After powder injection, in most cases, no significant desulphurization was observed. The results on the first order rate constant after powder injection are given in Table 4.8. The average value is 0.0004 (1/s). It is more than ten times less than that during powder injection. The relatively large standard deviation may be generated by the errors in sampling and sulphur analysis (See Section 4.4.2 for more details).

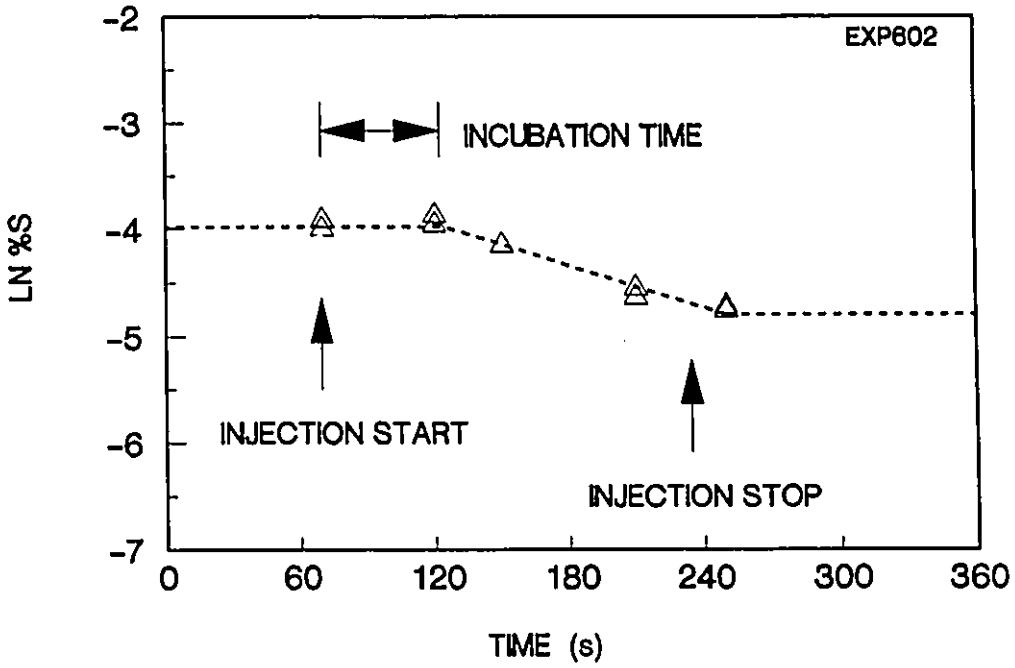

Figure 4.13 The change of sulphur content with time during an injection of calcium carbide at 0.21 kg/min and nitrogen gas flow rate 4.5 SLPM into iron-4.2% carbon-0.1% silicon melt with an initial temperature 1340°C. The lines were used to determine the first order rate constant and the incubation time.

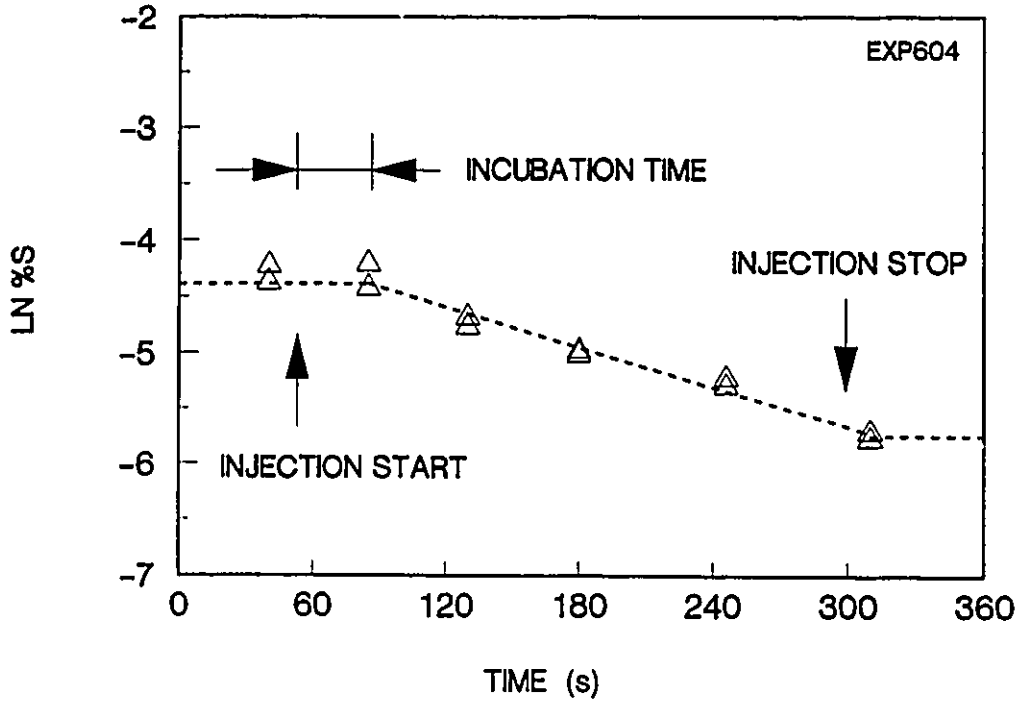

Figure 4.14 The change of sulphur content with time during an injection of calcium carbide at 0.12 kg/min and nitrogen gas flow rate 4.5 SLPM into iron-4.2% carbon-0.52% silicon melt with an initial temperature 1340°C. The lines were used to determine the first order rate constant and the incubation time.

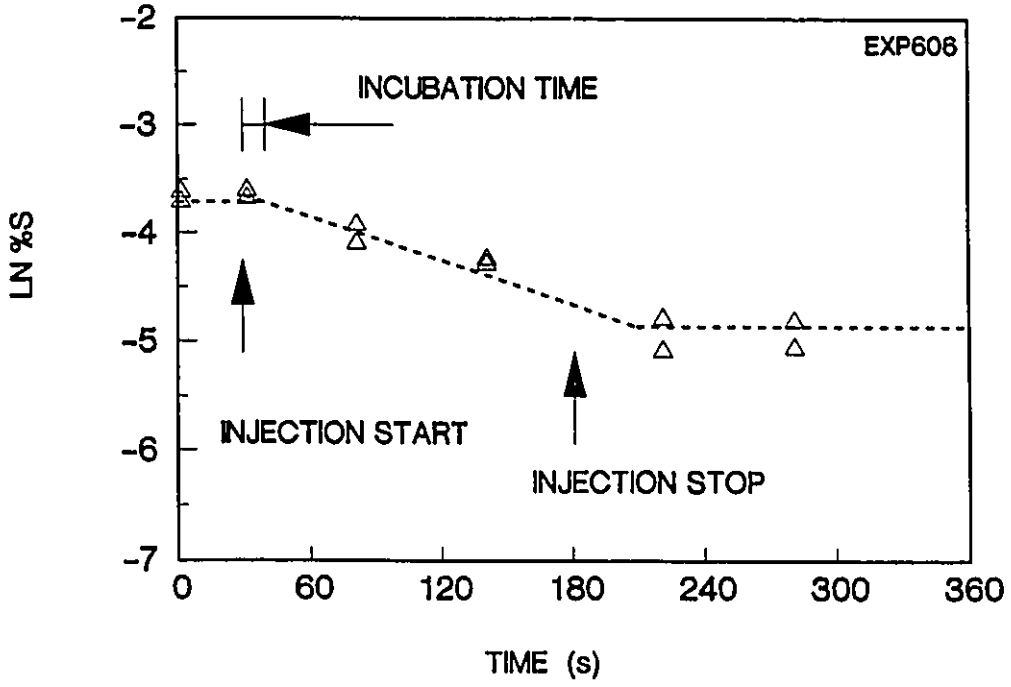

Figure 4.15 The change of sulphur content with time during an injection of calcium carbide at 0.21 kg/min and nitrogen gas flow rate 4.8 SLPM into iron-4.2% carbon-1.0% silicon melt with an initial temperature 1345°C. The lines were used to determine the first order rate constant and the incubation time.

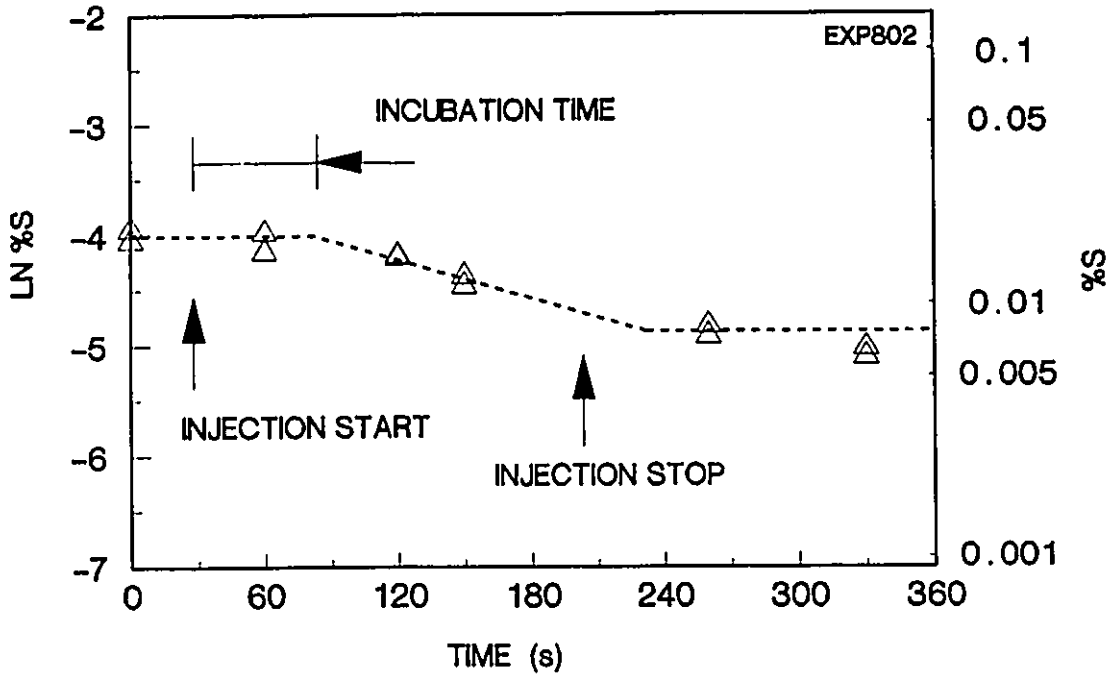

Figure 4.16 The change of sulphur content with time during an injection of calcium carbide at 0.16 kg/min and nitrogen gas flow rate 5.0 SLPM into iron-4.2% carbon-0.1% silicon melt with an initial temperature 1365°C. The lines were used to determine the first order rate constant and the incubation time.

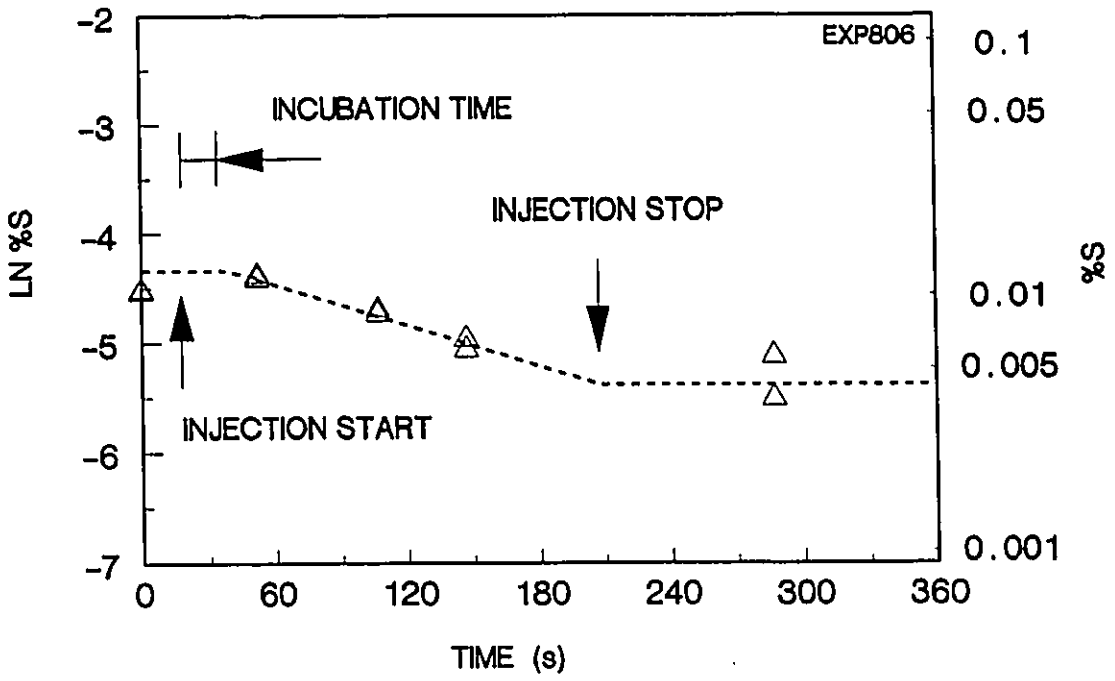

Figure 4.17 The change of sulphur content with time during an injection of calcium carbide at 0.14 kg/min and nitrogen gas flow rate 5.0 SLPM into iron-4.2% carbon-1.8% silicon melt with an initial temperature 1370°C. The lines were used to determine the first order rate constant and the incubation time.

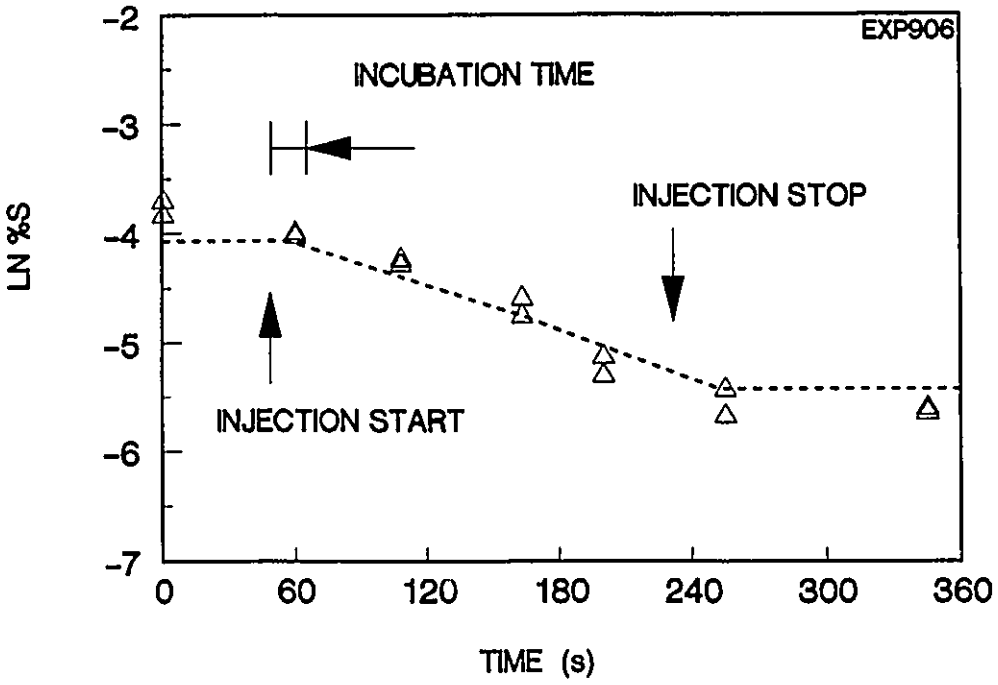

Figure 4.18 The change of sulphur content with time during an injection of calcium carbide at 0.21 kg/min and nitrogen gas flow rate 5.0 SLPM into iron-4.2% carbon-0.68% silicon melt with an initial temperature 1370°C. The lines were used to determine the first order rate constant and the incubation time.

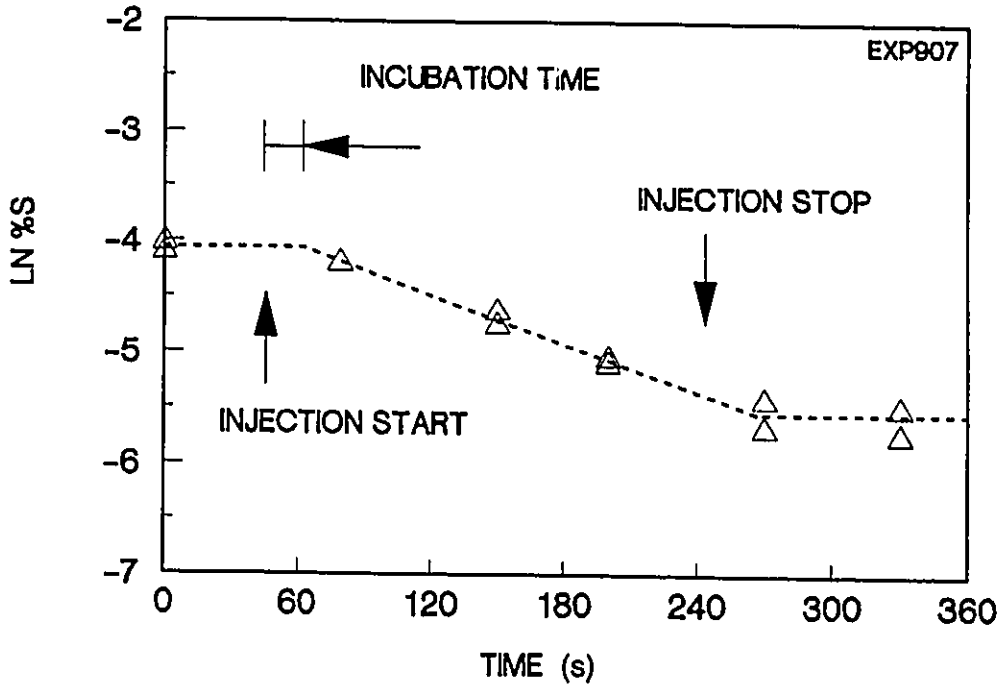

Figure 4.19 The change of sulphur content with time during an injection of calcium carbide at 0.17 kg/min and nitrogen gas flow rate 5.2 SLPM into iron-4.2% carbon-0.66% silicon melt with an initial temperature 1368°C. The lines were used to determine the first order rate constant and the incubation time.

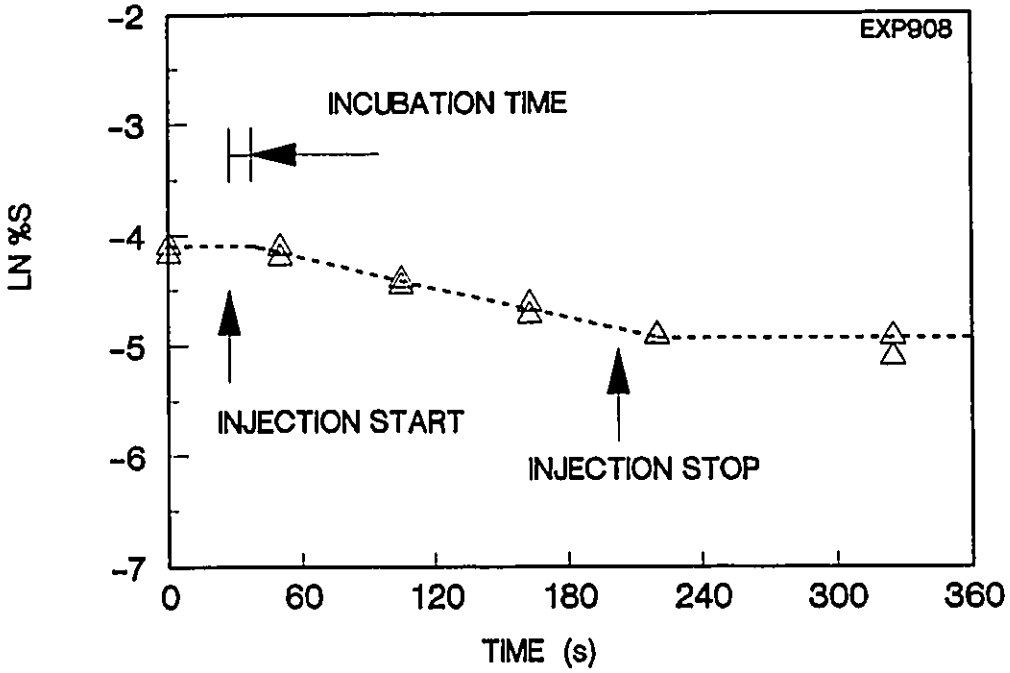

Figure 4.20 The change of sulphur content with time during an injection of calcium carbide at 0.1 kg/min and nitrogen gas flow rate 5.2 SLPM into iron-4.2% carbon-0.68% silicon melt with an initial temperature 1365°C. The lines were used to determine the first order rate constant and the incubation time.

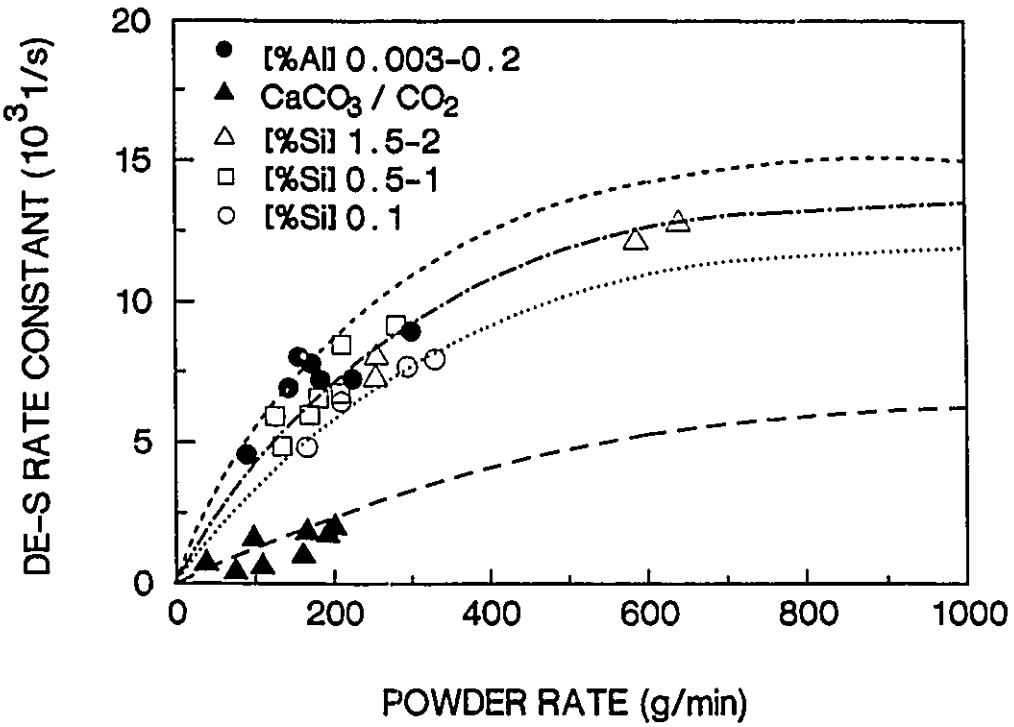

Figure 4.21 The first order rate constants as a function of the powder rate for the various conditions. The lines are predicted from the kinetic model. The details will be discussed in Chapter 5.

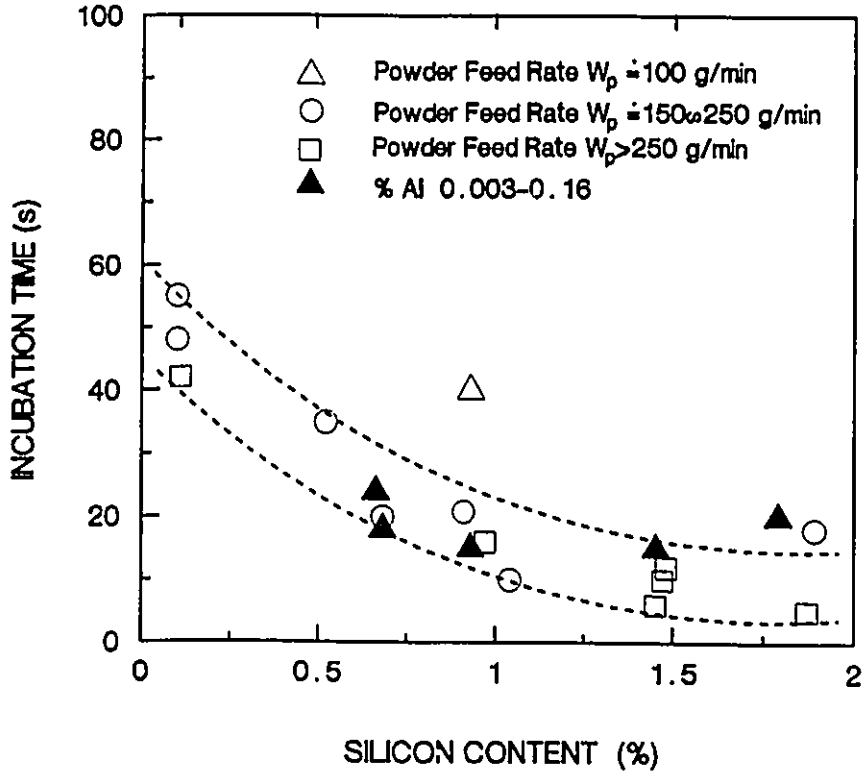

Figure 4.22 The dependence of the incubation time on the silicon content of the iron during calcium carbide injections. The incubation time is also affected by the powder feed rate. The upper dashed line corresponds to low rate, and the lower one to high rate.

TABLE 4.7

DESULPHURIZATION RATE CONSTANT DURING POWDER INJECTIONS

Run No.	Powder Rate	Si	C	Al	Constant $K_s \times 10^1$
	g/min	%			s^{-1}
8-002	165	0.10	4.2		4.79
6-002	209	0.10	4.0	<0.001	6.40
7-002	294	0.12	3.6		6.78
11-001	329	0.11	4.0		7.93
6-004	125	0.52	3.4		5.88
10-001	134	0.93	4.0		4.81
9-002	169	0.91	4.7		5.94
9-006	180	0.68	4.6	<0.001	6.24
9-004	180	0.80	4.8		6.54
6-006	208	1.03	4.0		6.71
11-002	280	0.97	4.4		9.13
10-002	254	1.48	4.2		9.10
10-004	255	1.47	4.3	<0.001	7.99
10-006	585	1.44	4.1		10.6
11-008	639	1.87	4.4		12.7
9-008	88	0.68	4.7	0.009	4.51
8-006	142	1.79	4.7	0.003	6.89
8-004	144	0.93	3.9	0.009	6.95
9-007	171	0.66	4.0	0.016	7.77
10-008	182	1.45	4.1	0.008	7.18
11-003	224	1.89	4.7	0.001	8.37
7-004	299	0.12	3.9	0.199	8.92
13-010	37	0.85	4.2		0.66
12-002	74	0.12	4.2		0.36
13-002	97	0.93	4.8		1.54
12-004	108	0.11	4.2	<0.001	0.55
12-006	160	0.11	4.5		0.95
13-008	165	0.88	4.2		1.79
13-004	191	0.91	4.6		1.69
13-012	200	0.83	4.1		1.96

TABLE 4.8

DESULPHURIZATION RATE CONSTANT AFTER POWDER INJECTIONS

Run No.	Si	C	Al	Constant $K_S \times 10^3$
	%			s^{-1}
6-006	1.03	4.0	<0.001	2.4
7-006	0.12	3.7	0.127	-3.0
8-002	0.10	4.2	<0.001	3.3
8-004	0.93	3.9	0.009	0.4
8-006	1.79	4.7	0.003	5.7
8-007	1.75	4.5	0.002	-1.6
9-002	0.91	4.8	<0.001	-8.3
9-004	0.80	4.8	<0.001	0.8
9-006	0.68	4.6	<0.001	0.9
9-007	0.66	4.0	0.016	1.1
9-008	0.68	4.7	0.009	0.9
10-004	1.47	4.3	<0.001	2.3
Average Value				0.4
Standard Deviation				3.4

TABLE 4.9

THE EXPERIMENTAL DATA OF INCUBATION TIME

Run No.	Wp (g/min)	%Si	%Al	τ_i (s)
6-002	209	0.10	/ [a]	55
6-004	125	0.52	/	35
6-006	208	1.04	/	10
8-002	165	0.10	/	48
8-004	155	0.93	0.009	15
8-006	142	1.79	0.003	20
9-002	170	0.91	/	23
9-006	210	0.68	/	20
9-007	171	0.66	0.16	24
9-008	88	0.68	0.009	18
10-001	134	0.93	/	40
10-002	254	1.48	/	12
10-004	255	1.47	/	10
10-006	585	1.45	/	6
10-008	182	1.45	0.008	15
11-001	329	0.11	/	42
11-002	280	0.97	/	16
11-003	224	1.89	0.001	18
11-008	639	1.87	/	5

a less than 0.001

4.2.2 The Changes in the Sulphur Activity with the Oxygen Activity during Injection

It has been shown that the sulphur contents and the oxygen activities varied simultaneously during injections of calcium carbide (More experimental results can be seen in Appendix II). As discussed in Chapter 2, a diagram of log h_O-log h_S can be use to show the reaction path, an example of the desulphurization trajectory is given in Figure 4.23 which is an enlargement of an area in Figure 2.3 (The sulphur activities are calculated from the sulphur contents based on the thermodynamic data given in Chapter 2). In this example, the initial path is horizontal which corresponds to the incubation time, that is, the incubation time coincides with a period of deoxidation. The subsequent trajectory is approximately parallel to the CaO-CaS equilibrium line. More interesting information can be observed when more trajectories of refining are superimposed on a same diagram (Figure 4.24). The trajectories are divided into three groups in general according to the initial oxygen activities: high oxygen (greater than 10^{-4}, given by dashed lines), middle oxygen (greater than 0.1×10^{-4} and less than 10^{-4}, given by solid lines) and low oxygen (less than 0.1×10^{-4}, given by dash-dot lines). When the initial oxygen is high, the trajectories are approximately parallel to the line of the CaO-CaS equilibrium. As the initial oxygen content becomes lower, the refining trajectories become more vertical, indicating that more calcium carbide is being used for desulphurization, and comparatively little for deoxidation. Finally, when the initial oxygen is extremely low (due to high aluminum additions), the initial trajectory is almost vertical,

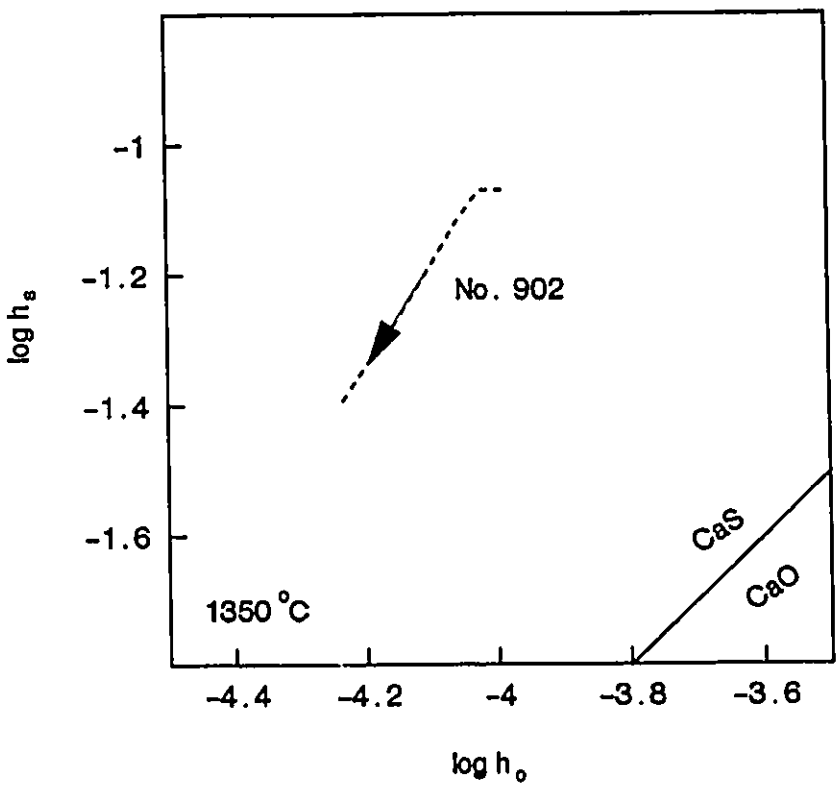

Figure 4.23 The change in the sulphur activity with the oxygen activity during a calcium carbide and nitrogen injection into iron-4.2% carbon-0.91% silicon melt with an initial temperature 1350°C. The equilibrium between CaO and CaS is also shown.

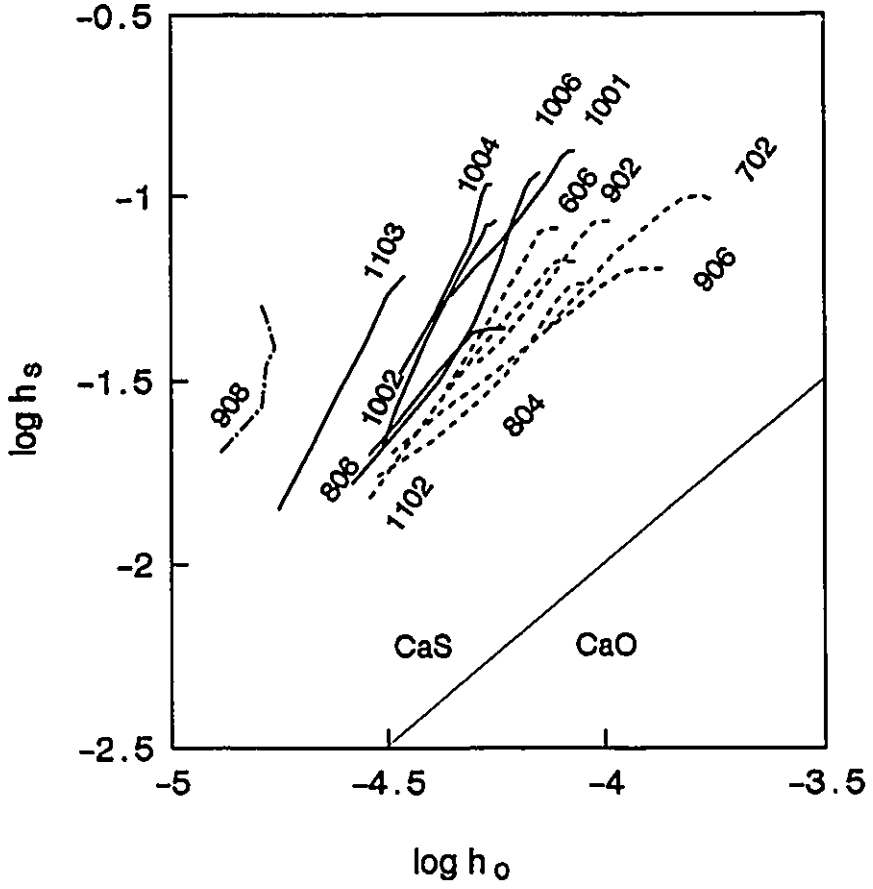

Figure 4.24 The changes in the sulphur activities with the oxygen activities during calcium carbide and nitrogen injections (the dashed lines for high oxygen activity, the solid lines for middle oxygen activity, and the dash-dot line for low oxygen activity). The equilibrium between CaO and CaS is shown at 1350°C.

which suggests that the oxygen activity of the melt is still controlled by aluminum at the initial stage of calcium carbide injection; then, as the injection proceeds, the deoxidation is governed by calcium carbide, thus, the trajectory turns left.

4.2.3 The Effect of the Gas and Powder Flow Rates on the Bath Cooling Rate

Since the electric power was shut off during injection, substantial temperature drops occurred due to the heat losses from the liquid iron. As seen in Figure 4.10 a, nitrogen gas was injected into the melt continuously throughout the test. A small amount of gas was used before and after the powder injection to prevent the lance from plugging. Much more gas was applied during the powder injection to carry solid particles into the melt. Figure 4.10 c shows clearly that the reduction of temperature was relatively slow before 60 seconds and after 220 seconds, indicating that the bath cooling was primarily affected by the injection of calcium carbide.

The experimental data of the bath cooling rates during powder injections were analyzed in a manner similar to that of Section 4.1.2. The heat transfer constant, K_T, which was defined in Equation 4.2 is used to determine the dependence of the bath cooling rates on the conditions of injections. As shown in Figure 4.25, the heat transfer constant, K_T, not only depends on the gas flow rate, but even more strongly on the powder feed rate. The experimental data used in Figure 4.25 are tabulated in Table 4.10. Multiple linear regression gives

$$K_T=[(10.3\pm0.3)+(0.398\pm0.04)Q+(0.0101\pm0.0007)W_p]\times10^{-5} \quad (R^2=0.92) \tag{4.8}$$

Here, Q is the gas flow rate in SLPM; W_p is the powder flow rate in g/min. It can be seen that first two terms of Equation 4.8 are almost identical to the corresponding terms of Equation 4.4 for the injection of nitrogen alone.

$$K_T=[(10.74\pm0.38)+(0.376\pm0.034)Q]\times10^{-5} \quad (R^2=0.94) \tag{4.4}$$

The bath temperature fell continuously even after powder injection. However, the cooling rate was much lower than during the powder injection. An example has been shown in Figure 4.10 c. The experimental data after powder injection were also analyzed by linear regression, the results are listed in Table 4.11. It is found that

$$K_T=[(10.05\pm0.73)+(0.289\pm0.20)Q]\times10^{-5} \quad R^2=0.24 \tag{4.9}$$

This equation has a very small correlation coefficient and quite large standard errors. The reason is that the computer recording time after powder injection was not long enough to eliminate the effect of the signal fluctuation noise. Even so, it can see that the constant and the coefficient of gas flow rate,

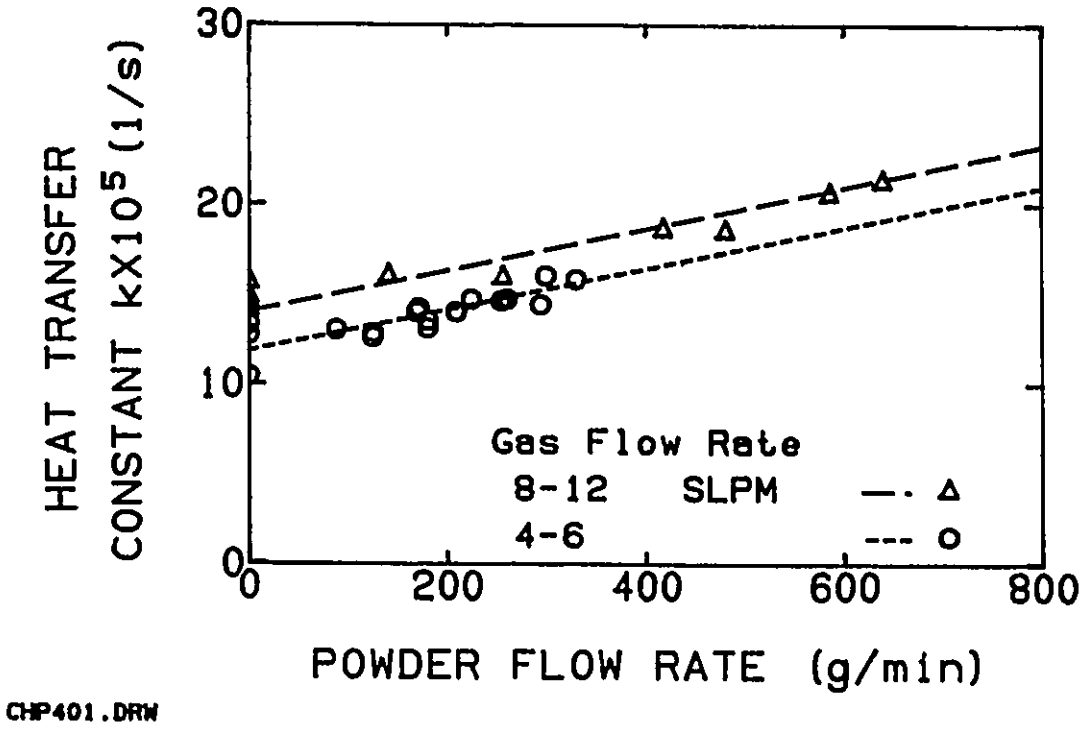

Figure 4.25 The dependence of the heat transfer rate constant on the gas flow rate and powder feed rate during calcium carbide injections. The dashed lines are given by linear regression.

TABLE 4.10

HEAT TRANSFER CONSTANT DURING POWDER INJECTIONS

Run No.	Gas Flow Rate	Powder Rate	Loading	Temperature	Constant K_T
	SLPM	g/min	kg/Nm^3	°C	10^5 1/s
3-002	12.5	0	0.0	1345	15.6
3-003	11.2	480	42.9	1344	18.5
3-004	0.0	0	/	1380	10.4
3-005	10.2	417	40.9	1348	18.6
5-002	8.8	140	15.9	1376	16.0
6-002	4.4	209	47.1	1333	14.0
6-003	10.3	0	0.0	1327	14.8
6-004	4.5	125	27.8	1330	12.8
6-005	8.2	0	0.0	1310	14.1
6-006	4.7	208	44.3	1344	14.0
7-002	4.0	294	72.6	1338	14.4
7-004	4.3	299	68.7	1340	16.0
7-006	4.8	125	25.9	1340	12.6
9-001	10.2	0	0.0	1358	14.1
9-002	5.2	169	32.5	1340	14.0
9-003	10.3	0	0.0	1358	14.5
9-004	5.0	180	36.0	1338	13.1
9-006	5.0	210	42.0	1365	13.5
9-007	5.0	171	34.2	1360	14.2
9-008	5.1	88	17.3	1365	13.0
10-002	5.0	254	50.8	1340	14.6
10-003	10.4	0	0.0	1340	14.8
10-004	9.5	255	26.8	1328	15.9
10-006	9.0	585	65.0	1340	20.6
10-007	5.1	0	0.0	1333	13.3
11-001	5.5	280	59.8	1354	15.8
11-002	4.5	260	62.0	1345	14.7
11-003	5.2	224	43.1	1340	14.7
11-007	10.2	0	0.0	1341	14.1
11-008	8.0	639	79.9	1350	21.3
13-003	5.2	0	0.0	1332	12.7

TABLE 4.11

THE BATH COOLING RATE CONSTANT AFTER POWDER INJECTION

Run No.	Gas Flow Rate (SLPM)	K_T (1/s)	Correlation Coefficient	Standard deviation
		$\times 10^5$	/	$\times 10^5$
3-005	5.0	11.6	0.56	0.18
6-006	4.5	11.4	0.93	0.06
10-002	2.0	10.5	0.88	0.09
10-004	5.0	11.7	0.83	0.09
10-006	3.0	9.54	0.55	0.12
11-002	2.0	11.7	0.89	0.10
11-003	3.0	11.2	0.65	0.15
11-008	2.0	10.4	0.78	0.09

Q, are very close to the corresponding terms of Equations (4.4) and (4.8). These results indicate that the top slag had a very small effect on the bath cooling rate.

4.3 LIMESTONE-CALCIUM CARBIDE-NITROGEN/CALCIUM CARBIDE-CARBON DIOXIDE INJECTION

When carbon dioxide was used as a carrier gas, or limestone was injected with calcium carbide, the rate of desulphurization was slow, and the oxygen activities did not drop substantially below the silicon-oxygen equilibrium.

An example of the change in the sulphur content and the oxygen activity during an injection of limestone-calcium carbide mixture are shown respectively in Figures 4.26 a and b. The desulphurization rate was much slower than that during calcium carbide injection at the same powder feed rate. The first order rate constant was 1.54×10^{-3} s^{-1}, almost three times less than the rate constant during injection of calcium carbide. The oxygen activity, as shown in Figure 4.26 b, followed the silicon-oxygen equilibrium, and declined as the temperature fell.

Similar results were observed during calcium carbide injections when carbon dioxide was used as a carrier gas. Figure 4.27 a and b shows the changes of the sulphur and oxygen activity as calcium carbide with carbon dioxide was injected into the melt. It was found that the desulphurization was also rather slow (Figure 4.27 a). The first order rate constant was only 1.96×10^{-3} s^{-1}. The

oxygen activity was very close to the silicon-oxygen equilibrium throughout the injection. Since there was no difference in the desulphurization rates between injections with limestone-calcium carbide-nitrogen and calcium carbide-carbon dioxide, the experimental results will be presented together in the following text.

The results on the first order rate constants for the injections with limestone or carbon dioxide have been tabulated in Table 4.7 and plotted as a function of the powder flow rate in Figure 4.21. It can be seen that the desulphurization rate increases with the powder flow rate during limestone-calcium carbide-nitrogen injection or calcium carbide-carbon dioxide injection. Note that the desulphurization rate during injection of calcium carbide-limestone-nitrogen or calcium carbide-carbon dioxide is much lower than that during the calcium carbide/nitrogen injection. It is evident that limestone or carbon dioxide retarded desulphurization.

The incubation was also observed during injection of calcium carbide-limestone-nitrogen or calcium carbide-carbon dioxide. It was very difficult to determine the incubation periods accurately because the desulphurization was too slow.

Comparing with calcium carbide powder injection, the bath cooling rate did not change significantly during injection of calcium carbide-limestone-nitrogen or calcium carbide-carbon dioxide despite the endothermic decomposition of $CaCO_3$. An explanation for this will be given in Section 5.3.5.

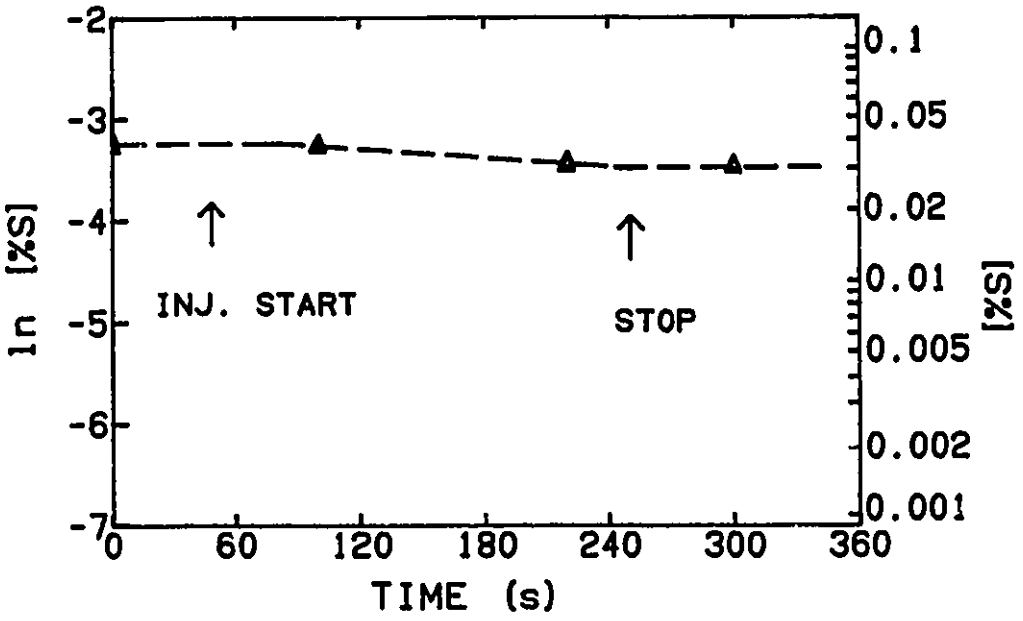

CHP4567.DRW SU1308

Figure 4.26 a The change of sulphur content with time during an injection with a mixture of 21% limestone-43% calcium carbide -36% lime at 0.1 kg/min and nitrogen gas flow rate 5 SLPM into iron-4.2% carbon-0.93% silicon melt with an initial temperature 1350°C. The lines were used to determine the first order rate constants.

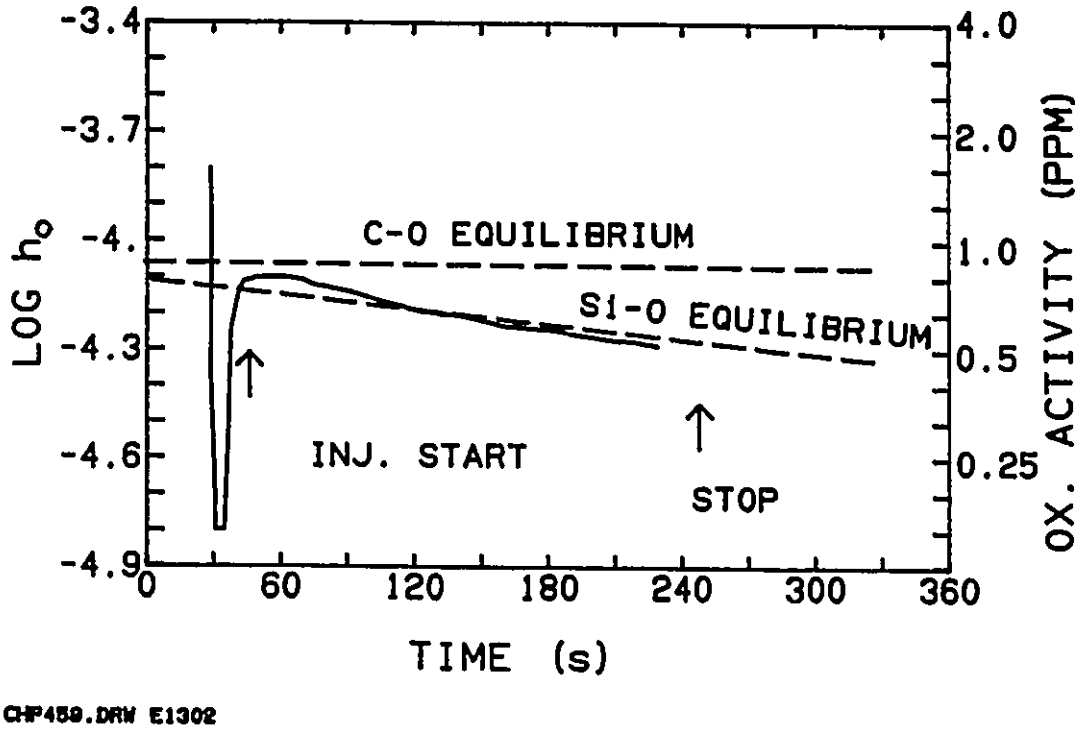

Figure 4.26 b The oxygen activity during the same injection as in Figure 4.26 a. The carbon-carbon monoxide and silicon-silica equilibria are also shown.

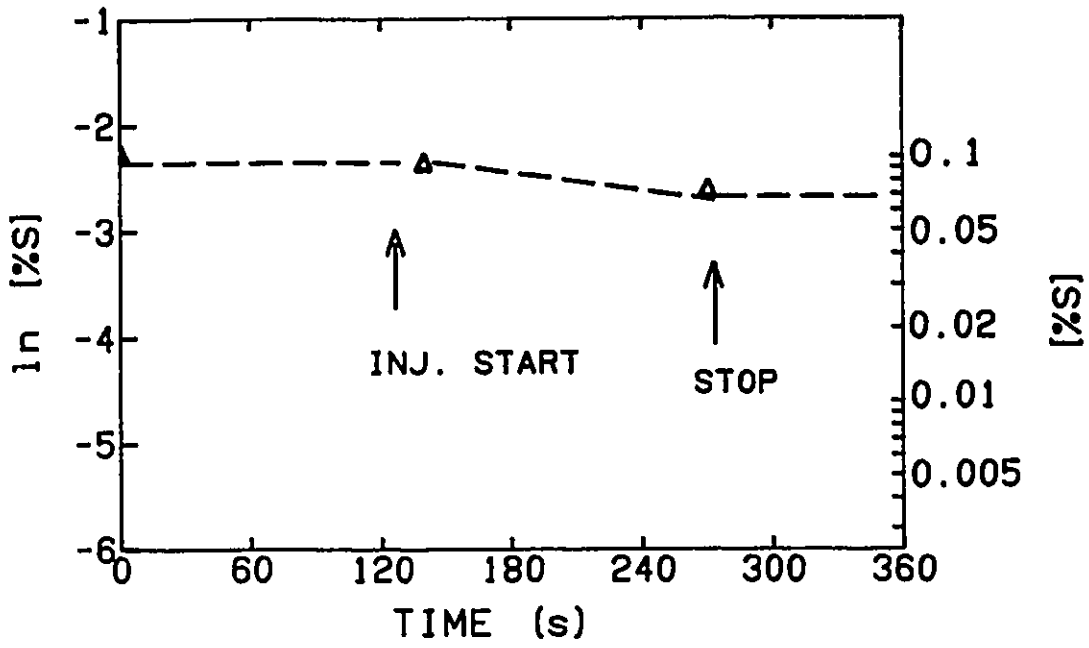

Figure 4.27 a The change of sulphur content with time during an injection with calcium carbide at 0.2 kg/min and carbon dioxide gas flow rate 12.5 SLPM into iron-4.2% carbon-0.83% silicon melt with an initial temperature 1350°C. The lines were used to determine the first order rate constants.

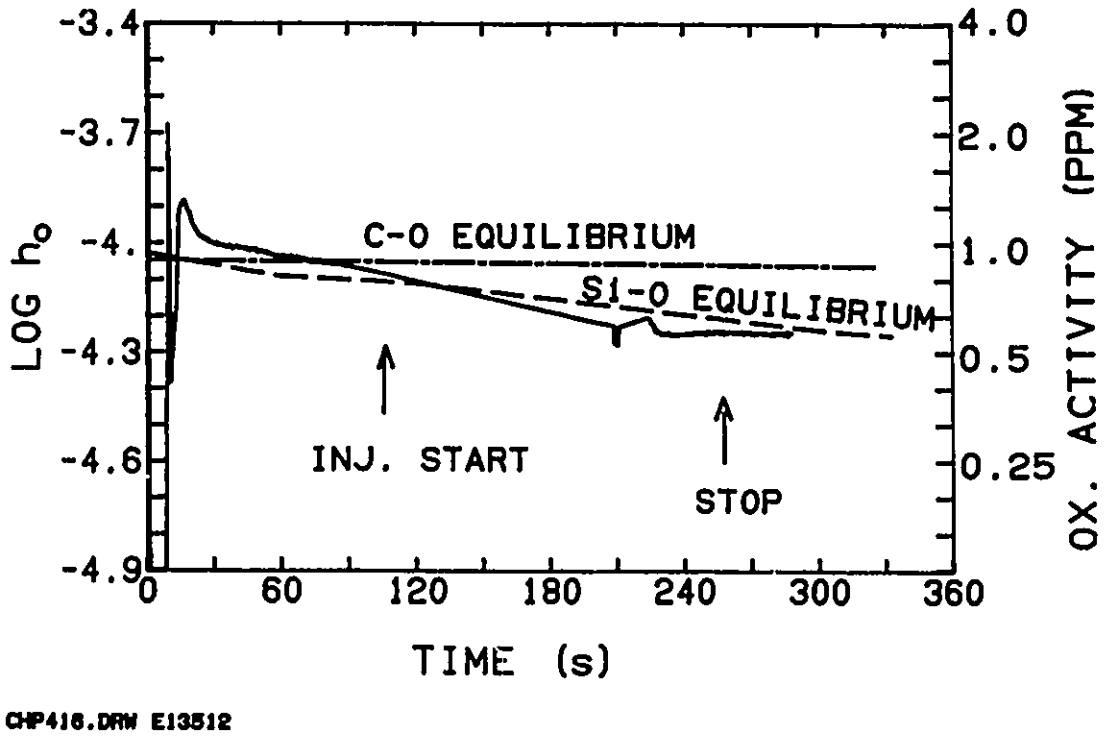

Figure 4.27 b The oxygen activity during the same injection as in Figure 4.27 a. The carbon-carbon monoxide and silicon-silica equilibria are also shown.

4.4 EXPERIMENTAL ERRORS

The general information on the measurement and chemical analysis uncertainties has been presented in Chapter 3. This section is confined to discussion of the following errors:

- the errors in sampling and chemical analysis
- the errors in determination of the incubation time and determination of the first order rate constant of desulphurization
- the errors in the bath temperature measurement and the bath cooling rate constant analysis
- the errors in determination of the melt oxygen activity

4.4.1 The Errors in Sampling and Chemical Analysis

The pin samples taken from the melt during injection tests were cut into small pieces weighing less than a half gram. Two or three pieces (about one gram) were taken at random for sulphur content analysis. All samples were analyzed in duplicate. More than five hundred sulphur analyses were made. The uncertainty of sulphur determination by combustion-iodate titration method (Leco, Model 577-100) was checked with the samples of standard reference materials. The results are given in Table 4.12. The absolute error is ±0.002% S.

Errors in sampling might arise from the composition inhomogeneity. To identify the errors in sampling, the sulphur contents of the samples which were taken during gas injections were analyzed by using statistical techniques. The standard deviation is only 0.001% S (See Table 4.13). Such small deviation is expected because the melts were vigorously stirred by the bubbling gas in all experiments.

TABLE 4.12

THE SULPHUR ANALYSIS RESULTS OF STANDARD REFERENCE MATERIALS

No.	%S analyzed
1 2 3 4	0.026 0.023 0.025 0.027
Average	0.025
%S certified by NBS [89]	0.025
Error	±0.002

The ingot samples taken before and after injections were analyzed for silicon, carbon and aluminum contents by optical emission spectrometry (Jarrell-Ash ICAP Solid Sampling System 900). The uncrtainty of the chemical composition determination by this method was checked by analyzing several

standard samples. The results compared in Table 4.14 indicate that errors involved in high carbon content determinations are much greater than errors involved in silicon and aluminum. Thus, some pin samples were analyzed by using direct combustion method (Leco, Model 577-100). The results are presented in Table 4.15. It shows that the deviation from combustion method is smaller than that from spectrometry. The average value of 4.2% C was used in the thermodynamic equilibrium calculations.

4.4.2 The Errors in Incubation Time and Desulphurization Rate Constant Determination

As mentioned in Section 4.2.1, an incubation period was observed at the beginning of calcium carbide injection. The overall error of the incubation time is estimated to be in the range of 5 to 10 seconds. The error in determination of incubation time comes from the deviations of:

- the sampling time of the pin samples
- the injection starting time
- the sulphur analysis and
- the linear regression of the time-ln [%S] relation

The first order rate constants of desulphurization were determined by linear regressions of the logarithm of sulphur contents on time. The correlation coefficients and the standard deviations are given in Table 4.16. The average

correlation coefficient is 0.94. The relative error is only 9 per cent. These results provide a further evidence that the kinetics of desulphurization can be considered as first order with respect to the sulphur content in the iron after incubation.

4.4.3 The Errors in the Melt Temperature Measurement and Cooling Rate Constant Determination

The melt temperature was measured with Pt/Pt-13% Rh thermocouple. The uncertainty of the temperature measurement was mainly limited by the resolution of the data logging computer. The uncertainty in the measurement was estimated to be ±3°C. As mentioned in Section 2.3, the melt oxygen activity is calculated from the emf and the temperature measured. No doubt, the accuracy of the oxygen activity determination is affected by the accuracy of the temperature measurement. Further analysis will be given in the next section.

Some deviations of the cooling rate constants might be caused by the errors in the temperature measurement. However, the cooling rate constants were determined by linear regression of hundreds of data points (See Section 4.2.3). Therefore, the random temperature fluctuations of 3°C would not result in any substantial errors to the cooling rate constants. Table 4.17 lists the correlation coefficients and the standard deviations of cooling rate constants. The average correlation coefficient is 0.97. The relative value of the deviations is only 0.7%. Such error level is considered to be acceptable in this work.

4.4.4 The Errors in Determination of the Oxygen Activity

The MgO-stabilized ZrO_2 cells with Cr/Cr_2O_3 reference electrode were supplied by Electro-Nite Co. The problems related to determination of the oxygen activity in hot metal have been reviewed in Chapter 2. The chemical analysis and the cell dimension have been given in Chapter 3.

Most experiments in this work were performed at a melt temperature of about 1350°C. The oxygen activity emf was between -80 and -50 mv. The corresponding oxygen activity was between 0.5 and 5×10^{-4}. The contact with the melt and Cr/Cr_2O_3 electrode was made with molybdenum wire, hence, no thermal emf correction was needed. The following text will discuss the possible errors caused by:

- the uncertainty of the temperature measurement
- partial electronic conduction of ZrO_2 electrolyte
- polarization at the electrolyte interfaces, and
- reduction of ZrO_2 electrolyte

As discussed in the section above, the uncertainty in the measurement was estimated to be ±3°C. The accuracy of the oxygen activity determination is affected by the accuracy of the temperature measurement. For the MgO-stabilized ZrO_2 electrolyte cell with Cr/Cr_2O_3 reference and a molybdenum wire, the relationship between the oxygen activity and emf is

TABLE 4.13

ERROR STATISTICS OF SULPHUR CONTENT FOR GAS INJECTIONS

Run No.	Quantity of Samples	Mean Sulphur (%)	Standard deviation	Relative Value
6-001	10	0.020	0.002	0.107
6-003	12	0.015	0.001	0.099
6-005	14	0.027	0.002	0.089
7-001	12	0.037	0.001	0.037
7-003	14	0.017	0.001	0.043
7-005	12	0.002	0.000	0.126
8-001	6	0.018	0.001	0.064
8-003	6	0.021	0.001	0.044
8-005	6	0.012	0.001	0.059
9-001	6	0.029	0.001	0.048
9-003	6	0.018	0.001	0.062
9-005	6	0.021	0.001	0.048
10-003	6	0.033	0.001	0.041
10-005	5	0.036	0.001	0.014
10-007	6	0.040	0.001	0.019
11-004	6	0.028	0.001	0.033
11-007	6	0.039	0.001	0.012
12-001	6	0.046	0.003	0.056
12-003	6	0.030	0.001	0.019
12-005	6	0.043	0.001	0.031
13-003	6	0.054	0.001	0.014
13-005	4	0.010	0.002	0.016
Average			0.001	0.049

TABLE 4.14

CHEMICAL COMPOSITION OF SEVERAL STANDARD REFERENCE MATERIALS AND RESULTS FROM OPTICAL EMISSION SPECTROMETRY

No	Standard Specimen		C %	Si %	Mn %	Al %	S %
1	1144A	Certified [a]	4.32	0.18	1.23	<0.005	0.083
		Spectr. [b]	3.86	0.178	1.12	<0.001	0.071
2	1144A	Certified	4.32	0.18	1.23	<0.005	0.083
		Spectr.	3.29	0.153	1.19	<0.001	0.075
3	1144A	Certified	4.32	0.18	1.23	<0.005	0.083
		Spectr.	3.81	0.164	1.15	<0.001	0.063
4	1145	Certified	2.85	0.29	0.04	(0.045)	0.21
		Spectr.	1.95	0.25	0.05	n.d [c]	0.34
5	MCM [d]	Certified	0.37	0.193	1.14	<0.005	0.017
		Spectr.	0.20	0.186	1.12	<0.001	0.017
6	1263A	Certified	0.62	0.74	1.50	0.24	0.006
		Spectr.	0.57	0.715	1.47	0.229	0.048
7	1264A	Certified	0.87	0.067	0.26	(0.008)	0.025
		Spectr.	0.63	0.062	0.25	0.017	0.013

a The composition of standard reference materials is taken from NBS [89].

b analyzed by spectrometry technique

c n.d = not determined

d The specimen of MCM is McMaster University in house reference material [90].

TABLE 4.15

COMPARISON OF CARBON CONTENTS ANALYZED WITH SPECTROMETRY AND COMBUSTION METHOD

Sample No.	C %	
	Spectrometry	Combustion
8-001-2	3.90	3.83
8-004-1	4.32	4.02
8-007-1	4.95	4.11
10-001-1	3.96	4.31
10-005-1	4.35	4.08
10-008-1	4.04	3.93
13-001-1	4.70	4.21
13-003-1	4.82	4.09
13-011-1	4.17	4.15
Average	4.36	4.08
Standard Deviation	0.36	0.14

TABLE 4.16

STANDARD DEVIATION OF THE FIRST ORDER RATE CONSTANTS OF DESULPHURIZATION

Run No.	$K_S \times 10^3$ (1/s)	Correlation Coefficient R	Standard Deviation (10^3)	Relative Value (%)
6-002	6.40	0.97	0.43	0.07
6-004	5.88	0.79	0.98	0.17
6-006	6.71	0.93	0.63	0.09
8-002	4.79	0.95	0.40	0.08
8-004	6.95	0.94	0.56	0.08
8-006	6.89	0.98	0.46	0.07
9-002	5.94	0.93	0.65	0.11
9-006	6.24	0.96	0.67	0.11
9-007	7.77	0.98	0.42	0.05
9-008	4.51	0.98	0.26	0.06
10-004	7.99	0.99	0.17	0.02
10-008	7.18	0.97	0.65	0.09
11-001	7.93	0.99	0.40	0.05
11-003	8.37	0.98	0.60	0.07
13-002	1.54	0.91	0.17	0.11
13-008	1.79	0.79	0.48	0.27
Average		0.94	/	0.09

TABLE 4.17

STANDARD DEVIATION OF COOLING RATE CONSTANTS

Run No.	$K_T \times 105$ (1/s)	Correlation Coefficient R^2	Standard deviation (10^5)	Relative Value %
3-002	16.0	0.97	0.10	0.64
3-003	18.5	0.77	0.51	2.77
3-004	10.0	0.96	0.07	0.70
3-005	18.6	0.97	0.16	0.85
5-002	16.0	0.99	0.05	0.34
6-002	14.0	0.98	0.08	0.59
6-003	15.0	0.98	0.09	0.64
6-004	12.8	0.98	0.07	0.52
6-005	14.0	0.99	0.04	0.29
6-006	14.0	0.97	0.11	0.81
7-002	14.4	0.98	0.09	0.62
7-004	16.0	0.98	0.08	0.52
7-006	12.6	0.94	0.13	1.02
9-001	14.0	0.99	0.05	0.38
9-002	14.0	0.98	0.10	0.69
9-003	15.0	0.99	0.06	0.38
9-004	13.1	0.98	0.08	0.60
9-006	13.5	0.98	0.08	0.61
9-007	14.2	0.98	0.09	0.64
9-008	13.0	0.98	0.09	0.71
10-003	15.0	0.98	0.08	0.57
10-007	13.0	0.98	0.09	0.67
10-002	14.6	0.98	0.10	0.66
10-004	15.9	0.96	0.19	1.19
10-006	20.6	0.99	0.11	0.53
11-007	14.0	0.97	0.11	0.75
11-001	15.8	0.98	0.11	0.70
11-002	14.7	0.98	0.08	0.54
11-003	14.7	0.99	0.07	0.46
11-008	21.3	0.97	0.18	0.85
13-003	13.0	0.98	0.06	0.44
Average		0.97	/	0.70

$$\log h_O = 4.62 - \frac{13580 - 10.08E}{T} \qquad (4.10)$$

where T is the absolute temperature in K and E is the emf in mv. The electronic contribution to the oxygen activity is ignored. The possible error in the oxygen activity determination caused by the temperature error can be determined from the derivative of h_O with respect to T.

$$\frac{\Delta h_O}{h_O} = (13580 - 10.08E)\frac{\Delta T}{T^2} \qquad (4.11)$$

For a typical case of temperature 1350°C and emf -50 mv, a temperature error of 3°C leads to a relative error in the oxygen activity less than 2 per cent.

The effect of the partial electronic conduction can be eliminated by considering a specific parameter $P_{e'}$ (See Equation (2.19)). The chemical composition of the cells used in this study is close to that one used by Janke and Richter [67] (See Table 2.7). Thus, their equation of the $P_{e'}$-temperature dependence was adopted.

Errors in determination of oxygen activity involved in the uncertainty of $P_{e'}$ have been discussed in Section 2.3. According to the experimental data of $P_{e'}$ (as given in Table 2.7), in a typical instance (temperature 1350°C and emf -50

mv), the relative error is less than 10 per cent. Certainly, different values of P_{e^-} will result in different values of oxygen activity as converted from the same emf reading.

Equation (2.19) is valid only if the chemical equilibrium is reached at the electrolyte interfaces. If the equilibrium is disturbed, the polarization effect has to be taken into account. Unfortunately, there is no theory which can calculate polarization successfully. In practice, the polarization can be detected as the absolute value of emf decreases gradually and continuously. Figures 4.28-4.31 illustrate four different examples of the emf curve decline during the experiments. The temperature variations of the melts were very small and would not cause any significant changes on the emf readings. The emf value was nearly constant when the emf was greater than -80 mv (Figure 4.28). When the initial emf was -100 mv, the absolute emf value started to decrease after five minutes of cell immersion (Figure 4.29). Only one and half minutes after the cell was put into the melt with 0.008% Al, the curve declined quickly from -150 mv to -120 mv, as shown in Figure 4.30. Once the cell was put into the melt with 0.2% Al, the emf curve immediately dropped from its peak (Figure 4.31).

For most experiments, the initial emfs were greater than -80 mv and the injections lasted for only about three minutes. Thus, polarization was not a considerable problem. For the melts with high aluminum contents, the oxygen activities which were calculated from the response of the continuous probes did not agree with the values predicted by the Al-Al_2O_3 equilibrium. The deviation

generated by polarization of the oxygen probes in highly deoxidized liquid alloys cannot be ignored. These observations were confirmed by the work of Niedrighaus on the oxygen activity measurements made in Fe-$C_{sat'd}$-Al alloys [70].

The decomposition of zirconia and other oxides could result in a change of the local oxygen content or polarization at the electrolyte interface. The stabilities of some oxides at 1350°C have been discussed in Chapter 2 (See Figure 2.9). It was observed that the cell surface remained smooth when the melt oxygen activity was greater than 0.5×10^{-4}. When the melt was deoxidized with high aluminum, and the oxygen activity was lower than 0.05×10^{-4}, the surface became a little rough after three minutes of immersion in the melt, indicating chemical reactions on the cell surface.

Most of the experiments were performed under the conditions of the oxygen activity between 0.5 and 5×10^{-4} and the temperature of about 1350°C. For these cases, based on the above discussion, the influence of polarization, decomposition of ZrO_2 cells and uncertainty of P_{e^-} can be ignored, except for the melts containing aluminum. As shown in Section 4.1.1, there is an excellent agreement between the measured and literature values of oxygen activities for the carbon-silicon-iron melt. These results provide further confidence in these oxygen probes and their calibration.

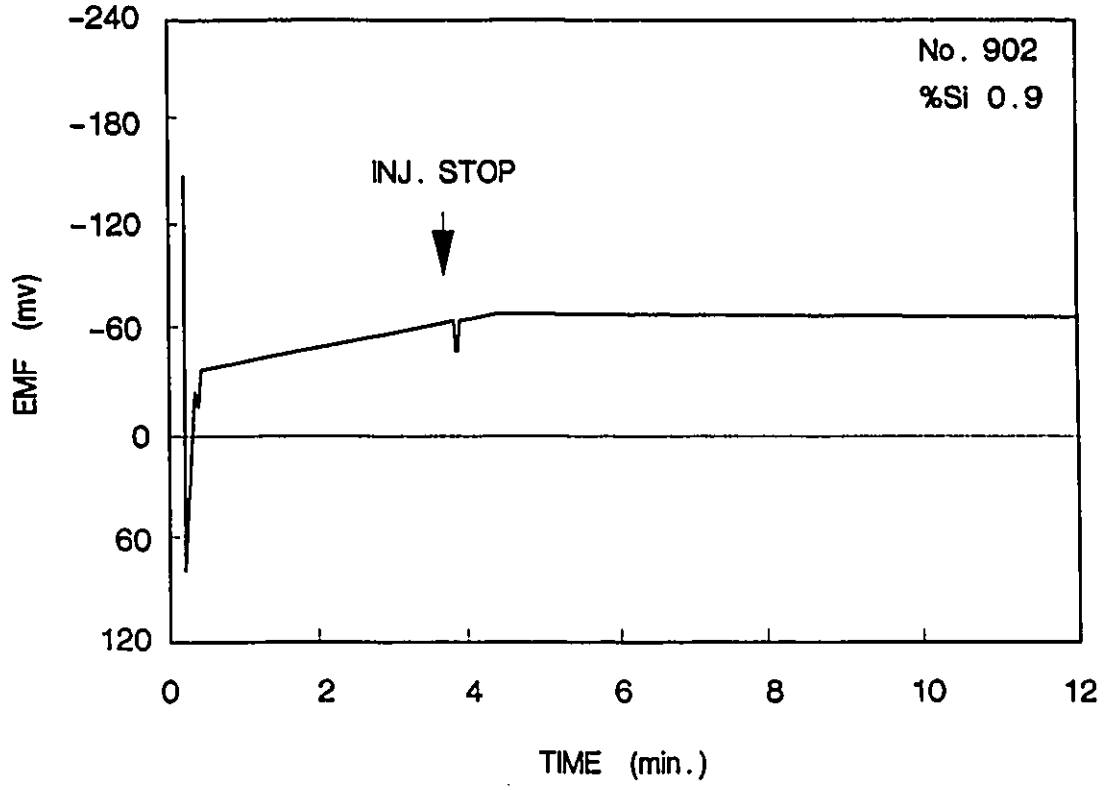

Figure 4.28 An example of the response of cell potential to electrolyte polarization. Here, the emf reading is greater than -80 mv. No decay of the emf absolute value was observed.

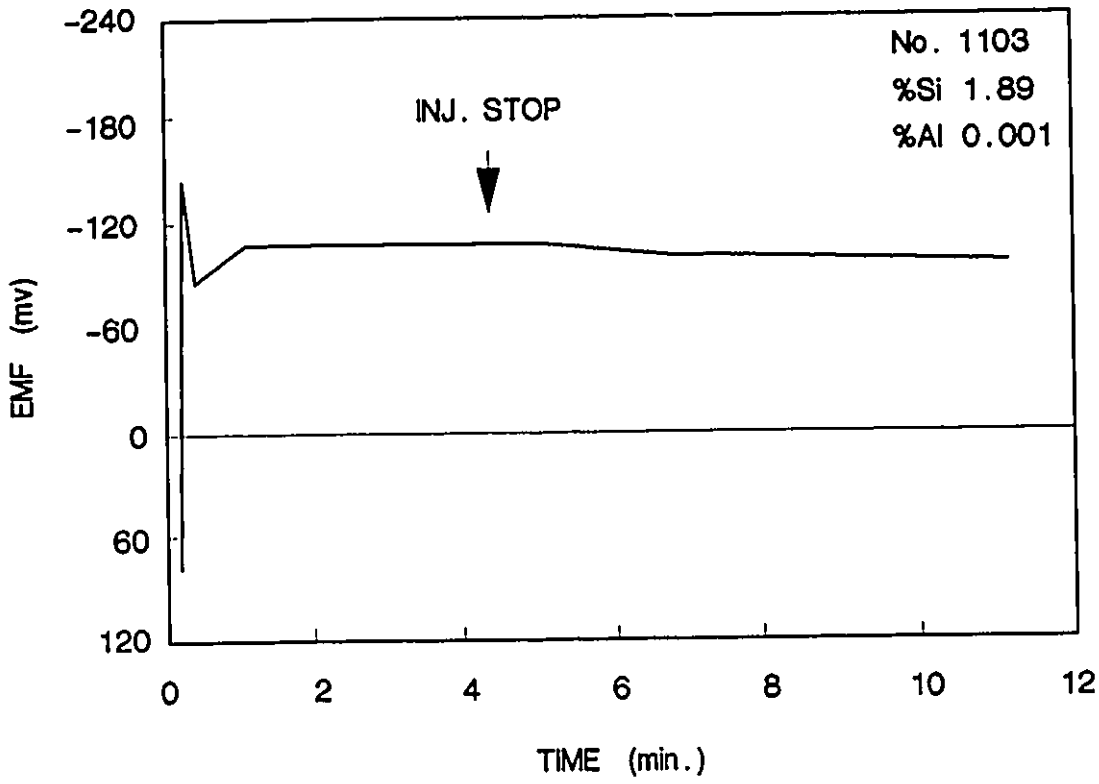

Figure 4.29 An example of the response of cell potential to electrolyte polarization. Here, the reading is greater than -100 and less than -80 mv. A small decline of the curve was observed after five minutes of the cell immersion.

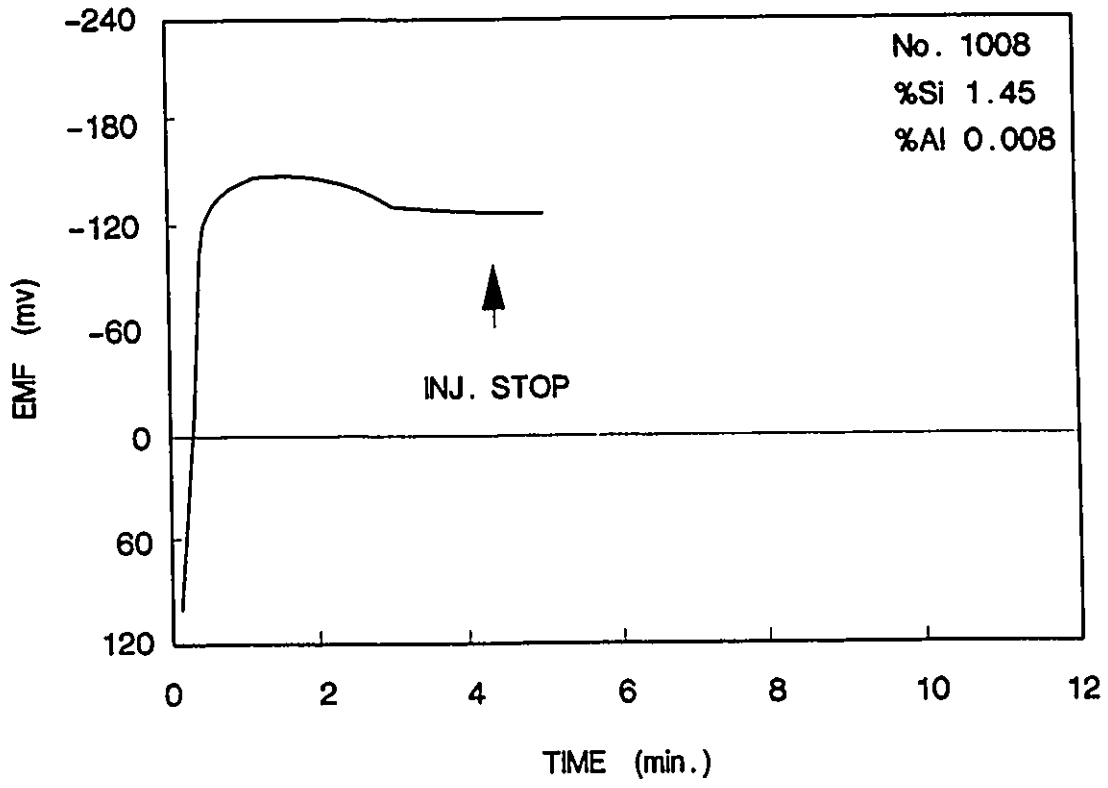

Figure 4.30 An example of the response of cell potential to electrolyte polarization. In this case, the iron contained 0.008% Al. The decline of the curve was observed after one and half minutes of the cell immersion.

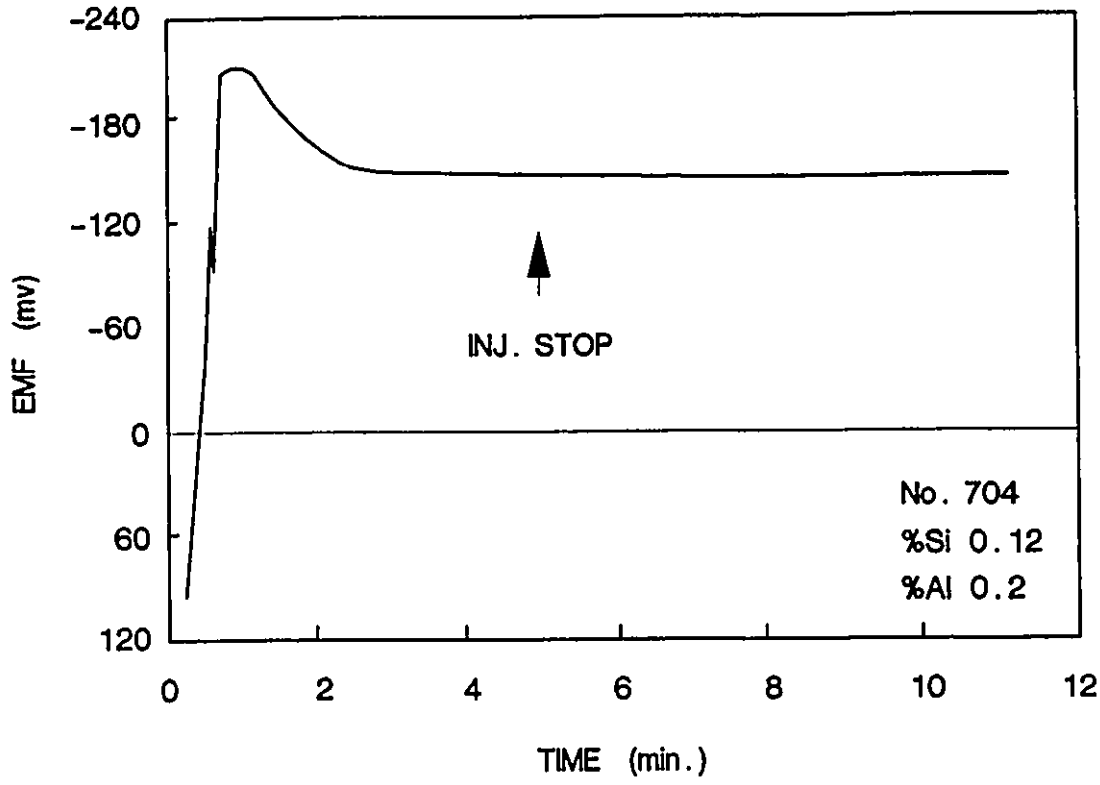

Figure 4.31 An example of the response of cell potential to electrolyte polarization. In this case, the iron contained 0.2% Al. The decline of the curve was observed immediately.

CHAPTER 5
DISCUSSION

The objective of Chapter 5 is to provide theoretical analyses for the experimental results. The discussion is presented in the following sequence:

- the reasons why the oxygen activity in hot metal is controlled by the silicon-silica equilibrium
- an analysis of the bath cooling rates during gas and powder injections
- a kinetic mechanism for the role of oxygen and carbon dioxide on the hot metal desulphurization

5.1 THE EFFECT OF THE SILICON-SILICA EQUILIBRIUM ON THE OXYGEN ACTIVITY IN HOT METAL

It has been reported that the oxygen activity in hot metal appeared to be controlled by its silicon content [91-93]. Ghorpade et al. observed that the oxygen activity increased with increasing temperature as predicted by the silicon-

silica equilibrium [91]. Pal and Patil investigated hot metal desulphurization and found that although the carbon-carbon monoxide equilibrium was thermodynamically more favourable, in reality, the oxygen activity is characteristic of the silicon-silica equilibrium [93]. In these studies, the oxygen activities were taken before and after powder injection with commercial single-use probes.

These findings were confirmed by the present study. Moreover, this work demonstrated clearly how the silicon-silica equilibrium was developed during nitrogen gas bubbling. The progress of the oxygen activity approaching the silicon-silica equilibrium had not been appreciated previously. As mentioned in Chapter 4, the progress was divided into three steps:

(a) Before gas injection, the oxygen activity in hot metal was higher than predicted from the silicon-silica equilibrium.

(b) During nitrogen gas bubbling, the silicon-silica equilibrium dropped throughout the injection as the bath temperature fell. The oxygen activity tended to approach and follow the silicon-silica equilibrium.

(c) After gas injection, the variation of the oxygen activities with temperatures and silicon contents agreed with those predicted from the silicon-silica equilibrium.

It was considered that the difficulties associated with nucleation and growth of CO bubbles seemed to be the reasons why the oxygen activity in hot metal was controlled by the silicon-silica equilibrium [91]. However, no further analysis was provided. For a reasonable explanation of the experimental observations, the following two questions must be addressed:

(a) It was expected that during nitrogen bubbling, the conditions for nucleation and growth of CO bubbles would have been improved. Why was the oxygen activity not controlled by carbon-carbon monoxide equilibrium?

(b) Nucleation and growth of silica particles in the melt were also necessary for silicon deoxidation to occur. Why was the oxygen activity able to approach silicon-oxygen equilibrium without any significant difficulties?

These problems will be examined in the following sections.

5.1.1 The Effect of Nitrogen Gas Bubbling on the Deoxidation Process

The deoxidation reactions by carbon and silicon could take place homogeneously in the melt or heterogeneously at two possible sites: the surface of nitrogen gas bubbles or the interface between liquid iron and the MgO crucible.

$$[C]+[O]=CO(g) \qquad (5.1)$$

$$[Si]+2[O]=SiO_2(s) \qquad (5.2)$$

Carbon deoxidation will be discussed first, and silicon deoxidation will be discussed in the next section.

As pointed out in reference [94], the theory of homogeneous nucleation predicted a supersaturation of 10^4-10^5 atm for nucleation of gas bubbles in pure liquid metal with surface tension of 0.01-0.016 kg·m/s^2. In the present experiments, the carbon content was 4.2 per cent. The oxygen activity was about 10^{-4}. The corresponding equilibrium pressure of CO was one atmosphere in magnitude. This indicates that homogeneous nucleation was impossible in the present experimental system. Only heterogeneous nucleation should be take into account.

The phenomena occurring during nitrogen injection are shown schematically in Figure 5.1. Many nitrogen bubbles are released from the lance. The total pressure in a bubble is approximately one atmosphere. The partial pressure of CO may be much lower than one because the CO formed at the gas-liquid interface is diluted with nitrogen. Therefore, carbon deoxidation is favoured thermodynamically during the injection of nitrogen. However, the

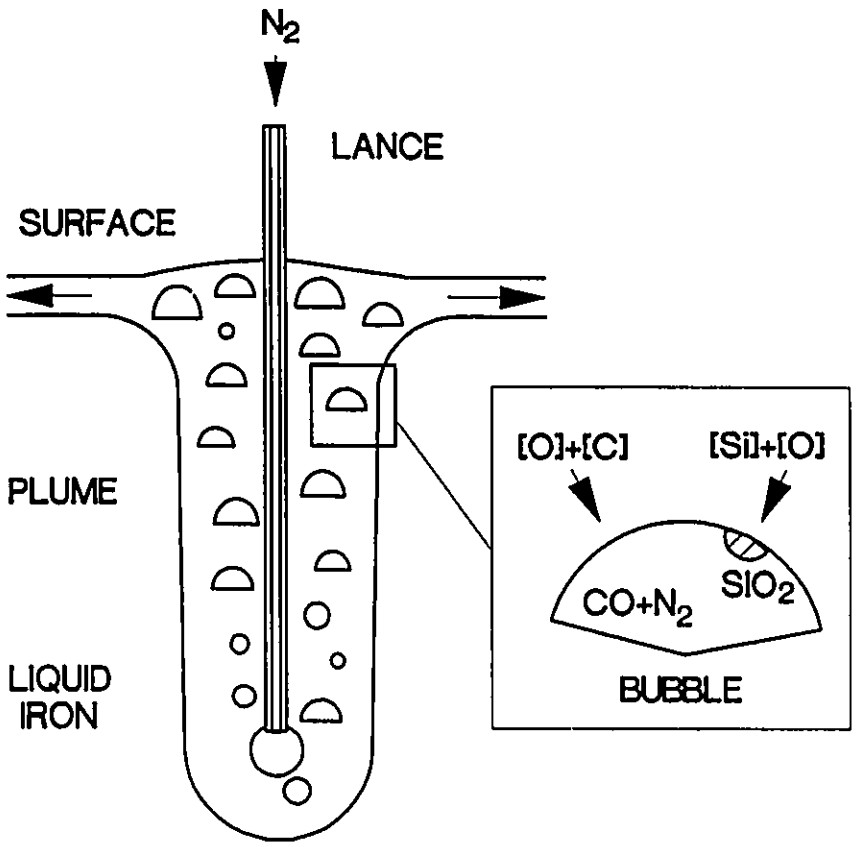

Figure 5.1 Schematic diagram of the physical and chemical phenomena during nitrogen injection. The nitrogen gas bubbles release from the lance and rise to the surface. At the surface of individual bubbles, oxygen reacts with carbon and silicon; carbon monoxide diffuses into gas phase, and silica particles nucleate at the bubble interface.

reaction rate is not determined by the CO pressure alone. Other kinetic conditions must be considered.

At individual bubbles, oxygen and carbon diffuse across the gas-liquid interface. In order to calculate the mass transfer rate, several simplifying assumptions are employed:

(a) The gas bubbles are uniform in their size. Changes in the bubble volume due to bubble rise and chemical reaction are negligible.

(b) Mass transfer resistance due to chemical reaction rate is negligible. The carbon-oxygen equilibrium is reached at the gas-liquid interface.

(c) The rate of mass transfer is controlled by diffusion of oxygen across the liquid boundary layer.

The carbon content in the melts was much higher than the oxygen content. Thus, carbon diffusion is not the governing step in mass transfer.

According to these assumptions, the deoxidation rate can be written as

$$\frac{d[\%O]}{dt} = -\frac{k_m A}{V}([\%O]-[\%O]_i) \qquad (5.3)$$

where [%O] is the oxygen content in the melt, and $[\%O]_i$ is the oxygen content at the gas-liquid interface, V is the volume of the liquid iron, and A is the surface area of bubbles, k_m is the mass transfer coefficient.

The surface renewal or penetration theory of Higbie [95] has been used extensively for mass transfer in liquids. In terms of the mass transfer coefficient k_m, Higbie's penetration theory is expressed as

$$k_m = 2\left(\frac{D}{\pi t_c}\right)^{1/2} \tag{5.4}$$

where D is the oxygen diffusivity, 2.5×10^{-9} m^2/s [96]; and t_c is the time of contact of the liquid element with the surface layer.

At a given gas flow rate, the bubble diameter, d (m), can be determined from Irons' work [97]. Then, the contact time is given by

$$t_c = \frac{d}{u_b} \tag{5.5}$$

where u_b is the bubble velocity (m/s). u_b can be calculated from the equation derived by Davies and Taylor [98]:

$$u_b = 0.72(gd)^{0.5} \tag{5.6}$$

where g is the gravitational acceleration constant. The mass transfer coefficient, k_m, can be determined for gas bubbling by combining Equations (5.4)-(5.6).

High purity nitrogen was used as carrier gas in this work. The partial pressure of oxygen was almost zero. Thus, for the bubbles just released from the lance, the equilibrium oxygen concentration at the gas-liquid interface is negligible. According to Equation (5.3), a maximum deoxidation rate can be expected. That is

$$\frac{d[\%O]}{dt} = -\frac{k_m A}{V}[\%O] \tag{5.7}$$

Integrating Equation (5.7) gives

$$[\%O] = [\%O]_o \exp\left(-\frac{k_m A t}{V}\right) \tag{5.8}$$

where $[\%O]_o$ is the initial oxygen content. For a typical nitrogen injection in this work, the gas flow rate was 10 SLPM, and the weight of the melt was 75 kg. The bubble diameter is taken to be 0.05 m [97], and the calculated bubble velocity is 0.5 m/s. After three minutes of nitrogen injection, the oxygen content calculated from Equation (5.8) is reduced by 10 per cent only. The details of the calculation conditions and results are listed in Table 5.1.

TABLE 5.1

THE CALCULATION OF OXYGEN TRANSPORT DURING NITROGEN GAS BUBBLING

Quantity		Unit	Symbol	From	Value
Lance Diameter	Inside	m	d_{in}	Experimental Data	0.0032
	Outside		d_{out}		0.0254
Gas flow rate		m^3/s	Q		9.9×10^{-4}
Temperature		°C	T		1350
Lance Depth		m	L		0.1
Crucible Diameter		m	d_o		0.23
Bubble Diameter		m	d	[96]	0.05
Bubble velocity		m/s	u_b	[97]	0.5
Residence Time		s	τ	L/u_b	0.2
Bubble Frequency		1/s	N	$6Q/\pi d^3$	15
Resident Bubbles		/	n	$N\times\tau$	3
Area of Bubbles		m^2	A	$n\pi d^2$	2.43×10^{-2}
Mass transfer coefficient		m/s	k_m	$2[D/\pi t_c]^{1/2}$	1.8×10^{-4}
Mass Transfer Rate Constant		s^{-1}	K_b	k_mA/V	0.56×10^{-3}
Area of the Melt Surface		m^2	A_m	$\pi d_o^2/4$	0.042
Crucible-Melt Interface Area		m^2	A_o	$\pi d_o(h+d_o/4)$	18.6×10^{-2}

Therefore, under the present experimental conditions, in spite of the fact that the nitrogen gas bubbling reduced the difficulties associated with nucleation and growth of CO bubbles, the area provided by the nitrogen gas bubbles was not large enough to enhance carbon deoxidation significantly. As listed in Table 5.1, the melt-crucible interfacial area was almost ten times greater than the gas bubble surface area. Thus, the melt-crucible interface might play an important part in the reactions of deoxidation. The rate of deoxidation should be much greater if deoxidation was not restricted by nucleation and growth of CO bubbles at the melt-crucible interface. In the following section, the problems associated with nucleation and growth of CO bubbles will be examined.

5.1.2 The Effect of the Liquid-Crucible Interface on Deoxidation Process

At flat crucible walls, CO bubble nucleation is almost impossible. For heterogeneous nucleation of a bubble at a flat solid-liquid iron interface, the supersaturation required is given by [99]:

$$\frac{p'}{p} \doteq 1.12B^{1/2} \tag{5.9}$$

and

$$B=(2-\cos\phi)(1+\cos\phi)^2/4 \tag{5.10}$$

where p' and p are the supersaturation of homogeneous and heterogeneous nucleation respectively; ϕ is the solid-liquid contact angle. B cannot be less than 1/16 for any solid-liquid combination [99]. This means that P' is approximately 1000 atm in magnitude. Thus, at a flat solid-liquid interface, CO bubble nucleation is not a feasible mechanism.

At rough refractory walls, the formation of CO bubbles is limited by the number of the crevices appropriate to CO bubble growth. It has long been recognized when a melt is held in a refractory crucible with a rough surface, bubble nucleation takes place much easier. If a bubble is to grow, its pressure must be less than the equilibrium pressure corresponding to the CO pressure for the carbon content and the oxygen activity in the melt. This condition leads to a minimum value of cavity radius, r_{min}, which can sustain bubble growth. r_{min} is determined by [100]

$$r_{min} = \frac{2\sigma}{P_{CO} - (P_a + P_s)} \tag{5.11}$$

where P_{CO} is the pressure of CO in equilibrium with carbon-oxygen-liquid iron, P_s is the liquid static pressure over the bubble, P_a is atmospheric pressure, σ is the surface tension of the liquid. On the other hand, not all pores will be available for bubble nucleation. Some cavities will be so large that they fill with the liquid. The maximum value of cavity radius is [100]

$$r_{max} = -\frac{2\sigma}{P_a + P_s}\cos\theta \qquad (5.12)$$

The validity of Equations (5.11)-(5.12) has been tested experimentally by Alexander et al. with pore sizes varying in the range 0.001-0.1 mm [100]. In the present experiments, the carbon content of the iron was 4.2 per cent. When the silicon content was 0.2 per cent, and no aluminum was added into the melt, the measured oxygen activity was about 2×10^{-4} at temperature of 1350°C. Under these conditions, the equilibrium CO pressure could reach 3 atm (The thermodynamic data has been given in Chapter 2). If σ is taken as 1.2 N/m, P_a as 1 atm and P_s as 0, the minimum cavity radius is found to be 0.01 mm. While, if θ is taken as 140°, the maximum value of cavity radius is found to be 0.02 mm. According to Alexander et al. [100], for the refractory materials like those used in this work, the measured pore sizes were in the range of 0.01-0.1 mm, with the majority at about 0.05 mm. Thus, it can be seen that not many sites are available for CO bubble nucleation and growth on the crucible walls. The higher the silicon content, the lower the oxygen activity is. As a result, fewer sites appropriate for CO bubble nucleation and growth are available. Most of the experiments were performed in the melts with silicon contents more than 0.2 per cent. Therefore, it can be understood that neither the nitrogen gas bubbles nor the crucible walls provided enough area for the reaction of carbon deoxidation. This may explain why the oxygen activity did not appeared to be controlled by the carbon-carbon monoxide equilibrium.

On the other hand, silica nucleation will occur preferentially at the interface between the MgO crucible and liquid iron. This can be proved with a simplified nucleation model. Figure 5.2 shows a silica particle forming in contact with a perfectly flat crucible wall. The particle has the shape of a spherical cap with a contact angle, ϕ, where

$$\gamma_{lw}-\gamma_{sw}-\gamma_{sl}\cos\phi \qquad 0\le\phi\le180^{o} \tag{5.13}$$

γ_{sw}, γ_{lw} and γ_{sl} are interfacial tensions between phases of liquid, silica and the crucible wall. The formation of such a silica particle will be associated with an excess free energy which is given by

$$\Delta G_{het}=-V\Delta G_{v}+A_{sl}\gamma_{sl}+A_{sw}\gamma_{sw}-A_{sw}\gamma_{lw} \tag{5.14}$$

Here, V is the volume of silica particle, A_{sl} and A_{sw} are the areas of the solid particle/liquid and solid particle/wall interfaces, ΔG_{v} is the free energy change per unit volume. The free energy needed for homogeneous nucleation of a such solid particle is

$$\Delta G_{hom}=-V\Delta G_{v}+A_{sl}\gamma_{sl} \tag{5.15}$$

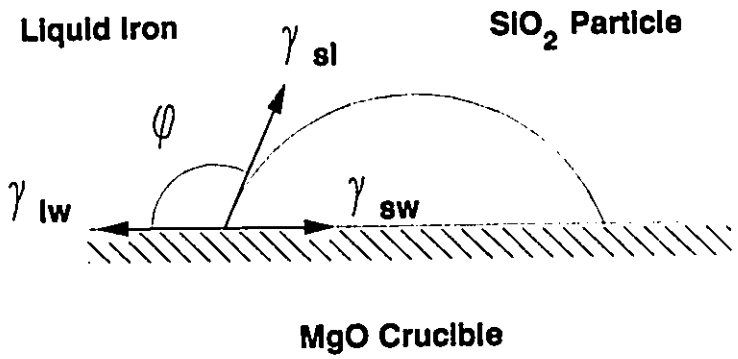

Figure 5.2 Schematic diagram of a SiO_2 particle formed on MgO crucible wall submerged in liquid iron.

where A is the total area of the particle surface and

$$A = A_{sl} + A_{sw} \tag{5.16}$$

The difference of the free energy change between heterogeneous and homogeneous nucleations is

$$\Delta G = \Delta G_{het} - \Delta G_{hom} \tag{5.17}$$

Combining Equations (5.13)-(5.17) yields

$$\Delta G = A_{sw}(\gamma_{sw} - \gamma_{lw} - \gamma_{sl}) \tag{5.18}$$

Substituting Equation (5.13) into Equation (5.18) gives

$$\Delta G = -A_{sw}\gamma_{sl}(1 - \cos\phi) \tag{5.19}$$

If $\phi = 0^{\circ}$, the crucible has no affinity for silica, and the free energy difference is zero, indicating the crucible-liquid interface is not favourable for silica nucleation. If $\phi \geq 0^{\circ}$, Equation 5.19 yields negative ΔG, indicating the crucible-liquid interface is favourable for silica nucleation.

The exact value of the contact angle of silica on a magnesia refractory surface is not available. But, it is certain that magnesia has a very strong

chemical affinity for silica at high temperature, because the former is basic, and latter is acid. Thus, it can be expected that the contact angle should be very close to 180°. For this reason, silica nucleation is feasible on a magnesia refractory surface. As mentioned above, the area of the crucible-liquid iron interface was almost ten times larger than the area created by gas bubbles. Thus, the mass transfer rate constant to the melt-crucible interface should be much greater than that to the melt-bubble interface. Consequently, silicon deoxidation was able to approach its equilibrium in a shorter time than carbon deoxidation.

The above analysis confirms that the difficulties associated with nucleation and growth of CO bubbles impede carbon deoxidation to approach equilibrium, whereas, silica nucleation is favoured on the crucible refractory surface. Thus, silicon deoxidation in hot metal is able to approach equilibrium. As a result, the oxygen activity in hot metal appears to be controlled by silicon-silica equilibrium.

5.2 THE HEAT TRANSFER ASPECTS OF GAS AND POWDER INJECTIONS

Heat transfer during gas and powder injections is an important issue. The energy cost of steelmaking is affected by the heat losses during ladle treatment. A better understanding of the heat transfer aspects is necessary for the process control of ladle metallurgy.

It is known that the utilization efficiency of reagents is associated with the residence time that particles have in the melt. Therefore, the particle-liquid contact patterns are considered to be a fundamental aspect of submerged injection. Because of high temperature of liquid iron, so far, it has not been possible to determine the particle-liquid contact patterns directly. Farias and Irons indirectly measured the particle-liquid contact fraction [2]. They injected sand into liquid lead and observed that the bath cooling rate was only 30 percent of that which would be expected if all the particles were at the melt temperature. Stimulated by their findings, it was decided to measure the bath cooling rate very carefully during injection. The following text will analyze the experimental results. Then, the bath cooling rate will be used as an indirect indicator of particle-liquid iron contact.

5.2.1 The Bath Cooling Rate during Gas and Powder Injections

The following text will focus on the cases of nitrogen gas injection and calcium carbide powder injection. The cases of limestone and carbon dioxide injection will be discussed in Section 5.3.6.

As was stated in Chapter 4, the bath cooling rate constant was determined by fitting the measured bath temperature to a first order differential equation:

$$\frac{dT_l}{dt} = -K_T(T_l - T_R) \tag{4.3}$$

Then, using linear regression, it was found that the bath cooling rate constant was directly related to nitrogen flow rate for gas injection:

$$K_T=[(10.7\pm0.38)+(0.376\pm0.034)Q]\times10^{-5} \quad (R^2=0.94) \tag{4.4}$$

During calcium carbide powder injection, K_T not only depended on gas flow rate alone, but even more strongly on the powder feed rate, i.e.

$$K_T=[(10.3\pm0.30)+(0.398\pm0.04)Q+(0.0101\pm0.0007)W_p]\times10^{-5} \quad (R^2=0.92) \tag{4.8}$$

The bath cooling rate after powder injection was

$$K_T=[(10.05\pm0.73)+(0.289\pm0.2)Q]\times10^{-5} \quad (R^2=0.24) \tag{4.9}$$

It has been pointed out that the first two terms of Equation (4.8) are almost identical to the corresponding terms of Equations (4.4) and (4.9).

These results will be analyzed on a fundamental basis. The discussion will be presented in the following sequence:

- bath cooling before gas and powder injection
- bath cooling during nitrogen gas injection
- bath cooling during nitrogen gas and calcium carbide powder injection
- bath cooling after powder injection

(1) Bath Cooling before Gas and Powder Injection

In the case of no gas and powder, the drop of the bath temperature was due to heat losses from the melt. The overall heat transfer involved convection in the liquid iron, conduction through the crucible wall and lining materials, and convection and radiation to the atmosphere and surroundings. As mentioned in Chapter 3, the furnace was covered with an insulating alumina board under a lid, the lid was filled with alumina fibre. In such circumstances, radiation was not a dominant factor. Thus, a total heat transfer rate constant can be used to consider all heat losses together. A heat balance of the liquid yields:

$$C_p^l M_l \frac{dT_l}{dt} = -H_o(T_l - T_R) \qquad (5.20)$$

where T_l is the melt temperature, T_R is the room temperature (°C); C_p^l is the heat capacity (J/kg/K); M_l is the weight of liquid iron (kg); H_o is the total heat transfer constant (W/K). Equation (5.20) can be simplified as

$$\frac{dT_l}{dt} = -K_{T,0}(T_l - T_R) \qquad (5.21)$$

where

$$K_{T,0} = \frac{H_o}{C_p^l M_l} \tag{5.22}$$

According to Equations (4.4) and (4.9), when the gas flow rate and powder feed rate are equal to zero, the value of $K_{T,0}$ is 10^{-4} 1/s approximately. The rate constant, H_o, can be calculated easily. In the following text, the value of $K_{T,0}$ obtained from the experiments will be examined on a fundamental basis. It has been seen in Figure 3.2 that the crucible was contained in a water cooled induction furnace. The furnace was covered with an insulating alumina board under a lid, the lid was filled with alumina fibre. In such circumstances, heat transfer was dominated by conduction through the crucible wall and lining material to the water coils. The effect of radiation was very small as compared with the transverse conduction (which will be seen more clearly from the following calculation). In order to estimate the predominant transverse heat transfer, a planar heat transfer model is presented and shown in Figure 5.3. This estimation is order-of-magnitude only.

The overall thermal resistance, R ($m^2 \cdot K/W$), can be written as

$$R = \frac{A}{H_o} = \frac{1}{h_m} + \frac{\delta_1}{k_1} + \frac{\delta_2}{k_2} \tag{5.23}$$

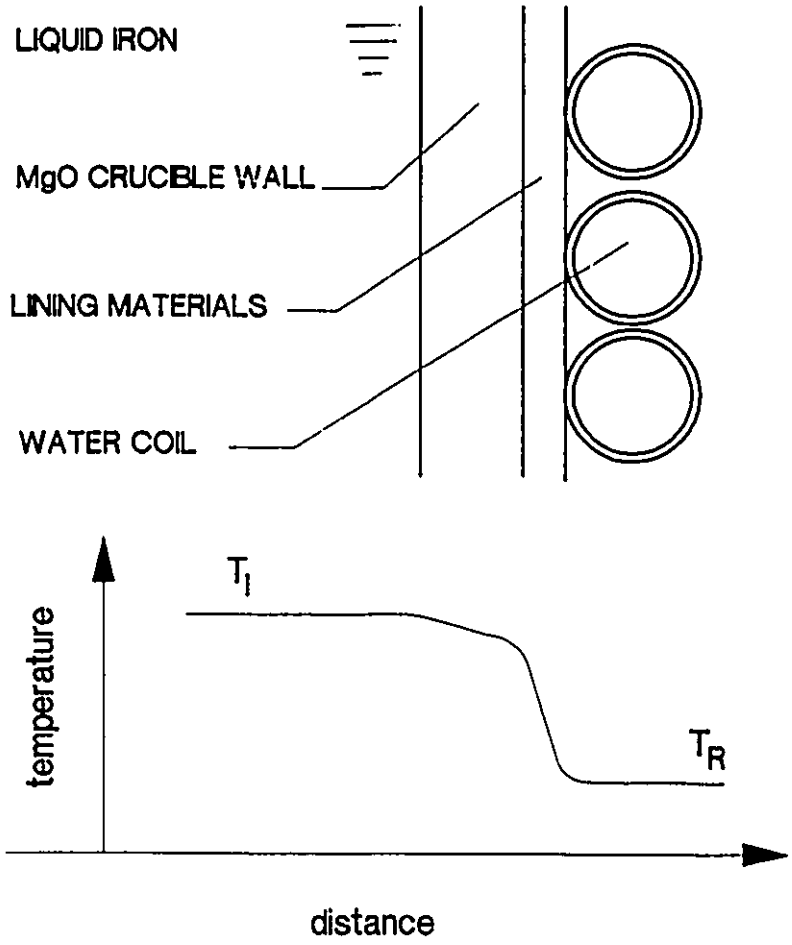

Figure 5.3 The plane heat transfer model. The thermal resistance mainly comes from the lining materials layer.

where A is the heat exchange area between the crucible and the melt; h_m is the effective heat transfer coefficient of the melt to the crucible surface ($W/m^2/K$); k_1 and k_2 are the thermal conductivities of the crucible wall and lining materials (W/m/K); δ_1 and δ_2 are their thickness (m).

The resistance of water cooling is very small compared with the resistances of the crucible and the lining materials. Thus, it is ignored. Heat transfer in the melt is by natural convection. For natural convection near a vertical plane, a commonly-used heat transfer correlation is [101]

$$Nu = 0.411(Pr \cdot Gr)^{1/4} \tag{5.24}$$

where

$$Pr = \frac{C_p^l \mu}{k_l} \tag{5.25}$$

$$Gr = \frac{g\rho_l^2 L^3 \beta \Delta T}{\mu^2} \tag{5.26}$$

$$Nu = \frac{h_m L}{k_l} \tag{5.27}$$

Here, k_l is the conductivity (W/m/K) and μ is the viscosity of liquid iron (kg/m/s); β is the volume expansion efficiency (1/K); ΔT is the temperature difference between the crucible surface and the melt (K); L is the dimension for the calculation (m).

The numerical values used for the calculation are summarized in Table 5.2. The estimation of the thermal resistance is listed in Table 5.3. One can see that the estimated thermal resistance (0.0224 $m^2 \cdot K/W$) is only 20 per cent less than that deduced from the measured bath cooling rate (0.0295 $m^2 \cdot K/W$). It is also apparent that the resistance mainly comes from the lining materials. This justifies the assumption used above that heat transfer was dominated by the transverse conduction.

(2) Bath Cooling during Gas Injection

In the case of nitrogen injection, a heat balance on the liquid yields:

$$C_p^l M_l \frac{dT_l}{dt} = -H_1(T_l - T_R) \tag{5.28}$$

where H_1 is the heat transfer rate constant during gas injection (W/K). Equation (5.28) can be rearranged as

$$\frac{dT_l}{dt} = -K_{T,1}(T_l - T_R) \tag{5.29}$$

TABLE 5.2

THE NUMERICAL VALUES USED FOR CALCULATION

Quantity		Symbol	Unit	Value	Ref.
Hot Metal	Density	ρ_l	kg/m^3	7000	[102]
	Heat Capacity	C_p^l	J/kg/K	840	[102]
	Conductivity	k_l	W/m/K	40	[103]
	Viscosity	μ	kg/m/s	7.6×10^{-3}	[104]
	Volume Expansion Efficiency	β	1/K	1.0×10^{-4}	[105] [a]
Calcium Carbide	Heat Capacity	C_p^p	J/kg/K	1218	[106]
	De-S Enthalpy	ΔH	J/mole	401700	[107]
Crucible	Conductivity	k_1	W/m/K	6.9	[108]
Lining Materials	Conductivity	k_2	W/m/K	0.67	[109]

a Based on the density-temperature dependence given by [105], β is calculated by

$$\beta = -\frac{1}{\rho_l}\left(\frac{\partial \rho_l}{\partial T}\right)_p$$

TABLE 5.3

THE ESTIMATION OF THE THERMAL RESISTANCE

Quantity		Symbol	Unit	Value
Melt	Conductivity	k_l	W/m/K	40
	Viscosity	μ	kg/m/s	7.6×10^{-3}
	Volume Expansion Efficiency	β	1/K	1.0×10^{-4}
	Dimension	L	m	0.2
	Temperature difference	ΔT	K	1
	Prandtl Number	Pr	/	0.16
	Grashof Number	Gr	/	6.99×10^{6}
	Nusselt Number	Nu	/	13
	Heat Transfer Coefficient	h_m	$W/m^2/K$	2673
	Thermal Resistance	R_m	$m^2\cdot K/W$	3.4×10^{-4}
Crucible	Conductivity	k_1	W/m/K	6.9
	Thickness	δ_1	m	0.019
	Thermal Resistance	R_1	$m^2\cdot K/W$	0.0027
Lining Materials	Conductivity	k_2	W/m/K	0.67
	Thickness	δ_2	m	0.013
	Thermal Resistance	R_2	$m^2\cdot K/W$	0.019
Estimated Thermal Resistance		R	$m^2\cdot K/W$	0.0224
Measured	Bath Cooling Rate Constant	K_T	1/s	10^{-4}
	Thermal Resistance	R	$m^2\cdot K/W$	0.0295

where

$$K_{T,1} = \frac{H_1}{C_p^l M_l} \tag{5.31}$$

According to the experimental results, H_1 is a function of gas flow rate during gas injection. Heat transfer during gas injection occurs in a complex way. Convection and radiation may have some effects which cannot be ignored. The simplified planar conduction model cannot explain why the heat transfer rate constant changes with the gas flow rate. The following points may account for that change:

- Gas stirring under the lid was enhanced by gas injection. As a result, heat transfer to the lid by convection and heat losses to the atmosphere by radiation may have increased.

- The sensible heat in the gas caused additional heat losses from the melt.

- Gas injection created liquid circulation and volume expansion. As a result, heat transfer in the melt by convection increased. More heat was lost through the crucible wall and lining material to the water coil.

According to Equation 4.4, if the gas flow rate changes from 0 to 5 SLPM, the heat transfer rate constant increases approximately by 10 per cent. Less than

2 per cent comes from the increase of sensible heat in the gas, and another 2 per cent is from the melt volume expansion due to gas injection. The remaining difference may result from enhanced radiation and gas convection during injection. Unfortunately, these factors are probably the least understood and most complex of heat transfer steps. Further research work may be needed to understand it in detail.

Choosing a linear function of gas flow rate, Q, to express the heat transfer constant, $K_{T,1}$, gives

$$K_{T,1} = \alpha_1 + \beta_1 Q \tag{5.32}$$

where α_1 and β_1 are constants. The first term is a constant, indicating that there is no significant change of the thermal conditions from one injection to another. The second one indicates that the heat losses increase with gas flow rate due to the gas sensible heat, and radiation and convection to the surroundings.

(3) Bath Cooling during Powder Injection

For calcium carbide injection, the heat balance on the melt and particles is given by

$$C_p^l M_l \frac{dT_l}{dt} = -H(T_l - T_R) - C_p^p W_p (T_p - T_R) + q \tag{5.33}$$

Here, H is the total heat transfer constant during powder injection (W/K); C_p^p and W_p are the heat capacity (J/kg/K) and the mass flow of powder (kg/s); T_p is the average particle temperature at the melt surface (°C); and q is the heat release rate by chemical reaction (W). Compared with the other terms in Equation (5.32), q is very small (less than two percent), thus, for the calculation of the bath cooling rate constant, q is neglected temporarily (A correction will be made for the calculation of the particle temperature discussed in Section 5.2.2).

Equation (5.32) can be rearranged to

$$\frac{dT_l}{dt} = -\left[\frac{H}{C_p^l M_l} + \frac{C_p^p}{C_p^l M_l} \cdot \frac{T_p - T_R}{T_l - T_R} \cdot W_p\right](T_l - T_R) \qquad (5.34)$$

Introducing a heat transfer constant, $K_{T,2}$,

$$K_{T,2} = \frac{H}{C_p^l M_l} + \frac{C_p^p}{C_p^l M_l} \cdot \frac{T_p - T_R}{T_l - T_R} \cdot W_p \qquad (5.35)$$

gives the time dependence of the bath temperature as

$$\frac{dT_l}{dt} = -K_{T,2}(T_l - T_R) \qquad (5.36)$$

In a similar way to Equation (5.31), the first term on the right hand side of Equation (5.34) can be modelled as a linear function of gas flow rate. Because the ratio of $(T_p-T_R)/(T_l-T_R)$ is approximately a constant (as will be seen later), the second term is proportional to powder flow rate, W_p. Therefore, the bath cooling rate constant, $K_{T,2}$, can be described as a linear function of gas flow rate and powder feed rate:

$$K_{T,2}=\alpha+\beta Q+\gamma W_p \tag{5.37}$$

where α, β and γ are constants.

$$\alpha+\beta Q=\frac{H}{C_p^l M_l} \tag{5.38}$$

and

$$\gamma=\frac{C_p^p}{C_p^l M_l}\cdot\frac{T_p-T_R}{T_l-T_R} \tag{5.39}$$

It has been pointed out that the two terms on the right hand side of Equation (4.4) for gas injection are almost identical to the corresponding terms of Equation (4.9) for powder injection. Thus, according to Equations (5.31) and (5.36), one has

$$\alpha=\alpha_1 \tag{5.40}$$

$$\beta - \beta_1 \qquad (5.41)$$

The constants α, β and α_1, β_1 are associated with the conditions of heat transfer from the melt to the surroundings. Thus, Equations (5.39) and (5.40) may be considered as an indication that the thermal conditions were approximately same for gas and powder injections. The slag accumulated during powder injections has a little effect on heat transfer, as discussed in the following text.

(4) Bath Cooling after Powder Injection

As described in Chapter 4, the cooling rate after powder injection was lower than that during powder injection. The linear regression results of the experimental data after powder injection have been given by Equation (4.9). The constant term and the coefficient of Q of Equation (4.8) are very close to the corresponding terms of Equation (4.9). This indicates that no additional bath cooling was caused by the powder accumulated on the melt surface. A possible explanation is that the powder has a very small heat conductivity and bulk density. The powder on the melt surface could not be heated up very quickly. Thus, heat transfer from the melt to the powder on the melt surface was negligible.

5.2.2 The Average Particle Temperature and Particle-Liquid Contact Fraction

As shown schematically in Figure 5.4, some particles may be suspended in bubbles, the others positioned on the bubble interfaces or dispersed in the liquid. It is obviously very difficult to measure the fraction of the particles which come into contact with liquid directly. Farias and Irons injected sand into liquid lead and observed that the bath cooling rate was only 30 percent of that which would be expected if all the particles were heated to the melt temperature [2]. Chiang et al. studied the desulphurization kinetics of calcium carbide injection into 3 tonne heats; by comparison with a mathematical model of desulphurization, they found that the rate of desulphurization was consistent with approximately 30 percent of the particles entering the melt [1]. These findings suggest that significant fractions of calcium carbide particles do not come in contact with liquid during their rise with gas bubbles. Stimulated by these thoughts and observations, the present work was designed to explore in more detail the fraction of calcium carbide particles in contact with liquid iron. The analysis is based on the experimental data of the bath temperature, which was measured very carefully during injection.

As given in Equation (5.32),

$$C_p^l M_l \frac{dT_l}{dt} = -H(T_l - T_R) - C_p^p W_p (T_p - T_R) + q \qquad (5.32)$$

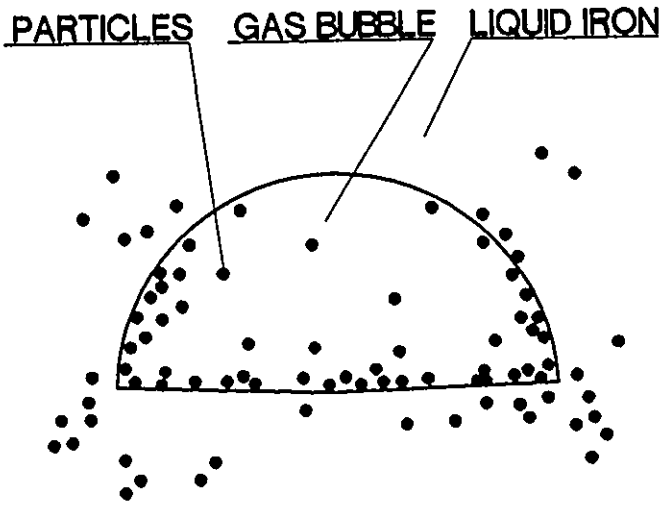

Figure 5.4 Schematic diagram of particle-liquid contact shows that some particles are suspended in bubble space, others are positioned on bubble interface or dispersed in the melt.

the average particle temperature, T_p, is assumed to be a constant at the melt surface. It has been pointed out that heat transfer from the melt to the powder accumulated on the melt surface was negligible. Thus, it can be understood that the particles were heated up to T_p mainly in the plume, not at the melt surface.

Equation (5.32) can be integrated as

$$T_l - T_R + (T_o - T_R)e^{-k't} - \frac{b}{k'}(T_p - T_R)(1 - e^{-k't}) + \frac{q'}{k'}(1 - e^{-k't}) \tag{5.41}$$

where T_o is initial temperature of the melt (°C); b and k' are constants which depend on the experimental conditions (1/s).

$$b = \frac{C_p^p W_p}{C_p^l M_l} \tag{5.42}$$

$$k' = \frac{H}{C_p^l M_l} \tag{5.43}$$

Comparing Equation (5.43) with Equation (5.37), one has

$$k' = \alpha + \beta Q \tag{5.44}$$

where the constants α and β have been determined from the regressions of the experimental data. Thus, at a given nitrogen flow rate, k' can be calculated easily.

The last term of Equation (5.41) represents the thermal effect of chemical reaction on the bath temperature (°C/s), and

$$q' = \frac{q}{C_p^l M_l} \tag{5.45}$$

During powder injection, the change of the oxygen content is negligible as comparing to the change of the sulphur content, thus, the thermal effect of deoxidation is ignored, only calcium carbide desulphurization is considered here.

$$CaC_2(s) + \underline{S} = CaS(s) + 2C(s) \tag{5.46}$$

and

$$q = \frac{\Delta(\%S) M_l \Delta H}{3200 \Delta t} \tag{5.47}$$

where Δ(%S) is sulphur content (%) removed during a time period of Δt (s); and ΔH is enthalpy change of calcium carbide desulphurization (as given in Table 5.2). The heat of desulphurization with calcium carbide can compensate for heat losses in small amount. For example, if Δ(%S) is taken as 0.03 per cent, and Δt as 180 s. The value of q is approximately 8 per cent of the total heat transfer rate.

By fitting the measured bath temperature to Equation (5.41), the average particle temperature is obtained. The results are tabulated in Table 5.4. It can be seen that the average particle temperature varies in the range of about 400 to 700°C.

There two limits to the way in which the magnitude of the bath cooling during powder injection can be interpreted:

(a) All the particles are heated to the same temperature between the initial particle temperature and the bath temperature.

(b) A fraction of the particles are heated to the melt temperature, and the remainder are essentially unheated.

Both of these interpretations are shown in Figure 5.5. The second one is likely closer to reality because

TABLE 5.4

THE AVERAGE PARTICLE TEMPERATURE AND THE PARTICLE-LIQUID CONTACT FRACTION

Run No.	M_l	Q	W_p	L	T_l	$k \times 10^5$	Δt	ΔS	T_p	f
	kg	SLPM	g/s	kg/Nm^3	°C	1/s	s	%	°C	%
3-003	72.6	11.2	8.0	42.9	1344	17.3	130	0.022	427	30
3-005	72.6	10.5	7.0	39.7	1348	17.5	130	<0.001	416	29
6-002	68.1	4.44	3.5	47.1	1333	14.0	230	0.014	418	30
6-006	68.1	4.70	3.5	44.3	1344	14.0	150	0.014	410	29
7-004	68.6	4.35	4.8	65.7	1340	16.0	220	0.015	599	43
10-002	70.4	5.00	4.2	50.8	1340	14.6	210	0.021	475	34
10-004	70.4	9.60	4.8	29.7	1328	15.9	120	0.019	455	33
10-006	70.4	9.00	9.8	65.0	1340	22.7	160	0.026	721	53
11-001	71.7	5.50	5.5	59.8	1354	16.8	180	0.030	705	51
11-002	71.7	4.50	4.3	57.8	1345	14.7	200	0.017	483	34
11-003	71.7	5.20	3.7	43.1	1340	14.7	220	0.012	439	31
11-008	71.7	8.00	12.7	95.0	1358	23.1	160	0.022	708	51

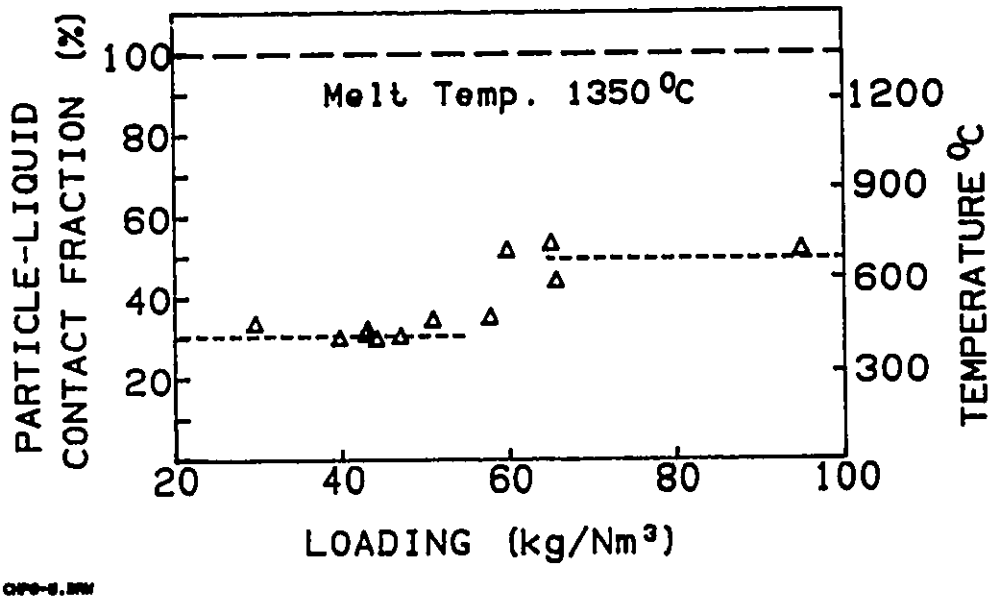

Figure 5.5 The fraction of particles in contact with liquid and the average particle temperature are related to loading.

- Such fine particles would be heated instantaneously to the melt temperature if they were in contact the melt.

- The iron in contact with 400-700°C particles would be solid, virtually preventing any desulphurization, which is obviously not the case.

Therefore, it appears that a significant fraction of the particles does not contact the melt. The average particle temperature should be proportional to the liquid-particle contact fraction, f, i.e.

$$f = \frac{T_p - T_R}{T_l - T_R} \qquad (5.48)$$

This equation is deducted directly from the second interpretation that a fraction of the particles are heated to the bath temperature, and the remainder are unheated. As mentioned earlier, the bath temperatures were about 1350°C, and the average particle temperatures were in the range of 400-700°C. Substituting these data into Equation (5.48), one can see that 30-50 percent of the particles come into contact with the liquid iron.

In Figure 5.5, the average particle temperature and the fraction of particles in contact with the melt are plotted against the loading L (kg/Nm^3), which represents the particle concentration in carrier gas. One can see that the fraction increases at 60 kg/Nm^3. The reason for the change at this loading is not very

clear. The previous work has shown that, at low loading, carrier gas bubbles form, and the particles penetrate the interface if they have sufficient momentum. At high loading, the gas and particles flow as a coupled pseudo-single phase mixture, this results in a jet of gas and particles forming without bubbles releasing at the nozzle [110,111]. In the jetting regime, there are more, smaller bubbles which may create more surface area for the particles to reside. Unfortunately, the transition criterion for powder injection in liquid iron is not well established. It is not certain that the bubbling-jetting transition is responsible for the improved particle-liquid contact.

In the above discussion it is shown that particle-liquid contact is only 30-50 per cent. For calcium carbide desulphurization, the particles must come in contact with the melt, thus improvements in particle-liquid contact should increase reaction rate and reagent efficiency. Farias and Irons found that use of angled lance and gas release agents improved particle-liquid contact [2]. More investigations will be required to confirm this in liquid iron.

5.3 THE EFFECT OF OXYGEN ON THE KINETICS OF HOT METAL DESULPHURIZATION DURING CALCIUM CARBIDE INJECTIONS

It has been recognized for some time that low oxygen activity is essential for effective steel desulphurization. As hot metal specifications become more

stringent, the role of oxygen becomes more important to hot metal desulphurization. The previous research efforts on the thermodynamic aspects have provided primary guidance in understanding the role of oxygen in hot metal desulphurization. However, on the kinetic aspects, experimental data and theoretical analyses relating the role of oxygen to hot metal desulphurization during calcium carbide injections are limited. The present work is the first time that the following trends were observed in experiments:

- The sulphur and oxygen activities varied simultaneously during injection of calcium carbide (See the reaction trajectories shown in Figure 4.24).

- The first order rate constants of desulphurization depended on the oxygen activities in the melts, as well as the powder injection rates (See Figure 4.21).

- The incubation period was related to the initial oxygen activity (see Figure 4.22).

- The limestone addition retarded desulphurization.

The objective of this section is to explain the above observations. To describe quantitatively the effect of oxygen in hot metal desulphurization during powder injection, a kinetic model is presented in the following section.

5.3.1 The Kinetic Model of Simultaneous Desulphurization and Deoxidation by Powder Injection

As described in Chapter 2, the powder was a mixture of calcium carbide, calcium oxide and calcium carbonate. The melt was almost saturated with carbon. In some experiments, silicon or aluminium was added into the melt. The possible reactions are:

$$[C]+[O]=CO(g) \tag{5.49}$$

$$[Si]+2[O]=SiO_2(s) \tag{5.50}$$

$$2[Al]+3[O]=Al_2O_3(s) \tag{5.51}$$

$$CaC_2(s)+[S]=CaS(s)+2C(s) \tag{5.52}$$

$$CaC_2(s)+[O]=CaO(s)+2C[s] \tag{5.53}$$

$$CaO(s)+[S]=CaS(s)+[O] \tag{5.54}$$

$$CaCO_3(s)=CaO(s)+CO_2(g) \tag{5.55}$$

The carbon dioxide may react with carbon, silicon or calcium carbide:

$$CO_2(g)+[C]-2CO(g) \tag{5.56}$$

$$CO_2(g)+\frac{1}{2}[Si]-\frac{1}{2}SiO_2(s)+CO(g) \tag{5.57}$$

$$CO_2(g)+\frac{1}{3}CaC_2(s)-\frac{5}{3}CO(g)+\frac{1}{3}CaO(s) \tag{5.58}$$

$$CO_2(g)+2CaC_2(s)-5C(gr)+2CaO(s) \tag{5.59}$$

As reviewed in Chapter 2, during powder injection, reactions occur at the melt surface with slag, and at the liquid-particle interface. They are referred as permanent reaction and transitory reaction respectively. Their relative contributions are difficult to determine. In the present work, they are not treated separately due to the following reasons:

- According to the experimental data given in Chapter 4, desulphurization after powder injection was very slow. The first order rate constant was more than ten times less than that during powder injection. This indicates that the powder accumulated on the melt surface only had little effect on the rate of desulphurization.

- According to the calculations which will be given in Section 5.3.2, the reaction area between the melt and slag is almost ten times smaller than the surface area of particles in contact with the melt. This indicates that the melt surface was not a major reaction site. This may explain why the effect of slag on the reaction rate was limited.

- The oxide on the melt surface was scraped off before powder injections. During injections, a large amount of powder in the bubbles was unreacted. The bubbles reached the bath surface and broke up. Then, the particles accumulated on the top. After incubation, the slag was mainly calcium carbide, reacting in a similar manner to calcium carbide in the bubbles.

It must be noted that slag played an important role as a sulphide product holder at the initial stage of injection. Previous work found that the incubation period was related to slag conditions [1]. The incubation phenomena will be discussed in Section 5.3.3. This section will focus on the kinetics of desulphurization and deoxidation after the incubation periods. The present work has confirmed that the kinetics of desulphurization can be described as first order process after incubation (See Section 4.2.1). A kinetic model is required to interpret the experimental data measured during powder injections.

A number of models have been developed to describe powder injection processes [1,45,46]. They were all based on the assumption that both permanent and transitory reactions were controlled by mass transfer. Many studies

demonstrated that the kinetics of desulphurization are approximately first order transport controlled process (Refer to Section 2.2). The reaction rate can be reasonably described as

$$\frac{dC_x}{dt} = -K_x(C_x - C_x^{eq}) \qquad (5.60)$$

where K_x is the overall mass transfer rate constant for species X; C_x and C_x^{eq} are the bulk concentration and the interfacial equilibrium concentration of X.

The rate of mass transfer is considered to be governed by several consecutive steps:

(a) The rate at which sulphur-rich liquid is pumped into the plume by entrainment.

(b) The rate at which sulphur diffuses through the liquid boundary layer to particles.

(c) The rate at which sulphur diffuses through the solid product layer of particles.

(d) The rate at which calcium carbide decomposes and calcium vapour diffuses through the solid product layer.

Several important findings of the previous work have been reviewed in Chapter 2. They are:

(a) The rate at which sulphur-rich liquid is entrained into the plume exerted little control over desulphurization process [1].

(b) Sulphur is less likely than calcium to be dominant transport species in the porous product layer [2].

(c) The rate of calcium vapour diffusion through the product layer is fast enough to be insignificant in controlling the overall reaction [1,52].

These findings lead to a conclusion that the reaction rate is controlled by sulphur diffusion through the liquid boundary layer to particles. These findings will be adopted by this work as a part of the primary assumptions for the kinetic model. More details are summarized in Appendix III.

In order to describe the role of oxygen activity in hot metal desulphurization quantitatively, a kinetic model is developed in this thesis with the following simplified assumptions:

(a) The equilibrium between CaC_2, CaS and CaO, which will be called as "Local equilibrium", only occurs at the reaction site, the melt-particle interface.

(b) The refining rate is controlled by mass transfer of oxygen and sulphur through the liquid boundary layer around the solid particles.

(c) The mass transfer rate constant for the particles on bubbles is very small as compared with the particles in liquid. The contribution of the particles on the bubbles and in the liquid will not be considered separately (The details will be given in Section 5.3.2).

(d) The mass transfer coefficients of oxygen and sulphur are equal. (The case of unequal coefficients will be discussed in Section 5.3.4.)

(e) No oxygen infiltrates the melt from the atmosphere or refractory.

The schematic concentration profiles of sulphur and oxygen near CaC_2 and CaO particles are given in Figure 5.6. C_S and C_O are the melt concentrations of sulphur and oxygen; $C_{S,1}^{\bullet}$ and $C_{O,1}^{\bullet}$ are the interfacial concentrations of sulphur and oxygen in equilibrium with calcium carbide particles; $C_{S,2}^{\bullet}$ and $C_{O,2}^{\bullet}$ are the interfacial concentrations of sulphur and oxygen in equilibrium with calcium oxide particles. All model calculations are made on a molar basis, but changed to the more familiar weight percent in the text.

To simplify the model formulation, the experimental conditions after the incubation period are divided into three cases:

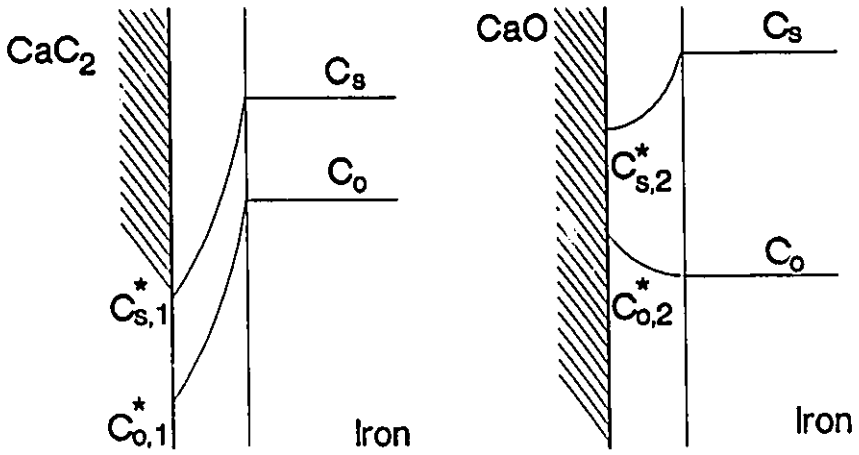

Figure 5.6 a Schematic representations of the concentrations of sulphur and oxygen near solid/liquid interface. The oxygen activity is lower than the silicon or carbon equilibrium.

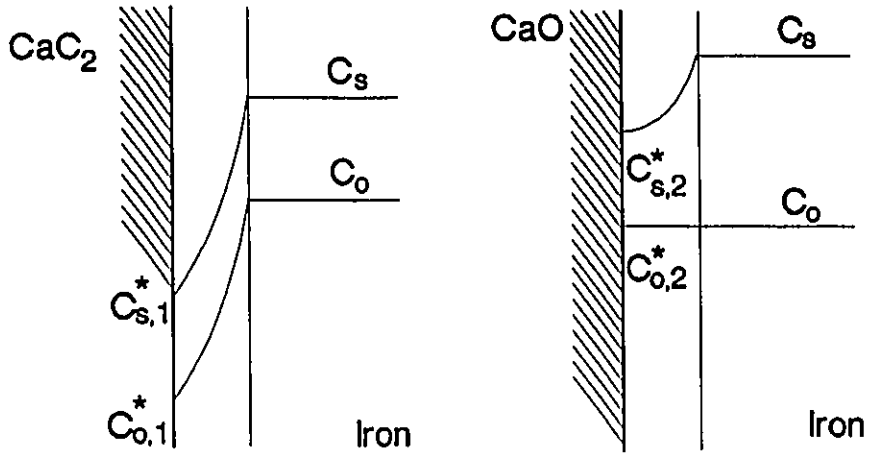

Figure 5.6 b Schematic representations of the concentrations of sulphur and oxygen near solid/liquid interface. The oxygen activity is controlled by carbon, silicon or aluminum, resulting a fixed oxygen activity.

Case 1: There was no limestone in the powder mixture. No aluminum was added into the melt. The oxygen activity was lower than that expected from the equilibrium with either silicon or carbon content (as shown in Figure 5.6 a).

Case 2: There was no limestone in the powder mixture. The oxygen activity was controlled by carbon, silicon or aluminium, resulting in a fixed oxygen activity (as shown in Figure 5.6 b).

Case 3: Limestone was added in the calcium carbide powder mixture, or carbon dioxide was used as a carrier gas.

Case 3 will be discussed in Section 5.3.6. Most experiments were carried out under the conditions of Case 1. For this case, Reactions (5.47)-(5.49) and (5.53)-(5.57) can be excluded from considerations. Only the reactions of sulphur and oxygen with calcium carbide and calcium oxide are involved.

(1) The Kinetic Model for Case 1

Desulphurization occurs at the surface of CaC_2 and CaO particles simultaneously. A sulphur balance for liquid iron can be written as

$$\frac{dC_s}{dt} = -K_1(C_s - C_{s,1}^*) - K_2(C_s - C_{s,2}^*) \qquad (5.61)$$

where the subscript 1 is for CaC_2, and 2 for CaO, as shown in Figure 5.6 a. At the surface of the CaC_2 particles, sulphur and oxygen are removed from the melt simultaneously. However, at the surface of CaO particles, as sulphur reacts with calcium oxide, oxygen is released from the reaction site and goes into the melt. A oxygen balance for liquid can be written as

$$\frac{dC_o}{dt} = -K_1(C_o - C_{o,1}^*) - K_2(C_o - C_{o,2}^*) \qquad (5.62)$$

where K_1 and K_2 are the mass transfer rate constants from the melt to the calcium carbide and oxide particles.

The flux of sulphur coming to and the flux of oxygen leaving from the interface of CaO particle must be equal. The stoichiometry of CaO-S-CaS-O reaction leads to

$$(C_s - C_{s,2}^*) + (C_o - C_{o,2}^*) = 0 \qquad (5.63)$$

Defining K_{eq} as the CaO-S-CaS-O equilibrium constant, the assumption of "local equilibrium" gives

$$K_{eq} = \frac{C_{s,2}^*}{C_{o,2}^*} \qquad (5.64)$$

Combining Equations (5.63) and (5.64) and substituting into Equations (5.61) and (5.62) yields

$$\frac{dC_s}{dt} = -(K_1+a)C_s + aK_{eq}C_o + K_1C_{s,1}^* \tag{5.65}$$

$$\frac{dC_o}{dt} = aC_s - (K_1+aK_{eq})C_o + K_1C_{o,1}^* \tag{5.66}$$

where a is a constant:

$$a = \frac{K_2}{K_{eq}+1} \tag{5.67}$$

Equations (5.65) and (5.66) are non-homogeneous coupled ordinary differential equations. The following steps were undertaken to find solutions:

(a) Solve the corresponding homogeneous equations.

(b) Find the particular solutions to the non-homogeneous equations by using the variable coefficient method.

(c) Find the final solutions which satisfy the initial conditions.

The homogeneous equations of Equations (5.65) and (5.66) are

$$\frac{dC_s}{dt} = -(K_1+a)C_s + aK_{eq}C_o \tag{5.68}$$

and

$$\frac{dC_o}{dt} = aC_s - (K_1+aK_{eq})C_o \tag{5.69}$$

Their characteristic equation is

$$\begin{vmatrix} -(K_1+a)-\lambda & aK_{eq} \\ a & -(K_1+aK_{eq})-\lambda \end{vmatrix} = 0 \tag{5.70}$$

for which, the characteristic roots are

$$\begin{aligned} \lambda_1 &= -K_1 \\ \lambda_2 &= -(K_1+K_2) \end{aligned} \tag{5.71}$$

Because the functions

$$\begin{aligned} f_1(t) &= e^{-K_1 t} \\ f_2(t) &= e^{-(K_1+K_2)t} \end{aligned} \tag{5.72}$$

are linearly independent, the general solutions of Equations (5.68) and (5.69) are

$$C_s = C_1 e^{-K_1 t} + C_2 e^{-(K_1+K_2)t} \tag{5.73}$$

and

$$C_o = \frac{C_1}{K_{eq}} e^{-K_1 t} - C_2 e^{-(K_1+K_2)t} \tag{5.74}$$

Assuming that the particular solutions of the non-homogeneous equations are two constants, A_1 and A_2, one has

$$\begin{aligned} A_1 &= C_{s,1}^* \\ A_2 &= C_{o,1}^* \end{aligned} \tag{5.75}$$

Thus, the general solutions of the non-homogeneous equations are given by

$$C_s = C_{s,1}^* + C_1 e^{-K_1 t} + C_2 e^{-(K_1+K_2)t} \tag{5.76}$$

$$C_o = C_{o,1}^* + \frac{C_1}{K_{eq}} e^{-K_1 t} - C_2 e^{-(K_1+K_2)t} \tag{5.77}$$

Applying the initial conditions

$$t=0 \qquad \begin{matrix} C_s=C_s^0 \\ C_o=C_o^0 \end{matrix} \tag{5.78}$$

one can determine the coefficients in Equations (5.76) and (5.77):

$$C_1=-\frac{K_{eq}}{K_{eq}+1}\left[(C_s^0+C_o^0)-(C_{s,1}^*+C_{o,1}^*)\right] \tag{5.79}$$

$$C_2=-\frac{1}{K_{eq}+1}\left[(C_s^0-K_{eq}C_o^0)-(C_{s,1}^*-K_{eq}C_{o,1}^*)\right] \tag{5.80}$$

In most of the experiments of calcium carbide injection, after the incubation period, the melt oxygen activity was below that expected from equilibrium with either silicon or aluminum content. Such performance falls into the category of Case 1. Two examples are shown in Figures 5.7 and 5.8, where the experimental results are compared with that calculated from the kinetic model. The determination of the mass transfer rate constants will be discussed in Section 5.3.2.

(2) The kinetic Model of Case 2

When silicon or aluminium concentrations are large, the initial oxygen activity is low. As more sulphur diffuses from

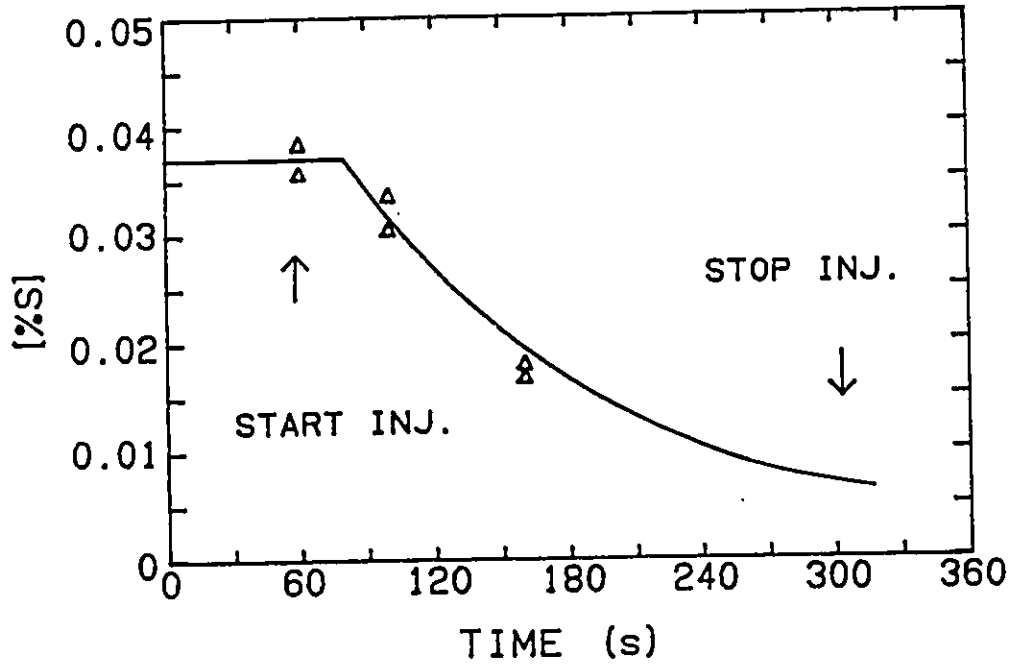

CHP441.DRW SU752

Figure 5.7 a The change of sulphur content with time during an injection of calcium carbide at 0.29 kg/min and nitrogen gas flow rate 4.1 SLPM into iron-4.2% carbon-0.12% silicon melt with an initial temperature 1350°C. The solid line is calculated from the kinetic model.

(Run No.7-002)

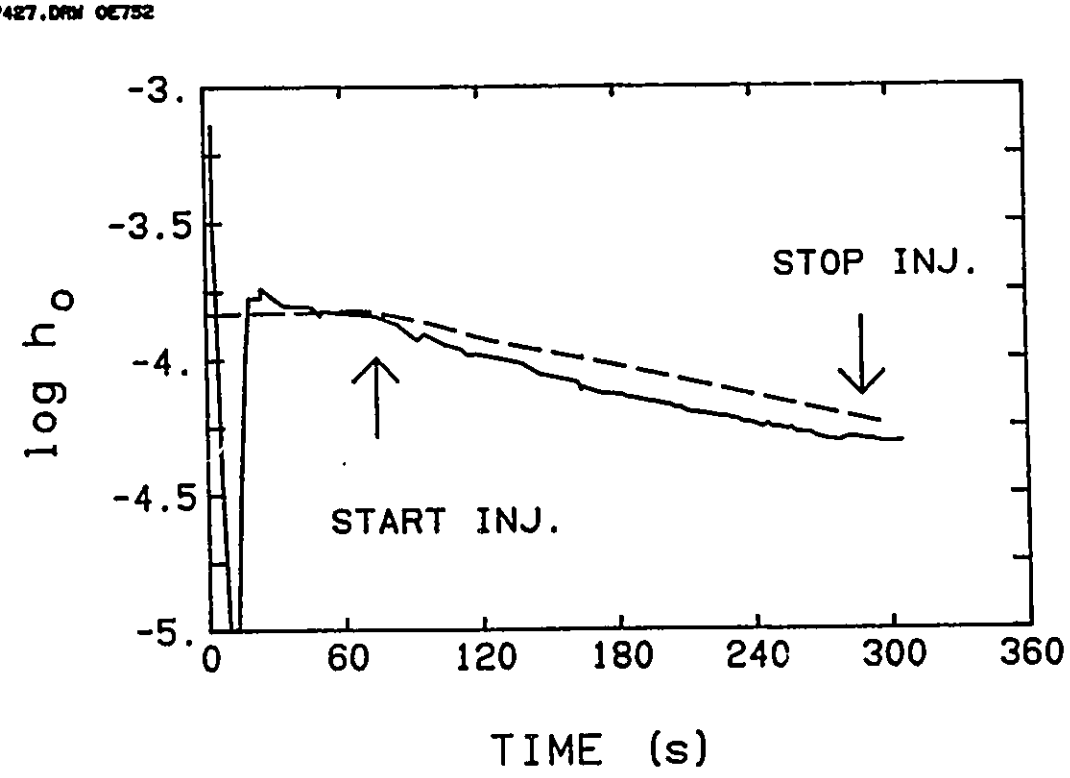

Figure 5.7 b The oxygen activity during the same injection as in Figure 5.7 a. The broken line is calculated from the kinetic model. (Run No. 7-002)

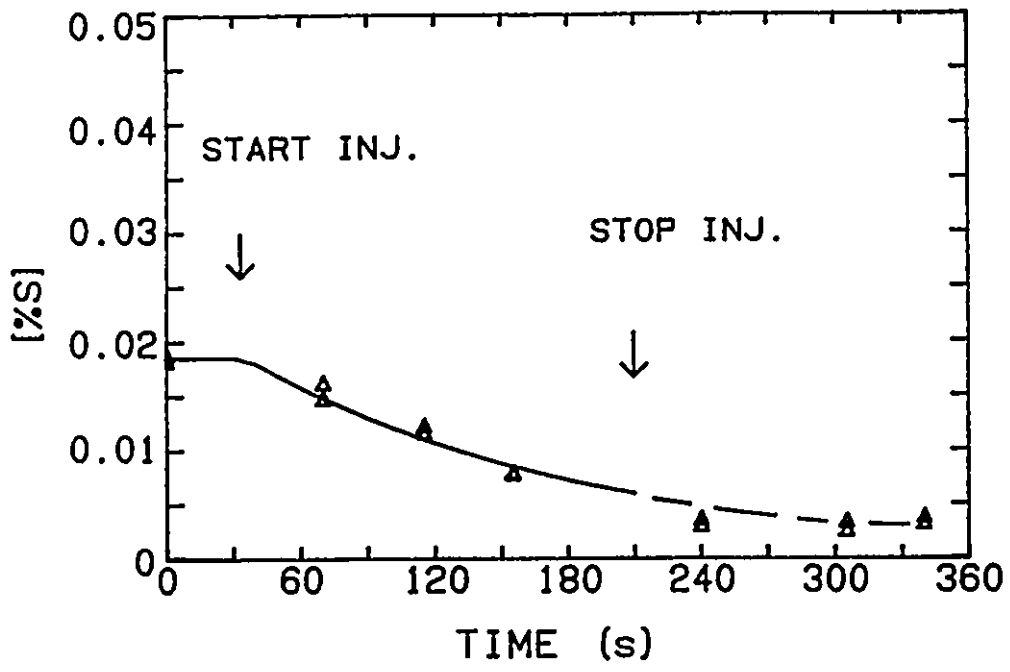

Figure 5.8 a The change of sulphur content with time during an injection of calcium carbide at 0.15 kg/min and nitrogen gas flow rate 5 SLPM into iron-4.2% carbon-0.93% silicon melt with an initial temperature 1365°C. The solid line is calculated from the kinetic model.

(Run No. 8-004)

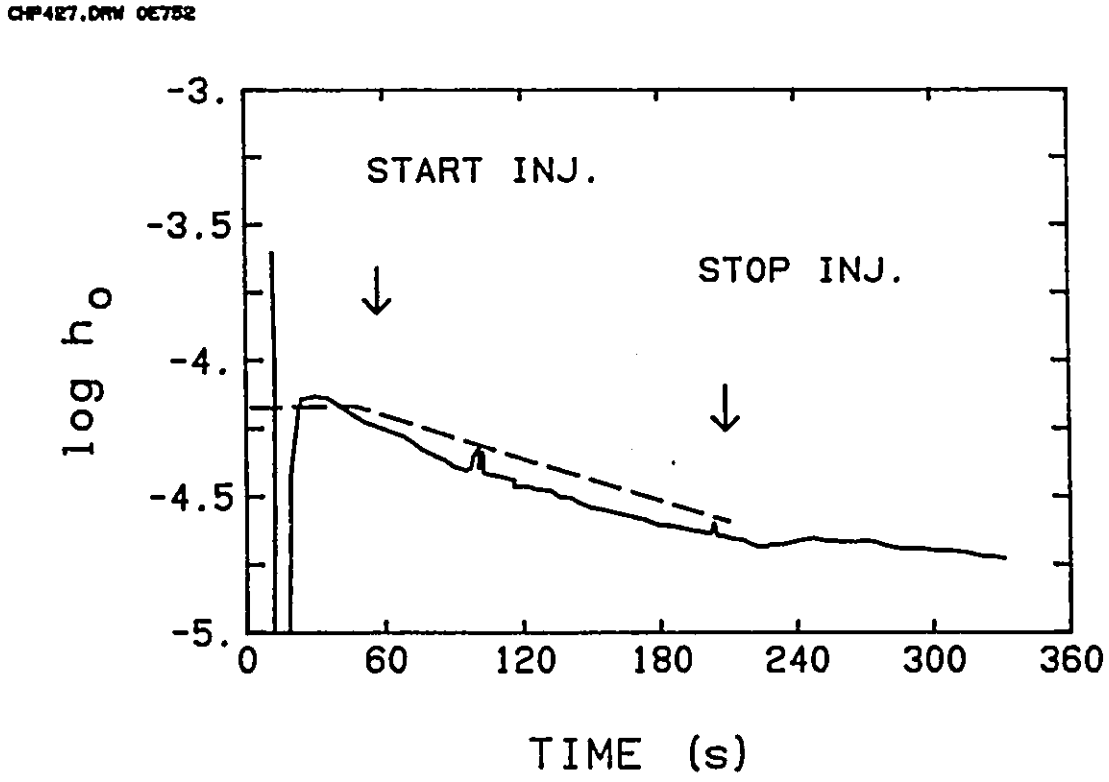

Figure 5.8 b The oxygen activity during the same injection as in Figure 5.8 a. The broken line is calculated from the kinetic model.
(Run No. 8-004)

the melt to CaO particles, more oxygen is released by CaO particles. The increase of the oxygen concentration on the CaO particle surface retards CaO desulphurization. The upper limit of the oxygen accumulated at CaO particle-melt interface is a constant which is equal to the melt oxygen determined by oxygen-silicon or aluminum equilibrium. Such performance falls into the category of Case 2. The concentration profile is given in Figure 5.6 b. In this case, Equation (5.62) is not needed because

$$C_o - C_o^* - C_{o,2}^* \tag{5.81}$$

where C_O^* is a constant which is equal to the melt oxygen determined by oxygen-silicon or aluminum equilibrium. The solution of Equation (5.61) is then found to be

$$C_s - \frac{K_1 C_{s,1}^* + K_2 K_{eq} C_o}{K_1 + K_2} + \left(C_s^0 - \frac{K_1 C_{s,1}^* + K_2 K_{eq} C_o}{K_1 + K_2} \right) e^{(-K_1 + K_2)t} \tag{5.82}$$

The equilibrium concentrations of sulphur and oxygen at the interface of calcium carbide particles, $C_{S,1}^*$ and $C_{O,1}^*$, as well as the equilibrium constant, K_{eq}, can be determined from the thermodynamic data [15].

$$CaC_2(s) + [O] - CaO(s) + 2C[s] \tag{5.53}$$

$$\Delta G^0 = RT\ln h_O^* = -462460 + 129.7T \quad (J) \tag{5.83}$$

$$C_{O,1}^* = \frac{10\rho_l h_O^*}{16 f_O} \tag{5.84}$$

$$CaO(s) + [S] = CaS(s) + [O] \tag{5.54}$$

$$\Delta G^0 = -RT\ln\frac{h_O^*}{h_S^*} = 104805 - 21.05T \quad (J) \tag{5.85}$$

$$C_{S,1}^* = \frac{10\rho_l h_S^*}{32 f_S} \tag{5.86}$$

and

$$K_{eq} = \frac{C_{S,1}^*}{C_{O,1}^*} \tag{5.87}$$

Here, T is the melt temperature (K). ΔG^0 is the free energy (J). The activity coefficients for sulphur and oxygen, f_S and f_O, can be calculated with the following interaction parameters (Refer to Table 2.6).

$$\begin{aligned} e_O^C &= -0.45 & e_O^{Si} &= -0.13 \\ e_S^C &= 0.11 & e_S^{Si} &= 0.063 \end{aligned} \tag{5.88}$$

The determination of mass transfer rate constants will be discussed in the following section.

5.3.2 The Determination of Mass Transfer Rate Constants

The overall mass transfer rate constant, K_m (1/s), is defined by

$$K_m = \frac{k_m A}{V} \tag{5.89}$$

where k_m is the mass transfer coefficient (m/s); V is the volume of the melt (m^3); A is the total area of the particles in contact with liquid (m^2). The surface areas of calcium carbide and calcium oxide particles depend on their fractions in the powder mixture. From equation (5.89), it is clear that the mass transfer rate constants for calcium carbide and calcium oxide will be determined by the fractions. For simplicity, it is assumed that the mass transfer rate constants of calcium carbide and calcium oxide, K_1 and K_2, are proportional to their fractions in the solid mixture (More discussion will be given in Section 5.3.4). Using f_1 and f_2 as the fractions of CaC_2 and CaO in the powder gives

$$\begin{aligned} K_1 &= f_1 K_m \\ K_2 &= f_2 K_m \end{aligned} \tag{5.90}$$

In Equations (5.76)-(5.77), two parameters, K_1 and K_2, are required to describe the variations of oxygen and sulphur with time. By using Equation (5.90), it can be seen that only one parameter, K_m, is unknown. The variations of the sulphur content and the oxygen activity with time have been obtained in the present experiments. In a such circumstance, a curve fitting computer program can be used to estimate the mass transfer rate constant, K_m. The K_m determined by curve fitting minimizes the differences between the results measured and the calculated from Equations (5.76)-(5.77) or (5.82). An example is given in Figure 5.7. The experimental results of the sulphur contents are plotted as triangles in Figure 5.7 a. The solid line in Figure 5.7 b shows the progress of the oxygen activity measured by the continuous oxygen probe. By fitting Equations (5.76) and (5.77) to these data, the mass transfer rate constant K_m is found to be 8.0×10^{-3} 1/s. The time dependencies of the sulphur content and the oxygen activity calculated from the kinetic model are also given in Figure 5.7 a and b. Figure 5.8 shows another example, in which the mass transfer rate constant K_m is found to be 8.3×10^{-3} 1/s. The variations of the sulphur content and oxygen activity are compared with those calculated from the kinetic in Figure 5.8 a and b, respectively. These examples demonstrate clearly that the variations of sulphur and oxygen with time are well fitted by the present kinetic model.

Table 5.5 is a summary of the mass transfer rate constants determined from the experimental data by curve fitting. The mass transfer rate constants are plotted against the powder feed rates in Figure 5.9. Multiple linear regressions

TABLE 5.5

THE MASS TRANSFER RATE CONSTANT DETERMINED FROM EXPERIMENTAL RESULTS OF DESULPHURIZATION

Run No.	Powder Feed Rate	Gas Flow Rate	Loading	De-S Rate constant K_s	Mass Transfer Rate Constant K_m
	g/min	SLPM	kg/Nm^3	10^3 1/s	
8-002	165	5	33	4.79	5.00
6-002	209	5	46	6.40	6.69
7-002	294	4	72	7.65	7.99
11-001	329	6	60	7.93	8.28
6-004	125	5	28	5.88	6.07
10-001	134	5	27	4.81	4.97
9-002	169	5	33	5.94	6.13
9-006	210	5	42	8.45	8.75
9-004	180	5	36	6.54	6.76
6-006	208	5	43	6.71	6.92
11-002	280	5	56	9.13	9.42
10-002	254	5	51	7.22	7.41
10-004	255	10	27	7.99	8.20
10-006	585	9	69	12.10	12.42
11-008	639	8	95	12.73	13.06
8-006	142	5	28	6.89	7.05
8-004	155	5	31	8.00	8.26
10-008	182	6	30	7.18	7.37
11-003	224	5	43	7.22	7.38

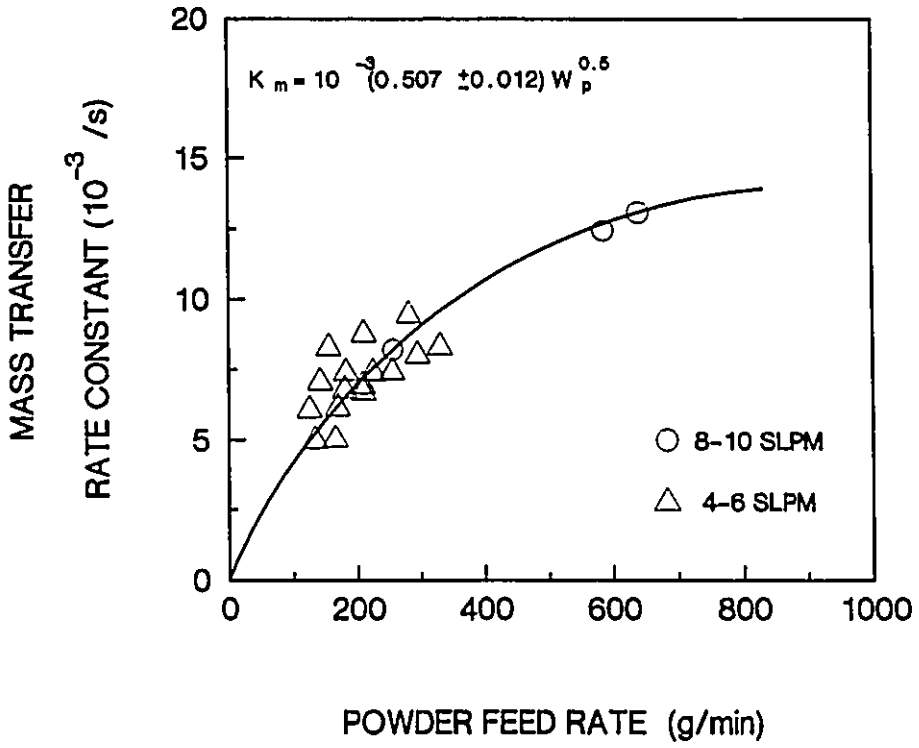

Figure 5.9 The experimental determined mass transfer rate constants are plotted as a function of powder rates. The regression result is shown in solid line.

of the mass transfer constants on the gas flow rates and the powder feed rates were performed resulting in

$$K_m = [(3.98 \pm 0.898) + (0.0132 \pm 0.00174) W_p + (0.0952 \pm 0.182) Q] \times 10^{-3} \qquad (5.91)$$
$$R^2 = 0.83$$

where the powder feed rate, W_p, is in g/min, and the gas flow rate, Q, is in SLPM. This result shows that the mass transfer rate constant increases with increasing powder feed rate. This result is expected because, at higher powder feed rate, more particles are in contact with liquid, and more interfacial area is provided. There is a small coefficient of Q with a large uncertainty which suggests that the mass transfer rate constant is not very sensitive to gas flow rate.

A similar conclusion was reported by Chiang et al. [1]. Their mathematical model calculations indicated that a higher gas flow rate led to an increase of the jet penetration and a decrease of the particle residence time in liquid. As a result, the gas flow rate had virtually no effect on the mass transfer rate constant. Thus, under the present experimental conditions, the mass transfer rate constant is considered to depend on the powder feed rate only. As shown in Figure 5.9, the mass transfer rate constant does not change with the powder feed rate linearly. Equation (5.92) is an empirical formula which is the regression of the experimental data on the square root of powder feed rate.

$$K_m = [(0.507 \pm 0.012) W_p^{0.5}] \times 10^{-3} \qquad (5.92)$$

$$R^2 = 0.82$$

In Section 5.3.1, it was assumed that the mass transfer rate constant for the particles on bubbles is very small as compared with the particles in liquid. The mass transfer coefficient k_m for a bubble can be estimated from Higbie's penetration theory [95]:

$$k_m = 2\left(\frac{D}{\pi t_c}\right)^{1/2} \qquad (5.3)$$

As given in Table 5.1, under the present experimental conditions, at the gas-liquid interface, the rate constant of mass transfer is only $0.56 \times 10^{-3}\ s^{-1}$, which is almost 10 times less than the determined from the experimental data. This justifies the assumption employed in this work that the contribution of the particles on bubbles is very small.

In the following text, the mass transfer rate constants determined from the experimental data will be compared with those calculated from the mass transfer theory. The mass transfer coefficient to a solid spheroid in liquid is given by the well-known Ranz-Marshall relation [112]

$$Sh = 2 + 0.6 Re^{1/2} Sc^{1/3} \qquad (5.93)$$

The dimensionless numbers are defined as

$$Sh = \frac{k_m d}{D} \tag{5.94}$$

$$Re = \frac{\rho_l V_t d}{\mu} \tag{5.95}$$

$$Sc = \frac{\mu}{\rho_l D} \tag{5.96}$$

For the particles at very small diameter, the particle-liquid relative velocity V_t (m/s) can be described by Stokes' law:

$$V_t = \frac{(\rho_l - \rho_s) d^2 g}{18\mu} \tag{5.97}$$

where ρ_l and ρ_s are the liquid and solid densities (kg/m^3); μ is the liquid viscosity (kg/m/s); d is the particle diameter (m); g is the gravitational acceleration constant (m/s^2); D is the diffusivity (taken to be 10^{-9} m^2/s at 1350°C [46]). It is found that the particle-liquid relative velocity is so small that value of the particle Sherwood number is very close to 2. The total area of particles in the melt is

$$A = N\pi d^2 \tag{5.98}$$

where the particles are assumed to be uniform in size. The particle diameter is considered to be equal to the area average diameter (as given in Table 3.4). The number of particles in liquid, N, is a function of powder feed rate, W_p, the fraction of particles in contact within liquid, f, and the particle residence time, τ.

$$N = \frac{6fW_p\tau}{\pi d^3 \rho_s} \tag{5.99}$$

The mass transfer rate constant, K_m, can be evaluated form Equations (5.93)-(5.99). The residence time of particles is determined by

$$\tau = \frac{U_p}{L_p} \tag{5.100}$$

where U_p is the plume velocity (m/s), L_p is the particle travelling distance (m). The mean plume velocity can be calculated by using the relationship [113-114]:

$$U_p = \beta\left[\frac{K'Qv_t}{R}\right]^{0.25} \tag{5.101}$$

where

$$K' = \left(\frac{6}{\pi}\right)^{2/3} \frac{0.8^2 g C_D}{18 C_\mu C^4 K_1^3} \tag{5.102}$$

$$v_t = 5.5\times10^{-3} L\left[\frac{(1-\alpha)gQ}{D}\right]^{1/3} \qquad (5.103)$$

where Q is the gas flow rate (m^3/s), α is the gas fraction in the plume, β is the fractional submergence of lance, D is the diameter of crucible (m), L is the bath depth (m). According to References [113-114], the dissipation rate constant, C_μ, has a value of 0.09, the parameter, C, is suggested to be 0.537, the constant, K_1, has a value of 0.18 ($m^{1/3}$), the drag coefficient of bubble, C_D, has a value of 0.44.

From the calculations, it is found that the mass transfer rate constant is a function of the powder feed rate, and the gas flow rate at a given contact fraction of the particles with the liquid. The data used for the calculations are given in Table 5.6. An example is shown in Figure 5.10. It can be seen that the mass transfer rate constant increases linearly with increasing powder feed rate, but decreases with increasing gas flow rate. This is reasonable because that, at a higher powder feed rate, more particles come into the liquid, resulting in greater mass transfer area, consequently, the mass transfer rate is higher. However, at a higher gas flow rate, the plume velocity is higher, resulting in shorter particle residence time, thus, the mass transfer rate is lower.

The mass transfer rate constant is very sensitive to the particle-liquid contact fraction. The three curves in Figure 5.11 are related to three different contact fractions. The mass transfer rate constants determined from the

experimental data (Refer to Table 5.5 and Figure 5.9) are superimposed in Figure 5.11. As given in Table 5.5, high powder feed rates were usually accompanied by high gas flow rates. To simulate this situation, high gas flow rates are used in the calculations for the cases of high powder feed rates. As a result, in Figure 5.11, the calculated mass transfer constants do not change with the powder feed rates linearly. It can be seen that most of the points fall to the region between two curves of the particle-liquid contact fraction equal to 0.3 and 0.5.

The melt temperature measured during injection was analyzed by applying calorimetric principles. The particle-liquid contact fraction was also found to be in the range of 0.3 to 0.5 (See Figure 5.5). Thus, the results obtained from the mass transfer model approximately coincide with those from the heat transfer model.

5.3.3 The effect of the Oxygen Activity on the Incubation Time

As described in Section 4.2.1, the incubation time, τ_i, for powder injection depends on powder feed rate, silicon content and aluminum content. From multiple linear regression:

$$\tau_i = (45.3 \pm 5.2) - (0.0143 \pm 0.00168) W_p - (18.6 \pm 4.2)[\%Si] - (47.5 \pm 62.1)[\%Al] \quad (4.7)$$

$$(R^2 = 0.64)$$

TABLE 5.6

ESTIMATION OF THE MASS TRANSFER RATE CONSTANT

Quantity	Symbol	Unit	Value
Melt temperature	T_l	°C	1350
Gas Flow Rate	Q	SLPM	5-10
Melt Viscosity	μ	kg/m/s	7.6×10^{-3}
Bubble Drag Coefficient	C_D	/	0.44
Dissipation Rate Constant	C_μ	/	0.09
Constant	C	/	0.537
	K_1	$m^{1/3}$	0.18
	K'	$s^{-1/2}$	5.41×10^{3}
Bath Depth	L	m	0.2
Gas Fraction in Plume	α	/	0.1-0.5
Diameter of Crucible	D_c	m	0.23
Turbulent Kinematic Viscosity	ν_t	m^2/s	3×10^{-4}
Fraction of Lance Submergence	β	/	0.5
Mean Plume Velocity	U_p	m/s	0.24-0.29
Particle Residence Time	τ	s	0.7-0.85
Particle Contact Fraction	f	/	0.3,0.5,1.0
Powder Feed Rate	W_p	kg/s	0.003-0.01
Particle Diameter	d	m	1.2×10^{-5}
Particle Surface Area	A	m^2	0.28
Solid Density	ρ_s	kg/m^3	2200
Particle Velocity	v_p	m/s	5×10^{-5}
Particle Schmidt Number	Sc	/	1000
Particle Reynolds Number	Re	/	5.5×10^{-4}
Particle Sherwood Number	Sh	/	2.14
Sulphur Diffusivity	D_s	m^2/s	10^{-9}
Mass Transfer Coefficient	k_m	m/s	1.79×10^{-4}
Mass Transfer Rate Constant	K_m	1/s	0.004-0.03

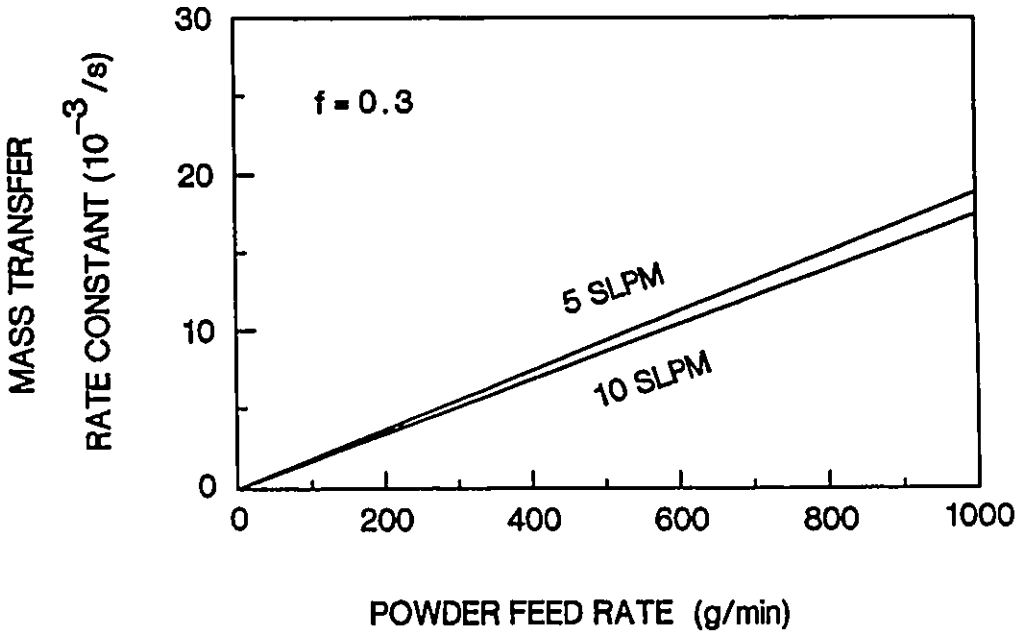

Figure 5.10 The mass transfer rate constants are calculated for two specific gas flow rates and plotted as a function of powder rates. The solid-liquid contact fraction is assumed to be 0.3.

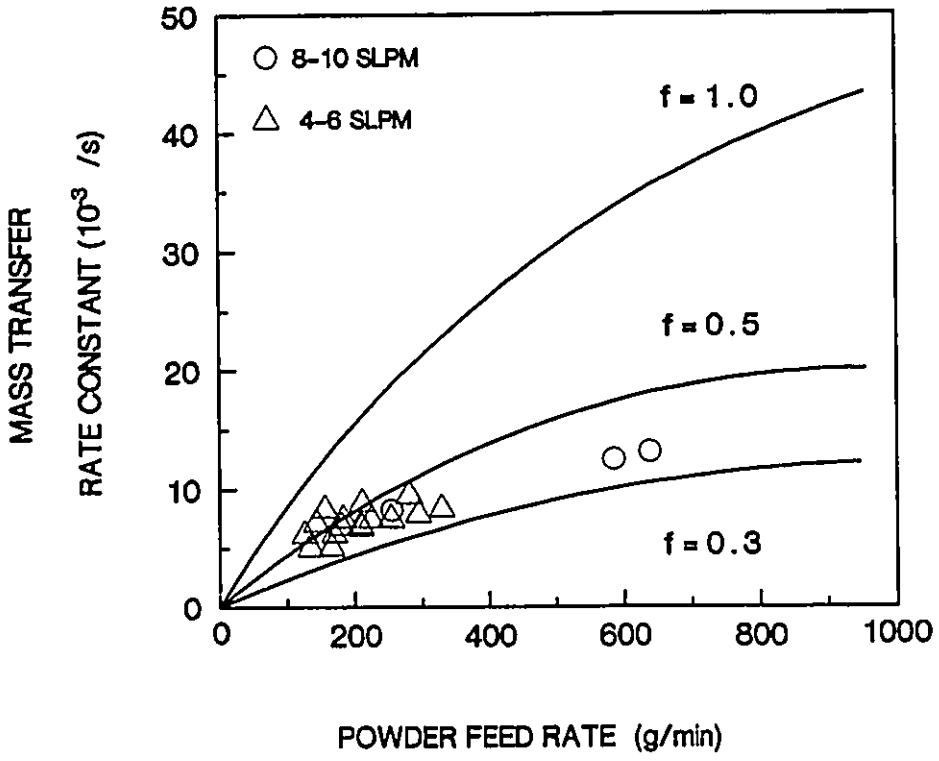

Figure 5.11 The experimental determined mass transfer rate constants are plotted as a function of powder rates. The estimated results are shown in lines (The data used in the calculations are given in Table 5.6). It can be seen that most of the experimental points fall between the two lines of the particle-liquid contact fractions equal to 0.3 to 0.5.

As mentioned in Section 4.1.1, the oxygen activity in the melt was directly related to the silicon content or the aluminum content. Thus, the incubation time can be considered as a function of the melt oxygen activity.

Chiang et al. reported that the incubations during injections with calcium carbide are associated with slag composition [1]. The incubation periods were observed when no slag and dry slag was initially present on the iron surface. They explained that in the case of no slag injections, a liquid layer of FeO was formed when the melt was initially uncovered, the calcium sulphide product resulting from the plume reaction was fluxed by FeO. This highly oxidizing slag was not able to hold sulphur, thus, sulphur reverted from the slag to the melt, resulting in an incubation period. A similar situation is thought to exist for dry slag (a solid mixture of calcium oxide and silica). The liquid slag had sufficiently high sulphide capacity and immediately dissolved the calcium sulphide reaction products. Thus, no incubation was observed for liquid slag.

In the following text, a kinetic model will be presented to describe the role of the oxygen activity on the incubation time. This model is based on the following assumptions:

(a) There are two reaction sites: the particle-melt interface in the plume (a so-called plume reactor) and the slag-melt interface (a so-called top slag reactor).

(b) "local equilibrium" occurs at these two reaction sites.

(c) The reaction rates are controlled by diffusion of oxygen and sulphur through the liquid layers near the melt-particle interface and near the melt surface.

(d) The mass transfer rate constants of sulphur and oxygen are equal.

(e) During the incubation periods, compared with the melt concentrations, the equilibrium sulphur and oxygen contents at the melt-particle interface are negligible.

(f) No oxygen infiltrates the melt from the atmosphere or refractory.

Therefore, the rates of desulphurization and deoxidation reactions can be described as

$$\frac{dC_S}{dt} = -k_p C_S - k_t (C_S - C_S^i) \tag{5.104}$$

$$\frac{dC_O}{dt} = -k_p C_O - k_t (C_O - C_O^i) \tag{5.105}$$

where k_t and k_p are the mass transfer rate constants for the top slag reaction and the plume reaction respectively. The schematic concentration profiles of sulphur and oxygen near the melt surface are given in Figure 5.12. C_S and C_O are the melt concentrations of sulphur and oxygen; C_S^i and C_O^i are the melt-slag interfacial concentrations of sulphur and oxygen in equilibrium with the slag. It must be noted that before powder injection the melt surface was initially uncovered, thus a liquid layer of FeO could form on the iron surface. During powder injection, the particles of calcium carbide, calcium oxide and the sulphide products reached the bath surface. At the initial stage of injection, calcium carbide quickly converted into calcium oxide due to the presence of FeO on the surface. The desulphurization capacity of such top slag may be estimated from

$$CaS+\underline{O}=CaO+\underline{S} \qquad (5.106)$$

The stoichiometry leads to

$$(C_S^i-C_S)+(C_O^i-C_O)=0 \qquad (5.107)$$

Reversion of sulphur from slag to the melt during the incubation period indicates

$$C_S^i>C_S \qquad (5.108)$$

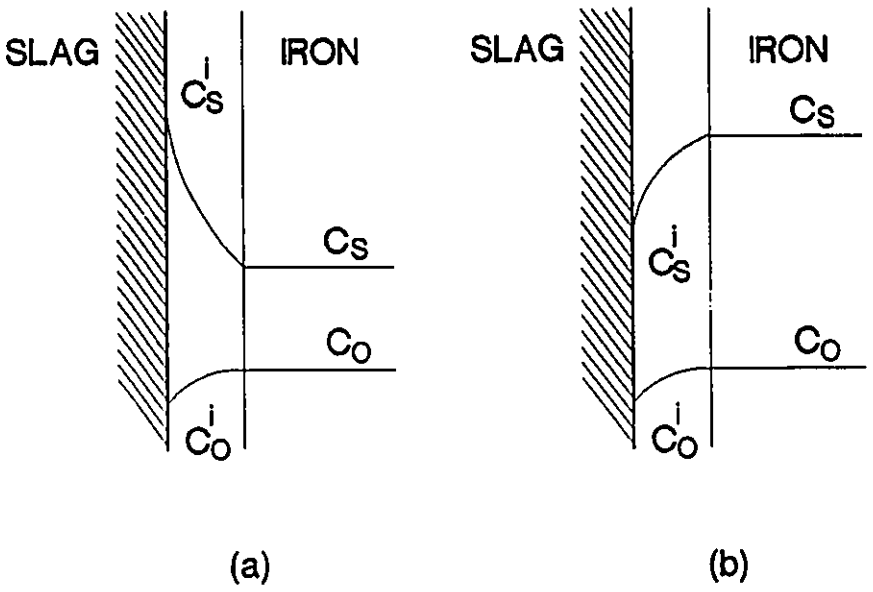

Figure 5.12 Schematic representations of the concentrations of sulphur and oxygen near slag/liquid interface. (a) Sulphur reverts from slag to the melt, resulting in an incubation period. (b) Slag desulphurization takes place after the incubation period.

Combining Equations (5.107) and (5.108) yields

$$C_O^i < C_O \tag{5.109}$$

Substituting Equation (5.109) into Equation (5.105), one has

$$\frac{dC_O}{dt} < 0 \tag{5.110}$$

Equation (5.110) indicates that deoxidation exists during an incubation period. This analysis gives an explanation for the experimental observations that the incubation times coincide with periods of deoxidation, before desulphurization proceeds (Refer to Section 4.2.2). The equilibrium constant of reaction (5.106) is

$$K_{eq} = \frac{a_{CaS} a_O}{a_{CaO} a_S} \tag{5.111}$$

The sulphur concentration at the melt-slag interface can be described by:

$$C_S^i = \frac{16}{32} \frac{f_O}{f_S} \left(\frac{a_{CaS}}{a_{CaO}} \right) \frac{C_O^i}{K_{eq}} \tag{5.112}$$

This equation can be used to explain the experimental observations. Before powder injection, the melt surface was initially oxidized by exposure to air. Thereby, a small amount of oxidized iron and silicon was likely present on the iron surface. The melt with a low silicon content or low aluminum content

had a high oxygen activity, resulting in a high oxygen concentration on the melt surface. Consequently, according to Equation (5.112), the sulphur concentration on the melt surface was high. As a result, the second term on the right hand side of Equation (5.104) is positive. Thus, sulphur reversion took place. The sulphur reversion counteracted desulphurization in the plume (which is represented by the first term on the right side hand of Equation (5.104)). Thus, the melt sulphur level did not decrease significantly. As more powder was injected, the unreacted calcium carbide and calcium oxide accumulated in the slag, lowering its oxygen potential and increasing its volume and basicity. The sulphur concentration at the melt-slag interface decreased continuously. Finally, reversion ceased, ending the incubation period. A higher oxygen activity in the melt means a higher oxygen potential at the melt-slag interface. As a consequence, more calcium carbide or calcium oxide is needed to modify the slag. Thus, longer injection time or greater powder feed rate is required to end the incubation period. This explains why the incubation times change with the powder feed rates and the oxygen activities as seen in Figure 4.22.

5.3.4 The Effect of Oxygen on the Reaction Trajectory

In Section 4.2.2, a diagram of log h_s-log h_o was used to describe the trajectories of refining. It was found that the trajectories were strongly affected by the initial oxygen activities. The role of the oxygen activities in the reaction paths will be examined on the basis of the kinetic model described in Section 5.3.1.

Before using the kinetic model to simulate the injection process, the impact of two assumptions employed to develop the kinetic model will be assessed and discussed.

(1) The Diffusivities of Sulphur and Oxygen in Liquid Iron

In the kinetic model, it was assumed that the mass transfer coefficients of sulphur and oxygen were equal. Based on this assumption, the reaction paths with pure calcium carbide and pure calcium oxide are determined from the kinetic model, as illustrated in Figure 5.13. The reaction path, labelled A-C, represents the trajectory with calcium carbide. The starting point is A (corresponding to the initial sulphur content 0.05 percent and oxygen activity 0.0001). One can see that the desulphurization path of calcium carbide is initially parallel to the CaO-CaS equilibrium line, and finally approaches point C which is the limit of desulphurization and deoxidation with calcium carbide. The reaction path, labelled A-B, represents the trajectory with calcium oxide. In this case, the oxygen activity has a constant value of 10^{-4} because the oxygen is controlled by the silicon or aluminum content added in the melt. The oxygen released from lime desulphurization is removed by silicon or aluminum. Therefore, the melt oxygen appears to be unchanged. As a result, A-B is a vertical line, and point B is the limit of desulphurization with calcium oxide. Obviously, the reaction path will deviate from curve AC if the mass transfer coefficients of sulphur and oxygen have different values. For the injection with calcium carbide, the rate of desulphurization and deoxidation are given by:

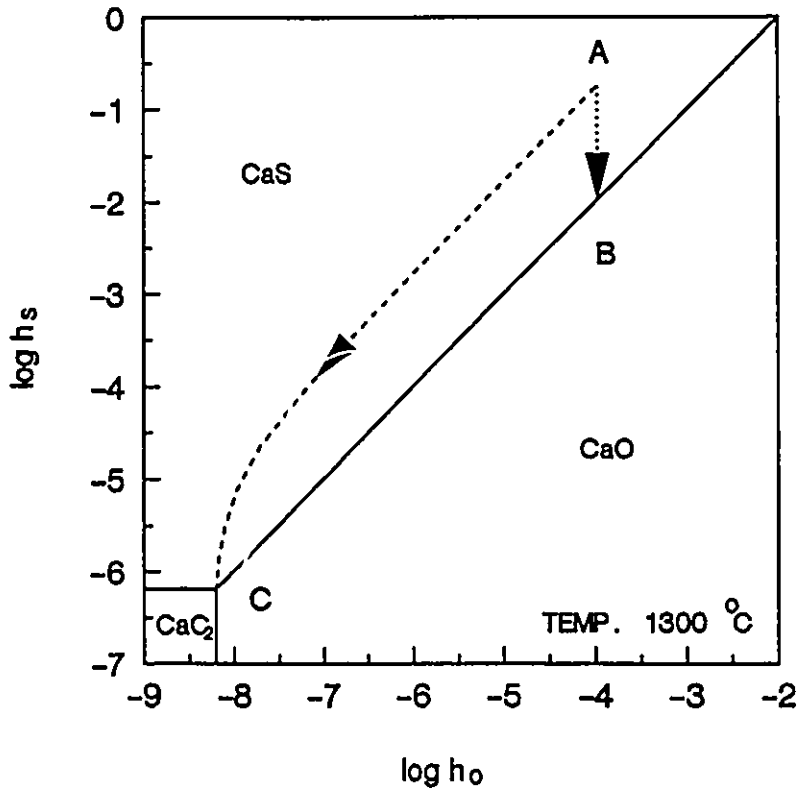

Figure 5.13 Phase stability diagram for calcium compounds at 1300°C as a function of Henrian activities in molten iron. The reaction paths for calcium carbide, A to C, and for calcium oxide, A to B, are determined from the kinetic model.

$$\frac{dC_s}{dt} = -\frac{k_s A}{V}(C_s - C_{s,1}^*) \tag{5.113}$$

$$\frac{dC_O}{dt} = -\frac{k_o A}{V}(C_o - C_{o,1}^*) \tag{5.114}$$

where k_s and k_o are the mass transfer coefficients of sulphur and oxygen (m/s), A is the area of the particles in contact with liquid (m^2), V is the melt volume (m^3). $C_{S,1}^*$ and $C_{O,1}^*$ have been shown in Figure 5.6.

Integrating Equations (5.113) and (5.114) yields

$$\frac{d\log(C_s - C_{s,1}^*)}{d\log(C_o - C_{o,1}^*)} \propto \frac{k_s}{k_o} \tag{5.115}$$

At the initial stage of desulphurization, $C_{O,1}^* << C_O$, $C_{S,1}^* << C_S$. Thus,

$$\frac{d\ \log C_S}{d\ \log C_O} \propto \frac{k_S}{k_O} \tag{5.116}$$

As demonstrated in Section 5.3.2, the particle Sherwood number is almost a constant. Substituting Equation (5.94) into Equation (116) and converting concentrations to activities lead to

$$\frac{d\ \log h_S}{d\ \log h_O} \propto \frac{D_S}{D_O} \qquad (5.117)$$

This indicates that the slope of the reaction path in a log h_o-log h_s diagram depends on the ratio of the sulphur and oxygen diffusivities.

Unfortunately, the diffusivities of oxygen and sulphur in liquid iron are not well established, since the experimental errors are very large as a result of experimental difficulties [115]. McCarron and Belton obtained the diffusivity for sulphur in liquid iron of $1.7\ (\pm 0.2)\times 10^{-8}\ m^2/s$ at 1560°C [116]. Novokhatskiy and Ershorv obtained the diffusivity for oxygen in liquid iron of $1.22\times 10^{-8}\ m^2/s$ at 1550°C [117]. Kawakami and Goto obtained the diffusivity for oxygen in liquid iron of $1.9\times 10^{-8}\ m^2/s$ at 1550°C [118]. It can be seen from these studies that the diffusivities of oxygen and sulphur in liquid iron are approximately in the same order of magnitude. This justifies the simplification employed in this work that the diffusivities of sulphur and oxygen are equal.

(2) The Sizes of CaO and CaC_2 Particles

Equation (5.89) indicates that the mass transfer rate constant is proportional to the mass transfer area. It was assumed in Section 5.3.2 that the mass transfer rate constants for the particles of calcium carbide and calcium oxide, K_1 and K_2, were proportional to their percentages in the solid mixture:

$$K_1 = f_1 K_m \qquad (5.90)$$
$$K_2 = f_2 K_m$$

This equation can be employed only if the lime and calcium carbide particles have same sizes. The surface area is proportional to the square of the particle diameter. Thus, the mass transfer rate constants strongly depend on the particle sizes. Figure 5.14 is an example showing the effect of the particle size on the reaction path. The conditions for the model calculations are given in Table 5.7. Three cases are shown in Figure 5.14.

All three curves start from the point A. It is assumed that the particle sizes of calcium carbide are same (12 μm) for all cases. Only the sizes of calcium oxide particles are different from case to case. The mass transfer rate constants can be estimated for different particle sizes in the way as described in Section 5.3.2. Case 1 is taken as a standard for comparison. The particle diameter is assumed to be 12 μm, (which is the surface area mean diameter of the powder used in the present experiments). The powder feed rate is 0.3 kg/min. The mass transfer rate constant of CaC_2 is about 0.005 1/s, and the mass transfer rate constant of CaO is about 0.002 1/s (Refer to Table 5.6 and Figure 5.10). The particle size of CaO in Case 2 is assumed to be 24 μm, twice of the particle size in Case 1. So, the surface area of each CaO particle in Case 2 increases by four times, but the number of particles decreases by four times. Consequently, the mass transfer rate constant of CaO in Case 2 decreases to 0.0005 1/s. The reaction path moves

upwards as compared with Case 1. The particle size of CaO in Case 3 is assumed as 6 μm, a half of the particle size in Case 1. Thus, the surface area of CaO particles in Case 3 is four times larger than in case 1. Consequently, the mass transfer rate constant of CaO in Case 3 increases to 0.008 1/s. The reaction path moves downwards as compared with that of Case 1, and then almost follows the equilibrium of CaO-CaS to approach the point C. From this example, it can be seen that the particle size has a very important effect on the process of desulphurization by calcium carbide. Unfortunately, for a mixture of calcium carbide and calcium oxide, it is very difficult to determine the particle size distributions separately.

The mass transfer rate constants may be also affected by the particle-liquid wetting properties. No information is available about the wetting characteristics of calcium oxide and calcium carbide.

TABLE 5.7

THE CONDITIONS USED IN THE MODEL CALCULATIONS

Melt Initial Conditions		Powder Feed Rate 0.3 kg/min	
[C] 4.2%	[S] 0.05%	CaC_2 Particle Size	12×10^{-6} m
[Si] 1.0%	h_O 0.0001	CaO Particle Size	See Fig. 5.14
Temp. 1300°C		Powder Comps. (CaC_2/CaO)	72/28

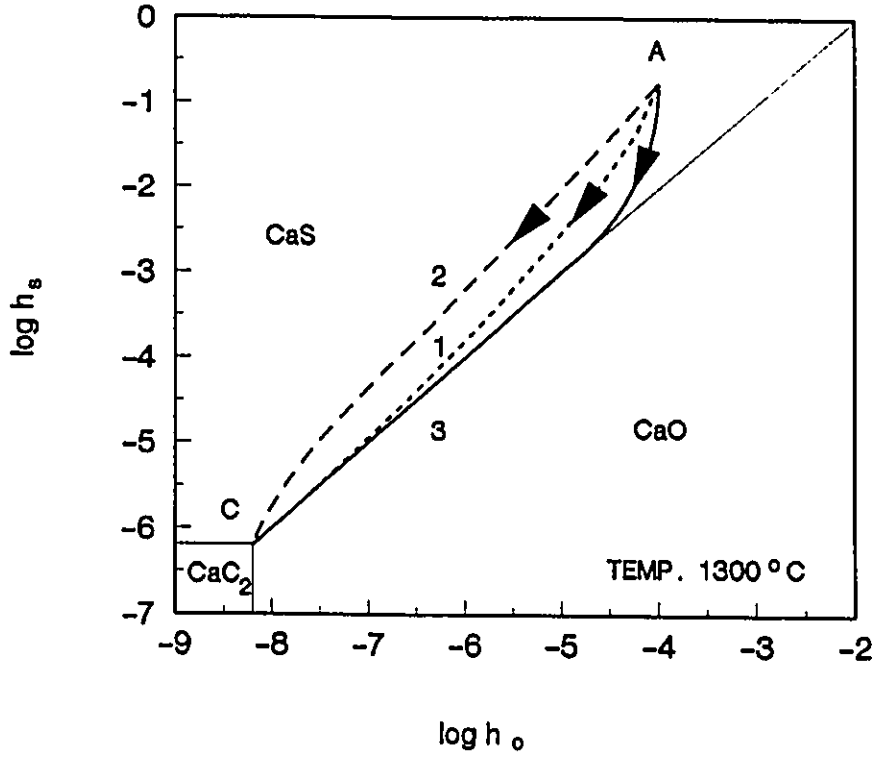

Mass Transfer Rate Constant of CaC_2 $0.005\ s^{-1}$

Diameter of CaC_2 Particles 12×10^{-6} m

Case No.	Diameter of CaO Particles	Mass Transfer Rate Constant of CaO
1	12×10^{-6} m	$0.002\ s^{-1}$
2	24×10^{-6} m	$0.0005\ s^{-1}$
3	5×10^{-6} m	$0.008\ s^{-1}$

Figure 5.14 The reaction paths for calcium carbide and calcium oxide mixtures are determined from the kinetic model (Refer to Table 5.7). The area-average diameters of lime particles for Case 2/Case 1/Case 3 are assumed as 24/12/6 μm. The corresponding mass transfer rate constants are also listed.

From the above discussion, it can be seen that the assumptions about diffusivities of sulphur and oxygen, and the particle sizes have very important effects on the model simulations. But, so far, the answers to these two problems are not very clear. Therefore, in the following analysis, the two assumptions will still be used. That is, the mass transfer coefficients of sulphur and oxygen are equal, and the mass transfer rate constants of CaC_2 and CaO are proportional to their percentages in the mixture.

The role of the oxygen activity in the reaction trajectories will be discussed on the basis of the model simulations. The paths are determined by three steps:

(a) Find the time dependence of oxygen and sulphur contents from the model for a given initial oxygen activity.

(b) Convert the oxygen and sulphur contents calculated from the kinetic model to activities.

(c) Show the reaction path in a log h_O-log h_S diagram.

For the mixture of calcium carbide and calcium oxide, the present model demonstrates that the reaction path depends on the starting oxygen activity of the melt. Three refining processes with different initial oxygen activities are simulated, as illustrated in Figure 5.15. (As given in Table 5.8, the conditions used for the model simulations are as same as given in Table 5.7, except the initial

TABLE 5.8

DATA FOR MODEL CALCULATIONS

Description		Case No.		
		1	2	3
Objective Sulphur Content		<0.01		
Initial Hot Metal Composition	[%C]	4.2		
	[%Si]	0-2.0		
	[%Al]	0-0.2		
	[%S]	0.005		
	h_o	0.00001-0.005	0.00001-0.001	0.00001-0.001
Powder	Rate (g/min)	200	200	0-1000
	CaC_2/CaO	72/28	0/100-100/0	72/28
Mass Transfer Rate Constant $K \times 10^3$ (s^{-1})		7	7	0-14

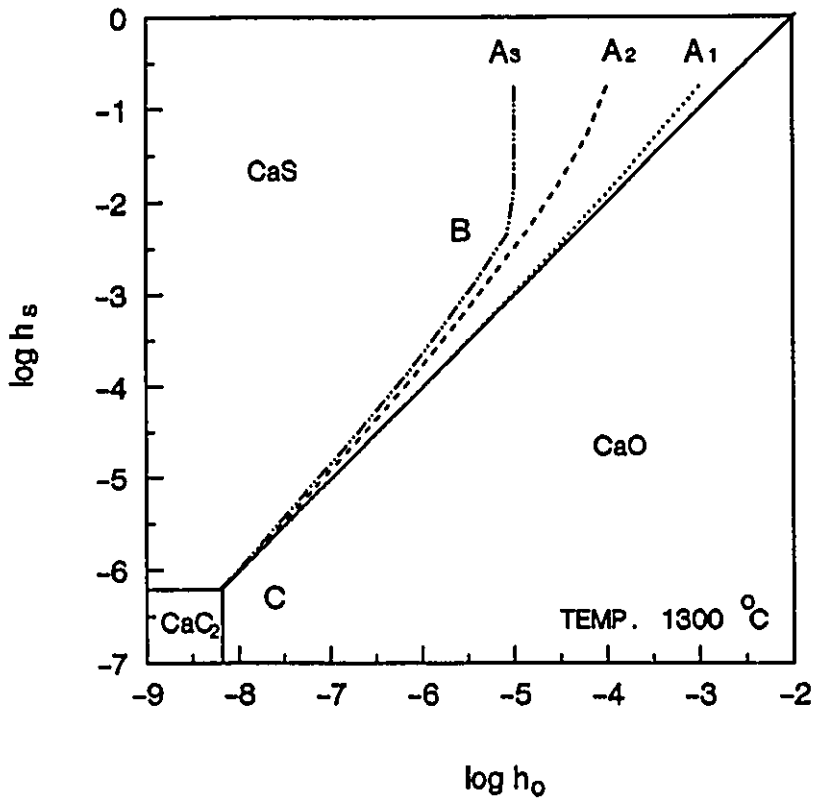

Figure 5.15 Phase stability diagram for calcium compounds at 1300°C as a function of Henrian activities in molten iron. The reaction paths for calcium carbide and oxide mixture at three different starting oxygen activities are determined from the kinetic model. The calculation conditions are given in Table 5.8.

oxygen activity). At a high initial oxygen activity (h_O=0.001), starting from point A_1, the trajectory is approximately parallel to the CaO-CaS equilibrium line. At a medium initial oxygen activity (h_O=0.0001), starting from point A_2, the trajectory is more vertical. At a very low initial oxygen (h_o=0.00001), which is generally achieved by high aluminum addition, starting from point A_3, the initial path A-B is vertical, indicating that the melt oxygen is still controlled by aluminum content. After point B, the reaction trajectory turns to point C because the oxygen released by lime desulphurization is less than that removed by calcium carbide. This is consistent with the experimental observations that the actual trajectories of the refining become more vertical as the starting oxygen is decreased (See Figure 4.24).

Figure 5.16 is an example which compares the trajectory determined from the kinetic model with that obtained from the experimental data. The corresponding variations of the sulphur content and the oxygen activity have been given in Figure 5.7. It can be seen that the present model predicts the reaction path very well. More reaction paths are shown in Figure 5.17-5.21. The solid lines represent the actual injection test, as labelled by the number. The dash lines are calculated by the kinetic model. The corresponding experimental conditions are used as the original data for the model calculations. These curves successfully reproduce the characteristics of the experimental results. It can be seen that as the oxygen activity is decreased, the reaction paths become more vertical. It must be pointed again that the present kinetic model is applicable only after the incubation periods. The horizontal lines in the figures, which are

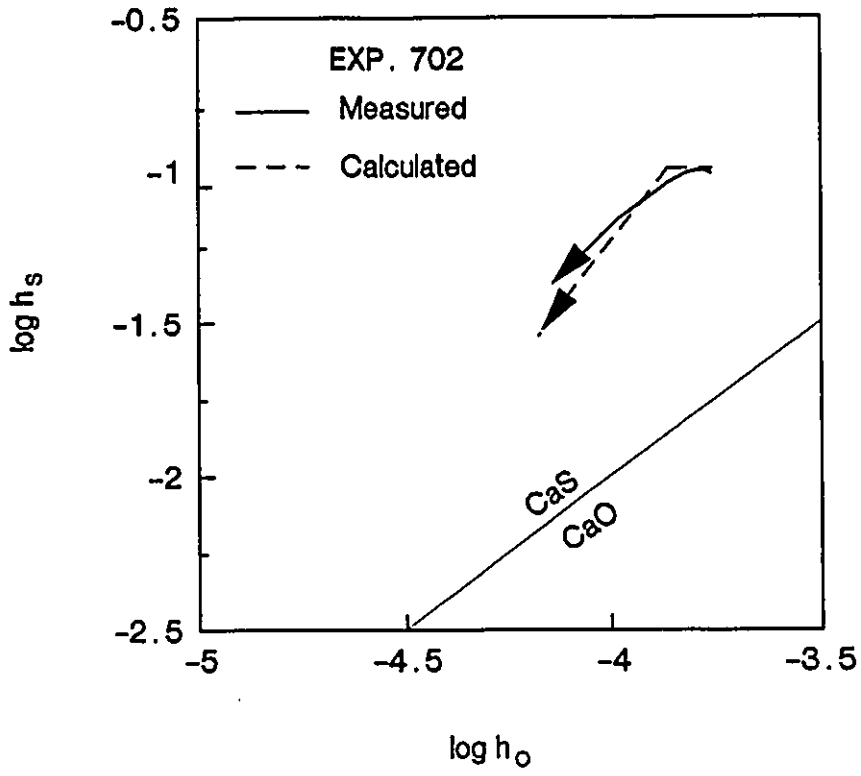

Figure 5.16 An example in which the reaction path during a calcium carbide injection test is compared with that determined from the present model. The equilibrium between CaO and CaS is also shown. The reaction path is nearly parallel to the CaO-CaS equilibrium line.

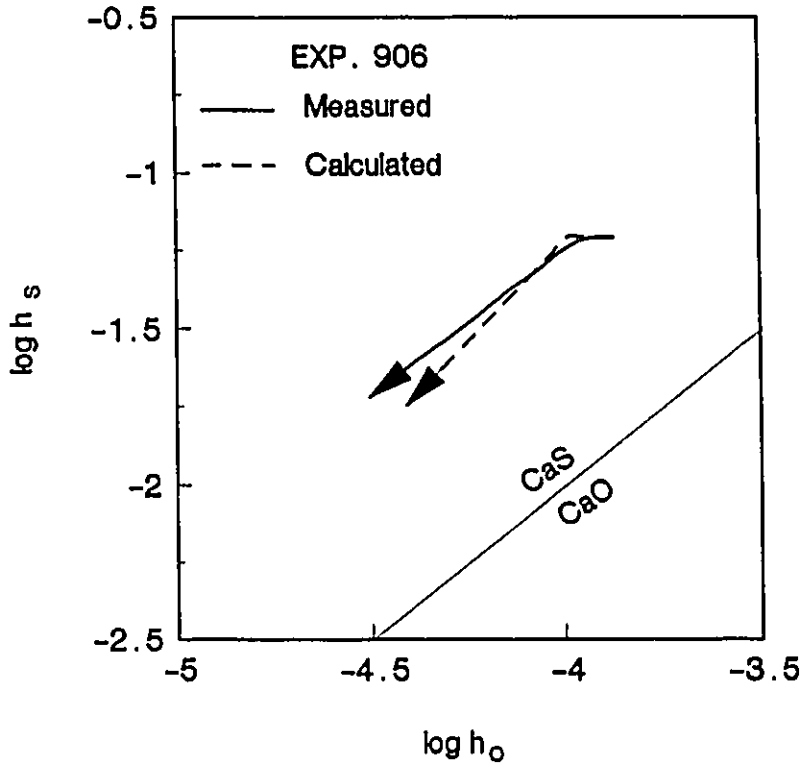

Figure 5.17 An example in which the reaction path during a calcium carbide injection test is compared with that determined from the present model. The equilibrium between CaO and CaS is also shown. The reaction path is nearly parallel to the CaO-CaS equilibrium line.

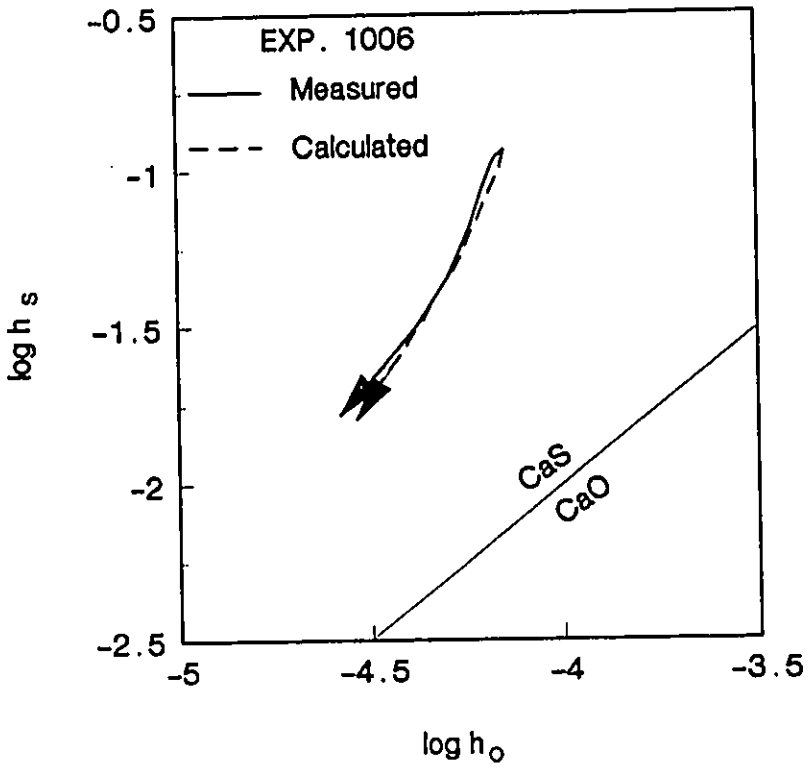

Figure 5.18 An example in which the reaction path during a calcium carbide injection test is compared with that determined from the present model. The equilibrium between CaO and CaS is also shown. The reaction path is more vertical as compared with the CaO-CaS equilibrium line.

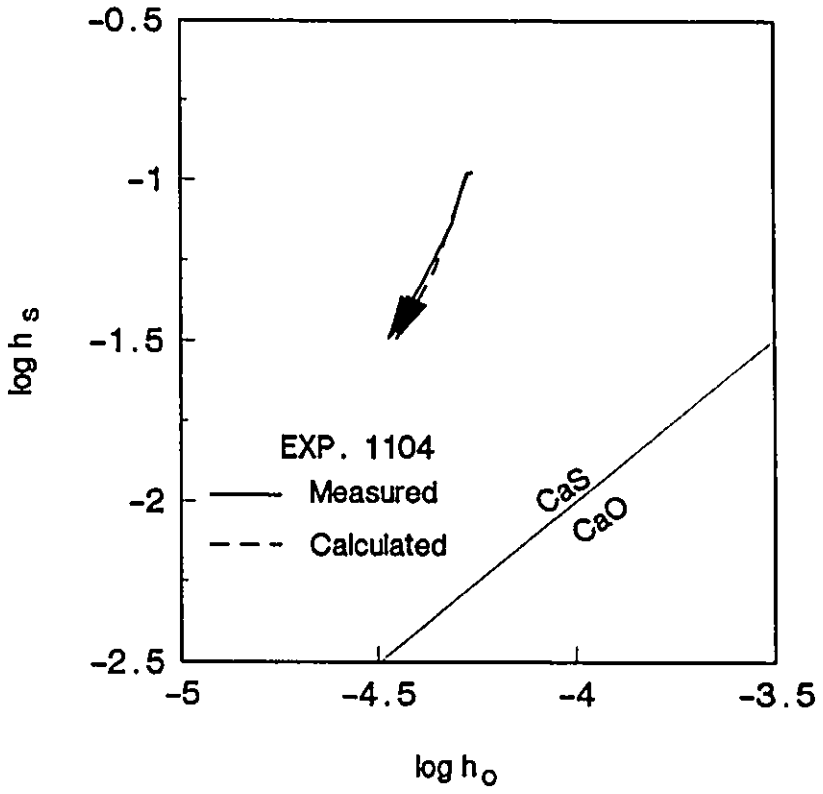

Figure 5.19 An example in which the reaction path during a calcium carbide injection test is compared with that determined from the present model. The equilibrium between CaO and CaS is also shown. The reaction path is more vertical as compared with the CaO-CaS equilibrium line.

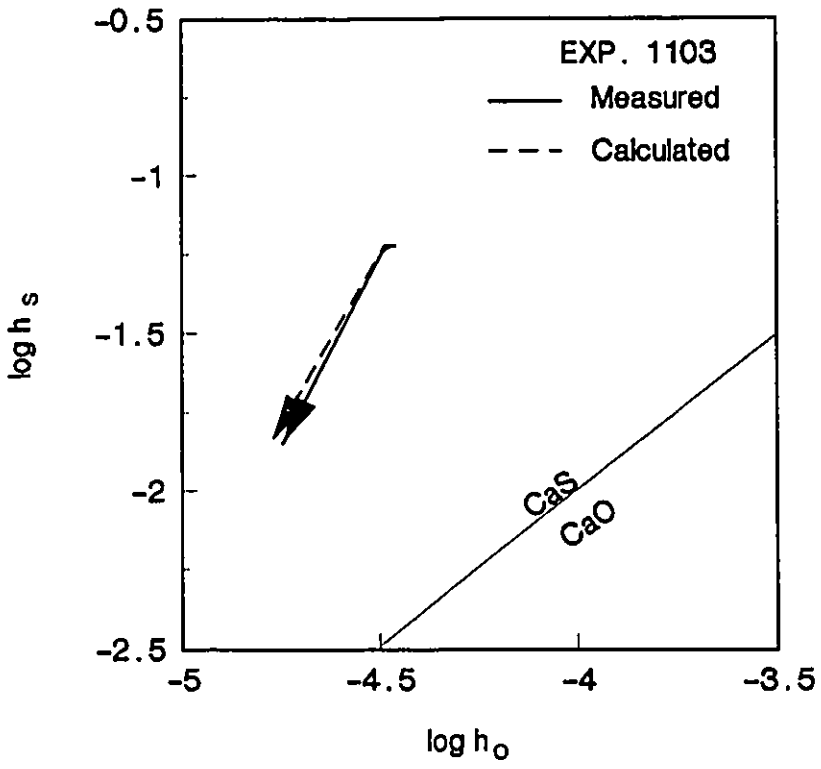

Figure 5.20 An example in which the reaction path during a calcium carbide injection test is compared with tnat determined from the present model. The equilibrium between CaO and CaS is also shown. The reaction path is more vertical as compared with the CaO-CaS equilibrium line.

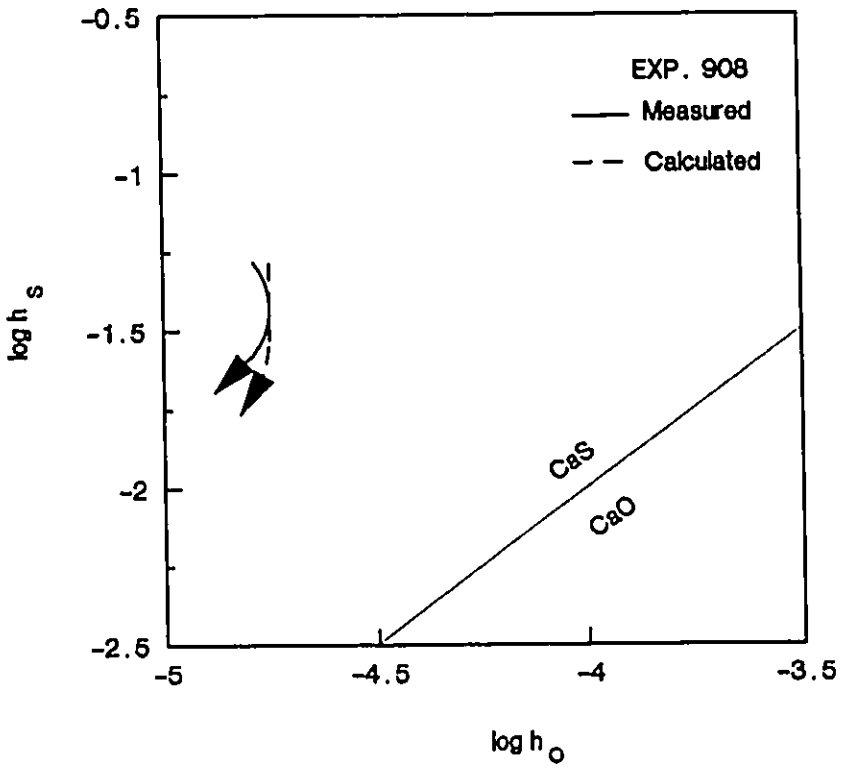

Figure 5.21 An example in which the reaction path during a calcium carbide injection test is compared with that determined from the present model. The equilibrium between CaO and CaS is also shown. The reaction path is nearly vertical as compared with the CaO-CaS equilibrium line.

related to the incubation periods, are simply drawn from the starting points. They are not calculated from the kinetic model. The incubation phenomena have been discussed in Section 5.3.3.

5.3.5 The Effect of Oxygen Activity on the Rate of Desulphurization Reaction

The experimental results have shown that the rate of desulphurization depends on the oxygen activity in the melts (Refer to Section 4.2.1). In this section, the kinetic model will be used to study the effect of the oxygen activity on the desulphurization rate. The procedures are as follows:

- Use the kinetic model to calculate the variation of sulphur with time.

- Fit the calculated sulphur-time relation to Equation (4.5) to get the first order rate constant.

- Compare the model calculations with the experimental results to achieve better understanding the role of oxygen activity.

Three cases will be discussed in the following text:

(a) Different starting oxygen activities with a fixed powder feed rate and a fixed CaC_2/CaO proportion.

(b) Different starting oxygen activities and CaC_2/CaO proportions with a fixed powder feed rate.

(c) Different starting oxygen activities and powder feed rates with a fixed CaC_2/CaO proportion.

All the data used in the model calculations are given in Table 5.8. According to the model calculations, the first order rate constant of desulphurization is a function of the starting oxygen activity. Figure 5.22 shows an example, where the powder feed rate is given as 0.2 kg/min, and the proportion of CaC_2/CaO is 72/28. When the starting oxygen activity decreases from 0.003 to 0.0001, the desulphurization rate constant increases by 40 per cent. However, with further decreases in oxygen activity, the rate constant increases very little. In the present example, the optimum initial oxygen activity should be around 0.0001. No significant improvements on the desulphurization rates can be expected by further deoxidation. For the steelmaking industry, the optimum starting oxygen activity can be determined by the present model to achieve fast desulphurization rate with less deoxidant.

Figure 5.23 shows the dependence of the rate constant on the CaC_2/CaO proportion in the powder. The three curves in Figure 5.23 correspond to three different starting oxygen activities. Generally, the desulphurization rate decreases as the lime fraction increases. Moreover, the rate constant is strongly affected by the starting oxygen activity. At a high starting oxygen activity

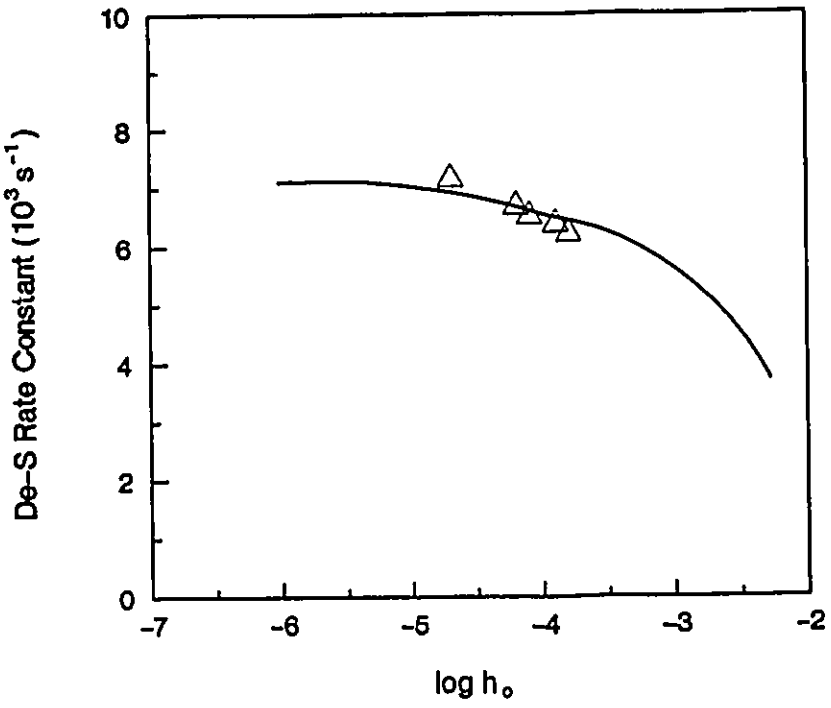

Figure 5.22 The first order desulphurization rate constant as a function of the starting oxygen activity is determined from this model at 200 g/min of powder injection rate. The points show the experimental results (Refer to Table 5.9).

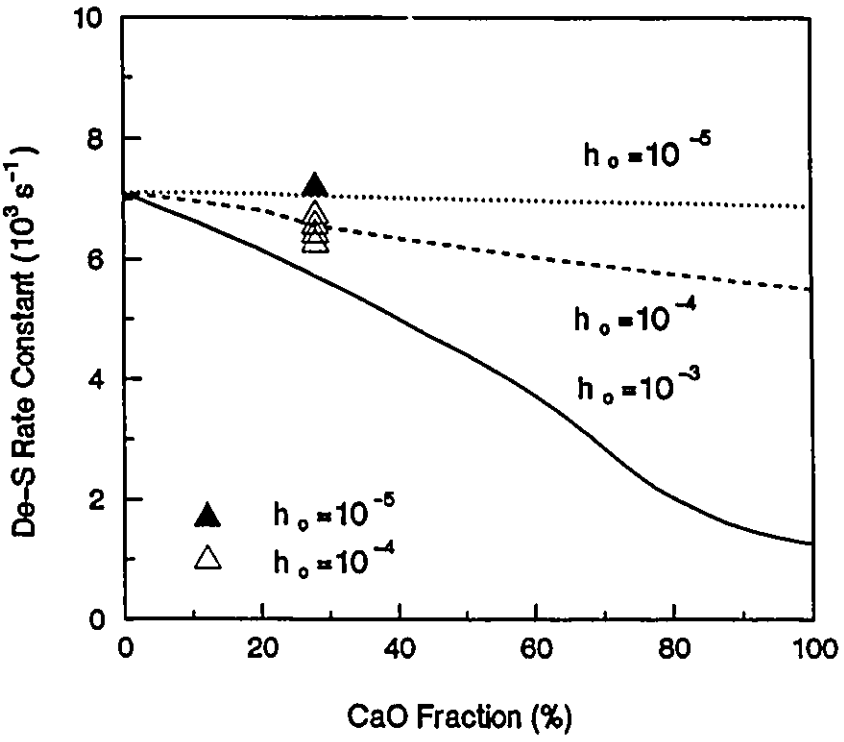

Figure 5.23 The dependence of the first order desulphurization rate constant on the starting oxygen activity and calcium carbide/oxide proportion is determined from this model at 200 g/min of powder injection rate. The points show the experimental results (Refer to Table 5.9).

TABLE 5.9

THE DESULPHURIZATION RATE CONSTANT

DETERMINED FROM EXPERIMENTAL RESULTS

Run No.	Powder Feed Rate	Gas Flow Rate	log h_o	De-S Rate constant K_s
	g/min	SLPM	/	10^3 l/s
6-002	209	5	-3.9	6.4
6-006	182	5	-4.2	6.7
9-004	180	5	-4.1	6.5
9-006	180	5	-3.8	6.2
10-008	182	6	-4.7	7.2

(h_o>0.001), the melt can not be desulphurized below 0.01 by using lime as desulphurizer alone. The desulphurization rate increases quickly as more calcium carbide is added into the powder. At a low starting oxygen activity (h_o=0.0001), the rate constant is not very sensitive to the change of the CaC_2/CaO proportion. As the CaO fraction increases from 0 to 30 percent, the rate constant decreases less than 10 percent. At an extremely low starting oxygen activity (h_o<0.00001), the change of the CaC_2/CaO proportion has a little effect on the desulphurization rate constant. The present model can be used to optimize particular plants. It is known that commercial calcium carbide is produced from the reaction

$$CaO(s)+2C(s)=CaC_2(s) \qquad (5.118)$$

Commercial calcium carbide always contains unreacted lime from the production process. The production cost is directly related to the percentage of calcium carbide in the mixture. In order to reduce the reagent cost, obviously, a mixture with more lime and less calcium carbide is desired. Thus, the starting oxygen activity should be reduced to a low level. In steel industry, the common oxygen activities of hot metal are around 0.0001. According to the model calculations, a mixture of 30 per cent lime can be employed without causing significant delay of desulphurization.

As shown in Figure 4.21, the desulphurization rate constant increases with increasing silicon content. It has been pointed out that the oxygen activity in hot metal is controlled by its silicon content. Therefore, it is reasonable to say that

the rate of calcium carbide desulphurization increases with decreasing oxygen activity. In the experiments, high desulphurization rates were observed when the melts were pre-deoxidized with aluminum, or when the melts contained more than 0.5 per cent of silicon. However, when silicon contents were more than 1.5 per cent, the desulphurization rate constants of calcium carbide did not increase significantly. In order to simulate the results of the experiments, three starting oxygen activities are selected in the model calculations. The mass transfer rate constants used for the model calculations are determined from Equation (5.92). The results of the model simulations are illustrated in Figure 5.24, where the broken line represents the runs with $CaCO_3/CaC_2$ (which will be discussed in Section 5.3.6); the other three represent the runs with low-, medium-, and high-oxygen activity, respectively. The value of low oxygen activity is taken as 0.00001. The corresponding equilibrium aluminum content is 0.001 per cent. The value of medium oxygen activity is taken as 0.0001. The corresponding equilibrium silicon content is 1.0 per cent. The value of high oxygen activity is taken as 0.001. The corresponding equilibrium silicon content is less than 0.1 per cent. One can see that high oxygen corresponds to a low desulphurization rate. Lowering the starting oxygen from 0.001 to 0.0001 can increase the desulphurization rate. But, no significant change can be expected by further deoxidation. Compared with Figure 4.21, it may be seen that Figure 5.24 a good simulation for the experimental results. One may have noticed the difference between Figure 5.24 and Figure 4.21 (The latter does not show directly the dependence of the desulphurization rate constants on the oxygen activity). Because the experimental temperature was varied in the range of 1350±50°C, and

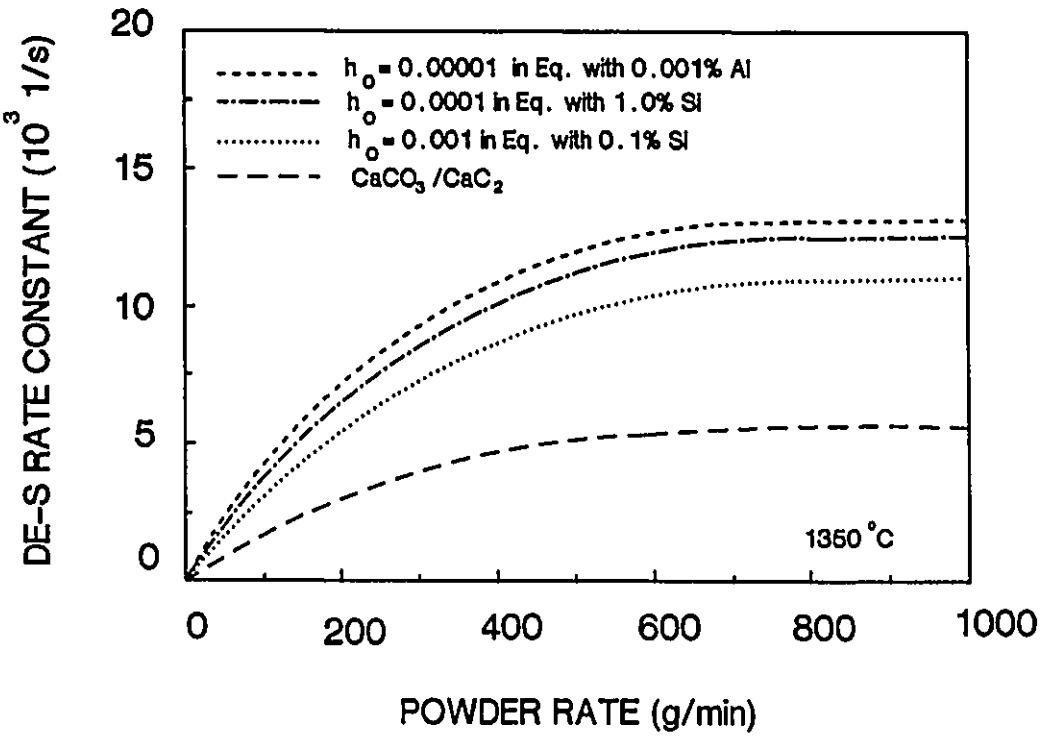

Figure 5.24 The first order desulphurization rate constant as a function of powder injection rate is calculated from this model for various conditions. One can see that this model simulation successfully reproduces the characteristics of Figure 4.21.

the silicon-silica equilibrium was more significantly affected by the temperature, the rate constants for desulphurization appeared to depend on the silicon content more clearly. Even so, one can see that Figure 5.24 is a reasonable explanation for the experimental results.

5.3.6 The Effect of Carbon Dioxide or Limestone on the Kinetics of Hot Metal Desulphurization

As has been said in Chapter 4, in some experiments, carbon dioxide was used as carrier gas or limestone was injected with calcium carbide. The oxygen activity did not drop below the silicon equilibrium, and the rate of desulphurization was relatively low (See Figure 4.21 and Table 4.7). These experiments fall into the category of Case 3 (see Section 5.3.1). A kinetic analysis will be presented in this section.

At hot metal temperature, limestone decomposes into carbon dioxide and calcium oxide very quickly:

$$CaCO_3(s) = CaO(s) + CO_2(g) \qquad (5.55)$$

and the carbon dioxide may reacted with carbon, silicon and calcium carbide:

$$CO_2(g) + [C] = 2CO(g) \qquad (5.56)$$

$$CO_2(g)+\frac{1}{2}[Si]=\frac{1}{2}SiO_2(s)+CO(g) \qquad (5.57)$$

$$CO_2(g)+\frac{1}{3}CaC_2(s)=\frac{1}{3}CaO(s)+\frac{5}{3}CO(g) \qquad (5.58)$$

$$CO_2(g)+2CaC_2(s)=2CaO(s)+5C(gr) \qquad (5.59)$$

Figure 5.25 illustrates the free energy changes of these reactions. The data used in the calculation are shown in Table 5.10. It is clear that carbon dioxide reacts with calcium carbide to form carbon and calcium oxide more favourably. Table 5.10 also shows the thermal effects of Reactions (5.53)-(5.57). If all the limestone decomposes and reacts with calcium carbide as in Reaction (5.59), the bath temperature will increase by 12°C. However, no significant changes of the bath temperatures were observed in the experiments (Refer to Table 4.2). This indicates that not only Reaction (5.59), but the other reactions also took place.

As described in Chapter 3, the initial powder composition was 43% CaC_2, 36% CaO and 21% $CaCO_3$. There are three possibilities according to stoichiometric relation:

(a) All calcium carbonate reacts with silicon or carbon, resulted in a equivalent composition of 52.6% CaO and 47.4% CaC_2.

(b) All calcium carbonate reacts with calcium carbide according to Equation (5.58). The equivalent composition is 57.3% CaO and 42.7% CaC2.

(c) All calcium carbonate reacted with calcium carbide according to Equation (5.59). The equivalent composition is 81.6% CaO and 18.4% CaC_2.

It can be seen that the fraction of lime should be approximately in the range of 50-80 per cent, the fraction of calcium carbide in the range of 20-50 per cent.

The physical and chemical phenomena occurring during limestone-calcium carbide injection are shown in Figure 5.26 schematically. From the point of view of kinetics, the direct reaction of limestone and calcium carbide particles, which is a solid-solid reaction, should not be taken into account. Limestone decomposition is considered as the first step. As shown in Figure 5.26, some limestone particles may stay in nitrogen bubbles and decompose to lime and carbon dioxide. Then, the carbon dioxide reacts with calcium carbide particles in bubbles or silicon and carbon in the melt. Some limestone particles may penetrate into the liquid iron and decompose into lime and carbon dioxide. Then, the carbon dioxide will react with silicon or carbon in the melt. Thus, all four reactions (as described by (5.56)-(5.59)) probably occur. The evolution of CO and CO_2 forms a large number of bubbles. More particles may be positioned on the bubbles. The rate of mass transfer will be affected accordingly.

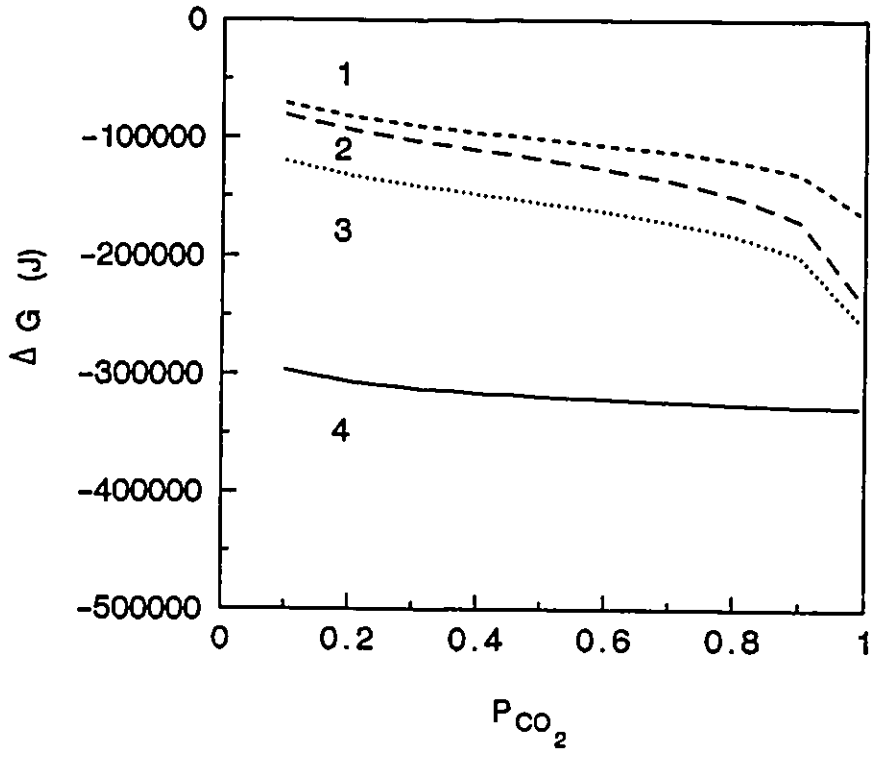

1 CO_2 (g) +1/2 [Si] = 1/2SiO_2(s) + CO (g)

2 CO_2 (g) + [C] = 2CO (g)

3 CO_2 (g) + 1/3CaC_2 (s) = 1/3CaO (s) + 5/3CO (g)

4 CO_2 (g) + 2CaC_2 (s) = 2CaO (s) + 5C (s)

Figure 5.25 The free energies of reaction of CO_2 with carbon, silicon and calcium carbide. The composition of 4.2% carbon and 0.5% silicon is assumed in the calculation.

TABLE 5.10

THERMODYNAMIC DATA AND EXPERIMENTAL CONDITIONS OF CHEMICAL REACTIONS OF LIMESTONE [a]

Temperature (°C)	1350	$CaC_2/CaO/CaCO_3$		43/36/21
Weight of the Melt (kg)	75	Carbon Content (%)		4.2
Powder Feed Rate (kg/min)	0.2	Silicon Content (%)		0.5
Reaction		ΔG^o (J)	ΔH^o (J)	ΔT (°C) [b]
$CaCO_3=CaO(s)+CO_2(g)$		168400-144T	163500	/
$CO_2(g)+[C]=2CO(g)$		139400-127T	167400	-6.6
$CO_2(g)+1/2[Si]=1/2SiO_2(s)+CO(g)$		-135400+27.6T	-168500	+0.1
$CO_2(g)+1/3CaC_2(s)=1/3CaO(s)+5/3CO(g)$		7606-96.7T	12100	-3.5
$CO_2(g)+2CaC_2(s)=2CaO(s)+5C(gr)$		-758400+265T	-764500	+12

a These standard free energies are calculated from the data compiled by Elliott et al. [15]

b The temperature change of the melt is caused by the reaction of limestone decomposition and the corresponding reaction on the left.

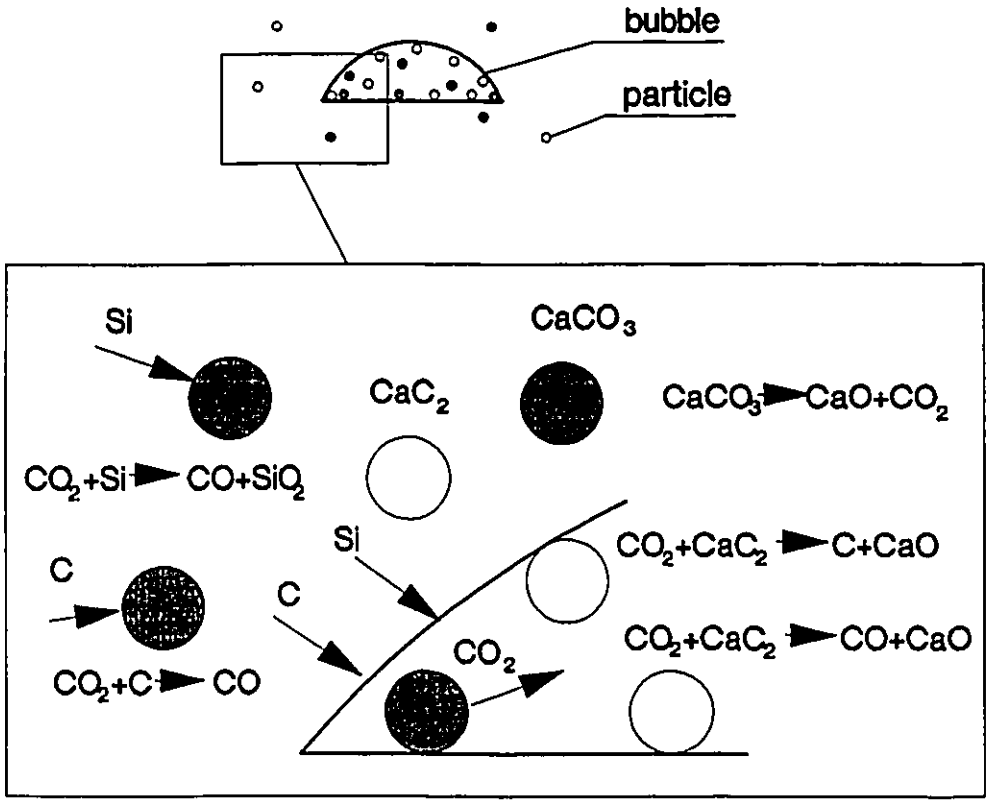

Figure 5.26 Schematic diagram of the physical and chemical phenomena associated with limestone-calcium carbide injection. The limestone particles dispersed in the melt may decompose and react with silicon and carbon. The particles positioned on bubble interface may decompose and react with calcium carbide or silicon and carbon in the melt.

The physical and chemical phenomena associated with limestone decomposition during calcium carbide injection are very complicated. So far, several problems are still not understood very well:

- the reaction mechanism of limestone and calcium carbide particles at the bubble surface, and limestone particles in the melt
- the amount of carbon monoxide or carbon dioxide generated from chemical reactions
- the fraction of particles which is in contact with the melt during limestone decomposition
- the determination of the mass transfer rate constant

Therefore, it is very difficult to develop a kinetic model which can satisfactorily describe mass transfer during desulphurization with limestone-calcium carbide injection. For simplicity, the kinetic model developed in Section 5.3.1 will be employed to the present case on the basis of the following assumptions:

(a) The refining rate is controlled by mass transfer of oxygen and sulphur through the melt to the particles.

(b) The mass transfer rate constants used for the model calculations are determined from Equation (5.92).

(c) The mass transfer rate constants are not affected by chemical reactions with CO or CO_2 and the chemical composition of the particles.

Based on these assumptions, the kinetic model can be applied to the cases of limestone-calcium carbide injections. The variations of sulphur with time are fitted to Equations (5.82) and (5.90). Then, the equivalent composition of the mixture that best fits the results is determined to be 33 per cent of calcium carbide and 67 per cent of calcium oxide. This indicates that a large amount of calcium carbide is consumed by limestone. On the basis of this composition, the first order rate constants of desulphurization are determined. The calculated results are shown with the broken line in Figure 5.24. One can see that the desulphurization rates with this 33/67 mixture of calcium carbide-lime are much lower than those with the commercial calcium carbide. It must be pointed out again that the phenomena associated with limestone decomposition during calcium carbide injection are very complicated. The above kinetic model only gives a simplifying approximation. More research may be needed in the future.

In the steelmaking industry, traditionally, the decomposition of limestone to produce carbon dioxide has been thought to improve mixing to account for the observed increase in calcium carbide utilization. Recently, Irons has shown that mixing is not rate controlling, and that gas release increases the interfacial area between gas and liquid [119]. According to his work, most of the particles are sitting on these interfaces, which more reasonably accounts for the observed increases in calcium carbide utilization.

On the other hand, the negative effect of limestone has to be taken into account. The present work demonstrated that low oxygen activity is required for effective hot metal desulphurization, and limestone is detrimental due to its evolution of carbon dioxide. Another problem of limestone is that its decomposition is a strong endothermic reaction, resulting in a drop of temperature of hot metal, or a decrease of silicon content to compensate the heat loss. Thus, limestone addition in calcium carbide is not suggested for desulphurization of hot metal.

In contrast to limestone, magnesium is a reducing and gas-releasing reagent at hot metal temperature. It can be expected that a large number of bubbles will be created by the vaporization of magnesium when the mixture of calcium carbide and magnesium is injected into liquid iron. Some magnesium may dissolve in the liquid iron. Desulphurization and deoxidation in the plume during injection will occur at three possible sites:

- the surface of the magnesium bubbles
- the interface between the liquid and the particles which reside on the bubble surface
- the interface between the liquid and the particles which enter the liquid

In Figure 5.27, the stability of possible calcium- and magnesium-containing phases is plotted as a function of oxygen and sulphur activity. The associated data are summarised in Table 5.11.

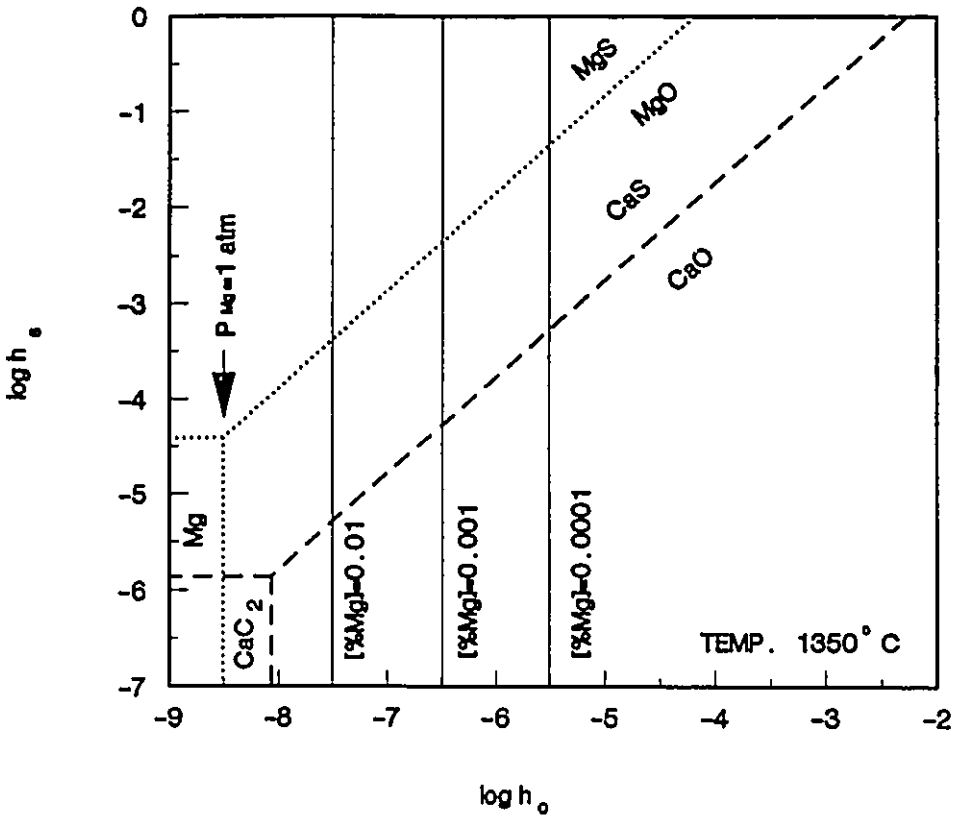

Figure 5.27 The stability of possible calcium- and magnesium-containing phases is plotted as a function of oxygen and sulphur activity for an iron- 4.2% carbon melt at 1350°C.

TABLE 5.11
THERMODYNAMIC DATA OF CHEMICAL REACTIONS OF MAGNESIUM

Reaction	ΔG^o (J)	Reference
Mg (g) + [O] = MgO (s)	-643500 + 217.7T	Marincek [123]
[Mg] + [O] = MgO (s)	-507500 + 150.2T	Marincek [123]
[Mg] + [S] = MgS (s)	-422800 + 175.8T	Elliott et al. [15] [a]
CaC_2 (s) + [O] = CaO (s) + 2C (s)	-462460 + 129.7T [b]	
CaO (s) + [S] = CaS (s) + [O]	104800 - 21.05T [c]	

a The standard free energy is calculated from the data compiled by Elliott et al. [15]

b Refer to Table 2.4

c Refer to Table 2.5

The activity of magnesium in an iron- 4.2% carbon melt at 1350°C is calculated from Equations (2.1)-(2.2). The interaction coefficient is determined from Reference [124].

$$e_{Mg}^{C} = 2.78 - \frac{4472}{T}$$

The aspects of desulphurization at the three reaction sites can be understood by reference to this diagram.

(a) Assuming magnesium vapour is one atmosphere, the local equilibrium oxygen activity near the bubble surface is lower than 10^{-8}, and the sulphur activity is lower than 10^{-4}. The liquid iron will be effectively desulphurized by the magnesium bubbles.

(b) The particles on the magnesium bubble surface will be exposed to a very low oxygen activity. Lime will have a very strong desulphurization capacity. Some lime will react with carbon, which is almost saturated in hot metal, and change to calcium carbide. It will then react with sulphur.

(c) If the dissolved magnesium content is more than 0.0001 per cent, the oxygen activity will be lower than 10^{-5}. The melt can be effectively desulphurized by the mixture of calcium carbide and lime. Moreover, the rate of desulphurization will not be affected by the CaO/CaC_2 proportion in the powder (Refer to in Figure 5.23).

Calcium carbide-magnesium mixtures have been found to be effective in hot metal desulphurization [120-122]. Although no experiments on magnesium-calcium carbide or lime mixtures were performed in the present work, according to the above discussion, it can be seen that a combination of magnesium and lime may also desulphurize very well.

CHAPTER 6
CONCLUSIONS

It was the primary purpose of this study to address the question of the role of the oxygen activity in the hot metal desulphurization with calcium carbide. In the present experiments in which calcium carbide was injected into 70 kg melts, desulphurization and deoxidation were studied by continuously measuring oxygen activity and frequently sampling for sulphur content. The oxygen activity was varied by changing the silicon (0.1-2.0%), and aluminum contents (0.001-0.2%). In some experiments, carbon dioxide was used (either as a carrier gas or as generated from calcium carbide/limestone mixtures) to simulate the effect of limestone decomposition which is used to enhance stirring in practice. The experimental results were analyzed from the point of view of kinetics. Several of the major findings are summarized below.

(1) The present experiments confirm that the oxygen activity in hot metal is controlled by the silicon-silica equilibrium, except when aluminum was added. The analysis demonstrates that the difficulties associated with nucleation and growth of CO bubbles prevent carbon

from reaching its equilibrium with CO; whereas, silica nucleation is favored on the crucible refractory surface. Therefore, the variation of the oxygen activity in hot metal has the characteristics of the silicon-silica equilibrium.

(2) The rate of desulphurization increased as oxygen activity decreased in order from carbon dioxide-containing injections into iron-carbon-silicon melts, to calcium carbide/nitrogen injections into iron-carbon-silicon melts, to finally calcium carbide/nitrogen injected into iron-carbon-aluminum melts.

(3) This is the first work which systematically demonstrates simultaneous sulphur and oxygen change during calcium carbide injection. In a log h_O-log h_S diagram, the trajectory of refining was associated with the deoxidation state of the melt. At a high initial oxygen activity (h_O=0.001), the trajectory is almost parallel to the CaO-CaS equilibrium line. As the oxygen activity is decreased, the trajectory becomes more vertical.

(4) The dependence of the incubation period with the melt oxygen activity is recognized. The incubation times coincide with periods of deoxidation before desulphurization proceeds. Melts with a low silicon content or aluminum content appear to exhibit long incubation periods. Thus, pre-deoxidation is required to reduce incubation time.

(5) A kinetic model was developed to describe the simultaneous deoxidation and desulphurization during calcium carbide injection. The model demonstrates that the rate of desulphurization is controlled by the melt oxygen activity and the powder feed rate. The refining trajectories determined from the kinetic model were found to be consistent with those obtained from the experiments.

(6) This kinetic model indicates that low oxygen is required for effective hot metal desulphurization. The model demonstrates that commercial calcium carbide which normally contains 30 percent of lime can be employed for the melts pre-deoxidized with silicon or aluminum, without causing significant delay of desulphurization.

(7) The present study demonstrates that the decomposition of limestone results in an increase of the melt oxidation and a decrease of calcium carbide utilization, consequently, the use of limestone retards desulphurization.

(8) The experimental bath cooling rate constants during gas and powder injections were analyzed on the basis of heat transfer theory. The experimental desulphurization rate constants were analyzed on the basis of mass transfer theory. The results from both analyses suggest that a significant fraction of particles does not contact the melt. The fraction of particles in contact with liquid is approximately 30-50 percent.

REFERENCES

1. L.K. Chiang, G.A. Irons, W-K. Lu and I.A. Cameron: Iron & Steelmaker, January 1990, pp.35-52.
2. G.A. Irons and L.R. Farias: Can. Metall. Quart., 1986, vol. 25, No.4, pp.297-306.
3. A. McLean: in Blast Furnace Ironmaking, W-K. Lu ed., McMaster University, 1989, vol. 1, pp.2-11.
4. R. S. Potocic and K. G. Leewis: in Proceedings of the McMaster University Symposium on the External Desulphurization of Hot Metal, W-K. Lu ed., 1975, pp.2-1.
5. P. Nilles and C. Marique: Proceedings of Scaninject V Conference, Lulea, Sweeden, June 6-8, 1989, pp.15-52.
6. Y. Yagi: Proceedings of the Sixth International Iron and Steel Congress, Nagoya, Japan. 1990, vol. 1, pp.7-16.
7. P. J. Koros: Proceedings of Scaninject III Conference, Lulea, Sweeden, June 15-17, 1983, pp.24.
8. I. A. Cameron: in Blast Furnace Ironmaking, McMaster University, Hamilton, Canada, W-K. Lu ed., 1989, vol. 3, pp.17.

9. W-K. Lu (ed.): Proceedings of the McMaster University Symposium on the External Desulphurization of Hot Metal, Hamilton, Canada, May, 1975.

10. W-K. Lu (ed.): Proceedings of the McMaster University Symposium on Developments in Hot Metal Preparation for Oxygen Steelmaking, Hamilton, Canada, May, 1983.

11. L-K. Chiang: Ph.D Thesis, McMaster University, 1987.

12. G. K. Sigworth and J. F. Elliott: Metal Science, vol. 8, 1974, pp.298-310.

13. The Japan Society for the Promotion of Science, The 19th Committee on Steelmaking: Steelmaking Data Sourcebook, Gogon and Breach Science Publishers, New York, NY, 1988.

14. R. J. Fruehan: Met. Trans., 1970, vol. 1, pp.865-70.

15. J. F. Elliott, M. Gleiser and V. Ramakrishna: Thermochemistry for Steelmaking, vol. II, Addison-Wesley Pub. Co., Inc., 1963.

16. E. T. Turkdogan: in The Making, Shaping and Treating of Steel, W. T. Lankford, Jr. ed., United Sates Steel, 1985, pp.367-506.

17. D. Ghosh and D. A. R. Kay: J. Electrochem. Soc., Vol. 124, 1977, pp. 1836-1845.

18. H. Schenck, E. Steinnmetz, K. K. Mehta: Arch. Eisenhuttenwes. Vol. 41, 1970, pp. 131-138.

19. M. W. Chase, Jr., A. A. Davies, J. R. Downey, Jr., D. J. Frurip, R. A. McDonad and A. N. Syverud: J. Phys. Chem. Ref. Data, 3rd ed., JANAF Thermochemical Tables, 1985, vol. 14, supp. 1.

20. D. A. R. Kay and S. V. Subramanian: in Proceedings of Second international Symposium on the Effects and Control of Inclusions and Residuals in Steels, J. D. Canmet et al. ed., Toronto, Canada, Aug. 17-20, 1986.

21. D. M. Edmunds and J. Taylor: J. Iron Steel Inst., 1972, vol. 210, pp.280-83.

22. T. Wakasugi and N. Sano: Metallurgical Transactions B, vol. 20B, 1989, PP.431-33.

23. J. H. Rai and N. W. Gregory: J. Phys. Chem., 1970, vol. 74, pp.529-34.

24. T. Sata, T. Sasamoto and K. Matsumoto: High temp. - High Press., 1982, vol. 14, pp.399-408.

25. O. Kubaschewski and C. B. Alcock: Metallurgical Thermochemistry, 5th ed., Pergamon Press Inc., New York, 1979.

26. P. V. Riboud, M. Olette: Rapport IRSID RE 525, April, 1978.

27. R. V. Kumar and D. A. R. Kay: et. Trans., Vol. 16B, 1985, pp. 287-294.

28. D. A. R. Kay and R. V. Kumar: in Perspectives in Metallurgical Development, The Metals Society, London, 1984.

29. L-C. Chang and K. M. Goldman: Trans. AIME, vol. 176, 1948, pp.309-327.

30. K. M. Goldman, G. Derge and W. O. Philbrook: Trans. AIME, vol. 200, 1954, pp.534.

31. S. Ramachandran, T. B. King, and N. J. Grant: J. Met., vol. 8, 1956, pp.1549.

32. R. G. Ward and K. A. Salmon: J. Iron Steel Inst., vol. 196, 1960, pp.393.

33. E. T. Turkdogan, R. A. Hancock and J. Pearson: JISI, vo. 179, 1955, PP.338.

34. T. B. King and S. Ramachandran: in Physical Chemistry of Steelmaking, J. F. Elliott ed., MIT Press, Cambridge, Mass., U.S.A., 1958, pp.125-135.

35. F. D. Richardson: Physical Chemistry of Melts in Metallurgy, vol. 2, Academic Press Inc. London, 1974.

36. W-K. Lu: Trans. Iron Steel Inst. Jpn, Vol. 11, 1971, pp. 32-39.

37. J. C. Fulton and J. Chipman: in Physical Chemistry of Steelmaking, J. F. Elliott ed., MIT Press, Cambridge, Mass., U.S.A., 1958, pp.113-116.

38. L. S. Darken and R. W. Gurry: Physical Chemistry of Metals, McGraw-Hill Book Co., New York, 1953.

39. B. Deo and P. Grieveson: Steel Research, vol. 57, 1986, No.10, pp.514-9.

40. D. G. C. Robertson, B. Deo and S Ohguchi: Ironmaking and Steelmaking, 1984, Vol. 11, No. 1, pp.41-45.

41. H. Y. Kim: Ph.D Thesis, University of Stathclyde, 1978.

42. T. Takenouchi and K. Suzuki: J. Iron Steel Inst. Japan, vol. 64, 1978, pp.1133.

43. T. Takenouchi et al.: J. Iron Steel Inst. Japan, vol. 64, 1978, pp.1704.

44. R. J. Fruehan: Ladle Metallurgy Principles and Practices, Iron and Steel Society inc., 1985.

45. N. El-Kaddah and J. Szekely: Ironmaking and Steelmaking, 1981, No. 6, pp. 269-278.

46. S. Ohguchi and D. G. C. Robertson: Ironmaking and Steelmaking, Vol. 11, 1984, No. 5, pp. 262-273.

47. T. Ototani, Y. Katarura and T. Degawa: Trans. ISIJ, vol.16, 1976, pp.304-308.

48. T. Ohya, F. Kodama, H. Matsunaga, M. Motoyoshi and M. Higashiguchi: Steelmakin Proceedings, vol. 60, 1977, pp.345.

49. L. E. K. Holappa: International Metal Reviews, vol. 27, 1982, No. 2, pp.53-75.

50. J. Parys, A. R. Romoro, J. Wrampelmeyer and D. Janke: Steel Reserch, 1985, No. 9, pp.457-64.

51. F. Oeters: Steel Research, vol. 56, 1985, No.2, pp.69-74.

52. M. Talballa, P. K. Tojan, W. C. Bigelow, R. A. Flinn and L. O. Brockway: AFS Transactions, vol. 122, 1976, pp.775-86.

53. T. Mitsuo, T. Shoji, Y. Hatta, H. Ono, H. Mori and T. Kai: Transactions of the Japan Institute of Metals, vol. 23, No. 12, 1982, pp.768-79.

54. F. Leclercq, J. P. Reboul, C. Gatellier, A. Chevaillier, P. Guglermina and A. Dufour: Proceedings of Scaninject III Conference, Lulea, Sweeden, June 15-17, 1983, No. 28.

55. S. Katz and Landefeld: AFS Transactions, vol. 30, 1985, pp.215-28.

56. R. J. Fruehan, J. Niedringhaus and A. H. Chan: Steelmaking Proceedings, vol. 67, 1984, pp.269-276.

57. F. Oeters, P. Strohmenger and W. Pluschkell: Arch. Eisenhuttenwes., vol. 44, 1973, No. 10, pp.727-33.

58. D. A. R. Kay, W-K. Lu and A. McLean: in Sulphide Inclusions in Steel, Proceedings of an International Symposium, J. J. deBarBadillo and E. Snape Ed., 7-8 November, New York, 1974, PP.23-43.

59. K. Kiukkola and C. Wagner: J. Electrochem. Soc., Vo. 104, May, 1957, pp. 308-316.

60. E. C. Subbarao: in Advaces in Ceramics, Vol. 3, A. Heuer and L. W. Hobbs ed., The American Ceramic Society, Inc., 1981, pp. 1-23.

61. C. Wagner: Advances in Electrochemistry and Electrochemical Engineering, vol.4, P. Delahay ed., 1966, pp. 1-46.

62. R. M. Dell and A. Hooper: Solid Electrolytes, Academic Press, New York, pp.291-313, 1978.

63. R. Littlewood: Canadian Metals Quarterly, Vol. 1966, pp. 1-17.

64. E. T. Turkdogan and R. J. Fruehan: Canadian Metallurgical Quarterly, Vol. 11, No. 2, 1972, pp. 371-384.

65. D. Janke: Advance in Ceramics, vol.12, N. Claussen, M. Ruhle and A. Heuer ed., The American Ceramic Society, Inc., 1984, pp. 636-645.

66. M. Iwase and A. McLean: Proceedings of The Six International Iron and Steel Congress, Nagoya, Japan, Vo. 1, 1991, pp. 521-528.

67. D. Janke and H. Richter: Arch. Eisenhuttenwes., Vol. 50, 1979, pp. 93-99.

68. K. Yamada, K. Iwasaki, H. Nakamura, O. Yamase, S. Kuriyama and E. Ogura: Trans. ISIJ, Vol. 23, 1983, pp. 87.

69. A. R. Romero, J. Harkki and D. Janke: Steel Research, Vol. 57, No. 12, 1986, pp. 636-644.

70. J. Niedringhaus: Ph.D Theses, Carnegie Mellon University. 1986.

71. H. Schmalzried: Ber. Bunsenges. Phys. Chem., Vol. 66, 1962, pp. 572-576.

72. P. H. Scaife, D. A. J. Swinkels and S. R. Richards: High temperature Science, Vo. 8, 1976, PP. 34-47.

73. M. J. U. T. Van Wijnggaarden, J. M. A. Geldenhuis and R. J. Dippenaar: Jnl. Appl. Electrochem., Vo. 18, 1988, pp. 724.

74. M. Iwase, E. Ichise, M. Takeuchi and Yamasaki: Trans. Japan Inst. Metals, Vol. 25, No.1, 1984, pp. 43-52.

75. M. J. U. T. van Wijnggaarden, Je. M. A. Geldenhuis and R. J. Dippenaar: I&SM, April 1988, pp. 35-44.

76. H. Schmalzried: Z. Phys. Chem., Vol. 38, 1963, pp. 87-102.

77. M. Iwase and T. Mori: Trans. ISIJ, Vol. 19, 1979, pp. 126-132.

78. M. Iwase, E. Ichise and K. T. Jacob: Advance in Ceramics, vol. 12, N. Claussen, M. Ruhle and Heuer ed., 1984, pp. 646-659.

79. A. Kumar, D. Rajadive and D. L. Doughlass: J. Amer. Ceram. Soc., Vo. 55, 1972, pp. 439.

80. T. A. Ramanarayanan and W. L. Worrell: Can. Metall. Soc., Vol. 13, 1974, pp. 325-329.

81. B. C. H. Steele, J. Drennan, R. K. Slotwinski, N. Bonanos and E. P. Butler: Advance in Ceramics, vol.3, A. H.Heuer and L. W. Hobbs ed., 1981, pp.289-309.

82. J. S. Schakelford, P. S. Nicholson and W. W. Smeltzer: Amer. Ceram. Soc. Bull., Vol. 53, 1974, pp. 865.

83. D. Schixue, C. R. Masson and P. D. Pacey: DongBei Gongxeyan XueBao, Vol. 43, 1985, pp. 10-16.

84. H. Schmalzried: Advance in Ceramics, Vol. 3, A. H. Heuer and L. W. Hobbs ed., 1981, pp. 254-271.

85. R. E. Odle and R. A. Rapp: Met. Trans., Vol. 8B, 1977, pp. 581-589.

86. Private Communication from Dresser Canada Inc., 1991.

87. Private Communication from Electronite Canada Limited, Hamilton, 1985.

88. Private communication from B. J. Barker: Cyanamid Canada Inc. Report, June 7, 1990.

89. National Bureau of Standards: Certificate of Analysis, 1976.

90. M. V. Oosten: Report of Reference Materals, McMaster University, 1986.

91. S.C. Ghorpade, R.W. Heine and C.R. Loper: AFS Trans., 1975, vol. 105, pp.193-98.

92. S. Katz, D.E. McInnis, D.L. Brink and G.A. Wilkinson: AFS Trans., 1980, vol. 85, pp.835-44.

93. U.B. Pal and B.V. Patil: Ironmaking and Steelmaking, 1986, vol. 13, No.6, pp.294-300.

94. E.T. Turkdogan: Physical Chemistry of High Temperature Technology, Academic Press, New York, 1980, pp.246.

95. R. Higbie: Trans. Inst. Chem. Eng. Sci., 1935, vol. 31, pp.365.

96. J.H. Swisher and E.T. Turkdogan: Trans. Met. Soc. AIME, 1967, vol. 239, pp.426.

97. G.A. Irons: Ph.D Thesis, McGill University, 1978.

98. R.M. Davies and G.T. Taylor: Proc. R. Soc., London, 200A, 1950, pp.375.

99. J. Campbell: Conf. on Solidification of Metals, Brighton, England, Dec. 1967, JISI Sp. Report, 1968, pp.18-26.

100. J. Alexander, G.S.F. Hazeldean, and M.W. Davies: Chemical Metallurgy of Iron and Steel, Iron and Steel Inst., London, 1973, pp.107.

101. B. Gebhart: Heat Transfer, 2nd, ed., McGraw-Hill, New York, 1971.

102. H.T. Angus: Cast Iron: Physical and Engineering Properties, Butterworth, London-Boston, 1976.

103. C.H. Ho, R.W. Powell and P.E. Liley: J. Phys. Chem. Ref. Data, 3, 1, 1974.

104. R. N. Barfield and J. A. Kitchnener: J. Iron and Steel Inst., Vol. 180, pp. 324-29, 1955.

105. L. D. Lucas: Compt. Rend., vol. 248, pp.2336-38, 1959.

106. K.K. Kelley: U.S. Bur. Mines Bull., No.584, 1960.

107. O. Kubaschwaki, E.L. Evans and C.B. Alcook: Metallurgical Thermochemistry, Pergamon Press, London, 1967.

108. A. Schack: Industrial Heat Transfer, Wiley, New York, 1965.

109. L. F. Lucks, C. L. Linebrink and K. L. Johnson: Trans. A.F.S, Vol. 55, pp.62, 1947.

110. L. R. Farias and G.A. Irons: Metallurgical Transactions B, Vol. 16B, pp.211-225, 1985.

111. G.A. Irons: ISS Transactions, Vol. 5, pp. 33-45, 1984.

112. W. E. Ranz and W. R. Marshall: Chem. Eng. Progr., Vo. 48, pp.141, 1952.

113. D. Mazumdar and R. I. L. Guthrie: Metallurgical Transactions B, Vol. 16B, pp.83-90, 1985.

114. Y. Sahai and R. I. L. Guthrie: Metallurgical Transactions B, Vol. 13B, pp.193-202, 1982.

115. T. Iida and R. I. L. Guthrie: The Physical Properties of Liquid Metals, Oxford Science Publifications, 1988.

116. R. L. McCarron and G. R. Belton: Tansactions of the Metallurgical Society of AIME, Vol. 245, pp.1161-66,1969.

117. I. A. Novokhatskiy and G. S. Ershov: Russ. Met., No. 2, pp.20-22, 1967.

118. M. Kawakami and K. S. Goto: Transactions ISIJ, Vol. 16, pp. 204-207, 1976.

119. G. A. Irons: Ironmaking and Steelmaking, Vol. 16, No. 1, pp.28-36, 1989.

120. H. Trout and L. Matanich: Steelmaking Conference Proceedings, pp. 345-49, 1990.

121. T. B. Bienosek: Proceedings of the Fifth International Iron and Steel Cogress, 1986, ISS of AIME, Washington, U.S.A, pp.429-439.

122. I. A. Cameron and R. A. Jackson: Steelmaking Conference Proceedings, pp. 367-75, 1990.

123. B. Marincek: Giesserei, No. 4, pp.56-59, 1965.

124. M. C. Speer and N. A. D. Parlee: A. F. S Cast Metals Reaserch Journal, Sep. 1972, pp. 122-128.

125. A. Murthy and J. Szekely: Metallurgical Transaction B, Vol. 17B, 1986, pp. 487-490.

126. K. Nakanishi, J. Szekely and C. W. Chang: Ironmaking and Steelmaking, No. 2, 1975, pp. 115-124.

APPENDIX I

THE EXPERIMENTAL DATA OF SULPHUR ANALYSIS

SULPHUR ANALYSIS FOR EXPERIMENT No.6 (6-1)

Pin Sample No.	Time (s)	Sulphur (%)
1-11	10	0.019
1-12	10	0.022
1-21	65	0.017
1-22	65	0.023
1-31	105	0.017
1-32	105	0.021
1-41	162	0.021
1-42	162	0.020
1-51	240	0.023
1-52	240	0.020
2-11	70	0.020
2-12	70	0.018
2-21	120	0.019
2-22	120	0.021
2-31	150	0.016
2-32	150	0.016
2-41	210	0.010
2-42	210	0.010
2-51	250	0.005
2-52	250	0.009
3-11	38	0.018
3-12	38	0.013
3-21	75	0.012
3-22	75	0.014
3-31	120	0.015
3-32	120	0.016
3-41	170	0.015
3-42	170	0.015
3-51	225	0.015
3-52	225	0.016
3-61	250	0.015
3-62	250	0.014

SULPHUR ANALYSIS FOR EXPERIMENT No.6 (6-2)

Pin Sample No.	Time (s)	Sulphur (%)
4-11	40	0.015
4-12	40	0.014
4-21	85	0.015
4-22	85	0.012
4-31	130	0.005
4-32	130	0.009
4-41	180	0.007
4-42	180	0.007
4-51	246	0.005
4-52	246	0.005
4-61	310	0.003
4-62	310	0.003
5-11	42	0.026
5-12	42	0.022
5-21	96	0.029
5-22	96	0.030
5-31	155	0.026
5-32	155	0.027
5-41	207	0.029
5-42	207	0.024
5-51	240	0.029
5-52	240	0.026
5-61	257	0.029
5-62	257	0.030
5-71	330	0.025
5-72	330	0.030
6-11	0	0.024
6-12	0	0.026
6-21	30	0.025
6-22	30	0.027
6-31	80	0.016
6-32	80	0.019
6-41	140	0.014
6-42	140	0.014
6-51	220	0.010
6-52	220	0.006
6-61	280	0.006
6-62	280	0.008

SULPHUR ANALYSIS FOR EXPERIMENT No.7 (7-1)

Pin Sample No.	Time (s)	Sulphur (%)
1-11	0	0.036
1-12	0	0.036
1-21	175	0.037
1-22	175	0.038
1-31	223	0.038
1-32	223	0.041
1-41	270	0.038
1-42	270	0.036
1-51	341	0.036
1-52	341	0.037
1-61	360	0.037
1-62	360	0.037
2-11	60	0.035
2-12	60	0.036
2-21	100	0.030
2-22	100	0.033
2-31	160	0.017
2-32	160	0.018
3-11	0	0.017
3-12	0	0.017
3-21	41	0.017
3-22	41	0.018
3-31	90	0.016
3-32	90	0.016
3-41	152	0.017
3-42	152	0.017
3-51	205	0.015
3-52	205	0.017
3-61	260	0.016
3-62	260	0.017
3-71	320	0.017
3-72	320	0.017

SULPHUR ANALYSIS FOR EXPERIMENT No.7 (7-2)

Pin Sample No.	Time (s)	Sulphur (%)
4-11	0	0.016
4-12	0	0.017
4-21	76	0.017
4-22	76	0.014
4-31	295	0.003
4-32	295	0.003
5-11	40	0.002
5-12	40	0.002
5-21	120	0.003
5-22	120	0.002
5-31	185	0.002
5-32	185	0.002
5-41	174	0.002
5-42	174	0.002
5-51	315	0.002
5-52	315	0.003
5-61	375	0.002
5-62	375	0.002
6-11	0	0.003
6-12	0	0.002
6-21	120	0.002
6-22	120	0.002
6-31	170	0.002
6-32	170	0.001
6-41	300	0.002
6-42	300	0.002
6-51	360	0.003
6-52	360	0.002

SULPHUR ANALYSIS FOR EXPERIMENT No.8 (8-1)

Pin Sample No.	Time (s)	Sulphur (%)
1-11	0	0.018
1-12	0	0.017
1-21	180	0.018
1-22	180	0.017
1-31	310	0.016
1-32	310	0.019
2-11	0	0.019
2-12	0	0.017
2-21	60	0.019
2-22	60	0.016
2-31	120	0.015
2-32	120	0.015
2-41	150	0.012
2-42	150	0.016
2-51	260	0.008
2-52	260	0.007
2-61	330	0.007
2-62	330	0.006
3-11	0	0.020
3-12	0	0.022
3-21	180	0.021
3-22	180	0.020
3-31	300	0.023
3-32	300	0.021

SULPHUR ANALYSIS FOR EXPERIMENT No.8 (8-2)

Pin Sample No.	Time (s)	Sulphur (%)
4-11	0	0.019
4-12	0	0.018
4-21	70	0.015
4-22	70	0.016
4-31	115	0.012
4-32	115	0.011
4-41	155	0.008
4-42	155	0.008
4-51	240	0.003
4-52	240	0.003
4-61	305	0.002
4-62	305	0.003
4-72	340	0.003
4-82	340	0.004
5-11	0	0.011
5-12	0	0.012
5-21	120	0.012
5-22	120	0.012
5-31	210	0.013
5-32	210	0.013
6-11	0	0.011
6-12	0	0.011
6-21	52	0.012
6-22	52	0.013
6-31	107	0.009
6-32	107	0.009
6-41	147	0.007
6-42	147	0.006
6-51	287	0.004
6-52	287	0.006
7-11	0	0.013
7-12	0	0.013
7-21	70	0.010
7-22	70	0.012
7-31	100	0.008
7-32	100	0.007
7-41	200	0.003
7-42	200	0.003
7-51	240	0.001
7-52	240	0.001
7-61	335	0.002
7-62	335	0.001

SULPHUR ANALYSIS FOR EXPERIMENT No.9 (9-1)

Pin Sample No.	Time (s)	Sulphur (%)
1-11	0	0.028
1-12	0	0.028
1-21	287	0.029
1-22	287	0.031
1-31	420	0.028
1-32	420	0.031
2-11	0	0.028
2-12	0	0.028
2-21	53	0.027
2-22	53	0.027
2-31	93	0.023
2-32	93	0.020
2-41	143	0.019
2-42	143	0.015
2-51	186	0.012
2-52	186	0.012
2-61	315	0.007
2-62	315	0.009
2-71	360	0.011
2-72	360	0.012
3-11	0	0.017
3-12	0	0.016
3-21	169	0.017
3-22	169	0.018
3-31	398	0.019
3-32	398	0.019

SULPHUR ANALYSIS FOR EXPERIMENT No.9 (9-2)

Pin Sample No.	Time (s)	Sulphur (%)
4-11	0	0.025
4-12	64	0.017
4-21	64	0.017
4-22	330	0.003
4-31	330	0.003
4-32	450	0.003
4-41	450	0.002
5-11	0	0.020
5-12	0	0.020
5-21	175	0.023
5-22	175	0.022
5-31	243	0.021
5-32	243	0.021
6-11	0	0.021
6-12	0	0.022
6-21	60	0.018
6-22	60	0.018
6-31	108	0.014
6-32	108	0.014
6-41	163	0.009
6-42	163	0.010
6-51	200	0.006
6-52	200	0.005
6-61	255	0.003
6-62	255	0.004
6-71	345	0.004
6-72	345	0.004

SULPHUR ANALYSIS FOR EXPERIMENT No.9 (9-3)

Pin Sample No.	Time (s)	Sulphur (%)
7-11	0	0.018
7-12	0	0.016
7-21	79	0.015
7-22	79	0.015
7-31	150	0.010
7-32	150	0.009
7-41	200	0.006
7-42	200	0.006
7-51	270	0.004
7-52	270	0.003
7-61	330	0.004
7-62	330	0.003
8-11	0	0.017
8-12	0	0.015
8-21	50	0.015
8-22	50	0.016
8-31	105	0.011
8-32	105	0.012
8-41	163	0.010
8-42	163	0.009
8-51	220	0.007
8-52	220	0.007
8-61	325	0.006
8-62	325	0.007
9-11	26	0.022
9-21	89	0.023
9-22	89	0.023
9-31	113	0.021
9-32	113	0.023
9-41	141	0.021
9-42	141	0.021
9-51	195	0.019
9-52	195	0.018
9-61	261	0.019
9-62	261	0.018
9-71	390	0.014
9-72	390	0.014

SULPHUR ANALYSIS FOR EXPERIMENT No.10 (10-1)

Pin Sample No.	Time (s)	Sulphur (%)
1-11	0	0.042
1-12	0	0.043
1-21	85	0.035
1-22	85	0.035
1-31	255	0.015
1-32	255	0.016
1-41	310	0.008
1-42	310	0.007
1-51	430	0.012
1-52	430	0.013
2-11	0	0.025
2-12	0	0.025
2-21	85	0.018
2-22	85	0.021
2-31	150	0.013
2-32	150	0.012
2-41	190	0.007
2-42	350	0.003
3-11	0	0.034
3-12	0	0.036
3-21	145	0.032
3-22	145	0.033
3-31	259	0.032
3-32	259	0.032
4-11	0	0.032
4-12	0	0.030
4-21	130	0.025
4-22	130	0.024
4-31	210	0.013
4-32	210	0.013
4-41	270	0.008
4-42	270	0.008
4-51	350	0.006
4-52	350	0.006

SULPHUR ANALYSIS FOR EXPERIMENT No.10 (10-2)

Pin Sample No.	Time (s)	Sulphur (%)
5-11	0	0.035
5-12	0	0.035
5-13	0	0.036
5-21	190	0.036
5-22	190	0.036
6-11	0	0.035
6-12	0	0.036
6-21	82	0.028
6-22	82	0.028
6-31	300	0.003
6-32	300	0.003
7-11	0	0.040
7-12	0	0.039
7-21	160	0.039
7-22	160	0.041
7-31	248	0.039
7-32	248	0.041
8-11	0	0.041
8-12	0	0.042
8-21	90	0.026
8-22	90	0.026
8-31	165	0.013
8-32	165	0.012
8-41	280	0.007
8-42	280	0.006

SULPHUR ANALYSIS FOR EXPERIMENT No.11 (11-1)

Pin Sample No.	Time (s)	Sulphur (%)
1-11	0	0.040
1-12	0	0.042
1-21	60	0.042
1-22	60	0.041
1-31	136	0.024
1-32	136	0.022
1-41	208	0.015
1-42	208	0.015
1-51	300	0.006
1-52	300	0.006
2-11	0	0.022
2-12	0	0.022
2-21	70	0.020
2-22	70	0.021
2-31	240	0.005
2-32	240	0.004
3-11	0	0.015
3-12	0	0.014
3-21	40	0.016
3-22	40	0.015
3-31	120	0.009
3-32	120	0.011
3-41	230	0.004
3-42	230	0.004

SULPHUR ANALYSIS FOR EXPERIMENT No.11 (11-2)

Pin Sample No.	Time (s)	Sulphur (%)
4-11	0	0.027
4-12	0	0.030
4-21	192	0.028
4-22	192	0.028
4-31	270	0.028
4-32	270	0.030
5-11	0	0.029
5-12	0	0.029
5-21	85	0.022
5-22	85	0.024
5-31	130	0.024
5-32	130	0.024
5-41	195	0.024
5-42	195	0.020
7-11	0	0.038
7-12	0	0.040
7-21	120	0.039
7-22	120	0.038
7-31	210	0.039
7-32	210	0.039
8-11	0	0.037
8-12	0	0.037
8-21	60	0.034
8-22	60	0.035
8-31	115	0.016
8-32	115	0.017
8-41	333	0.004
8-42	333	0.003

SULPHUR ANALYSIS FOR EXPERIMENT No.12 (12-1)

Pin Sample No.	Time (s)	Sulphur (%)
1-11	0	0.044
1-12	0	0.041
1-21	170	0.047
1-22	170	0.045
1-31	375	0.047
1-32	375	0.049
2-11	0	0.048
2-12	0	0.046
2-21	180	0.044
2-22	180	0.044
2-31	360	0.041
2-32	360	0.041
3-11	0	0.032
3-12	0	0.030
3-21	210	0.030
3-22	210	0.030
3-31	330	0.030
3-32	330	0.031

SULPHUR ANALYSIS FOR EXPERIMENT No.12 (12-2)

Pin Sample No.	Time (s)	Sulphur (%)
4-11	0	0.028
4-12	0	0.031
4-21	55	0.027
4-22	55	0.027
4-31	105	0.027
4-32	105	0.027
4-41	300	0.024
4-42	300	0.025
5-11	0	0.044
5-12	0	0.043
5-21	220	0.045
5-22	220	0.045
5-31	375	0.043
5-32	375	0.041
6-11	0	0.042
6-12	0	0.044
6-21	120	0.039
6-22	120	0.040
6-31	230	0.033
6-32	230	0.035

SULPHUR ANALYSIS FOR EXPERIMENT No.13 (13-1)

Pin Sample No.	Time (s)	Sulphur (%)
1-11	0	0.041
1-12	0	0.039
1-21	210	0.038
1-22	210	0.041
1-31	420	0.038
1-32	420	0.039
2-11	0	0.040
2-12	0	0.038
2-21	100	0.038
2-22	100	0.038
2-31	220	0.031
2-32	220	0.032
2-41	300	0.033
2-42	300	0.030
2-51	400	0.033
2-52	400	0.033
3-11	0	0.055
3-12	0	0.053
3-21	100	0.054
3-22	100	0.054
3-31	175	0.054
3-32	175	0.054
4-11	0	0.050
4-12	0	0.053
4-21	60	0.051
4-22	60	0.049
4-31	125	0.045
4-32	125	0.044
5-11	0	0.061
5-12	0	0.061
5-21	130	0.064
5-22	130	0.063

SULPHUR ANALYSIS FOR EXPERIMENT No.13 (13-2)

Pin Sample No.	Time (s)	Sulphur (%)
6-11	20	0.062
6-12	20	0.061
6-21	90	0.056
6-22	90	0.055
6-31	155	0.044
6-32	155	0.043
8-11	0	0.066
8-12	0	0.066
8-21	100	0.063
8-22	100	0.064
8-31	180	0.061
8-32	180	0.061
8-41	230	0.049
8-42	230	0.050
8-51	300	0.063
8-52	300	0.065
8-61	360	0.065
8-62	360	0.063
10-11	0	0.086
10-12	0	0.084
10-21	99	0.081
10-22	99	0.081
10-31	160	0.077
10-32	160	0.079
10-41	200	0.077
10-42	200	0.079
10-51	270	0.076
10-52	270	0.079
10-61	333	0.079
10-62	333	0.079
11-11	0	0.107
11-12	0	0.105
11-21	210	0.104
11-22	210	0.106
11-31	330	0.103
11-32	330	0.102
12-11	0	0.102
12-12	0	0.100
12-21	140	0.093
12-22	140	0.095
12-31	270	0.073
12-32	270	0.072

APPENDIX II

THE CHANGES OF SULPHUR CONTENTS AND OXYGEN ACTIVITIES WITH TIME

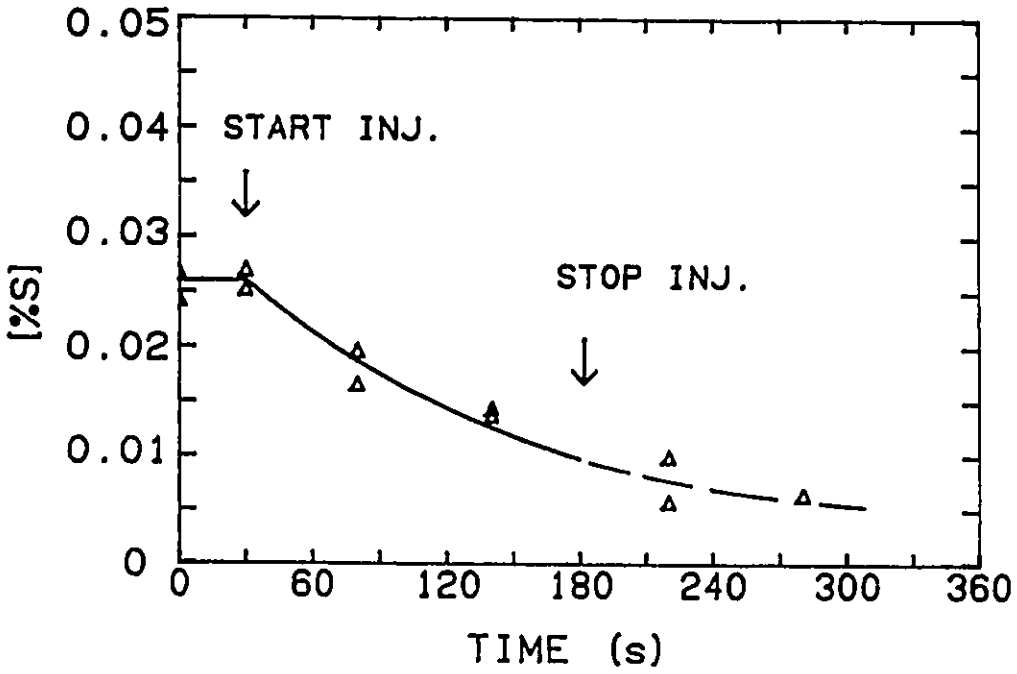

Figure A-1 The change of sulphur content with time during an injection of calcium carbide at 0.208 kg/min and nitrogen gas flow rate 4.6 SLPM into iron-4.2% carbon-1.04% silicon melt with an initial temperature 1345 °C. (Run No. 6-006)

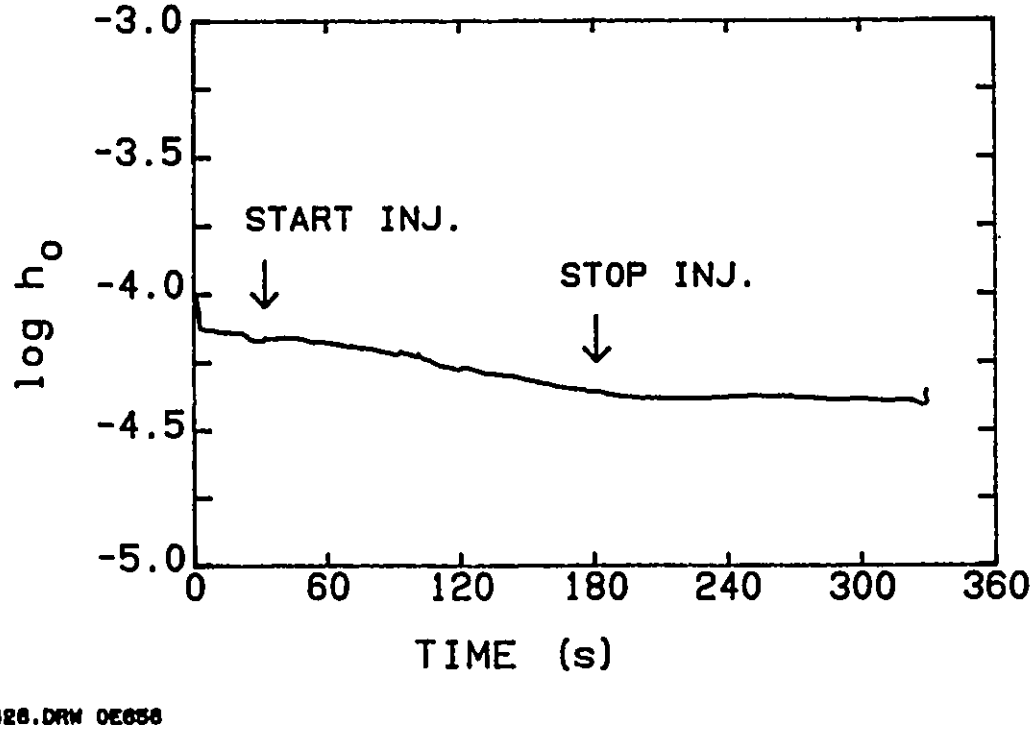

Figure A-2 The oxygen activity during the same injection as in Figure A-1. (Run No. 6-006)

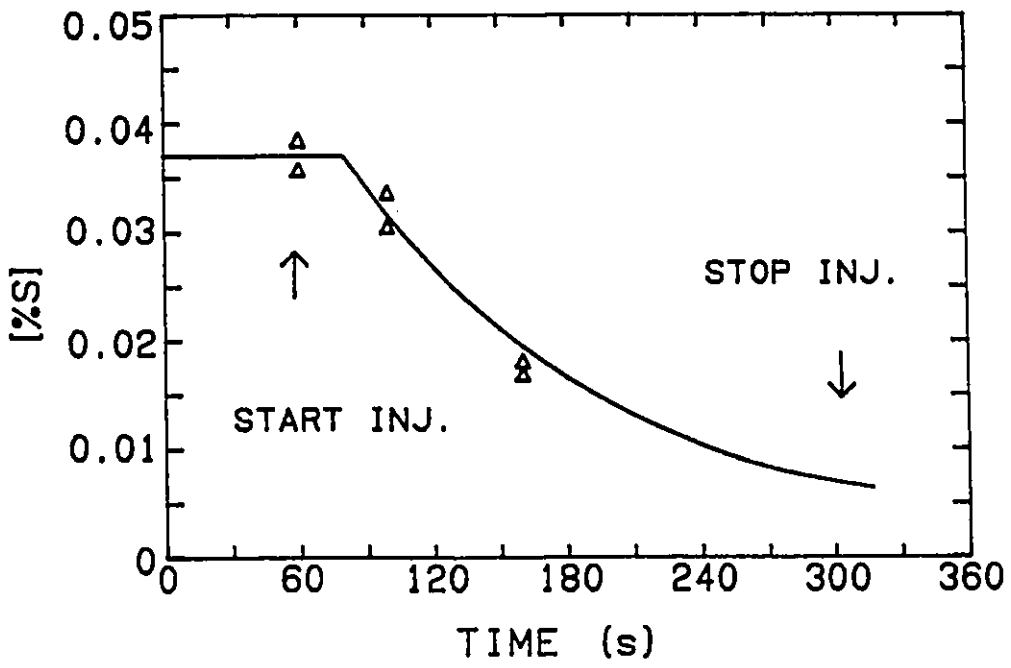

Figure A-3 The change of sulphur content with time during an injection of calcium carbide at 0.294 kg/min and nitrogen gas flow rate 4.1 SLPM into iron-4.2% carbon-0.12% silicon melt with an initial temperature 1350 °C. (Run No. 7-002)

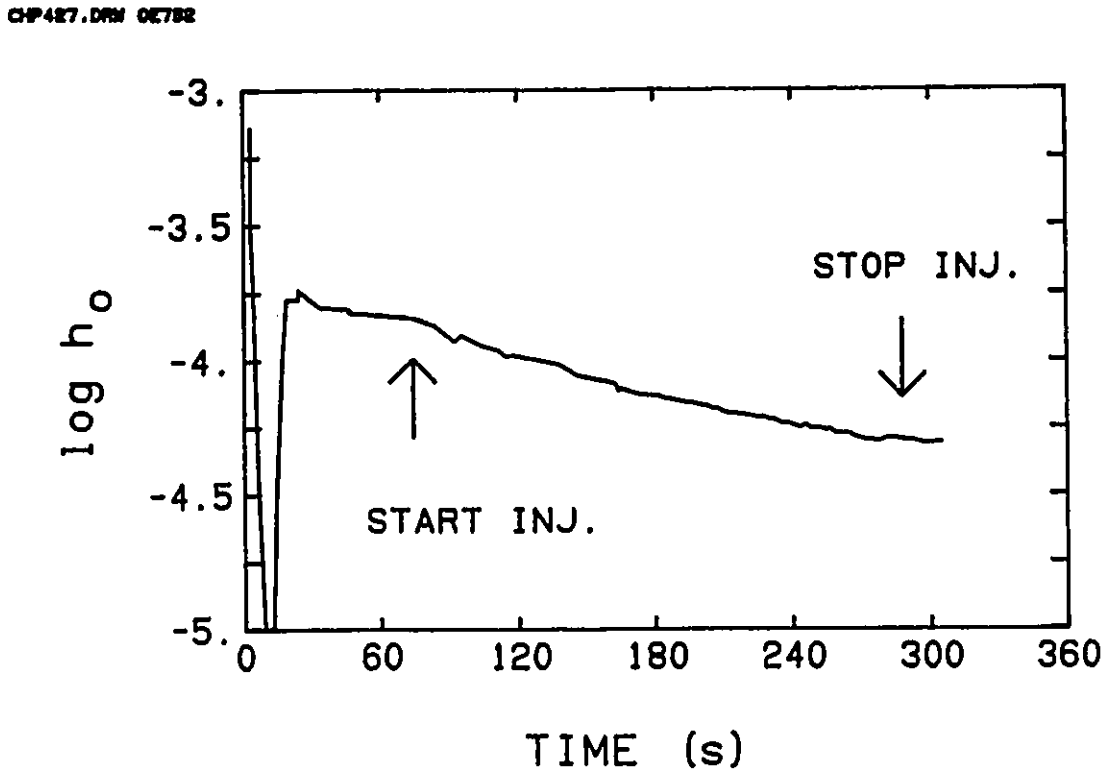

Figure A-4 The oxygen activity during the same injection as in Figure A-3. (Run No. 7-002)

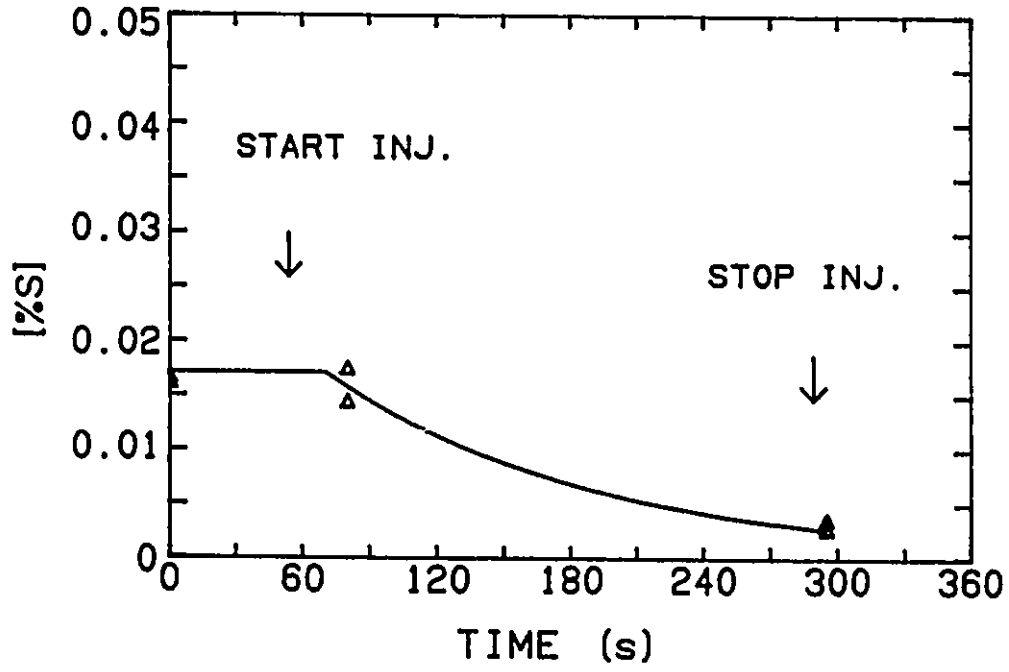

Figure A-5 The change of sulphur content with time during an injection of calcium carbide at 0.299 kg/min and nitrogen gas flow rate 4.4 SLPM into iron-4.2% carbon-0.12% silicon-0.199% aluminium melt with an initial temperature 1350 °C. (Run No. 7-004)

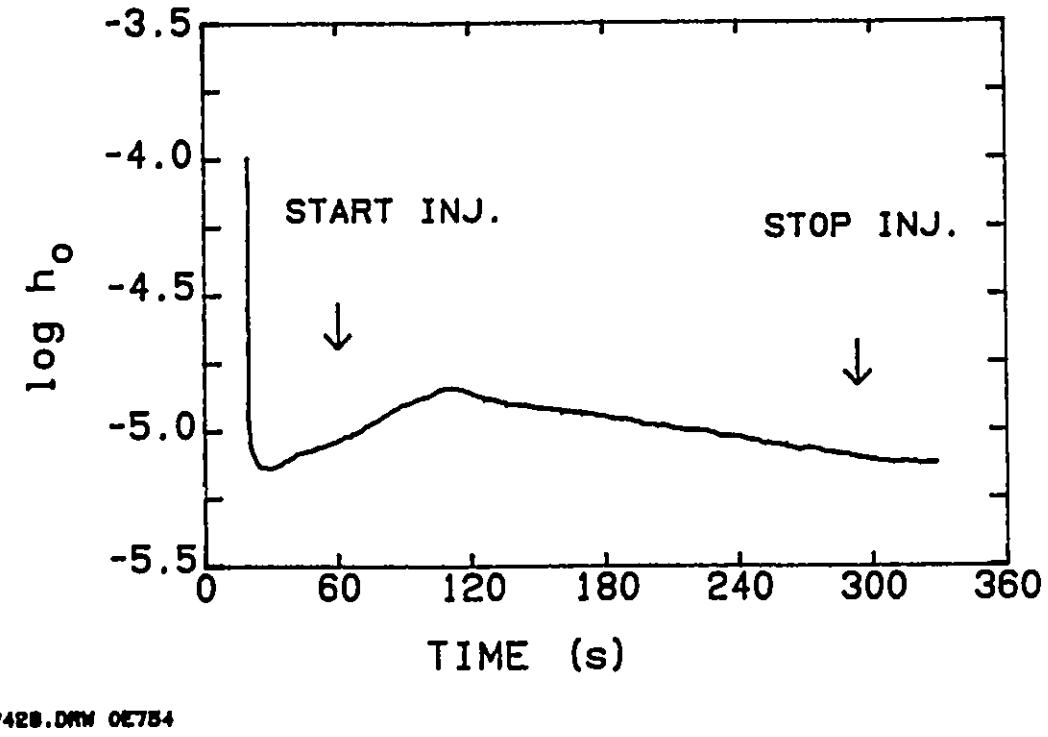

Figure A-6 The oxygen activity during the same injection as in Figure A-5. (Run No. 7-004)

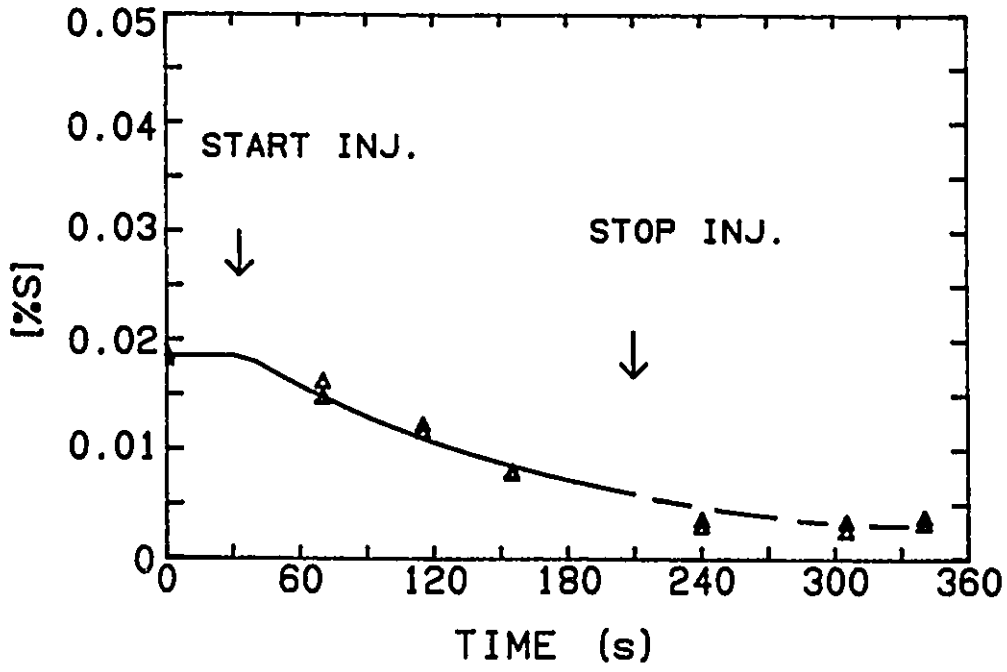

Figure A-7 The change of sulphur content with time during an injection of calcium carbide at 0.155 kg/min and nitrogen gas flow rate 5.0 SLPM into iron-4.2% carbon-0.93% silicon-0.009% aluminium melt with an initial temperature 1365 °C. (Run No. 8-004)

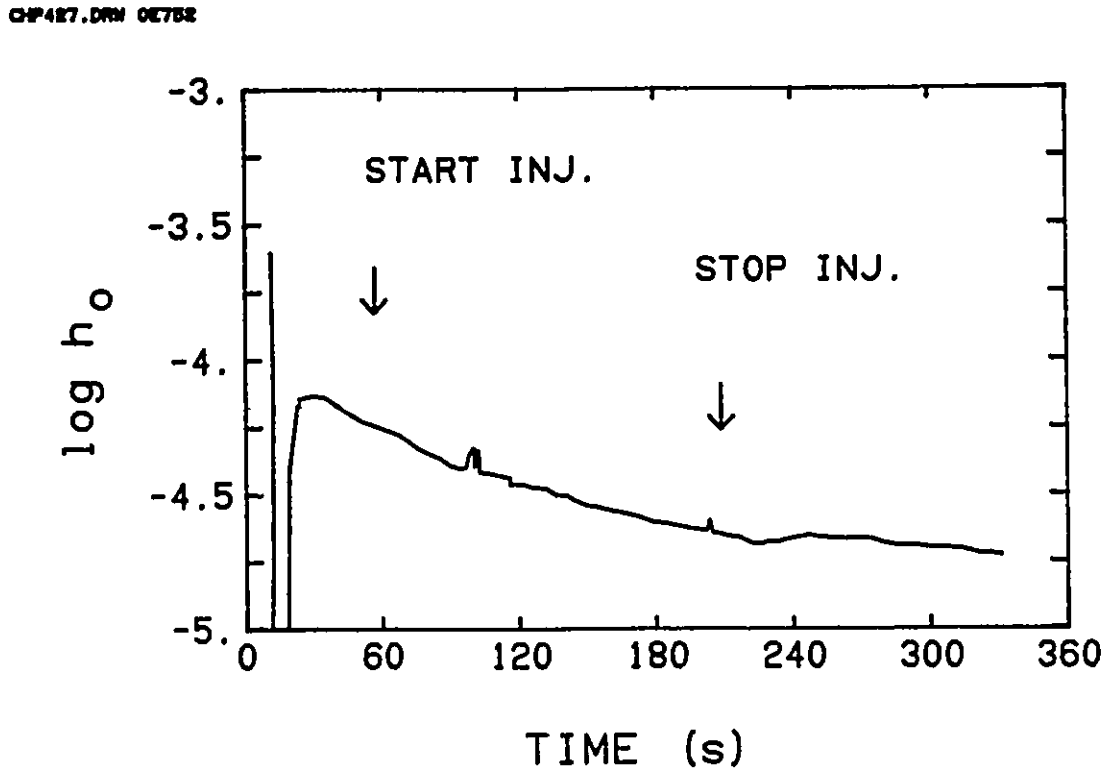

Figure A-8 The oxygen activity during the same injection as in Figure A-7. (Run No. 8-004)

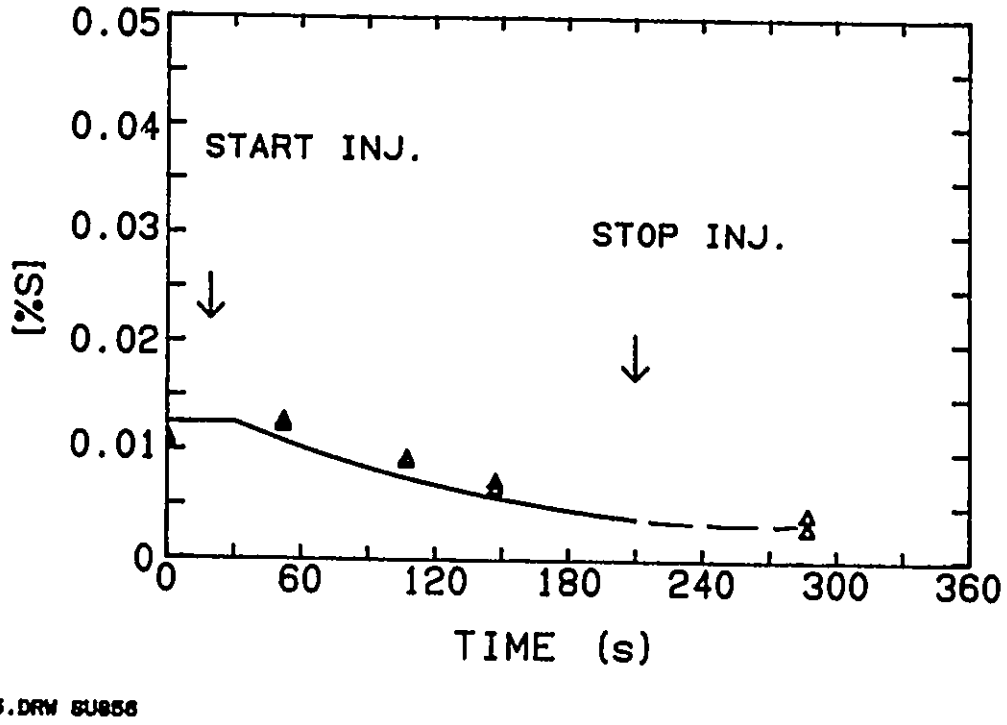

Figure A-9 The change of sulphur content with time during an injection of calcium carbide at 0.142 kg/min and nitrogen gas flow rate 5.0 SLPM into iron-4.2% carbon-1.79% silicon-0.003% aluminium melt with an initial temperature 1372 °C. (Run No. 8-006)

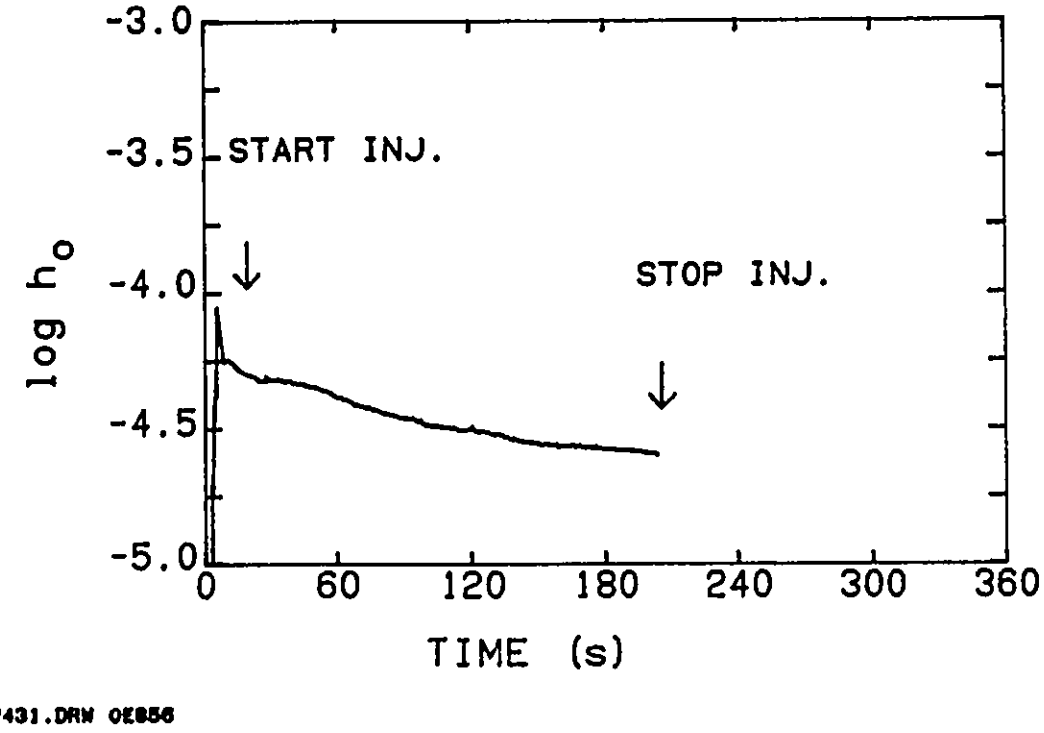

Figure A-10 The oxygen activity during the same injection as in Figure A-9. (Run No. 8-006)

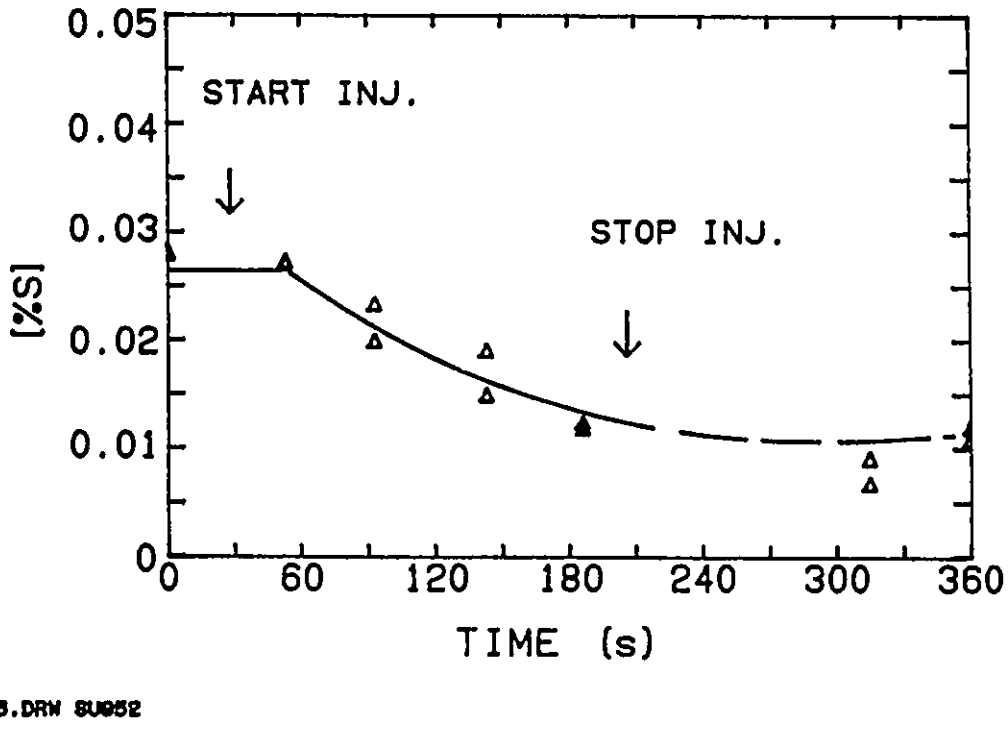

Figure A-11 The change of sulphur content with time during an injection of calcium carbide at 0.169 kg/min and nitrogen gas flow rate 5.2 SLPM into iron-4.2% carbon-0.91% silicon melt with an initial temperature 1350 °C. (Run No. 9-002)

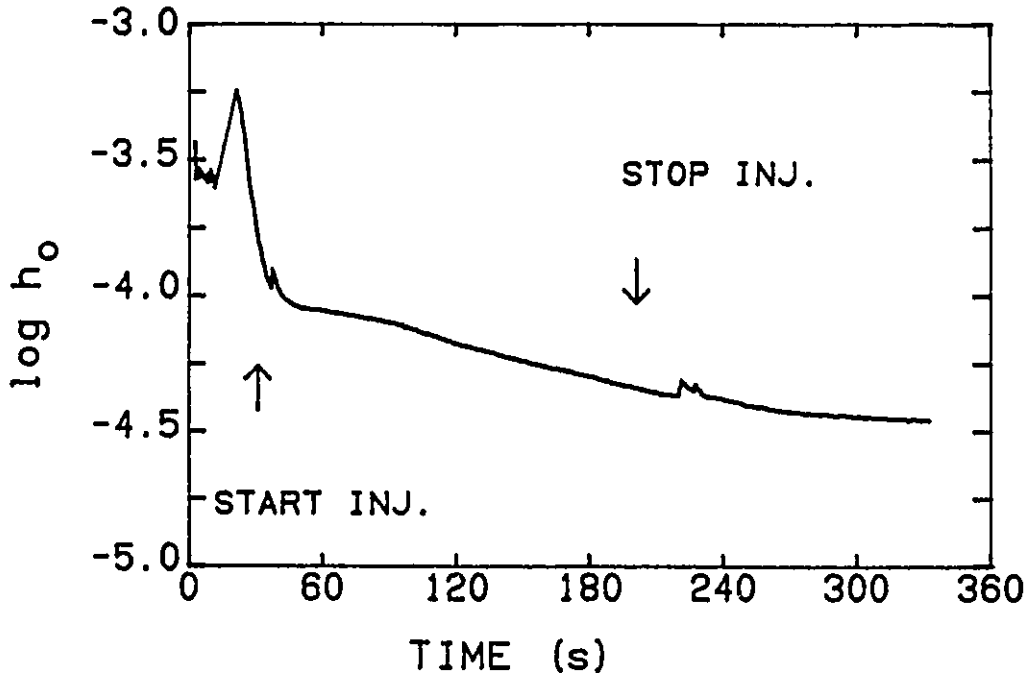

Figure A-12 The oxygen activity during the same injection as in Figure A-11. (Run No. 9-002)

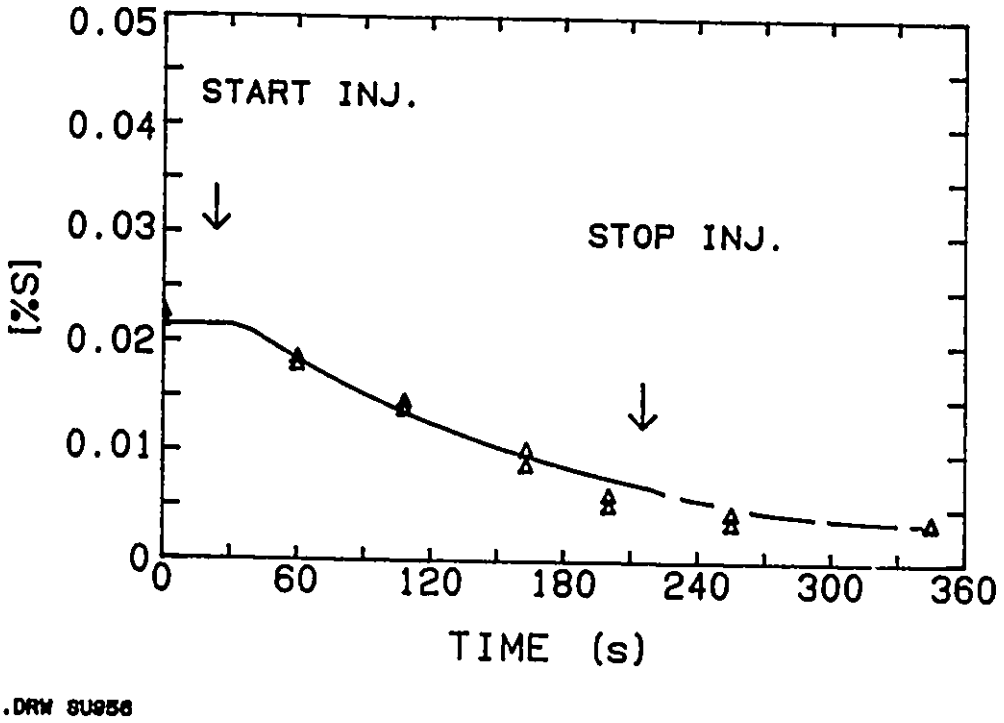

Figure A-13 The change of sulphur content with time during an injection of calcium carbide at 0.21 kg/min and nitrogen gas flow rate 5.0 SLPM into iron-4.2% carbon-0.68% silicon melt with an initial temperature 1372 °C. (Run No. 9-006)

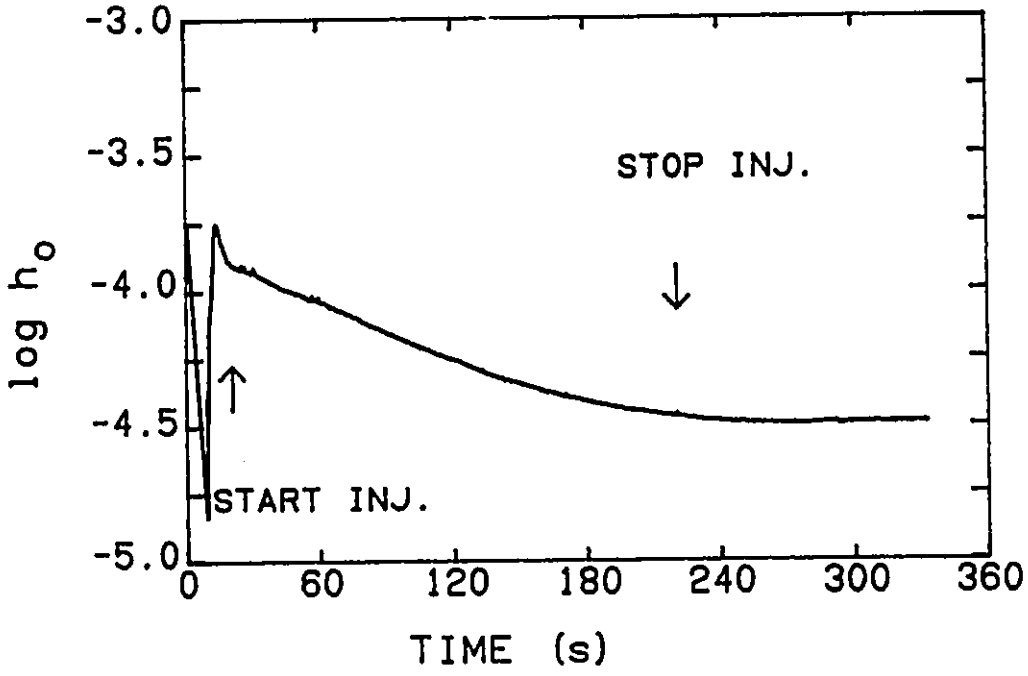

Figure A-14 The oxygen activity during the same injection as in Figure A-13.

(Tan No. 9-006)

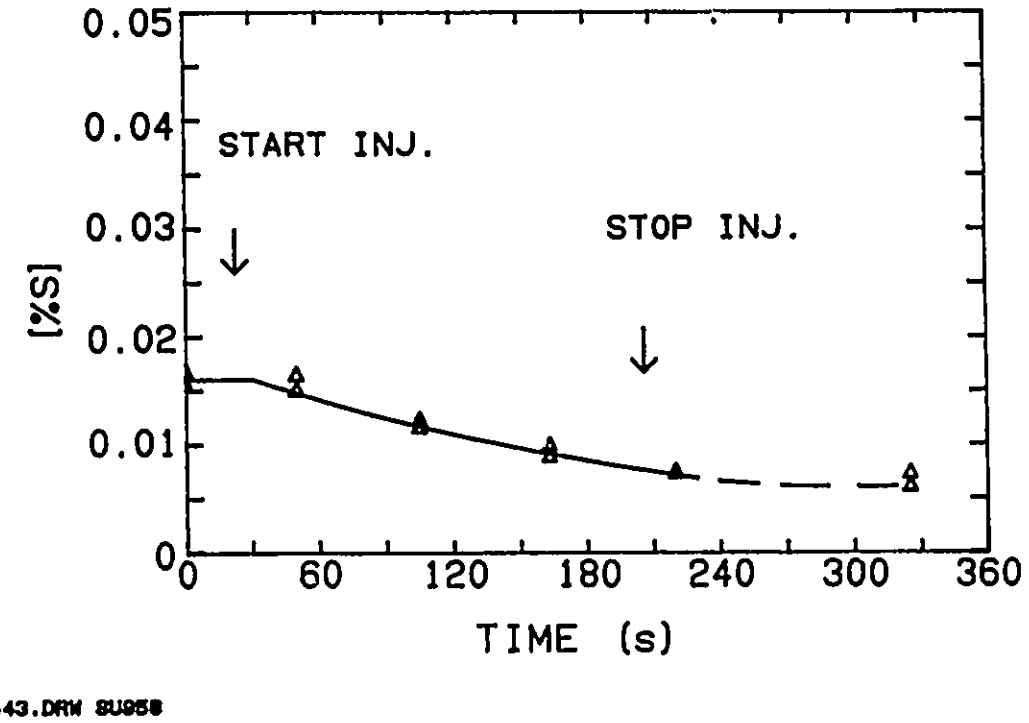

Figure A-15 The change of sulphur content with time during an injection of calcium carbide at 0.09 kg/min and nitrogen gas flow rate 5.2 SLPM into iron-4.2% carbon-0.68% silicon melt with an initial temperature 1365 °C. (Run No. 9-008)

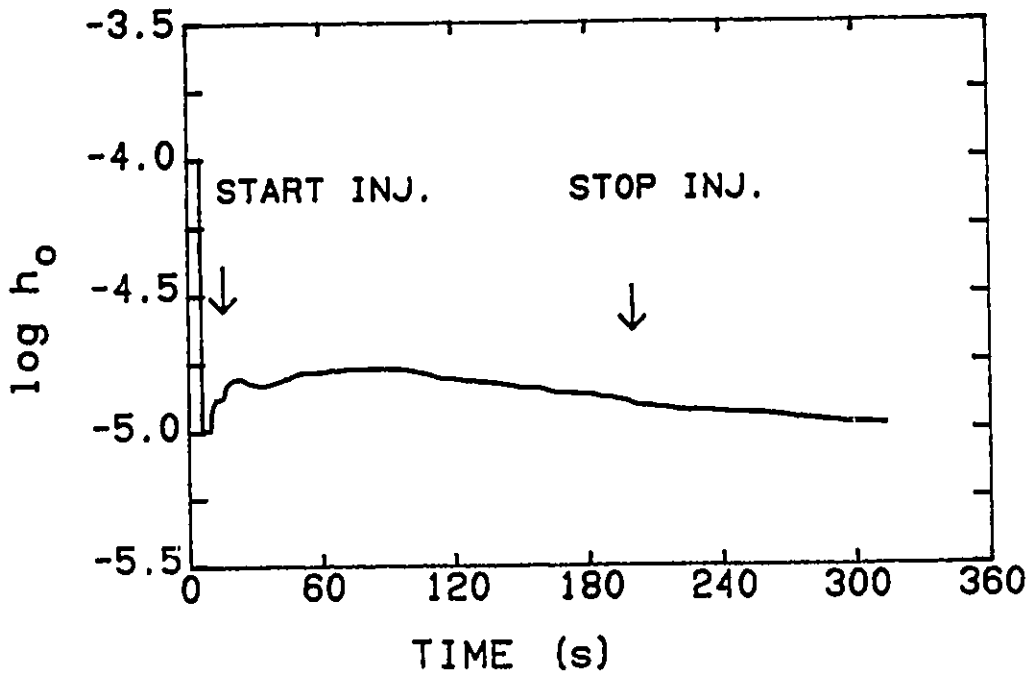

Figure A-16 The oxygen activity during the same injection as in Figure A-15.

(Run No. 9-008)

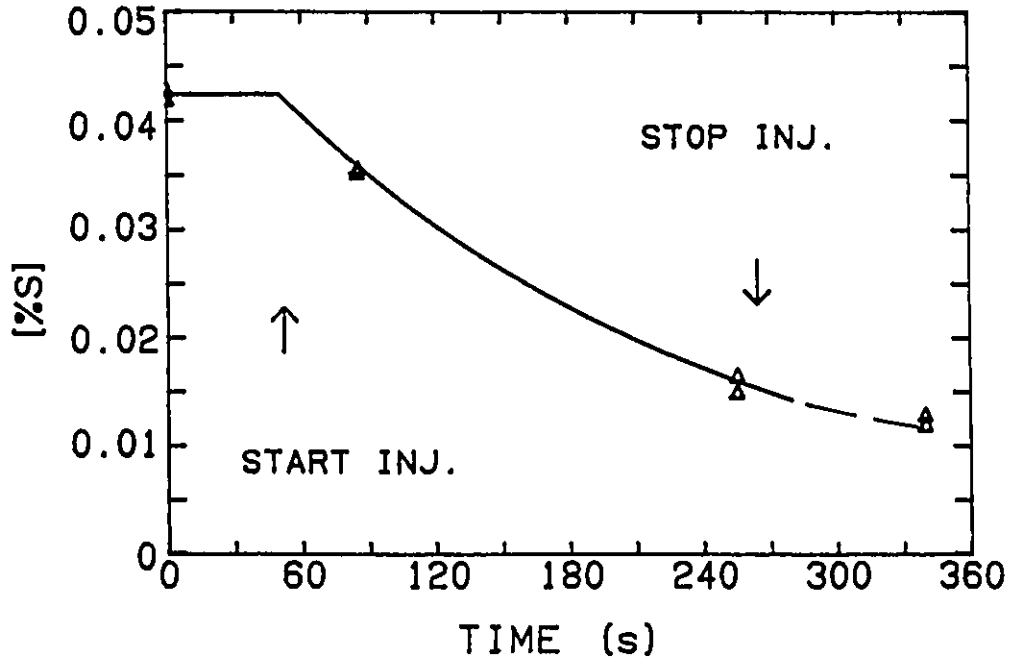

Figure A-17 The change of sulphur content with time during an injection of calcium carbide at 0.13 kg/min and nitrogen gas flow rate 5.0 SLPM into iron-4.2% carbon-0.93% silicon melt with an initial temperature 1350 °C. (Run No. 10-001)

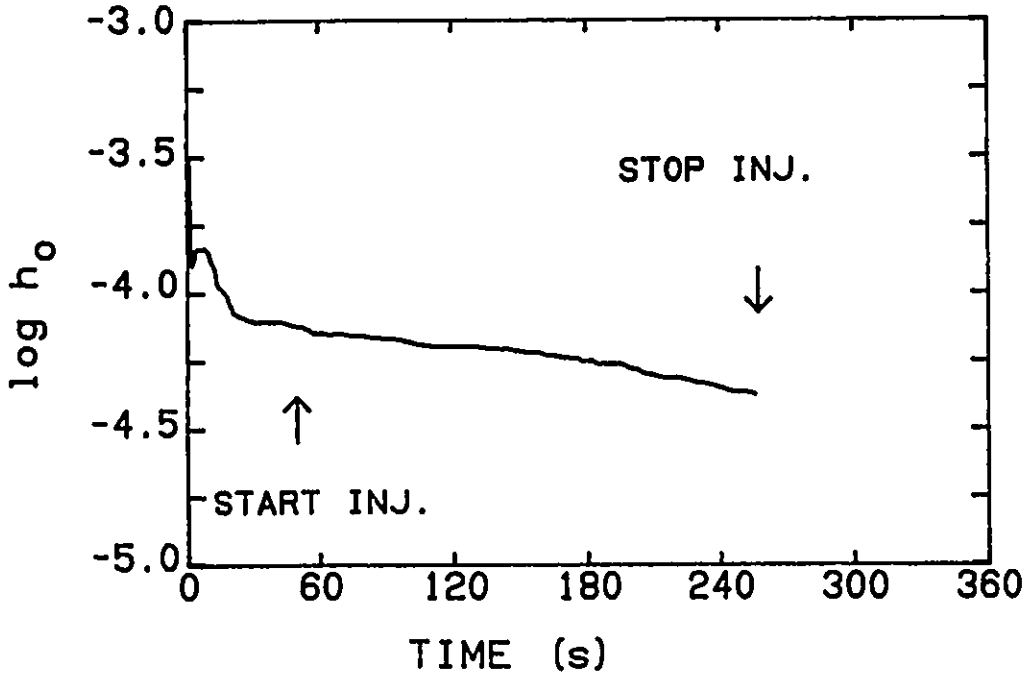

Figure A-18 The oxygen activity during the same injection as in Figure A-17. (Run No. 10-001)

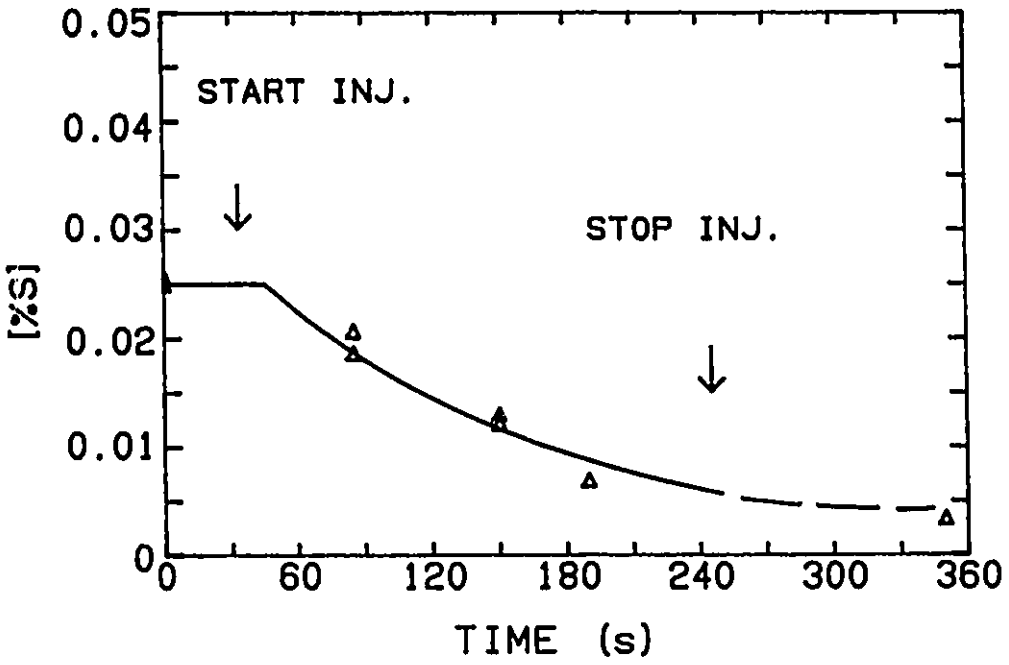

Figure A-19 The change of sulphur content with time during an injection of calcium carbide at 0.25 kg/min and nitrogen gas flow rate 5.0 SLPM into iron-4.2% carbon-1.48% silicon melt with an initial temperature 1355 °C. (Run No. 10-002)

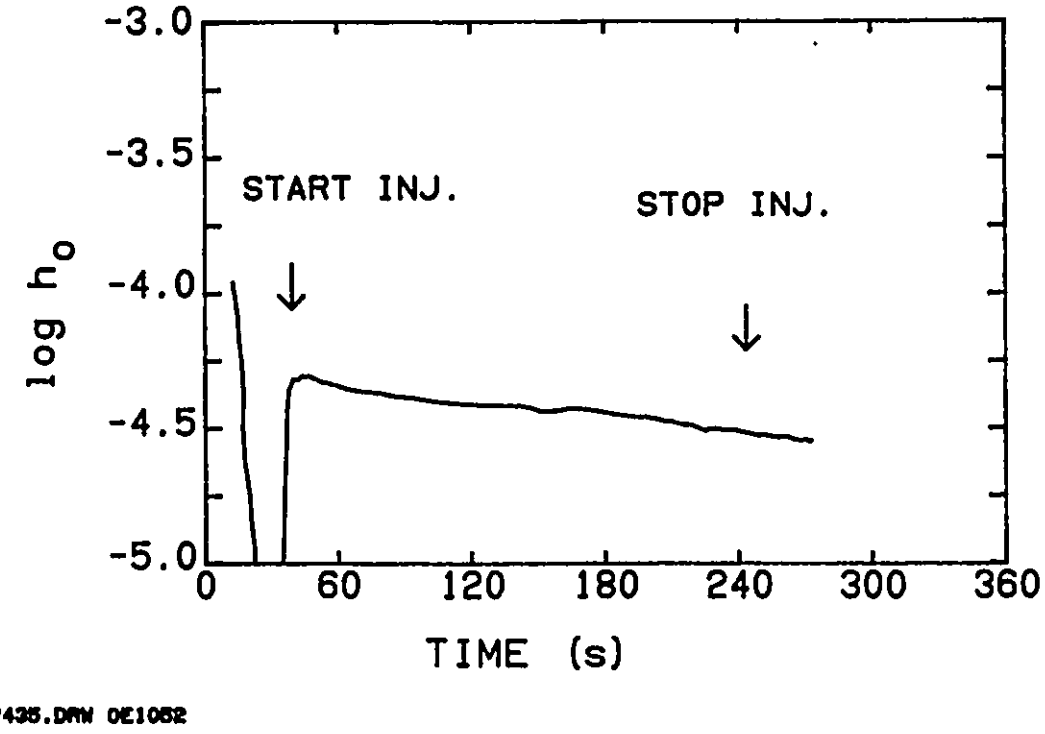

Figure A-20 The oxygen activity during the same injection as in Figure A-19. (Run No. 10-002)

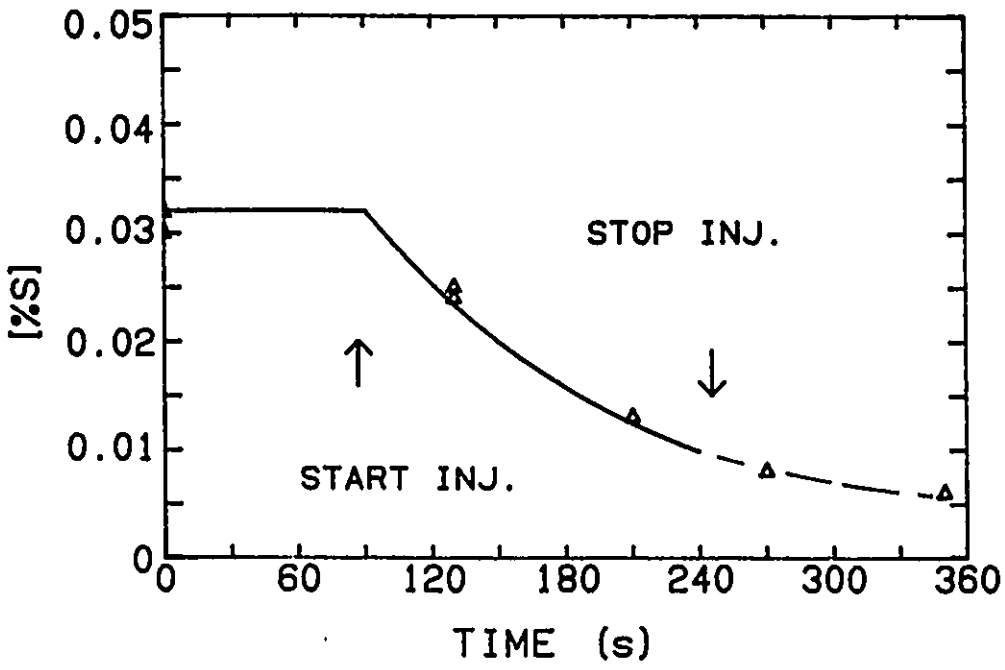

CHP450.DRW SU1054

Figure A-21 The change of sulphur content with time during an injection of calcium carbide at 0.26 kg/min and nitrogen gas flow rate 9.5 SLPM into iron-4.2% carbon-1.47% silicon melt with an initial temperature 1342 °C. (Run No. 10-004)

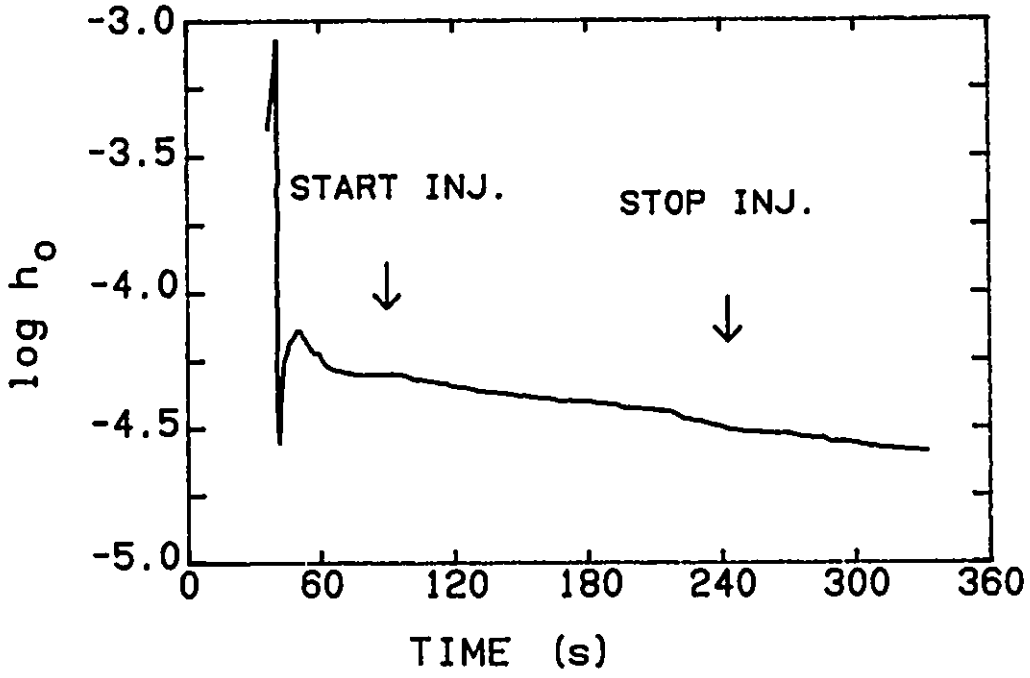

Figure A-22 The oxygen activity during the same injection as in Figure A-21. (Run No. 10-004)

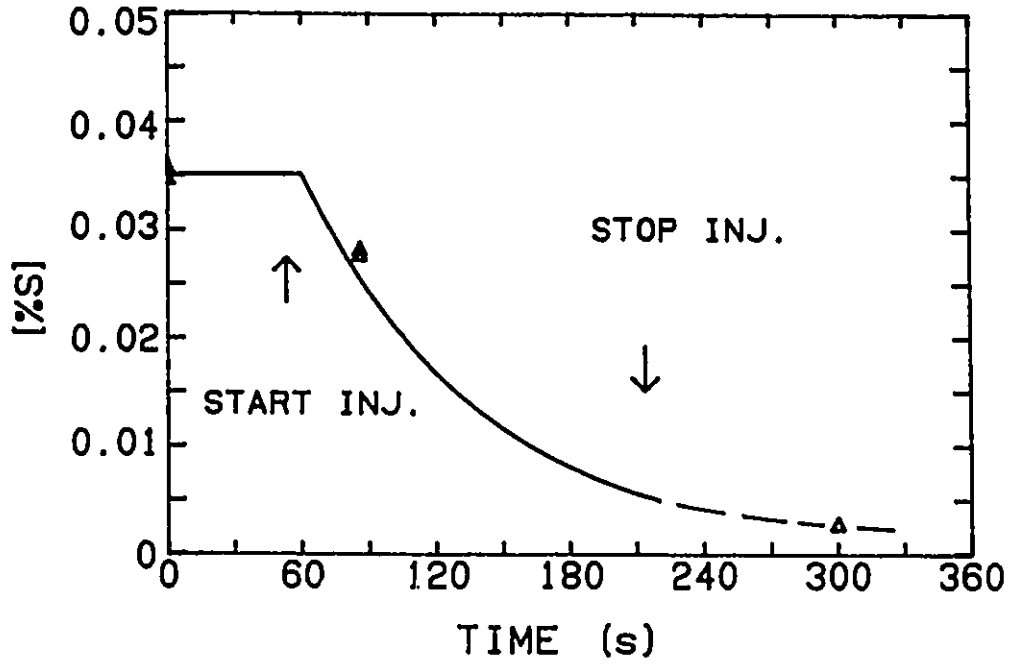

Figure A-23 The change of sulphur content with time during an injection of calcium carbide at 0.58 kg/min and nitrogen gas flow rate 8.5 SLPM into iron-4.2% carbon-1.45% melt with an initial temperature 1348 °C. (Run No. 10-006)

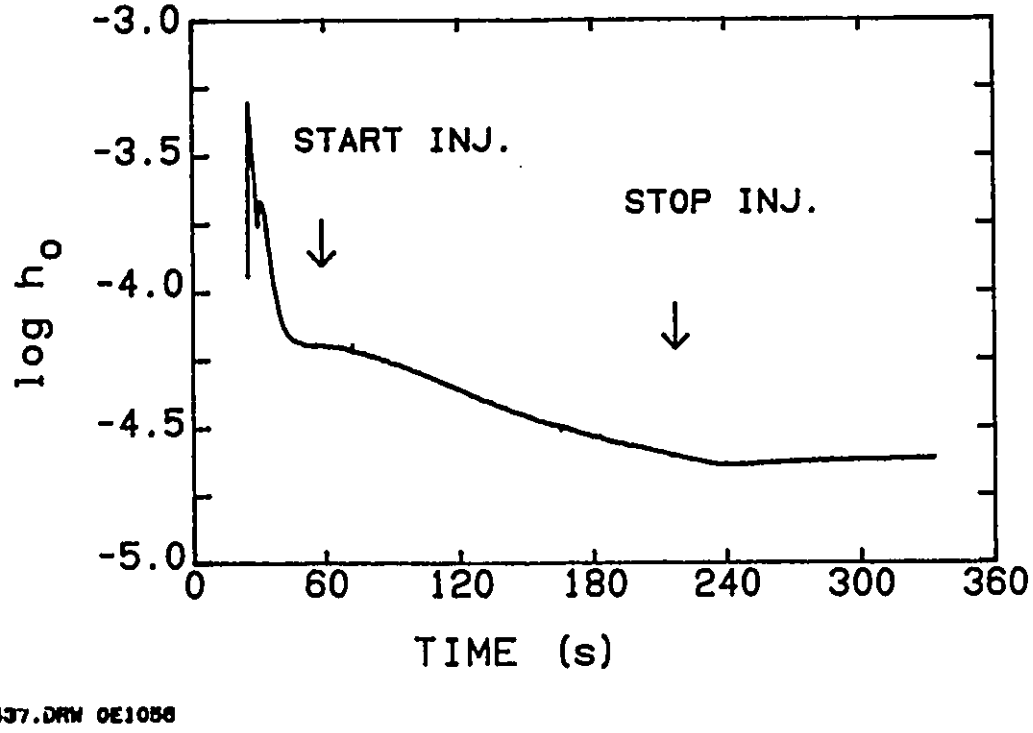

Figure A-24 The oxygen activity during the same injection as in Figure A-23. (Run No. 10-006)

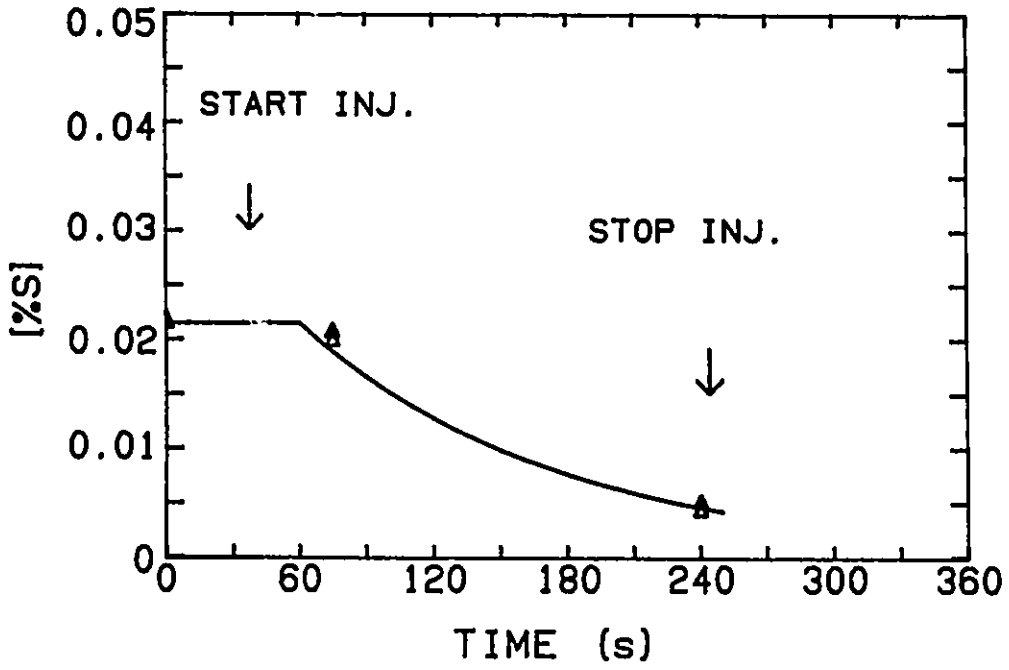

Figure A-25 The change of sulphur content with time during an injection of calcium carbide at 0.28 kg/min and nitrogen gas flow rate 5.0 SLPM into iron-4.2% carbon-0.97% silicon melt with an initial temperature 1353 °C. (Run No. 11-002)

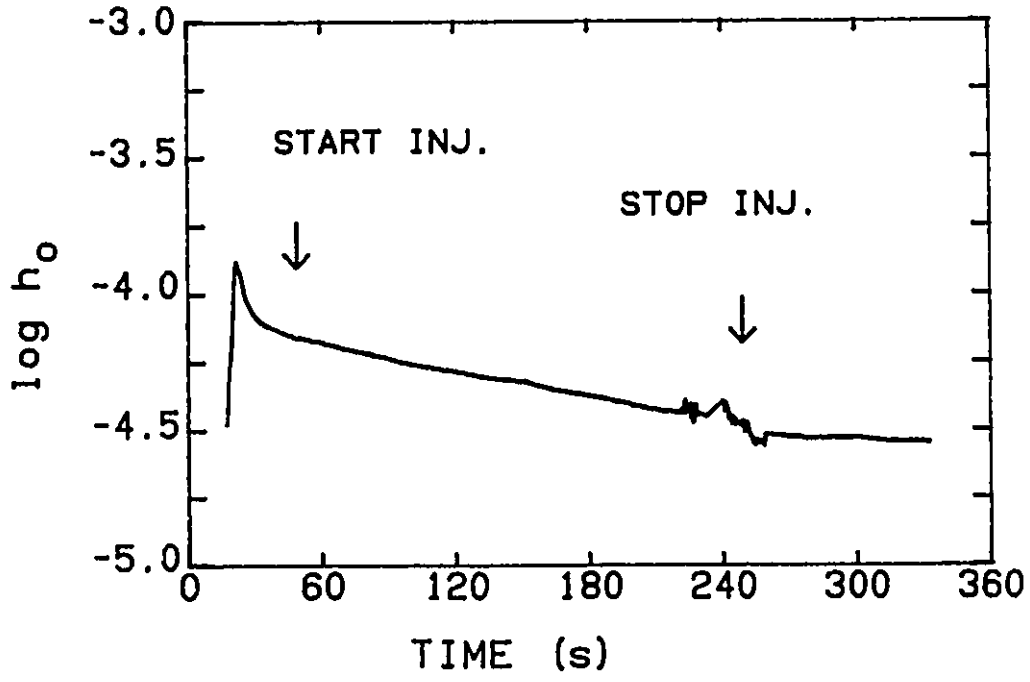

Figure A-26 The oxygen activity during the same injection as in Figure A-25. (Run No. 11-002)

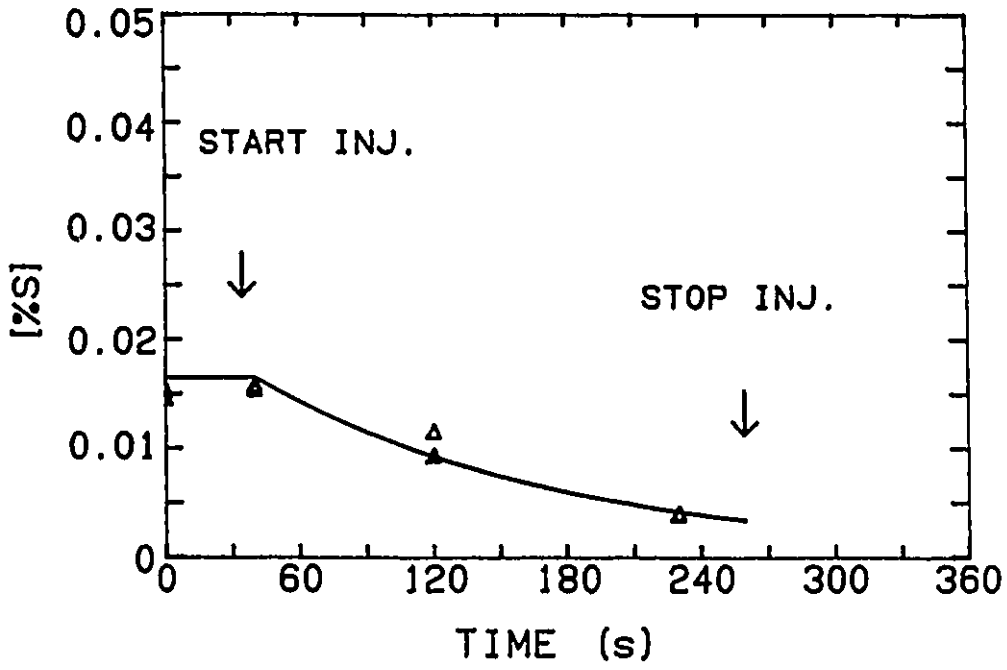

Figure A-27 The change of sulphur content with time during an injection of calcium carbide at 0.22 kg/min and nitrogen gas flow rate 5.2 SLPM into iron-4.2% carbon-1.89% silicon-0.001% aluminium melt with an initial temperature 1348 °C. (Run No. 11-003)

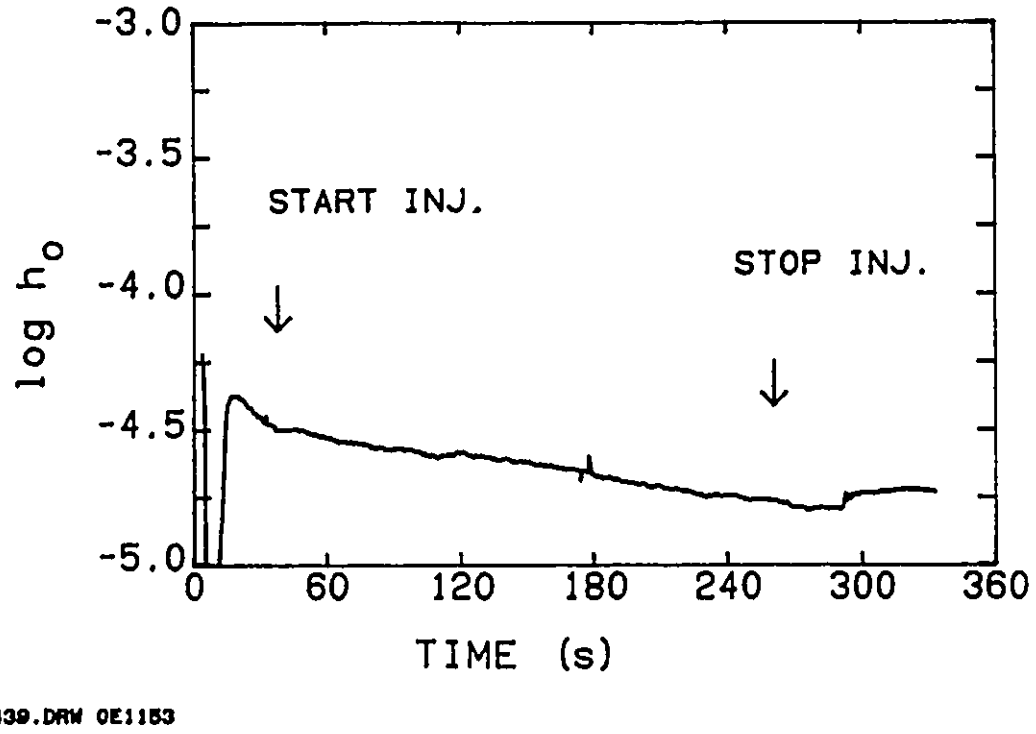

Figure A-28 The oxygen activity during the same injection as in Figure A-27. (Run No. 11-003)

APPENDIX III

THE RATE CONTROLLING STEP OF MASS TRANSFER

APPENDIX III

THE RATE CONTROLLING STEP OF MASS TRANSFER

Chiang, Irons and Lu recently studied calcium carbide desulphurisation of hot metal in 3 t ladles of iron, and developed a model for desulphurisation in the plume [1]. In his further work, Irons summarized the three possible rate controlling steps as [119]

(1). Pumping control. This step controls the rate when the rate of sulphur rich liquid pumped into the plume is relatively low. This is essentially the same as mixing control because the liquid is primarily mixed by convection.

(2). Contact control. This step is diffusion through the boundary layers, but is called contact control because it is very sensitive to the position of the particles. If the particles are in the liquid, the sulphur diffuses through their boundary layers, however, if the particles are positioned on the carrier gas bubble interfaces, sulphur diffuses through the boundary layers around the bubbles.

(3). Product layer control. The calcium sulphide reaction product grows on the outside of the particles as the reaction proceeds, and therefore reactants must diffuse through the layer. Based on the previous work [52], calcium vapour formed by partial decomposition of calcium carbide, is the most likely diffusion species, and furthermore, the rate of diffusion is relatively fast.

As discussed in Section 5.3.2, under the experimental conditions of this work, the mass transfer rate constant for the particles on bubbles is very small as compared with the particles in liquid. Thus, the contribution of the particles on bubbles will not be considered in the following text.

Figure A-29 is a schematic diagram of the three rate controlling steps. The resistance to mass transfer is represented by an analogue electrical circuit. Sulphur is pumped into plume region from the bulk, and then diffuses to the particle. Calcium vapour which is formed by partial decomposition of calcium carbide diffuses through the solid product layer. The overall mass transfer resistance, R_{ov}, is

$$R_{ov} = R_m + R_p + R_s \qquad (s/m^3) \qquad \text{(A-1)}$$

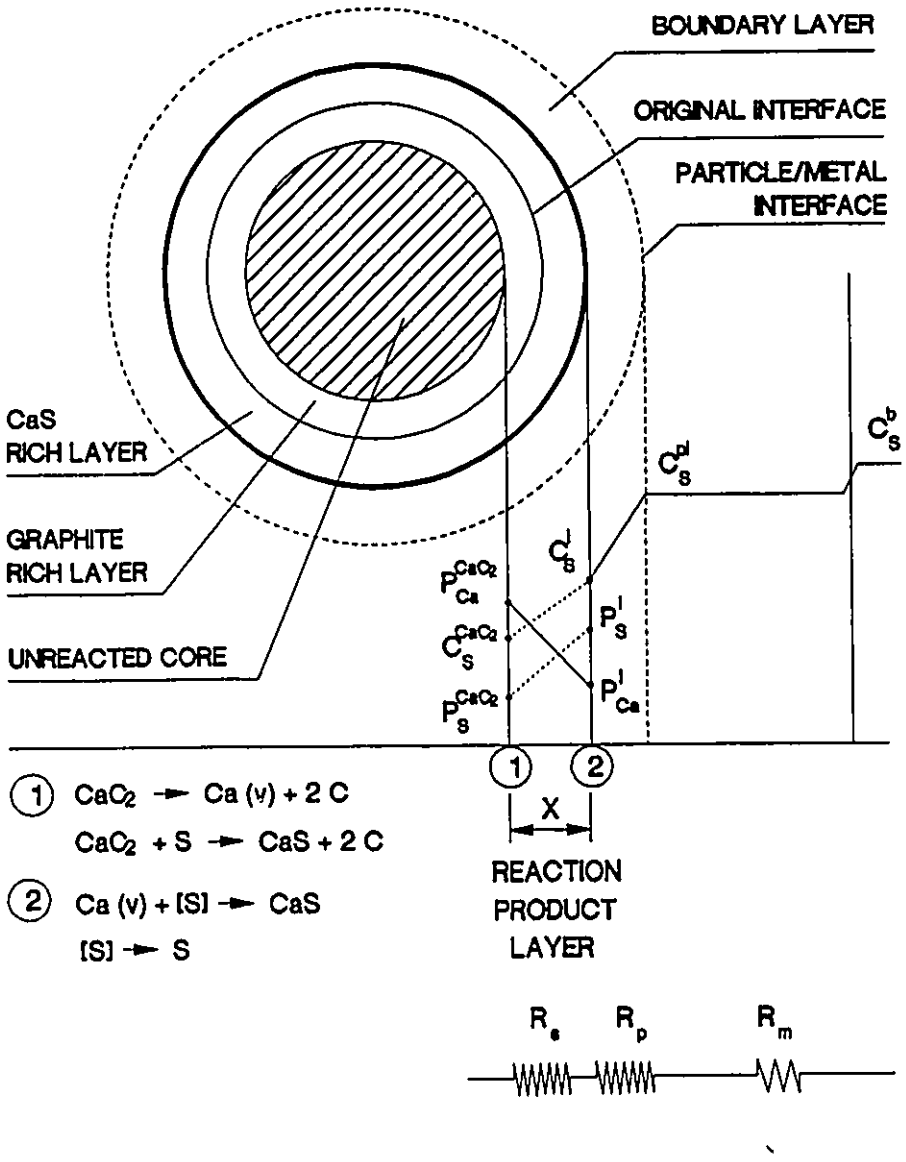

Figure A-29 Schematic representation of the concentration profile of calcium vapour and sulphur along a spherical calcium carbide particle in liquid iron. The electrical circuit analogue for resistance to mass transfer is also shown (Refer to [11] and [119]).

Here, R_m is the mass transfer resistance due to mixing. R_p is the mass transfer resistance due to sulphur diffusion to particles. R_s is the equivalent sulphur transport resistance which is introduced to describe the difficulty of calcium vapour diffusion through the product layer.

In the kinetic model of this work, it was assumed that the desulphurization is controlled by sulphur diffusion through the liquid boundary layer to particles. It was found that the kinetic model agreed very well with the experimental results. However, whether this assumption is reasonable is still a question. This appendix will discuss it in detail.

The rate controlling step can be determined from the relative magnitude of the resistance terms in Equation (A-1). If $R_m >> R_p + R_s$, the rate is controlled by pumping control. If $R_s >> R_p + R_m$, the rate is controlled by product layer control. If $R_p >> R_m + R_s$, the rate is controlled by contact control. The relative magnitude of the resistance terms under the experimental conditions will be estimated in the following text.

1. The Resistance due to Mixing and the Overall Resistance

The rate at which sulphur is pumped into the plume during injection is

$$N - V'_m(C_s^b - C_s^p) \qquad \text{(A-2)}$$

where V'_m is the volumetric flowrate of iron into the plume. The space-time T_s, the liquid volume divided by the liquid volumetric flowrate through the plume, is related to the mixing times in an idealised mixing case by

$$T_m = 3T_s \tag{A-3}$$

where T_m is the mixing time to reach 5 per cent away from perfect mixing [119][125]. According to Murthy and Szekely [125], T_m can be calculated by

$$t_m \sim \frac{8}{\eta^{1/3}} (L_v^2/P_t)^{0.333} \tag{A-4}$$

where L_v is the characteristic vessel dimension (m). The power conversion efficiency, η, is estimated to be 0.5 [125]. P_t is the specific power input (W/kg), which is usually taken as the buoyant potential energy of the gas rising from its point of injection to the bath surface [126]

$$P_t = \frac{2P_R Q_R}{M_l} \ln\left(1 + \frac{\rho_l g Z}{P_a}\right) \tag{A-5}$$

where P_R is the reference pressure (Pa), Q_R is gas flow rate at reference conditions (m^3/s), M_l is the mass of liquid (kg), ρ_l is the liquid density (kg/m^3), g is the gravitational constant (m/s^2), Z is the depth of liquid (m). Then, the resistance to mass transfer due to mixing can be determined by

$$R_m = \frac{T_m}{3V} \qquad \text{(A-6)}$$

where V is the volume of liquid in vessel (m^3).

The experimental conditions and the calculations are summarized in Table AIII-1. The resistance due to mixing is found to be 200 s/m^3 approximately. As mentioned in Section 5.3.2, the overall mass transfer rate constant is of the order of 5×10^{-3} 1/s, The corresponding overall resistance to mass transfer is 2×10^{4} s/m^3, which is 100 times greater than the resistance due to mixing. Thus, under the experimental conditions, mixing is not the rate controlling step.

2. The Resistances due to Sulphur Diffusion through the Liquid Boundary Layer and Calcium Vapour Diffusion through the Solid Product Layer

Because R_m is relatively very small, only two rate controlling steps will be considered in the following, i.e. solid product layer control and liquid boundary layer control.

Talballa et al. investigated the mechanism of desulphurization with calcium carbide [52]. They placed iron-carbon-sulphur alloys in holes in blocks of calcium carbide. According to their experiments, calcium carbide decomposes to form a layer of calcium sulphide over the graphite layer. The layers of

TABLE AIII-1

THE NUMERICAL VALUES FOR ESTIMATION OF THE RESISTANCE DUE TO MIXING

Quantity	Symbol	Unit	Value	From
Vessel Dimension	L_v	m	0.2	/
Power Conversion Efficiency	η	\	0.5	[125]
Gas Flow Rate	Q_R	m^3/s	4.5×10^{-4}	/
Reference Pressure	P_R	$kg/m/s^2$	10^5	/
Atmospheric Pressure	P_a	$kg/m/s^2$	10^5	/
Liquid Density	ρ_l	kg/m^3	7000	[102]
Mass of Liquid	M_l	kg	70	/
Depth of Liquid	Z	m	0.2	/
Specific Potential Energy Input	P_t	W/t	88	Eq. (A-5)
Mixing Time	t_m	s	6	Eq. (A-4)
Space-Time	t_s	s	2	Eq. (A-3)
Volumetric Flow Rate of Liquid	V'_m	m^3/s	5×10^{-3}	[119]
Resistance due to Mixing	R_m	s/m^3	200	Eq. (A-6)
Mass Transfer Rate Constant	K_{ov}	l/s	5×10^{-3}	Table 5.5
Volume of Liquid	V	m^3	0.01	/
Overall Resistance	R_{ov}	s/m^3	2×10^4	/
Resistance Ratio	R_m/R_{ov}	\	0.01	/

/ The data are determined from the experimental conditions.

graphite and calcium sulphide progressively thicken, so that the calcium vapour must diffuse through product layers. Furthermore, Chiang et al. pointed out that the diffusivity of sulphur in a calcium sulphide matrix is approximately 5×10^{-15} m^2/s between 1375 and 1600°C, which is several orders of magnitude too small to explain Talballa's or their own experimental results [1]. They also indicated that at 1350°C, for calcium carbide, the equilibrium partial pressure of calcium vapour is 1.5×10^{-4} atm; for iron with a sulphur content of 0.05 per cent, the equilibrium partial pressure of the sulphur monomer is 1.3×10^{-6} atm [1]. This value is almost two orders of magnitude lower than the value of the equilibrium partial pressure of calcium vapour. Thus, it is clear that sulphur is less likely than calcium to be the dominant transport species in the product layers.

In order to estimate the resistances to mass transfer due to sulphur diffusion through the liquid boundary layer and calcium vapour diffusion through the solid product layer, a simplified model is employed here (Refer to Chiang's work [11]). As shown in Figure A-29, a spherical and uniform calcium carbide particle is placed in liquid iron. A solid product layer is formed on the surface of the particle. The schematic concentration profile around the calcium carbide particle is also shown. The rate of diffusion of sulphur through the boundary layer can be described as:

$$N_S = k_p A(C_S^b - C_S^i) \qquad \text{(A-7)}$$

where A is the surface area of particle (m^2), C_S^b and C_S^i are shown in Figure A-29. The sulphur concentration can be calculated from the sulphur content of weight percent by

$$C_S = \frac{10[\%S]\rho_l}{32} \qquad \text{(A-8)}$$

The mass transfer coefficient to a particle, k_p (m/s) can be estimated by

$$Sh = \frac{k_p d}{D_S} \qquad \text{(A-9)}$$

where d is the diameter of the particle (m), D_S is the diffusivity of sulphur in liquid iron (m^2/s). The Sherwood Number for a spherical particle is usually taken to be 2.

The calcium gradient is assumed to be linearized across the thickness of the layer, X (m). At a low particle utilization, the thickness is relatively small as compared with the particle radius. Then, the rate of diffusion of calcium through the product layer can be estimated by a planar model:

$$N_{Ca} = \frac{D_{eff} A (C_{Ca}^{CaC_2} - C_{Ca}^i)}{X} \qquad \text{(A-10)}$$

where D_{eff} is the effective diffusivity of calcium vapour, which is approximately 7×10^{-7} m^2/s [1]. The calcium partial pressures at the inner surface and the outer surface can be calculated from [15]:

$$\begin{gathered} Ca(v)+2C(s)=CaC_2(S) \\ \Delta G^0=-212970+61.0T \quad (J) \\ \Delta G^0=-RT\ln\frac{1}{P_{Ca}} \end{gathered} \tag{A-11}$$

$$\begin{gathered} Ca(v)+[S]=CaS(S) \\ \Delta G^0=-572960+169.0T \quad (J) \\ \Delta G^0=-RT\ln K_{eq}^{i}=-RT\ln\frac{1}{P_{Ca}h_S} \end{gathered} \tag{A-12}$$

where the standard states for calcium sulphide, calcium carbide and carbon are pure solid; for calcium vapour, one atmosphere; and for sulphur in liquid iron, one weight per cent. R is the gas constant (J/mol/K), T is the temperature (K). Then, the equilibrium calcium vapour concentration can be determined from the calcium partial pressure by

$$C_{Ca}=\frac{1.013\times10^5 P_{Ca}}{RT} \qquad (mol/m^3) \tag{A-13}$$

Based on the mass balance, rearranging and combining Equations (A-7) and (A-10) yield [11]:

$$-(\frac{1}{k_p A}+\frac{X}{D_{eff,S} A K_{eq}})N_S=(C_S^b-\frac{C_S^{CaC_2}}{K_{eq}}) \qquad \text{(A-14)}$$

where $C_S^{CaC_2}$ is the hypothetical concentration in equilibrium with the pure calcium carbide. The equilibrium constant K_{eq} is calculated by

$$\begin{gathered}[S]=S(g) \\ \Delta G^0=293700-82.24T \quad (J) \\ \Delta G^0=-RT\ln K_{eq}\end{gathered} \qquad \text{(A-15)}$$

According to Equation (A-14), one can express the transport resistance due to sulphur diffusion as

$$R_p=\frac{1}{k_p A} \qquad \text{(A-16)}$$

and the resistance due to calcium diffusion as

$$R_s=\frac{X}{D_{eff,S} A K_{eq}} \qquad \text{(A-17)}$$

where $D_{eff,S}$ is the equivalent effective sulphur diffusivity. According to Chiang's work [11], $D_{eff,S}$ can be calculated by

$$D_{eff,S}=D_{eff}\frac{P_{Ca}^{CaC2}-P_{Ca}^{i}}{P_S^i-P_S^{CaC_2}} \qquad \text{(A-18)}$$

At steady state, the rate of calcium diffusion through the product layer is equal to the rate of sulphur diffusion through the liquid boundary layer:

$$N_{Ca}=N_S \qquad \text{(A-19)}$$

By rearranging and combining Equations (A-7)-(A-19), one can calculate the sulphur and calcium concentrations at the solid-liquid interface by:

$$C_S^i=\frac{-(C_{Ca}^{CaC_2}-B_0C_S^b)+\sqrt{(C_{Ca}^{CaC_2}-B_0C_S^b)^2+4B_0B_1}}{2B_0} \qquad \text{(A-20)}$$

$$C_{Ca}^i=\frac{B_1}{C_S^i} \qquad \text{(A-21)}$$

where

$$B_0=\frac{k_pX}{D_{eff}} \qquad \text{(A-22)}$$

$$B_1 = \frac{10^6 \rho_l}{32RTf_S K_{eq}^i} \qquad \text{(A-23)}$$

where the sulphur activity coefficient f_S is 3.3 for the present experimental conditions.

Based on the above equations, the resistances due to sulphur diffusion through the boundary layer can be compared with the resistance due to calcium diffusion through the product layer. The numerical values used for the calculation are summarized in Table AIII-2. The results are shown in Figure A-30 where the ratio of R_p/R_s is plotted as a function of the utilization of the particle and the sulphur concentration of the melts. Here, the utilization is defined as

$$\alpha = \frac{V_R}{V_O} \qquad \text{(A-24)}$$

where V_R is the volume of the reacted calcium carbide, V_O is the original volume of the particle. According to Talballa and his co-worker's work [52], the product layer consists of graphite and calcium sulphide. The volume of the product layer is larger than the volume of the reacted calcium carbide. The volume expansion of calcium carbide due desulphurization is defined as

TABLE AIII-2

THE NUMERICAL VALUES USED FOR ESTIMATION OF THE RESISTANCES DUE TO CALCIUM DIFFUSION AND SULPHUR DIFFUSION

Quantity	Symbol	Unit	Value	From
Utilization of Particle	α	\	0-0.5	/
Volume Expansion	β	\	1.2	/
Sherwood Number	Sh	\	2	Eq. (5.93)
Particle Diameter	d	m	1.2×10^{-5}	/
Diffusivity of Sulphur	m^2/s	D_S	10^{-9}	[46]
Sulphur Content	wt%	[%S]	0.01-0.1	/
Ca(v) Effective Diffusivity	D_{eff}	m^2/s	7×10^{-7}	[1]
Activity Coefficient	f_S	\	3.3	/
Temperature	T	K	1623	/

/ The data are determined from the experimental conditions.

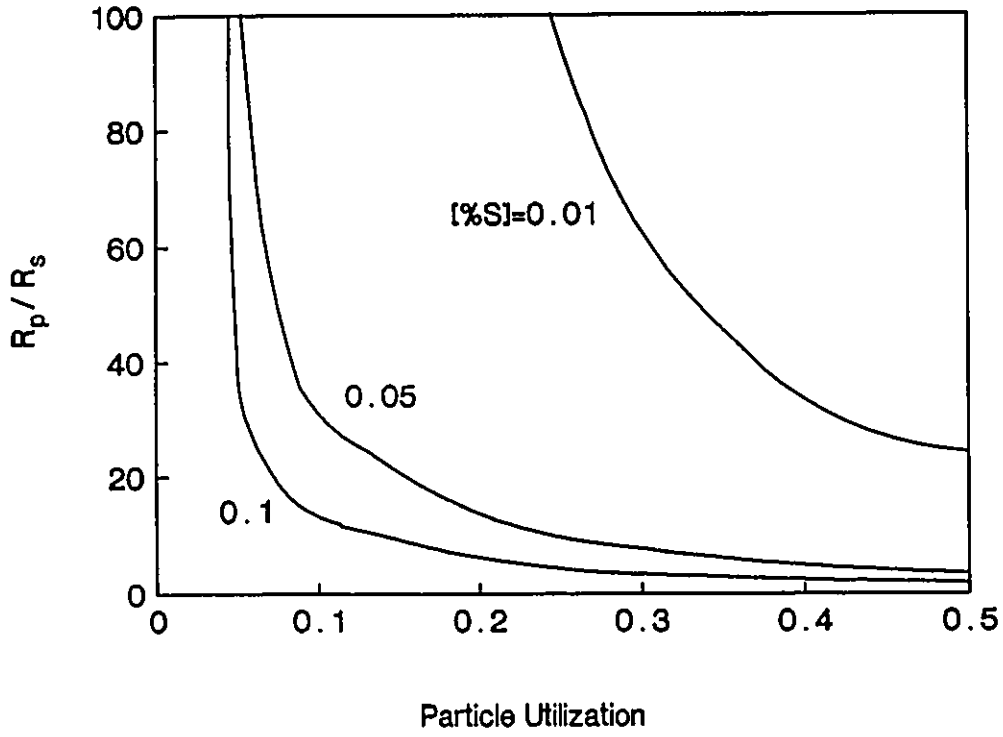

Figure A-30 The Ratio of the resistances due to calcium diffusion (R_s) and sulphur diffusion (R_p) plotted as function of utilization of the particle and sulphur content.

$$\beta = \frac{V_p}{V_R} \qquad \text{(A-25)}$$

where V_p is the volume of the product layer, β is the volume expansion coefficient. Since the density of calcium carbide, calcium sulphide and graphite are known, β can be calculated from the mass balance of calcium carbide desulphurization:

$$CaC_2(s) + [S] = CaS(s) + 2C(s) \qquad \text{(A-26)}$$

Accordingly, the thickness of the product layer is determined by

$$X = \left(\sqrt[3]{1+\alpha\beta-\beta} - \sqrt[3]{1-\beta}\right) r_0 \qquad \text{(A-27)}$$

where r_0 is the radius of the particle.

It can be seen from Figure A-30 that the ratio of R_p/R_s decreases as the sulphur concentration and the particle utilization increase. At 20 per cent utilization, when the sulphur content changes from 0.1 to 0.01 per cent, the ratio of R_p/R_s increases from less than 10 to more than 100. At 0.05 per cent S, when the utilization of the particle increases from 5 to 30 per cent, the ratio of R_p/R_s decreases from 100 to less than 10. In the present experiments, the utilization of the calcium carbide was usually less than 10 per cent of that injected, and the

sulphur contents of the melts were less than 0.05 per cent. As shown in Figure A-30, the resistance due to calcium diffusion through the product layer is more than 50 times greater than that due to sulphur diffusion through the boundary layer. This is sufficient to prove that calcium diffusion through the product layer does not provide significant resistance to mass transfer under the present experimental conditions.

3 Summary

The present analysis demonstrates that under the present experimental conditions, mixing and calcium vapour diffusion through the solid product layer do not significantly control the desulphurization rate during calcium carbide injection. The most important resistance is contact control which depends on mass transport through the liquid boundary layer to the particles surface. This justifies the assumption employed in the present kinetic model.